The Design and Preparation of Programmable Two-Dimensional Materials

Joshua Nicks

A thesis submitted in partial fulfilment of the requirements for the degree of Doctor of Philosophy

The University of Sheffield
Faculty of Science
Department of Chemistry

September 2021

Abstract

Supramolecular two-dimensional materials have emerged as a unique class of 2D materials with highly programmable structures that have seen them utilised in a range of diverse applications. In particular, metal-organic framework nanosheets (MONs) combine the vast external surface areas, nanoscopic dimensions, and hight aspect ratios of other 2D materials with the highly tuneable and periodic structures of metal-organic materials. The vast number of known layered MOFs has served as a useful starting point for the preparation of these nanosheets via top-down exfoliation. In particular, liquid exfoliation *via* ultrasonication has become a common route, but factors that influence this process are not well understood. In this thesis, the programmability of MONs was explored through pre- and post-synthetic processes, and the effects of these structural modifications on the functionality, morphology, and properties of the MONs formed were investigated. Novel supramolecular 2D materials and routes for towards preparation of metal-organic materials were also explored.

In **Chapter 3**, covalent post-synthetic functionalisation of layered MOFs is explored. A layered amino-benzenedicarboxylate framework was partially functionalised with sulfonate chains and exfoliated to form predominantly monolayer nanosheets, owing to the introduction of increased charge to the layers of the framework. These ultrathin MONs were able to efficiently catalyse a two-step acid–base reaction in one pot, with superior performances compared to their unfunctionalised and bulk analogues. In **Chapter 4**, the same layered amino-functionalised framework is converted through post-synthetic functionalisation of the bulk MOF to form azide functionalised frameworks in >99% yield. Ultrasonic liquid exfoliation is then used to form few-layer nanosheets, which are further functionalised through post exfoliation functionalisation using azide-alkyne click chemistry. This direct post-exfoliation functionalisation route enables a range of functional groups to be incorporated in high yields whilst simultaneously tuning the surface chemistry of the nanosheets. Addition of a fluorescent pyrene group to these nanosheets facilitated sensing of nitrobenzene.

Pre-synthetic modifications are explored in **Chapter 5**. An isoreticular series of layered MOFs based on linear benzenedicarboxylate derivatives of different lengths was prepared using two different copper salt sources. Nanosheets prepared from the nitrate source were found to be consistently monolayer, whereas those obtained from the acetate had large thickness and lateral size distributions. This is owed to the reduced particle sizes obtained, due to the increased reactivity of the acetate salt.

In **Chapter 6,** hydrogen bonded-organic nanosheets (HONs) are demonstrated as a novel class of supramolecular 2D materials. Two layered HOFs were prepared through self-assembly between carboxylate and amidinium groups with strong, charge-assisted hydrogen-bonding. Ultrasound-assisted liquid exfoliation readily produced monolayer HONs with micron-sized lateral dimensions, which exhibit remarkable stability even after boiling in water.

A novel approach to the preparation of metal-organic materials is explored in **Chapter 7**. Reactive inkjet printing was demonstrated as a versatile method for the patterning of surfaces with MOFs. An inkjet printer fitted with an angled jetting device was used to print picolitre volumes of separate metal and ligand inks onto a surface, which react to form MOFs. These MOFs could be printed in a variety of shapes, and the technique was successfully applied to a range of MOF architectures. Moreover, this technique allows for printing of multivariate MOF gradients, where the structure is gradually changed from one MOF to another by changing the ratio of ligand or metal ions used.

This thesis demonstrates the enhanced programmability of supramolecular 2D materials compared to their classically structured analogues, particularly in the case of MONs. It also offers insights into the effects of pre- and post-synthetic modifications on the liquid exfoliation of layered MOFs into ultrathin nanosheets. These supramolecular 2D materials are promising nanomaterials with highly controllable surface chemistry, which can be utilised in a number of fields.

Acknowledgements

where you guys go next. **Lee Cox**, Spooner Road wouldn't have been the same without you, thanks for putting up with me.

Listing my whole family here would take most of the page, but I am thankful to each and everyone of you. You have all supported me my entire life to get to this stage, you are all so selfless and giving and I am proud to call you my family. To **my grandparents**, **Craig**, **Mum**, and **Dad**, I would not be who I am today without you. None of this would have been possible without you. Thank you for inspiring me.

Grandad, I wish you could have been here to see this, I hope I've done you proud.

"The reward of the young scientist is the emotional thrill of being the first person in the history of the world to see something or to understand something. Nothing can compare with that experience."

- Prof. Cecilia H. Payne-Gaposchkin

Author's Declaration

This research has been performed between the months of October 2017 and October 2021, within the Department of Chemistry at the University of Sheffield, under the supervision of Dr Jonathan Foster.

I, the author, confirm that the Thesis is my own work. I am aware of the University's Guidance on the Use of Unfair Means (www.sheffield.ac.uk/ssid/unfair-means). This work has not been previously been presented for an award at this, or any other, university.

1st referee   Dr Lance Twyman, The University of Sheffield

2nd referee (external)   Prof. Ross Forgan, The University of Glasgow

List of Publications

Published Manuscripts

1. Tandem catalysis by ultrathin metal–organic nanosheets formed through post-synthetic functionalisation of a layered framework, **Joshua Nicks**, Jiawen Zhang and Jonathan A. Foster, *Chem. Commun.*, 2019, **55**, 8788-8791.

2. Monolayer nanosheets formed by liquid exfoliation of charge-assisted hydrogen-bonded frameworks, **Joshua Nicks**, Stephanie A. Boer, Nicholas G. White and Jonathan A. Foster, *Chem. Sci.*, 2021, **12**, 3322-3327.

3. Metal-organic framework nanosheets (MONs): programmable two-dimensional materials for catalysis, sensing, electronics, and separation applications, **Joshua Nicks**, Kezia Sasitharan, Ram R. R. Prasad, David J. Ashworth and Jonathan A. Foster, *Adv. Funct. Mater.*, 2021, **31**, 2103723.

Manuscripts in Preparation or Submission

1. Post-exfoliation functionalisation of metal-organic framework nanosheets via click chemistry, **Joshua Nicks** and Jonathan A. Foster, *manuscript in preparation.*

2. Liquid exfoliation of a series of expanded layered metal-organic frameworks to form nanosheets, **Joshua Nicks**, Michael Harris, David J. Ashworth, George Danczuk and Jonathan A. Foster, *manuscript in preparation*.

3. Reactive inkjet printing of metal-organic frameworks, David A. Gregory, **Joshua Nicks**, Joaquin Artigas-Arnaudas, Michael Harris, Jonathan A. Foster and Patrick J. Smith, *manuscript submitted for review.*

Other Manuscript Contributions

1. Continuous room temperature synthesis of ultrathin metal-organic framework nanosheets for enhancing the performance of organic photovoltaic cells, David. J. Ashworth, Justin Driver, Kezia Sasitharan, Ram R. R. Prasad, **Joshua Nicks**, Siddharth V. Patwardhan and Jonathan A. Foster, *manuscript in preparation*.

List of Conference Presentations

Oral Presentations

1. **Joshua Nicks** and Jonathan A. Foster, "Post-synthetically functionalised metal-organic nanosheets for tandem catalysis", RSC Macrocyclic and Supramolecular Chemistry Early Career Researcher Meeting (MASC-ECR), Manchester, July **2018**.

2. **Joshua Nicks** and Jonathan A. Foster, "Metal-organic nanosheets as programmable 2D catalysts", RSC Macrocyclic and Supramolecular Chemistry Early Career Researcher Meeting (MASC-ECR), Lincoln, July **2019**.
   - RSC presentation prize

3. **Joshua Nicks** and Jonathan A. Foster, "Metal-organic nanosheets: programmable 2D materials for multi-step catalysis", Solid State Chemistry Christmas Meeting, Liverpool, December **2019**.

4. **Joshua Nicks** and Jonathan A. Foster, "Liquid Exfoliation of Supramolecular Materials into Ultrathin, Programmable Nanosheets", RSC Macrocylic and Supramolecular Chemistry Virtual Seminar Series (vMASC), July **2021**.

Poster Presentations

1. **Joshua Nicks** and Jonathan A. Foster, "Metal-organic nanosheets as programmable 2D catalysts", Chemical Nanoscience Symposium, Newcastle, April **2019**.

2. **Joshua Nicks** and Jonathan A. Foster, "Metal-organic nanosheets as programmable 2D catalysts", RSC Dalton Division Northern Meeting, York, June **2019**.

3. **Joshua Nicks** and Jonathan A. Foster, "Post-synthetically functionalised metal-organic nanosheets as programmable 2D catalysts", RSC Macrocyclic and Supramolecular Chemistry Early Career Researcher Meeting (MASC-ECR), Lincoln, July **2019**.

4. **Joshua Nicks** and Jonathan A. Foster, "Metal-organic nanosheets as programmable 2D catalysts", RSC Poster Twitter Conference, March **2020**.

5. **Joshua Nicks** and Jonathan A. Foster, Metal-Organic Nanosheets (MONs): Programmable 2D Materials for Greener Catalysis, STEM for Britain, Houses of Parliament, Westminster, March **2020**.

6. **Joshua Nicks** and Jonathan A. Foster, "Programmable 2D Materials for Multi-step Catalysis", International Symposium on Macrocyclic and Supramolecular Chemistry (ISMSC) eConference, August **2020**.

7. **Joshua Nicks**, Stephanie A. Boer, Nicholas G. White and Jonathan A. Foster, "Ultrathin Hydrogen-Bonded Organic Nanosheets", RSC Poster Twitter Conference, March **2021**.

Table of Contents

List of Common Abbreviations

Please note, all abbreviations are defined at first use in each chapter. Some abbreviations are only used in one chapter, and are not included in this list, which is intended to summarise terms used across multiple chapters.

2D	Two-dimensional
3D	Three-dimensional
AcO	Acetate (or OAc)
AFM	Atomic force microscopy
ATR	Attenuated total reflectance
CAG	Contact angle goniometry
COF	Covalent organic framework
CON	Covalent organic framework nanosheet
CSD	Cambridge structural database
DLS	Dynamic light scattering
DMF	N,N-dimethylformamide
DMSO	Dimethylsulfoxide
EA	Elemental (micro)analysis
Et$_2$O	Diethyl ether
FT-IR	Fourier-transform infra-red (spectroscopy)
HOF	Hydrogen-bonded organic framework
HON	Hydrogen-bonded organic framework nanosheet
MeCN	Acetonitrile
MOF	Metal-organic framework
MON	Metal-organic framework nanosheet
LC-MS	Liquid chromatography mass spectrometry
NMR	Nuclear magnetic resonance (spectroscopy)
PXRD	Powder X-ray diffractometry/diffraction
PW	Paddlewheel

SBU   Secondary building unit

SC-XRD Single crystal X-ray diffractometry/diffraction

SD   Standard deviation

SEM   Scanning electron microscopy

TGA   Thermal gravimetric analysis

UV-Vis   Ultraviolet-visible (spectroscopy)

ZP   Zeta potential

Abbreviations of Framework Systems and Ligands:

ABDC   2-aminobenzenedicarboxylate (or BDC-NH$_2$)

BDC-N$_3$ 2-azidobenzenedicarboxylate

BDC   1,4-benzenedicarboxylate

BPDC   4,4'-biphenyldicarboxylate

HKUST-1   Hong Kong University of Science and Technology

NDC   Naphthalenedicarboxylate

UiO   University of Oslo (MOF)

ZIF   Zeolitic imidazolate framework

Chapter 1

Research Aims and Objectives

"If you want to have good ideas, you must have many ideas."

- Prof. Linus Pauling

Chapter 1

1.1. Supramolecular 2D Materials

The 2010 Nobel Prize in Physics was awarded to Andre Geim and Konstantin Novoselov "for groundbreaking experiments regarding the two-dimensional material graphene".[1] The subsequent characterisation of its enhanced mechanical,[2] optical,[3] electrical,[4] magnetic,[5] and thermal properties,[6] have lead two-dimensional (2D) materials to become a major player in materials chemistry.[7,8] 2D materials now pervade a range of different research fields, from composite materials to integrated devices.[9] Graphene is the archetype 2D material, consisting of an atomically thin layer of sp^2-hybridised carbon atoms, as shown in Figure 1a. This single atom thickness results in nanosheets that possess a distinct set of properties compared to graphene's bulk form, graphite. These properties have led to the implementation of graphene and its composites in a range of different applications,[7,10] simultaneously sparking interest into other 2D materials.
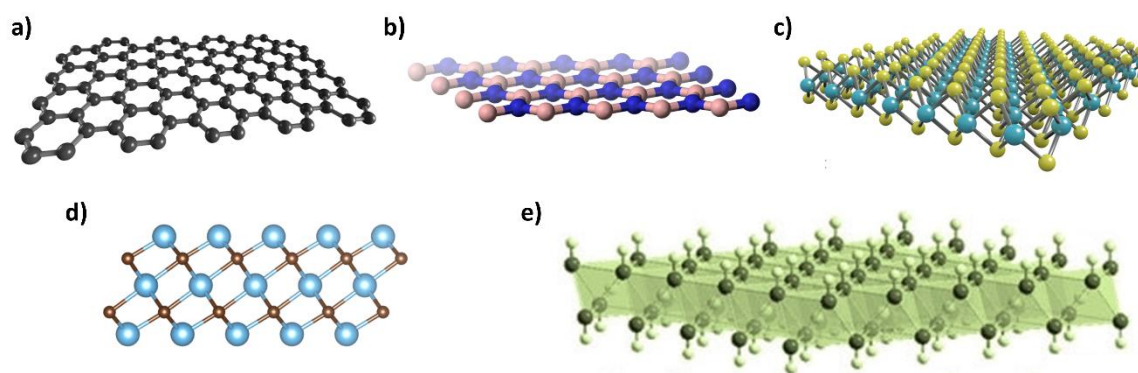
Figure 1. Representations of nanosheets of classically structured 2D materials: **a)** graphene,[1] **b)** hexagonal boron nitride,[11] **c)** molybdenum disulphide,[12] **d)** MXenes,[13] and **e)** layered double hydroxides.[14]

The majority of other classically structured 2D materials are inorganic and based on transition metals or main group elements. These include but are not limited to hexagonal boron nitride,[11] transition metal dichalcogenides,[12] MXenes,[13] and layered double hydroxides,[14] as shown in Figures 1b-e. Many of these bulk materials are naturally abundant, others are not, but all these materials possess similarly remarkable properties to graphene when exfoliated down to few or single layers. To date, these properties have been exploited in a variety of applications, including opto-electronics,[15,16] energy,[17,18] sensing,[19] and biomedical applications.[20] These 2D materials have outperformed standards in many of these fields, and their high surface areas and nanoscopic dimensions expose their actives sites and aid their integration into devices. However, a common issue with these classically structured 2D materials is the limited options available for the modification and optimisation of their structures towards these applications.

This difficulty arises from the simplistic, often mono or binary atomic structures of these materials. In the case of graphene, covalent modification causes a change in hybridisation from sp^2 to sp^3, disrupting the planarity of the layer and negatively impacting the properties of the nanosheets.[21] For inorganic nanosheets, modification is typically achieved by doping, a harsh process which generates defects in the layers, again to the detriment of the desired properties.[22] Furthermore, in both cases these modifications are random in nature, one cannot predict where on the sheet such changes may take place. On the other hand, non-covalent modifications of these materials *via* physisorption do not impact the unique properties of the sheets but instead lead to significantly less robust composite materials.[23] A potential solution to these issues is the use of supramolecular structures.
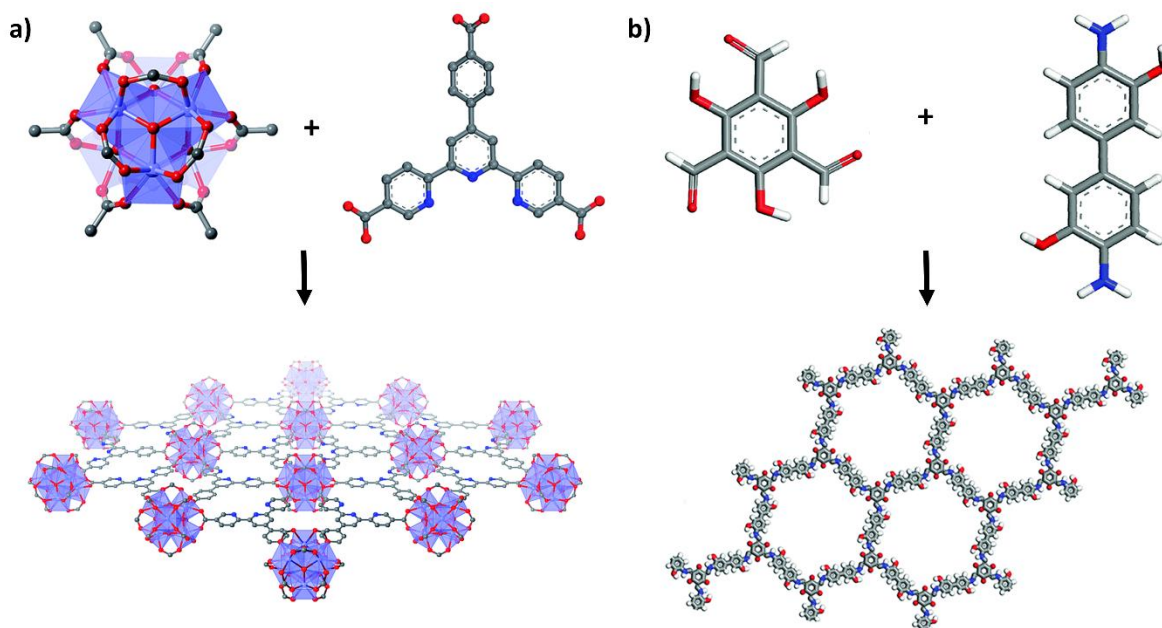
Figure 2. Components and structures of **a)** a MON based on $Hf_6(\mu_3\text{-}O)4(\mu_3\text{-}OH)_4(HCO_2)_6$ secondary building units and 4'-(4-car- boxyphenyl)-[2,2':6',2"-terpyridine]-5,5"-dicarboxylate ligands,[24] and **b)** a CON based on 1,3,5-triformylphloroglucinol and dihydroxybenzidine building blocks.[25]

A supramolecular approach to 2D materials involves the use of molecular building blocks which, upon assembly, form extended and potentially layered 2D structures. The use of these structures introduces the potential for programmability, by modification of the building blocks prior to assembly. Two main sub-classes of supramolecular 2D material have emerged (Figure 2), those formed using dynamic covalent bonds, forming covalent organic framework nanosheets (CONs),[26] or coordination bonds, forming metal-organic framework nanosheets (MONs).[27,28] This thesis focuses primarily on MONs and a detailed review of their properties and applications is provided in **Chapter 2**. The dynamic chemistry of MONs results in a larger potential library of structures, owing to the diversity of framework topologies that can be accessed by combining different secondary building units (SBUs) and organic linkers.[29,30] As such, modifications of these structures can be performed pre-synthetically by varying synthesis conditions, or post-synthetically at reactive sites on the as synthesised framework. Additionally, the periodic nature of these structures means that modifications are performed only at targeted locations on the framework, such as the SBU or a pendant linker moiety, meaning functionalities can be arranged on their surfaces. These potential opportunities associated with MONs make them highly "programmable" in comparison to classically structured 2D materials.

A key theme of this thesis will be the programmability of MONs and in this chapter, we will explore additional concepts which underpin this work. This chapter will also introduce the preparation methods by which MONs can be obtained, and this work will investigate reactive inkjet printing as a novel preparation method for both 3D and 2D MOF architectures. Furthermore, hydrogen-bonded organic nanosheets (HONs) will be introduced as a novel class of supramolecular nanosheet. The aims and objectives for the following chapters of this thesis will be laid out at the end of this chapter.

1.2. Programming of MOF Structures

At the beginning of this project in 2017, research into MONs was still in its infancy, with most reports prior to this focussing on the synthesis of novel systems. During the past four years, the literature has

grown exponentially, and the majority of papers published on MONs now demonstrate an application. This work aims to demonstrate that the isoreticular and post-synthetic chemistries associated with metal-organic frameworks and coordination polymers can be utilised to program the properties of MONs towards desired applications. The large number of known layered metal-organic frameworks (MOFs) make them an attractive starting point for exfoliation into nanosheets.[31] The sizable body of literature on both pre- (reticular) and post-synthetic modifications of three-dimensional MOFs offers a valuable starting point for the programming of MON surfaces.[32–38] These chemistries are an important toolkit for expanding and exploiting the properties of these materials and have been well-studied as a result.

Pre-synthetic modifications can be used to alter MOF components/functionalities or synthesise MOFs with related topologies but expanded/contracted pore sizes and volumes, known as reticular chemistry. This is achieved by replacing either the metal salt, organic linker, or both in the synthetic procedure, the only requirement is that the overall framework topology is maintained. This is perhaps best illustrated by Yaghi *et al.*'s 2002 work which reported an isoreticular series of MOF-5 systems, known as IRMOFs.[39] As shown in Figure 3, both the pore functionality and pore size could be easily modified by substituting the desired linker into the synthetic procedure. Isoreticular chemistry as an approach does come with caveats. The first is that introduction of certain functionalities, such as carboxylic acids, can be impaired by their ability to coordinate to metal ions and thus interfere with the formation of the framework. Furthermore, certain functional groups, such as azides, are often unstable under the solvothermal conditions commonly employed for MOF synthesis, and thus cannot be incorporated in this fashion.
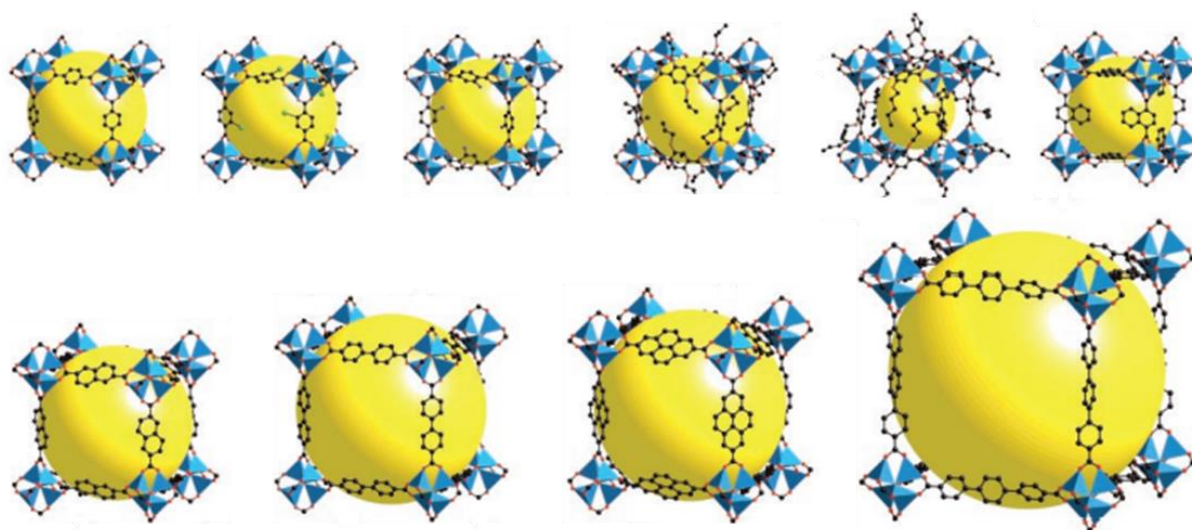
Figure 3. Selected examples of IRMOFs reported by Yaghi and co-workers, demonstrating modification that alter pore functionality (top row) and pore size (bottom row).[39]

Post-synthetic modification (PSM or PSF)[‡] serves as a method to introduce chemical functionality to MOFs that would otherwise prevent or disrupt the formation of the framework if attempted pre-synthetically. As such, PSF offers greater control and versatility over the number and types of functional groups that can be introduced. There are three well-established strategies for performing PSF: covalent functionalisation, coordinative functionalisation, or solvent-assisted ligand exchange

---

[‡]Note that post-synthetic functionalisation (PSF) and post-synthetic modification (PSM) are used interchangeably in the literature. In this thesis, PSF is used as the focus is on introducing functionality to MONs rather than modification of pore size, which is a typical focus in 3D MOF research.

(SALE). Covalent modification involves functionalisation at pendant linker sites, whereas coordinative functionalisation targets the SBU of a MOF. SALE involves an exchange reaction between a MOF and a concentrated solution of the linker to be introduced. Each of these strategies are facile ways of circumventing challenge related to MOF synthesis, and the optimal method typically depends on the MOF architecture being targeted or the desired functionality being introduced.

Covalent PSF has been well-studied in several MOF architectures, particularly those including pendant amine functionalities, as shown in Figure 4.[40] This is owed to the ease in which amine groups can be incorporated into MOFs pre-synthetically, and the breadth of organic reactions in which aromatic amines can participate as nucleophiles. However, covalent PSF has also been extended to other linker reaction sites, including: alkenes,[41] aldehydes,[42] alcohols,[43] halides, and sulfides.[44] These PSF reactions can also be followed by further modifications of the introduced functionality, such as coordinative post-synthetic metalation at introduced binding sites (Figure 4b).[45]

a)

b)
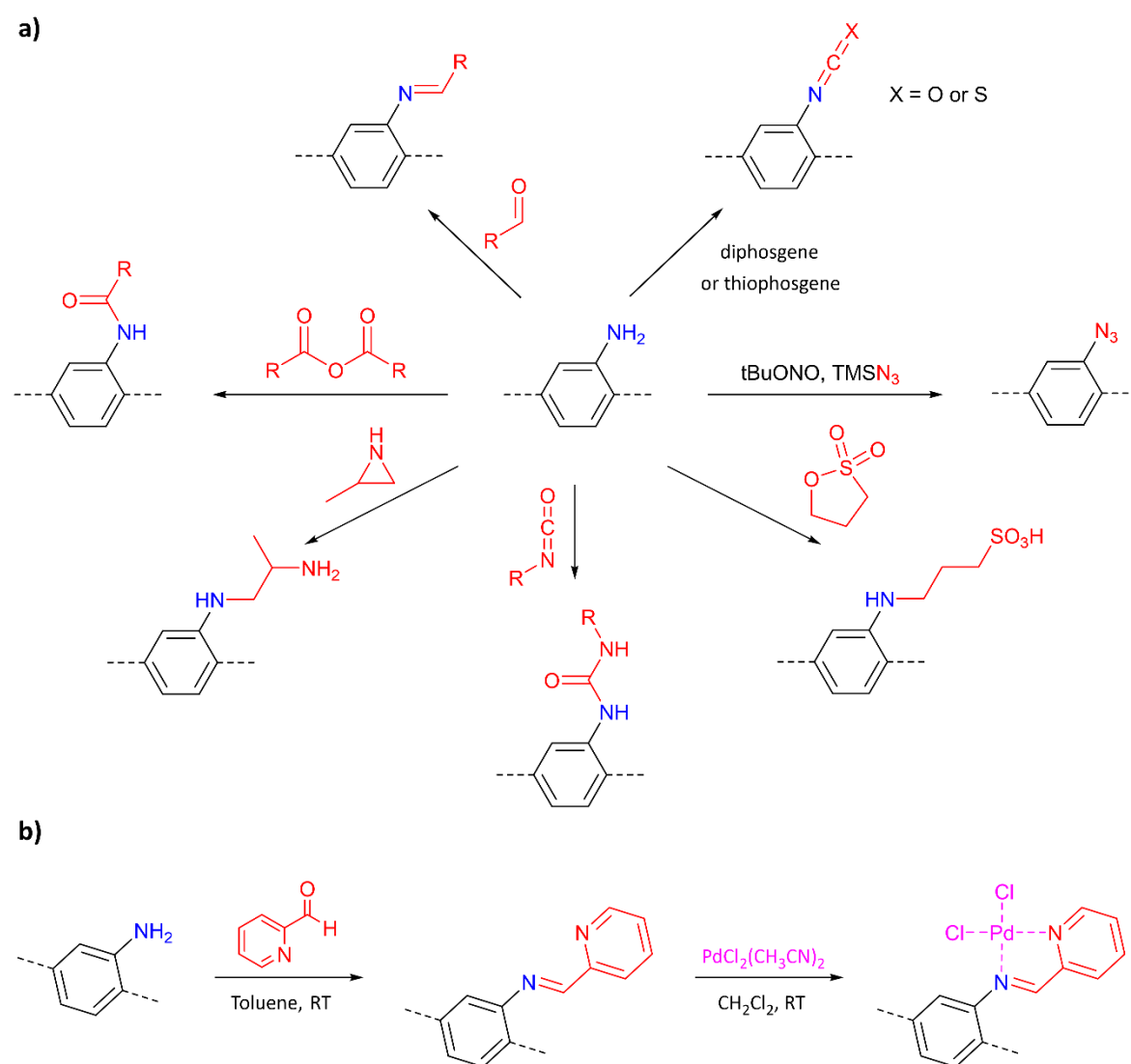
Figure 4. a) Reported PSF reactions of amine-tagged MOFs and their products.[40,46] **b)** The covalent PSF of UMCM-1–NH₂ (left) with 2-pyridinecarboxyaldehyde and subsequent coordinative covalent modification with PdCl₂(CH₃CN)₂ demonstrated by Yaghi and co-workers.[45]

Coordinative PSFs involving metalation at linker sites are well-established,[47] but other common examples involve coordinating ligands, often N-donors, binding to metal nodes of SBUs containing

unsaturated metal sites.[48] For example, Long and co-workers introduced ethylenediamine units to the unsaturated metal sites of the $H_3[(Cu_4Cl)_3(BTTri)_8]$ MOF, as shown in Figure 5a.[49] This modification significantly enhanced the CO_2 uptake at low temperatures.

Reports of SALE are similar, and can either replace fully coordinated linkers throughout the MOF,[50–52] or only pendant linkers on the surfaces of MOFs with larger groups. One such example of this was reported by Kitagawa *et al.*, who decorated the surface of DMOF-1 with carboxylic acid-functionalised BODIPY groups by linker exchange at SBUs exposed on the MOF surfaces, shown in Figure 5b.[53] This technique was one of the first to offer control over pore *vs.* surface functionalisation using a steric approach.
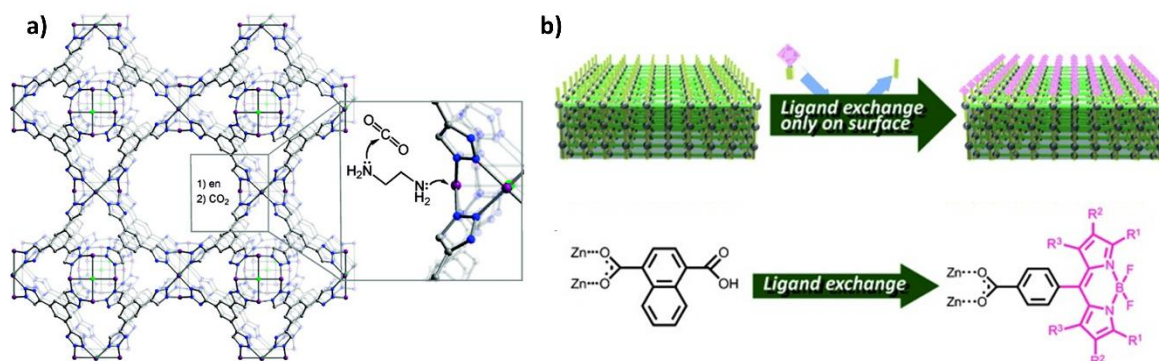
Figure 5. a) Long's coordinative PSF of a MOF at unsaturated metal sites with ethylenediamine for the enhanced adsorption of CO_2.[49] **b)** Surface PSF of DMOF-1 *via* ligand exchange with carboxylate-functionalised BODIPY dyes.[53]

Each of the previous methods for the programming of MOF structures can also be utilised as routes towards multi-functional systems. Through incorporation of multiple metal ions or organic linkers in the initial synthesis procedure, multi-component MOFs can be obtained that can exhibit more than one functionality.[54,55] This can also be achieved post-synthetically, either by a modification that does not go to completion, or by performing multiple PSF procedures. This can either be orthogonal PSF of multiple different reactive moieties,[56,57] or multiple different PSF reactions at a single reactive moiety.[58–60]

A pioneering example of multi-component MOFs comes from Yaghi *et al.*, who reported 23 MOFs incorporating different ratios of the linkers shown in Figure 6a by a reticular chemistry method.[61] Subsets of these MOFs were shown to have enhanced H_2 storage capacities, superior to their analogous single-component systems, demonstrating that multi-functional MOFs can exhibit properties that exceed the sum of their parts. Another example comes from Cohen and co-workers in 2011, who prepared a multi-component UiO-66 framework incorporating both amino- and bromo-benzenedicarboxylate linkers.[62] The authors then demonstrated orthogonal PSF at both sites, performing nucleophilic aromatic substitution of a cyanide group at the bromo- site, and a nucleophilic reaction of the amino- site with acetic anhydride, as shown in Figure 6b.
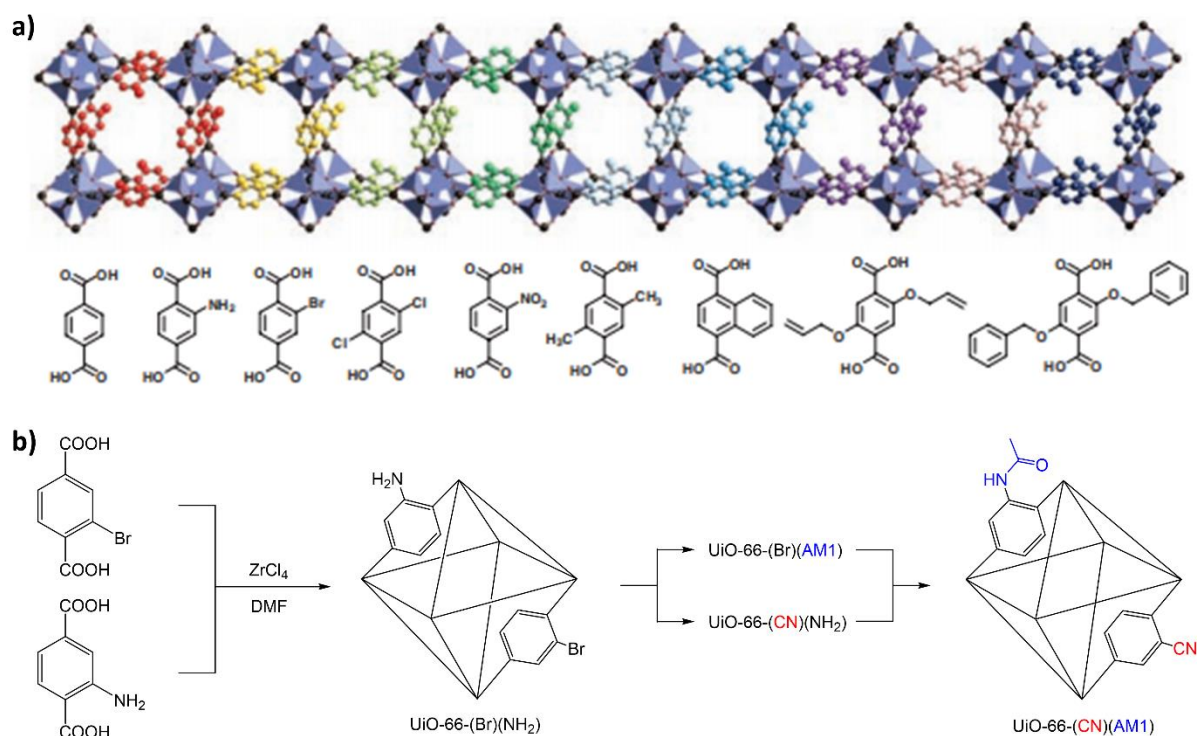
Figure 6. a) The linkers incorporated pre-synthetically into multi-component MOFs by Yaghi *et al.*[61] **b)** The procedure designed by Cohen *et al.* for post-synthetic functionalisation of a multi-component UiO-66 system.[62]

1.3. Programming of MON Surfaces

Though the discussed methods of MOF programming have been thoroughly demonstrated and utilised in a range of applications, few reports had exploited these methods for the programming of MONs prior to the beginning of this work. However, over the past four years, more reports on their use have been published.

A handful of authors have demonstrated the synthesis of series of MON systems with varying surface functionalities through isoreticular modification. Within the Foster group, research has focused on modifying the surface chemistry of MONs by introducing substituents of differing properties to the organic linkers used to synthesise the layered MOFs. Their early studies used Cu_2-paddlewheel systems incorporating benzenedicarboxylate linkers functionalised with alkyl-ether chains at the 2- and 5- positions.[63,64] As shown in Figure 7a, one system used hydrophilic methoxy-propyl chains whereas the other used more hydrophobic pentyl chains. Exfoliation of the two materials in a range of solvents with varying polarities demonstrated substantial differences in final concentrations of these systems. A similar study using differing alkyl chain length substituents (propyl – pentyl), showed shorter alkyl chains resulted in higher concentrations of exfoliated material in suspension.[65] The average thickness of these MONs was found to decrease from 35 ± 26 to 20 ± 12 nm with increasing chain length, shown in Figure 7b, indicating that the choice of ligand substituent can be used to tune nanosheet structure and properties. Finally, Ashworth and Foster reported a multi-component approach utilising both different length chains and differing hydrophilicities.[66] Blending of ligands with hydrophilic and hydrophobic moieties resulted in multi-component MONs which demonstrated enhanced dispersion in both polar and apolar solvents compared to the monofunctional systems. Furthermore, incorporation of multiple alkyl chains of different lengths allowed for the inclusion of ligands which do not form the framework structure individually.
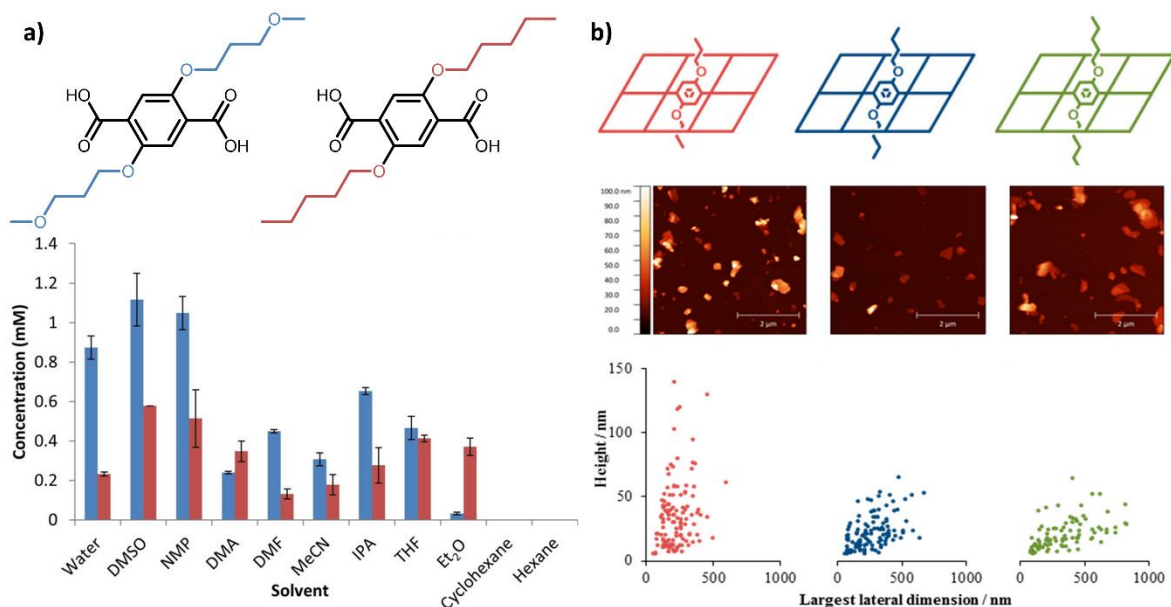
Figure 7. a) The hydrophilic (blue) and hydrophobic (red) linkers incorporated into Cu_2-PW MONs by Foster and Ashworth *et al.* and a bar chart representing the concentrations of the exfoliated systems in solvents of differing polarities.[64] **b)** Representations of MONs incorporating differing length alkyl chains and topographic AFM images of the nanosheets with associated scatter plots of their dimensions.[65]

Similar examples of modifying MON surfaces pre-synthetically have been reported by Coronado *et al.* and Zhao *et al.*, who both used isoreticular synthesis to demonstrate a series of novel MONs with differing exposed functionalities. Coronado *et al.* reported a series of five isostructural MONs based on Fe(II) centres and different benzimidazole linkers, as shown in Figure 8a.[67] The authors observed direct consequence on the systems' contact angle with water when altering the exposed functionality. Similarly, Zhao and co-workers reported the synthesis of NUS-8 nanosheets based on Zr_6 clusters and benzenetribenzoate linkers with differing R groups on the central benzene ring (R= H, CH_3, NH_2).[68] A final example of exploiting isoreticular chemistries was reported by Cui *et al.*, who demonstrated that MONs of opposite chiralities can be obtained by alternating the chirality of the linker used during synthesis. This pioneering example of chirality in MONs demonstrated high enantioselectivity in both catalysis and sensing applications.[69]
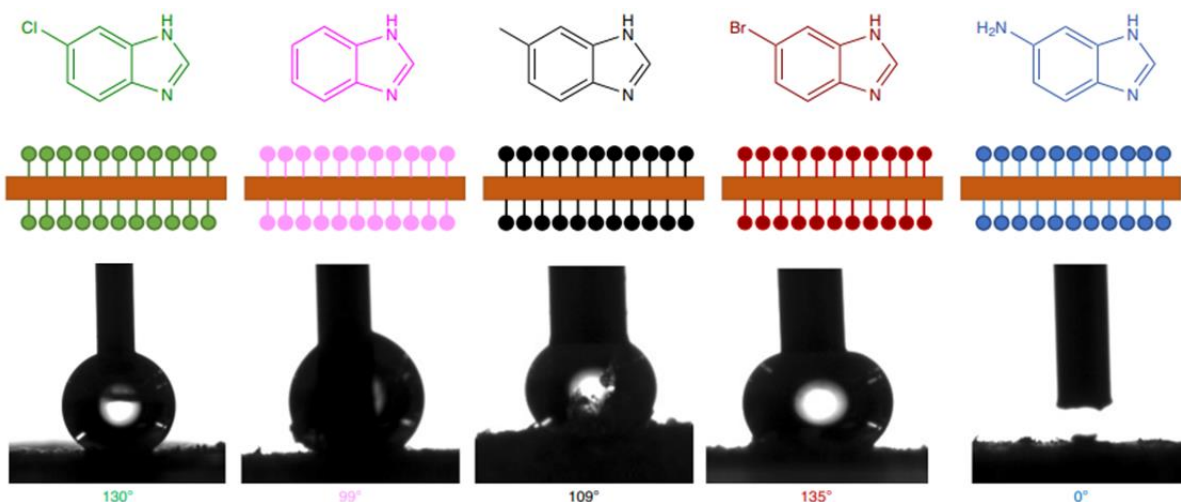
**Figure 8.** Illustrations of pre-synthetic surface modification in the MUV-1-X nanosheets reported by Coronado *et al.*, and images of the contact angles with water on each surface.[67]

Other isoreticular modifications have focused on altering the pore size of nanosheets by shortening or lengthening of the organic linker. This was first demonstrated by Gascon *et al.* in 2015, who amongst other systems, used a layering approach to synthesise both CuBDC nanosheets and Cu(2,6-NDC) nanosheets,[70] but this has also been demonstrated by Fu *et al.* more recently in 2019.[71] Neither of these reports investigated any difference in properties of the MONs based on this isoreticular expansion, instead focussing on incorporation within polymer membranes or fibre composites.

Perhaps the most reported example of MON programming is the altering of metal ions or nodes, which is often performed to tune the opto-electronic properties of the resulting nanosheets. This is well demonstrated in Zeng *et al.*'s work, where they observe a change in conductivity from semiconducting to metallic by substitution of Cu for Ni in $M_3(HITP)_2$ (HITP = hexaiminotriphenylene) MONs.[72] Nishihara and co-workers observed electrochromic behaviour in nanosheets films of their tris(terpyridyl)-based nanosheets, with different colours observed upon reduction for Co and Fe nanosheets.[73] Such systems based on square planar metal nodes and highly conjugated organic linkers have been frequently shown to lend themselves towards isoreticular modifications.[74–77] Furthermore, the electronics of such MONs can be further optimised by using multiple metals during the synthesis, and tuning the ratios based on the desired properties.[78] Porphyrin-based MONs offer two distinct metal sites, the metal node and the porphyrin centre. Ang and Hong have utilised tetracarboxyphenylporphyrin (TCPP) to construct nanosheets with different metals at each sites, by incorporating Fe(II) within the porphyrin centre and Zn, Cu, or Co at the paddlewheel nodes.[79]

Using benzenedicarboxylate derivatives (BDC, ABDC, DOBDC), numerous authors have reported multi-metal nanosheets in which varying the metals used or the stoichiometry of these metals in the MON structures has a significant effect on the final properties of the nanosheets.[80–88] An early example of this by Tang and co-workers shows that NiCo(BDC) MONs, compared to single metal NiBDC and CoBDC systems, have significantly reduced Tafel slopes and enhanced oxygen evolution reaction activities.[89] A more recent example reports the preparation of tri-metallic MONs incorporating Ni, Co, and Fe in a 2:2:1 ratio using benzenedicarboxylate linkers. These nanosheets also exhibited efficient oxygen evolution reaction activity with a similar Tafel slope of 48.1 mV dec^{-1}.[90]
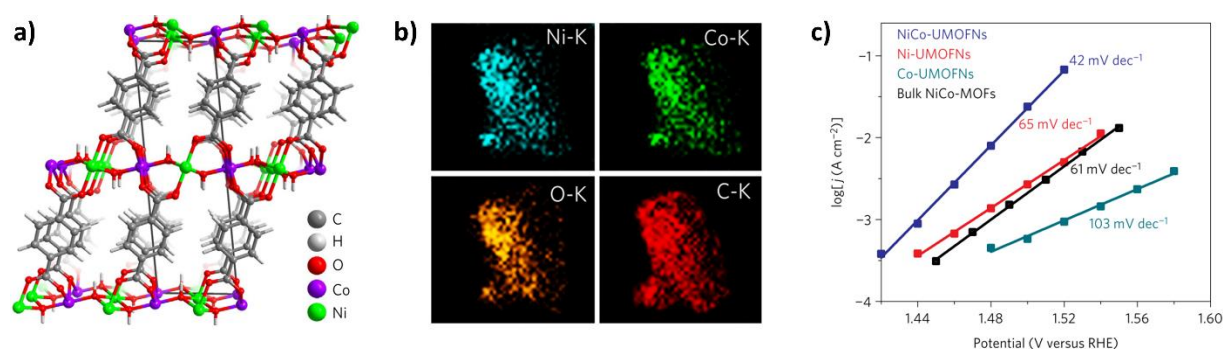
Figure 9. a) Crystal structure of the NiCo MONs reported by Tang *et al.*, **b)** TEM-EDS mapping images of NiCo MONs indicating incorporation of Ni and Co atoms throughout the material, and **c)** Tafel plots of NiCo MONs, Ni MONs, Co MONs and bulk NiCo MOFs, a flatter Tafel slope indicates the ease by which an electrochemical reaction can proceed.[89]

Almost all reports of post-synthetic functionalisation are limited to Zr_6/Hf_6 or Zr_{12}/Hf_{12}-type systems. The only notable exception is a report on transmetalation of Zn^{2+} metal nodes to Fe^{2+}, Co^{2+}, and Pb^{2+} in highly conjugated square planar-type MONs by Schlüter *et al.*[91] There are multiple reasons why Zr_6/Hf_6-type MONs are attractive for post-synthetic functionalisations: (1) these MONs are typically prepared by incorporation of monotopic capping agents to the SBU's which can be post-synthetically

exchanged, (2) these systems have a variety of topologies and can facilely incorporate linkers with different functionalities pre-synthetically, and (3) Zr_6/Hf_6 clusters are highly stable and thus these systems can be functionalised by a range of reactions in a variety of reaction media. Most of the research in this area has been performed by the groups of Wenbin Lin and Cheng Wang, who have demonstrated multiple methods for the modification of these materials.

The first report from Wang and Lin *et al.* came in 2016, where the authors utilised a pre-synthetic method to incorporate equal ratios of benzenetribenzoate and 4'-(4- benzoate)-(2,2',2''-terpyridine)-5,5''-dicarboxylate into a single MON, followed by PSF of the terpyridine moiety with $FeBr_2$ to introduce catalytically active Fe sites.[92] This pre-synthetic incorporation of metal binding sites would then become a staple of their future work,[24,93–98] and also become adopted by other authors.[99,100] In 2017, the authors combined this approach with coordinative PSF, by substituting the capping groups on the Hf_6 clusters of their MONs with gluconic acid, which increased the hydrophilicity of the nanosheets.[101] The authors and would then extend this method by attaching groups to the clusters capable of binding metal complexes,[102–104] capable of further organic reactions,[105] or photoactive groups.[98,106–108] From this point, Lin and Wang would instead exploit pre-synthetic incorporation of metal complexes at linker sites, in combination with post-synthetic modification of the clusters, allowing for the arrangement of multiple functional sites on one nanosheet surface. By utilising pre-synthetic metalation rather than post-synthetic metalation, the authors are able to achieve full conversion of binding sites, negating any unwanted side reactions during future modifications.[96,105,109,110] A final, unique example of covalent PSF from Lin *et al.* in 2021. The authors utilised amino- functionalised benzenetribenzoate linkers in Zr_6-based nanosheets to introduce isothiocyanate-tagged dyes by formation of a thiourea group.[107]
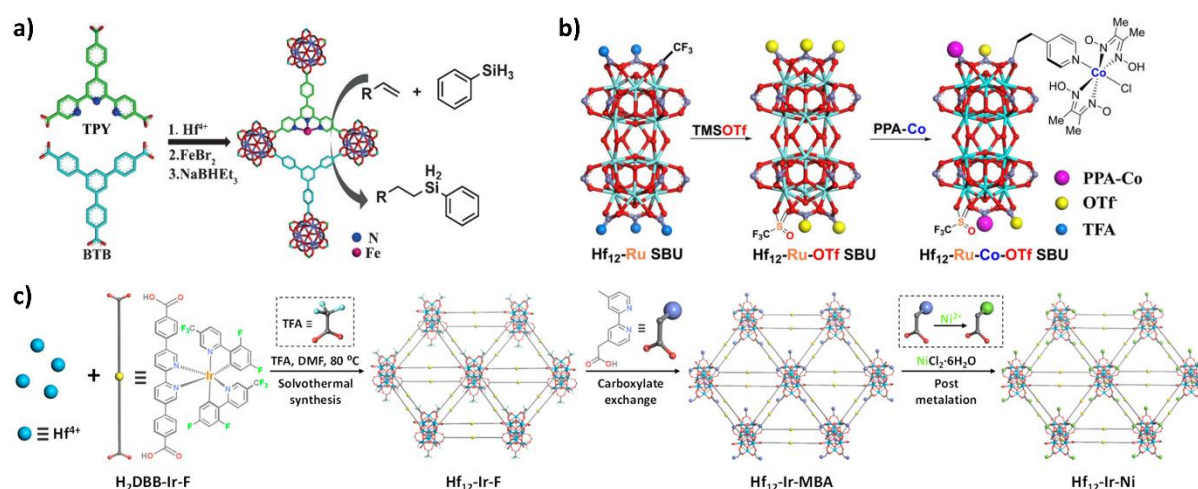
Figure 10. Selected representations of the types of modifications performed by Lin and Wang *et al.*: **a)** post-synthetic metalation of linker binding sites,[92] **b)** post-synthetic exchange of capping agents at SBU sites,[104] and **c)** pre-synthetic metalation of linkers binding sites, followed by post-synthetic exchange of capping agents.[96]

These reports highlight the potential of MONs when this toolkit of pre- and post-synthetic chemistries are utilised. The applications of these modified Zr/Hf cluster MONs are both numerous and diverse, including photo-,[94,111,112] electro-,[113] and heterogeneous catalysis,[104,114,115] photo- and radiodynamic therapy,[93,106,109] and chemo- and biomedical sensing applications.[99,100,105]. However, these reports are limited only to these UiO-type frameworks, and do not explore the rules for functionalisation of the many other established MON systems.

1.4. MON Preparation

As discussed in **Chapter 1**, the preparation of MONs can be separated into two broad categories: bottom-up synthesis and top-down exfoliation. Bottom-up methods employ a direct synthesis of MONs from their constituent metal ions and organic linkers. These procedures typically require intricate and arduous setup, but often produce MONs of high quality albeit in low concentrations or yields. Top-down methods focus on the exfoliation of layered MOFs, in which the procedure strips the layers of the MOF apart into MONs. Top-down methods are typically harsher than bottom-up methods, and as such will often produce large lateral size distributions and MONs of varying thicknesses and yields. Furthermore, the large number of reported layered MOFs service as a useful starting point when considering top-down approaches.[31] A summary of the bottom-up and top-down methods that have been applied to MONs is given in Figure 11.
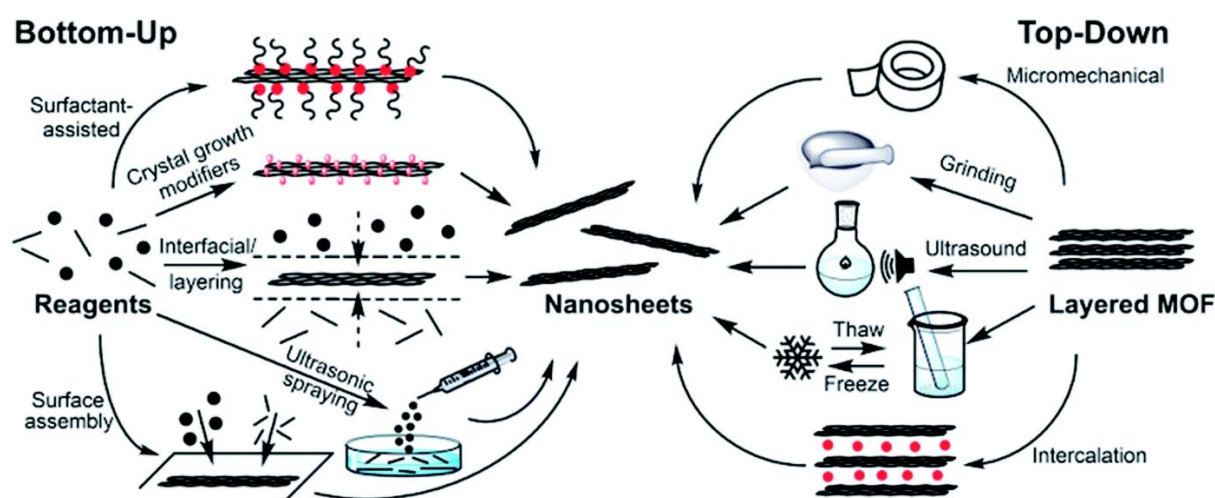
Figure 11. Scheme illustrating the different bottom-up and top-down methodologies used to prepare MONs.[28]

Of the top-down approaches, liquid-assisted ultrasonic exfoliation is prevalent throughout the 2D materials literature,[116] and has been widely used for the preparation of MONs.[117] In this method, layered MOF particles are first treated with a solvent system of choice, before being subject to shear forces that originate from acoustic cavitation's which arise from microbubble collapse during ultrasonication. Through this process, multiple exfoliation modes can occur, including bubble collapse, shear effect, compressive stress wave effect, fragmentation, and edge effect exfoliation (Figure 12).[118]
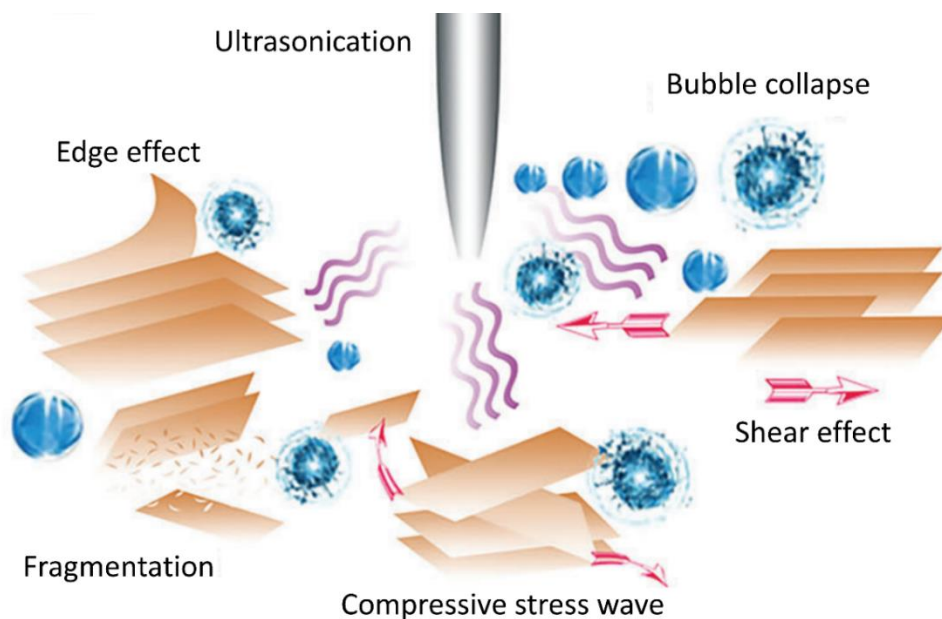
Figure 12. A scheme illustrating the different modes of exfoliation through ultrasonication.[118]

A standardised method for liquid-assisted ultrasonication does not exist within the MON literature. Variables such as time, temperature, power, frequency, sonication mode and sonication technique (probe or bath) are often not reported or not comparable between studies. As such, it is difficult to use the literature to determine what provides a "successful" exfoliation. Some authors have offered evidence-based hypotheses on why their techniques have produced high quality MONs.

Moorthy *et al.* have used relative fluorescence intensity as a means by which to evaluate the suitability of different solvents as exfoliation media for the preparation of their MONs. In two examples, the authors noted that the fluorescence intensity and thus the concentration of their nanosheets post-exfoliation correlated with the solvents Gutmann parameter, as shown in Figure 13.[119,120] This parameter represents the solvents hydrogen-bond accepting ability, and in both examples the authors utilised MONs with both hydrogen-bond accepting and donating groups. Similarly, Yang *et al.* observed that a mixed solvent medium of methanol and n-propanol was most appropriate for the exfoliation of their layered $Zn_2(bim)_4$ MOF.[121] This was attributed to the ability of the smaller methanol molecules to penetrate between the layers, whilst the larger propanol molecules adsorbed onto the MON surfaces, stabilising the sheets with their hydrophilic alkane tails. Reports by Ni *et al.* and Wang *et al.* have observed enhanced exfoliation of $Zn_2(bim)_4$ and MAMS-1 ($Ni_8(5\text{-}bbdc)_6(\mu\text{-}OH)_4$) frameworks respectively, into high concentration ultrathin nanosheets.[122,123] In these instances, the authors utilise ionic liquids as both the exfoliation medium and as surfactants which stabilise the nanosheets as they form, with higher exfoliation yields at increased ionic liquid volumes.
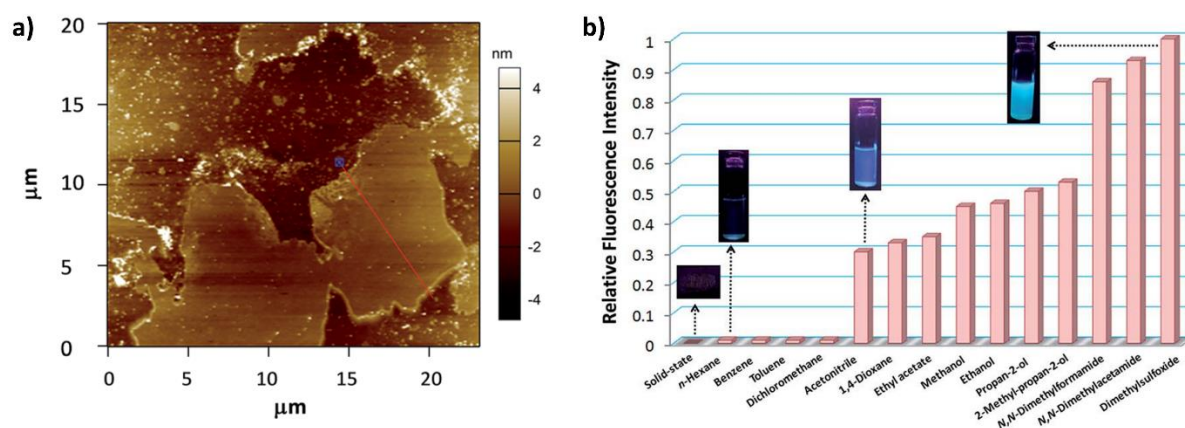
Figure 13. a) AFM image of Moorthy *et al.*'s Cd-TPA MONs and b) relative fluorescence intensities of the colloidal suspensions of Cd-TPA in various solvents.[120]

Within our group, Ashworth and Foster *et al.* have established a protocol in which layered MOFs in glass vials are treated with a solvent of choice (5 mg in 6 mL) followed by exfoliation in a sonicator bath at a frequency of 80 kHz for a pre-determined length of time whilst stirring to prevent hot spots, under water-cooled temperatures. The larger particles are removed by centrifugation, followed by separation of the nanosheet suspension.[124,125] The techniques applied in this thesis derive directly from these works, due to the reproducible nature of the procedure and the ability to perform parallel operation for scaled up preparation.

This thesis will examine the effects of different processes, including pre-synthetic and post-synthetic chemistries, on the morphologies of MONs produced by liquid exfoliation. Additionally, this work will explore novel techniques for the preparation of related materials.

1.5. Aims of this Work

This thesis aims to explore the preparation and programmable nature of MONs as supramolecular 2D materials. The main body of this work will explore three routes towards the programming of MON structures: pre-synthetic isoreticular expansion of layered MOFs, post-synthetic functionalisation of layered MOFs, and post-exfoliation functionalisation of MONs directly. This goal is to develop a toolkit of chemistries for the modification of MONs and to understand how structural changes affect the process of liquid exfoliation and the resulting morphologies of these nanosheets.

This thesis will also explore whether the technique of liquid exfoliation can be extended to other, not yet explored supramolecular structures. Specifically, the exfoliation of layered hydrogen-bonded frameworks based on charge-assisted hydrogen bonds will be investigated. Finally, this work will explore a novel bottom-up approach, the use of reactive inkjet printing of MOFs for preparation of both 3D and 2D architectures.

The following chapters of this thesis are based on five research papers which test the following hypotheses:

Chapter 3. How does post-synthetic functionalisation of a layered MOF effect its exfoliation into nanosheets, and can any bi-functional nanosheets formed be used for tandem catalysis?

Chapter 4. Can click chemistry be utilised as a versatile technique to functionalise MONs post-exfoliation? Can photoactive groups be introduced this way to be exploited for chemo-sensing?

Chapter 5. Can an isoreticular series of MONs with linkers of different lengths be prepared, and how does the choice of starting metal salt effect the morphologies of the resultant nanosheets?

Chapter 6. Can the technique of liquid-assisted ultrasonication be applied to hydrogen-bonded organic frameworks (HOFs) to produce nanosheets?

Chapter 7. Can reactive inkjet printing be utilised to prepare 3D and 2D MOFs, and can this technique be employed to prepare multi-component MOFs.

Insights from chapters 3-8 will be drawn together in **Chapter 8** to provide an overall conclusion to this thesis.

1.6. References

1   K. S. Novoselov, A. K. Geim, S. V Morozov, D. Jiang, Y. Zhang, S. V Dubonos, I. V Grigorieva and A. A. Firsov, *Science*, 2004, **306**, 666–669.

2   U. Stöberl, U. Wurstbauer, W. Wegscheider, D. Weiss and J. Eroms, *Appl. Phys. Lett.*, 2008, **93**, 98–101.

3   R. R. Nair, P. Blake, A. N. Grigorenko, K. S. Novoselov, T. J. Booth, T. Stauber, N. M. R. Peres and A. K. Geim, *Science*, 2008, **320**, 1308.

4   I. V. G. and A. A. F. K. S. Novoselov, A. K. Geim, S. V. Morozov, D. Jiang, Y. Zhang, S. V. Dubonos, 2016, **306**, 666–669.

5   R. R. Nair, M. Sepioni, I.-L. Tsai, O. Lehtinen, J. Keinonen, A. V. Krasheninnikov, T. Thomson, A. K. Geim and I. V. Grigorieva, *Nat. Phys.*, 2012, **8**, 199–202.

6   Y. Xu, Z. Li and W. Duan, *Small*, 2014, 2182–2199.

7   M. J. Allen, V. C. Tung and R. B. Kaner, *Chem. Rev.*, 2010, **110**, 132–145.

8   T. Torres, *Chem. Soc. Rev.*, 2017, **46**, 4385–4386.

9   K. Khan, A. K. Tareen, M. Aslam, R. Wang, Y. Zhang, A. Mahmood, Z. Ouyang, H. Zhang and Z. Guo, *Recent developments in emerging two-dimensional materials and their applications*, Royal Society of Chemistry, 2020, vol. 8.

10   P. Solís-Fernández, M. Bissett and H. Ago, *Chem. Soc. Rev.*, 2017, **46**, 4572–4613.

11   G. Cassabois, P. Valvin and B. Gil, *Nat. Photonics*, 2015, **10**, 262–266.

12   S. Manzeli, D. Ovchinnikov, D. Pasquier, O. V Yazyev and A. Kis, *Nat. Rev. Mater.*, 2017, **2**, 17033.

13   B. Fan and X. Wang, *Chem. Soc. Rev.*, 2020, **49**, 6666–6693.

14   Q. Wang and D. O'Hare, *Chem. Rev.*, 2012, **112**, 4124–4155.

15   X. P. Zhai, B. Ma, Q. Wang and H. L. Zhang, *Phys. Chem. Chem. Phys.*, 2020, **22**, 22140–22156.

16   P. Yin, X. Jiang, R. Huang, X. Wang, Y. Ge, C. Ma and H. Zhang, *Adv. Mater. Interfaces*, 2021, **8**, 2100367.

17   K. Zhao, W. Zhu, S. Liu, X. Wei, G. Ye, Y. Su and Z. He, *Nanoscale Adv.*, 2020, **2**, 536–562.

18   Z. Wu, J. Qi, W. Wang, Z. Zeng and Q. He, *J. Mater. Chem. A*, 2021, **9**, 18793-18817.

19   N. R. Glavin, R. Rao, V. Varshney, E. Bianco, A. Apte, A. Roy, E. Ringe and P. M. Ajayan, *Adv. Mater.*, 2020, **32**, 1–22.

20   N. Rohaizad, C. C. Mayorga-Martinez, M. Fojtů, N. M. Latiff and M. Pumera, *Chem. Soc. Rev.*, 2021, **50**, 619–657.

21   J. Liu, J. Tang and J. J. Gooding, *J. Mater. Chem.*, 2012, **22**, 12435–12452.

22   L. Daukiya, J. Seibel and S. De Feyter, *Adv. Phys. X*, 2019, **4**, 1625723.

23   V. Georgakilas, J. N. Tiwari, K. C. Kemp, J. A. Perman, A. B. Bourlinos, K. S. Kim and R. Zboril, *Chem. Rev.*, 2016, **116**, 5464–5519.

24   Z. Lin, N. C. Thacker, T. Sawano, T. Drake, P. Ji, G. Lan, L. Cao, S. Liu, C. Wang and W. Lin, *Chem. Sci.*, 2017, **9**, 143–151.

25   Y. Li, M. Zhang, X. Guo, R. Wen, X. Li, X. Li, S. Li and L. Ma, *Nanoscale Horiz.*, 2018, **3**, 205–212.

26   D. Rodríguez-San-Miguel, C. Montoro and F. Zamora, *Chem. Soc. Rev.*, 2020, **49**, 2291–2302.

27   M. Zhao, Y. Huang, Y. Peng, Z. Huang, Q. Ma and H. Zhang, *Chem. Soc. Rev.*, 2018, **47**, 6267–6295.

28   D. J. Ashworth and J. A. Foster, *J. Mater. Chem. A*, 2018, **6**, 16292–16307.

29   M. J. Kalmutzki, N. Hanikel and O. M. Yaghi, *Sci. Adv.*, 2018, **4**, 10, 1-16.

30   H. Furukawa, U. Müller and O. M. Yaghi, *Angew. Chem.*, 2015, **54**, 3417–3430.

31   P. Z. Moghadam, A. Li, X.-W. Liu, R. Bueno-Perez, S.-D. Wang, S. B. Wiggin, P. A. Wood and D. Fairen, *Chem. Sci.*, 2020, **11**, 8373–8387.

32   R. J. Marshall and R. S. Forgan, *Eur. J. Inorg. Chem.*, 2016, **2016**, 4310–4331.

33   K. K. Tanabe and S. M. Cohen, *Chem. Soc. Rev.*, 2011, **40**, 498–519.

34   M. Kalaj and S. M. Cohen, *ACS Cent. Sci.*, 2020, **6**, 1046–1057.

35   Z. Wang and S. M. Cohen, *Chem. Soc. Rev.*, 2009, **38**, 1315–1329.

36   H. Jiang, D. Alezi and M. Eddaoudi, *Nat. Rev. Mater.*, 2021, **6**, 466–487.

37   A. Kirchon, L. Feng, H. F. Drake, A. Joseph and H. Zhou, *Chem. Soc. Rev.*, 2018, **47**, 8611–8638.

38   Z. Chen, S. L. Hanna, L. R. Redfern, D. Alezi, T. Islamoglu and O. K. Farha, *Coord. Chem. Rev.*, 2019, **386**, 32–49.

39   M. Eddaoudi, J. Kim, N. Rosi, D. Vodak, J. Wachter, M. O'Keeffe and O. M. Yaghi, *Science*, 2002, **295**, 469–472.

40   K. K. Tanabe and S. M. Cohen, *Chem. Soc. Rev.*, 2011, **40**, 498–519.

41   R. J. Marshall, T. Richards, C. L. Hobday, C. F. Murphie, C. Wilson, S. A. Moggach, T. D. Bennett and R. S. Forgan, *Dalton Trans.*, 2016, **45**, 4132–4135.

42   A. Jaafar, C. Platas-Iglesias and R. A. Bilbeisi, *RSC Adv.*, 2021, **11**, 16192–16199.

43   T. Gadzikwa, O. K. Farha, K. L. Mulfort, J. T. Hupp and S. T. Nguyen, *Chem. Commun.*, 2009, 3720–3722.

44   A. D. Burrows, C. G. Frost, M. F. Mahon and C. Richardson, *Chem. Commun.*, 2009, 4218–4220.

45   C. J. Doonan, W. Morris, H. Furukawa and O. M. Yaghi, *J. Am. Chem. Soc.*, 2009, **131**, 9492–9493.

46   Z. Wang and S. M. Cohen, *Chem. Soc. Rev.*, 2009, **38**, 1315–1329.

47   J. D. Evans, C. J. Sumby and C. J. Doonan, *Chem. Soc. Rev.*, 2014, **43**, 5933–5951.

48   B. Li, Y. Zhang, D. Ma, L. Li, G. Li, G. Li, Z. Shi and S. Feng, *Chem. Commun.*, 2012, **48**, 6151–6153.

49   A. Demessence, D. M. D'Alessandro, M. L. Foo and J. R. Long, *J. Am. Chem. Soc.*, 2009, **131**, 8784–8786.

50   M. Kim, J. F. Cahill, Y. Su, K. A. Prather and S. M. Cohen, *Chem. Sci.*, 2012, **3**, 126–130.

51   M. Kim, J. F. Cahill, H. Fei, K. A. Prather and S. M. Cohen, *J. Am. Chem. Soc.*, 2012, **134**, 18082–18088.

52   Z. Hu, S. Faucher, Y. Zhuo, Y. Sun, S. Wang and D. Zhao, *Chem. Eur. J.*, 2015, **21**, 17246–17255.

53   M. Kondo, S. Furukawa, K. Hirai and S. Kitagawa, *Angew. Chem.*, 2010, **49**, 5327–5330.

54   I. Abánades Lázaro, C. J. R. Wells and R. S. Forgan, *Angew. Chem.*, 2020, **59**, 5211–5217.

55   J. Jiao, W. Gong, X. Wu, S. Yang and Y. Cui, *Coord. Chem. Rev.*, 2019, **385**, 174–190.

56   U. Fluch, B. D. McCarthy and S. Ott, *Dalton Trans.*, 2019, **48**, 45–49.

57   H. Liu, F. G. Xi, W. Sun, N. N. Yang and E. Q. Gao, *Inorg. Chem.*, 2016, **55**, 5753–5755.

58   G. Tuci, A. Rossin, X. Xu, M. Ranocchiari, J. A. Van Bokhoven, L. Luconi, I. Manet, M. Melucci and G. Giambastiani, *Chem. Mater.*, 2013, **25**, 2297–2308.

59   T. Gadzikwa, O. K. Farha, C. D. Malliakas, M. G. Kanatzidis, J. T. Hupp and S. B. T. Nguyen, *J. Am. Chem. Soc.*, 2009, **131**, 13613–13615.

60   K. M. L. Taylor-Pashow, J. Della Rocca, Z. Xie, S. Tran and W. Lin, *J. Am. Chem. Soc.*, 2009, **131**, 14261–14263.

61   H. Deng, C. J. Doonan, H. Furukawa, R. B. Ferreira, J. Towne, C. B. Knobler, B. Wang and O. M. Yaghi, *Science*, 2010, **327**, 846–850.

62   M. Kim, J. F. Cahill, A. Prather and S. M. Cohen, *Chem. Commun.*, 2011, **47**, 7629–7631.

63   J. A. Foster, S. Henke, A. Schneemann, R. A. Fischer and A. K. Cheetham, *Chem. Commun.*, 2016, **52**, 10474–10477.

64   D. J. Ashworth, A. Cooper, M. Trueman, R. W. M. Al-Saedi, L. D. Smith, A. J. H. M. Meijer and J. A. Foster, *Chem. Eur. J.*, 2018, **24**, 17986–17996.

65   D. J. Ashworth, T. M. Roseveare, A. Schneemann, M. Flint, I. D. Bernáldes, P. Vervoorts, R. A. Fischer, L. Brammer and J. A. Foster, *Inorg. Chem.*, 2019, **58**, 10837–10845.

66   D. J. Ashworth and J. A. Foster, *Nanoscale*, 2020, **12**, 7986–7994.

67   J. López-Cabrelles, S. Mañas-Valero, I. J. Vitórica-Yrezábal, P. J. Bereciartua, J. A. Rodríguez-Velamazán, J. C. Waerenborgh, B. J. C. Vieira, D. Davidovikj, P. G. Steeneken, H. S. J. van der Zant, G. Mínguez Espallargas and E. Coronado, *Nat. Chem.*, 2018, **10**, 1001–1007.

68   H. Yuan, G. Liu, Z. Qiao, N. Li, P. J. S. Buenconsejo, S. Xi, A. Karmakar, M. Li, H. Cai, S. J. Pennycook and D. Zhao, *Adv. Mater.*, 2021, **33**, 2101257.

69   C. Tan, K. Yang, J. Dong, Y. Liu, Y. Liu, J. Jiang and Y. Cui, *J. Am. Chem. Soc.*, 2019, **141**, 17685–17695.

70   T. Rodenas, I. Luz, G. Prieto, B. Seoane, H. Miro, A. Corma, F. Kapteijn, F. X. Llabrés I Xamena and J. Gascon, *Nat. Mater.*, 2015, **14**, 48–55.

71   L. Zhang, H. Chen, X. Bai, S. Wang, L. Li, L. Shao, W. He, Y. Li, T. Wang, X. Zhang, J. Chen and Y. Fu, *Chem. Commun.*, 2019, **55**, 8293–8296.

72   S. Chen, J. Dai and X. C. Zeng, *Phys. Chem. Chem. Phys.*, 2015, **17**, 5954–5958.

73   K. Takada, R. Sakamoto, S. T. Yi, S. Katagiri, T. Kambe and H. Nishihara, *J. Am. Chem. Soc.*, 2015, **137**, 4681–4689.

74   M. Tang, H. Shen and Q. Sun, *J. Phys. Chem. C*, 2019, **123**, 43, 26460-26466.

75   N. Lahiri, N. Lotfizadeh, R. Tsuchikawa, V. V. Deshpande and J. Louie, *J. Am. Chem. Soc.*, 2017, **139**, 19–22.

76   A. J. Clough, N. M. Orchanian, J. M. Skelton, A. J. Neer, S. A. Howard, C. A. Downes, L. F. J. Piper, A. Walsh, B. C. Melot and S. C. Marinescu, *J. Am. Chem. Soc.*, 2019, **141**, 41, 16323-16330.

77   Z. Wang, G. Wang, H. Qi, M. Wang, M. Wang, S. Park, H. wang, M. Yu, U. Kaiser, A. Fery, S. Zhou, R. Dong and X. Feng, *Chem. Sci.*, 2020, **11**, 7665-7671.

78   B. Cui, C. Wang, S. Huang, L. He, S. Zhang, Z. Zhang and M. Du, *J. Colloid Interface Sci.*, 2020, **578**, 10–23.

79   H. Ang and L. Hong, *ACS Appl. Mater. Interfaces*, 2017, **9**, 28079–28088.

80   L. Zhuang, L. Ge, H. Liu, Z. Jiang, Y. Jia, Z. Li, D. Yang, R. K. Hocking, M. Li, L. Zhang, X. Wang, X. Yao and Z. Zhu, *Angew. Chem.*, 2019, **131**, 13699–13706.

81   Y. Liang, R. Shang, J. Lu, W. An, J. Hu, L. Liu and W. Cui, *Int. J. Hydrog. Energy*, 2019, **44**, 2797–2810.

82   J. Wang, Q. Zhong, Y. Zeng, D. Cheng, Y. Xiong and Y. Bu, *J. Colloid Interface Sci.*, 2019, **555**, 42–52.

83   Y. Xu, S. Yu, T. Ren, S. Liu, Z. Wang, X. Li, L. Wang and H. Wang, *ACS Appl. Mater. Interfaces*, 2020, **12**, 31, 34728-34735.

84   D. Tian, N. Song, M. Zhong, X. Lu and C. Wang, *ACS Appl. Mater. Interfaces*, 2020, **12**, 1280–1291.

85   W. Cheng, X. F. Lu, D. Luan and X. W. Lou, *Angew. Chem.*, 2020, **59**, 18234–18239.

86   W. Li, W. Fang, W. Chen, K. N. Dinh, H. Ren, L. Zhao, C. Liu and Q. Yan, *J. Mater. Chem. A*, 2020, **8**, 3658–3666.

87   Y. Chi, W. Yang, Y. Xing, Y. Li, H. Pang and Q. Xu, *Nanoscale*, 2020, **12**, 10685–10692.

88   P. Thangasamy, S. Shanmuganathan and V. Subramanian, *Nanoscale Adv.*, 2020, **2**, 2073–2079.

89   S. Zhao, Y. Wang, J. Dong, C. T. He, H. Yin, P. An, K. Zhao, X. Zhang, C. Gao, L. Zhang, J. Lv, J. Wang, J. Zhang, A. M. Khattak, N. A. Khan, Z. Wei, J. Zhang, S. Liu, H. Zhao and Z. Tang, *Nat. Energy*, 2016, **1**, 1–10.

90   Q. Li, Y. Liu, S. Niu, C. Li, C. Chen, Q. Liu and J. Huo, *J. Colloid Interface Sci.*, 2021, **603**, 148–156.

91   Z. Zheng, L. Opilik, F. Schiffmann, W. Liu, G. Bergamini, P. Ceroni, L. T. Lee, A. Schütz, J. Sakamoto, R. Zenobi, J. Vandevondele and A. D. Schlüter, *J. Am. Chem. Soc.*, 2014, **136**, 6103–6110.

92   L. Cao, Z. Lin, F. Peng, W. Wang, R. Huang, C. Wang, J. Yan, J. Liang, Z. Zhang, T. Zhang, L. Long, J. Sun and W. Lin, *Angew. Chem.*, 2016, **55**, 4962–4966.

93   G. Lan, K. Ni, R. Xu, K. Lu, Z. Lin, C. Chan and W. Lin, *Angew. Chem.*, 2017, **56**, 12102–12106.

94   R. Xu, Z. Cai, G. Lan and W. Lin, *Inorg. Chem.*, 2018, **57**, 10489–10493.

95   R. Xu, T. Drake, G. Lan and W. Lin, *Chem. Eur. J.*, 2018, **24**, 15772–15776.

96   G. Lan, Y. Quan, M. Wang, T. Nash, E. You, Y. Song, S. S. Veroneau, X. Jiang and W. Lin, *J. Am. Chem. Soc.*, 2019, **141**, 15767–15772.

97   W. Shi, L. Zeng, L. Cao, Y. Huang, C. Wang and W. Lin, *Nano Res.*, 2020, **12**, 1–6.

98   Y. Quan, W. Shi, Y. Song, X. Jiang, C. Wang and W. Lin, *J. Am. Chem. Soc.*, 2021, 143, 8, 3075-3080.

99   G. B. Hu, C. Y. Xiong, W. Bin Liang, Y. Yang, L. Y. Yao, W. Huang, W. Luo, R. Yuan and D. R. Xiao, *Biosens. Bioelectron.*, 2019, **135**, 95–101.

100   Y. Yang, G. B. Hu, W. Bin Liang, L. Y. Yao, W. Huang, R. Yuan and D. R. Xiao, *Nanoscale*, 2019, **11**, 10056–10063.

101   W. Shi, L. Cao, H. Zhang, X. Zhou, B. An, Z. Lin, R. Dai, J. Li, C. Wang and W. Lin, *Angew. Chemie - Int. Ed.*, 2017, **56**, 9704–9709.

102   G. Lan, Z. Li, S. S. Veroneau, Y.-Y. Zhu, Z. Xu, C. Wang and W. Lin, *J. Am. Chem. Soc.*, 2018, 2018, **140**, 39, 12369–12373.

103   Y. Song, Y. PI, X. Feng, K. Ni, Z. Xu, J. S. Chen, Z. Li and W. Lin, *J. Am. Chem. Soc.*, 2020, **142**, 6866–6871.

104   Y. Quan, G. Lan, W. Shi, Z. Xu, Y. Fan, E. You, X. Jiang, C. Wang and W. Lin, *Angew. Chem.*, 2020, **60**, 3115–3120.

105   G. Lan, K. Ni, E. You, M. Wang, A. Culbert, X. Jiang and W. Lin, *J. Am. Chem. Soc.*, 2019, **141**, 18964–18969.

106   G. T. Nash, T. Luo, G. Lan, K. Ni, M. Kaufmann and W. Lin, *J. Am. Chem. Soc.*, 2021, **143**, 2194–2199.

107   X. Ling, D. Gong, W. Shi, Z. Xu, W. Han, G. Lan, Y. Li, W. Qin and W. Lin, *J. Am. Chem. Soc.*, 2021, **143**, 1284–1289.

108   Y. Guo, W. Shi, H. Yang, Q. He, Z. Zeng, J. Ye and X. He, *J. Am. Chem. Soc.*, 2019, **141**, 44, 17875–17883

109   G. Lan, K. Ni, S. S. Veroneau, Y. Song and W. Lin, *J. Am. Chem. Soc.*, 2018, **140**, 16971–16975.

110   Y. Quan, G. Lan, Y. Fan, W. Shi, E. You and W. Lin, *J. Am. Chem. Soc.*, 2020, **142**, 1746–1751.

111   R. Xu, T. Drake, G. Lan and W. Lin, *Chem. Eur. J.*, 2018, **24**, 15772–15776.

112   G. Lan, Z. Li, S. S. Veroneau, Y.-Y. Zhu, Z. Xu, C. Wang and W. Lin, *J. Am. Chem. Soc.*, 2018, **140**, 12369–12373.

113   Y. Guo, W. Shi, H. Yang, Q. He, Z. Zeng, J. Y. Ye, X. He, R. Huang, C. Wang and W. Lin, *J. Am. Chem. Soc.*, 2019, **141**, 17875–17883.

114   L. Cao, Z. Lin, F. Peng, W. Wang, R. Huang, C. Wang, J. Yan, J. Liang, Z. Zhang, T. Zhang, L. Long, J. Sun and W. Lin, *Angew. Chem.*, 2016, **55**, 4962–4966.

115   W. Shi, L. Cao, H. Zhang, X. Zhou, B. An, Z. Lin, R. Dai, J. Li, C. Wang and W. Lin, *Angew. Chem.*, 2017, **56**, 9704–9709.

116   J. N. Coleman, M. Lotya, A. O. Neill, S. D. Bergin, P. J. King, U. Khan, K. Young, A. Gaucher, S. De, R. J. Smith, I. V Shvets, S. K. Arora, G. Stanton, H. Kim, K. Lee, G. T. Kim, G. S. Duesberg, T. Hallam, J. J. Boland, J. J. Wang, J. F. Donegan, J. C. Grunlan, G. Moriarty, A. Shmeliov, R. J. Nicholls, J. M. Perkins, E. M. Grieveson, K. Theuwissen, D. W. Mccomb, P. D. Nellist and V. Nicolosi, *Science*, 2011, **331**, 568–572.

117   D. J. Ashworth and J. A. Foster, *J. Mater. Chem. A*, 2018, **6**, 16292–16307.

118   H. Tao, Y. Zhang, Y. Gao, Z. Sun, C. Yan and J. Texter, *Phys. Chem. Chem. Phys.*, 2017, **19**, 921–960.

119   S. Jindal, V. K. Maka, G. Anjum and J. N. Moorthy, *ACS Appl. Nano Mater.*, 2021, **4**, 1, 449–458.

120   P. Chandrasekhar, A. Mukhopadhyay, G. Savitha and J. N. Moorthy, *J. Mater. Chem. A*, 2017, **5**, 5402–5412.

121   Y. Peng, Y. Li, B. Yujie, H. Jin, W. Jiao, X. Liu and W. Yang, *Science*, **346**, 1356-1359.

122   D. Liu, B. Liu, C. Wang, W. Jin, Q. Zha, G. Shi, D. Wang and X. Sang, *ACS Sustain. Chem. Eng.*, 2020, **8**, 2167–2175.

123   X. Sang, D. Liu, J. Song, C. Wang, X. Nie, G. Shi, X. Xia, C. Ni and D. Wang, *Ultrason. Sonochem.*, 2021, **72**, 105461.

124   D. J. Ashworth, A. Cooper, M. Trueman, R. W. M. Al-Saedi, S. D. Liam, A. J. Meijer and J. A. Foster, *Chem. Eur. J.*, 2018, **24**, 17986–17996.

125   J. A. Foster, S. Henke, A. Schneemann, R. A. Fischer and A. K. Cheetham, *Chem. Commun.*, 2016, **52**, 10474–10477.

Chapter 2

Metal-Organic Framework Nanosheets: Programmable 2D Materials for Catalysis, Sensing, Electronics, and Separation Applications
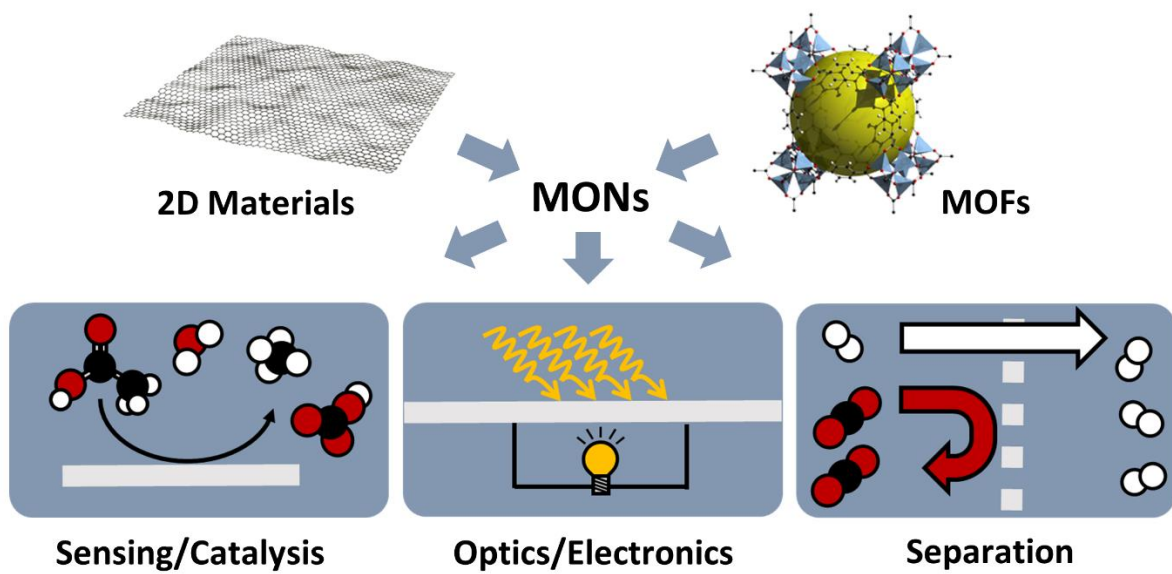
Chapter 2

Metal-Organic Framework Nanosheets: Programmable 2D Materials for Catalysis, Sensing, Electronics, and Separation Applications

Joshua Nicks, Kezia Sasitharan, Ram R. R. Prasad, David J. Ashworth, and Jonathan A. Foster

Author Contributions

Joshua Nicks	Lead author of sections 1, 3, and 6. Edited all sections and manuscript alongside JAF and compiled entire manuscript.
Ram R. R. Prasad	Author of section 2.
Kezia Sasitharan	Author of section 4.
David J. Ashworth	Author of section 5.
Jonathan A. Foster	Contributed to all sections and editing of the manuscript.

Metal-Organic Framework Nanosheets: Programmable 2D Materials for Catalysis, Sensing, Electronics, and Separation Applications

Joshua Nicks, Kezia Sasitharan, Ram R. R. Prasad, David J. Ashworth, and Jonathan A. Foster*

Metal-organic framework nanosheets (MONs) have recently emerged as a distinct class of 2D materials with programmable structures that make them useful in diverse applications. In this review, the breadth of applications that have so far been investigated are surveyed, thanks to the distinct combination of properties afforded by MONs. How: 1) The high surface areas and readily accessible active sites of MONs mean they have been exploited for a variety of heterogeneous, photo-, and electro-catalytic applications; 2) their diverse surface chemistry and wide range of optical and electronic responses have been harnessed for the sensing of small molecules, biological molecules, and ions; 3) MONs tunable optoelectronic properties and nanoscopic dimensions have enabled them to be harnessed in light harvesting and emission, energy storage, and other electronic devices; 4) the anisotropic structure and porous nature of MONs mean they have shown great promise in a variety of gas separation and water purification applications; are discussed. The aim is to draw links between the uses of MONs in these different applications in order to highlight the common opportunities and challenges presented by this promising class of nanomaterials.

1. Introduction

Metal-organic framework nanosheets (MONs) have rapidly established themselves as a distinct class of hybrid nanomaterials with a multitude of remarkable properties and potential applications.[1,2] MONs are free standing nanosheets approaching monolayer thickness formed by organic linkers coordinated to metal nodes in two-dimensions.[3] As with other 2D materials, MONs offer advantages over their bulk counterparts in terms of their high external surface areas, nanoscopic dimensions, and anisotropic structures. However, their metal-organic composition offers advantages over simple inorganic nanosheets in that a diverse range of physical and chemical properties can be programmed into their crystalline structure (**Figure 1**). This distinct combination of properties makes MONs ideal for a wide range of catalysis, sensing, electronics, and separation applications which will be the focus of this review.

Much of the early literature in this field focused on the development of novel MON architectures and new routes towards their synthesis. A diverse range of different metal ions and organic linkers have been used to construct MONs.[4] However the field has rapidly converged on a handful of popular secondary building units (SBUs) which dominate much of the literature thanks to their reliable formation of high aspect ratio nanosheets. Popular classes of MONs that have been widely applied by different groups in applications include those based on the metal paddle-wheel (PW) motif,[5–7] axially capped Zr and Hf clusters,[8–11] 2D zeolitic imidazolate frameworks (ZIFs),[12–14] and square planar Ni, Co, and Cu SBUs.[15–18] The modular structure of MONs, ease of functionalization and diverse range of materials they can be combined with means that MONs can be readily "programmed" to provide the desired topology and properties required for a given application.

A wide variety of methods have been explored to synthesize MONs, either "top-down" by the exfoliation of layered metal-organic frameworks (MOFs) or "bottom-up" by assembly of molecular building blocks directly into nanosheets. The majority of top-down approaches utilize mechanical energy to overcome inter-layer interactions, such as liquid-assisted ultrasonication,[19] shear-mixing,[20] and grinding/ball-milling,[13] or the less common freeze-thaw[21] and "scotch-tape" methods.[22,23] Other methods involving photochemical,[24] electrochemical,[25] and chemical intercalation,[26] have also been developed but are less widely used. Bottom-up methodologies typically utilize surfactants or modulators to inhibit crystal growth in one dimension,[12,27,28] or layering/interfacial methods to promote anisotropic growth.[15,29,30] The use of sacrificial 2D templates has also recently emerged a promising route.[31,32] Each approach has advantages and disadvantages in terms of the thickness, lateral dimensions, size distribution, quantity and quality of the MONs produced, and the best approach therefore varies depending on the application.

J. Nicks, Dr. K. Sasitharan, Dr. R. R. R. Prasad, Dr. D. J. Ashworth,
Dr. J. A. Foster
Department of Chemistry
The University of Sheffield
Brook Hill, Sheffield S3 7HF, USA
E-mail: jona.foster@sheffield.ac.uk

**ADVANCED
Science News**

www.advancedsciencenews.com

**ADVANCED
FUNCTIONAL
MATERIALS**

www.afm-journal.de
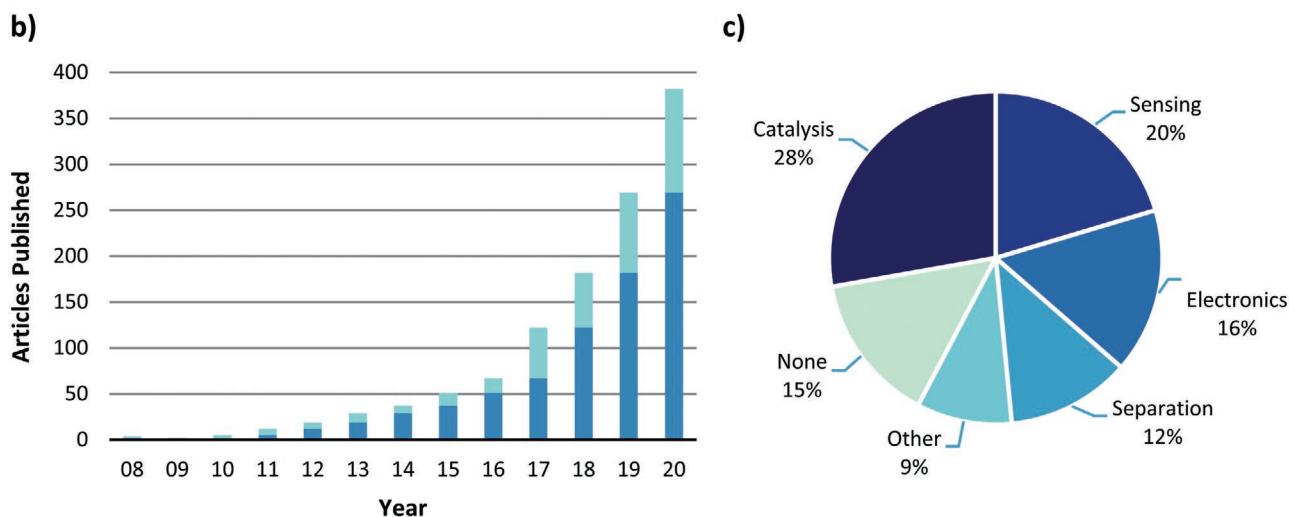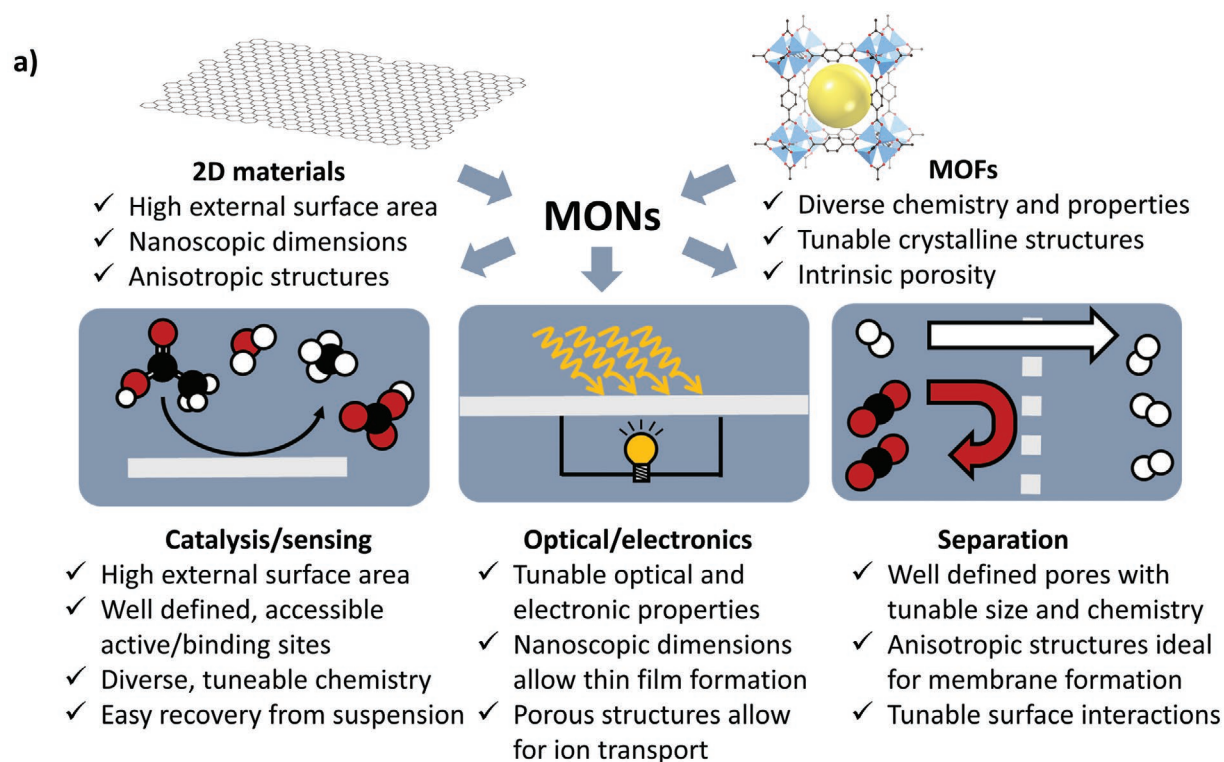
Figure 1. a) Scheme summarizing the key properties of MONs exploited in each application area. b) A chart showing the number of new articles involving MONs published each year (light blue) and the cumulative total of articles published in previous years (dark blue). c) Pie chart showing percentage of articles categorized based on application. Data based on a library of papers which meet our definition of MONs outlined in ref. [2].

These topics and the early literature have been reviewed by both us,[2] and others.[1,33,34] There has also been increasing recognition of MONs in reviews discussing other 2D materials,[35–38] or layered MOFs.[39] However, the field has advanced rapidly in recent years with more than 80% of the 382 papers we are aware of on this topic published since our previous review in 2017 (Figure 1). During this time, the focus has shifted from developing new synthetic methods and novel systems, towards utilizing their distinct properties in different applications.[40–43] This trend is reflected in many of the more recent reviews, which have focused on the use of MONs within a single specific application, including: functional devices,[40] gas separation,[43] membrane separation,[41] and electrocatalysis.[44] To give an indication of the extent of literature on MONs in each application, within our curated library of MON papers, the pie charts shown in Figure 1c highlight the percentage of papers demonstrating the various emerging applications of MONs. MONs possess the high-surface area, nanoscopic dimensions and anisotropic structures of 2D materials, as well as, the diverse chemistry, tuneable periodic structures, and intrinsic porosity of their bulk counterparts, MOFs. Different combinations of these features intuitively make them relevant

**ADVANCED
SCIENCE NEWS**
www.advancedsciencenews.com

**ADVANCED
FUNCTIONAL
MATERIALS**
www.afm-journal.de

for a wide range of different applications as summarized in Figure 1a.

In this review, we aim to bring together the current literature on the use of MONs in four diverse application areas. Following this introduction (Section 1), the review is split into sections based on the broad application areas of 2) catalysis, 3) sensing, 4) electronics, and 5) separation. The opening to each section provides a brief overview of the potential of MONs within this broad application area and the section is then organized by more specific applications. Our focus is on examining the underlying role of the MONs within each application and identifying examples where MONs have been able to outperform other 2D materials and metal-organic materials. Examples have been chosen to highlight the range of roles that the MONs can play within each application, as well as, to highlight particularly interesting or high performing systems. A perspective on the current literature for each application is offered at the end of each section whilst the final section 6) offers our overall perspective on the future opportunities and challenges for translating MONs into real-world applications. Our ambition is that by providing a holistic overview of the different ways MONs have been harnessed, the reader will gain inspiration from ideas, techniques, and materials used in one application to develop their own research in another area.

2. Exposed Active Sites for Catalysis

New catalysts are needed to reduce the cost and energy required to synthesize existing compounds, access new drugs and pesticides, split water, and capture carbon from the atmosphere. MONs combines many of the desirable aspects of homogeneous and heterogeneous catalysts in having well defined, tunable active sites but also allowing easy recovery from the reaction mixture or immobilization on supports or as thin films. A key limitation of 3D MOFs as catalysts is that their active sites are typically buried within the bulk of the framework which can limit the rate at which reagents and products can interact with them. In contrast, the high external surface area of MONs means their active sites are directly exposed to solution potentially leading to enhanced rates of catalysis compared to their 3D counterparts. MONs can be formed using a diverse range of metal-ions and ligands which can either be inherently catalytic themselves, or further functionalized with catalytic species. Multiple functionalities can also be brought together to create sophisticated catalysts to imbue selectivity or enable multistep cascade reactions. In the following section we discuss how MONs have so far been used for heterogeneous-, photo- and electro-catalysis and highlight the different approaches and reactions that have been investigated in each case.
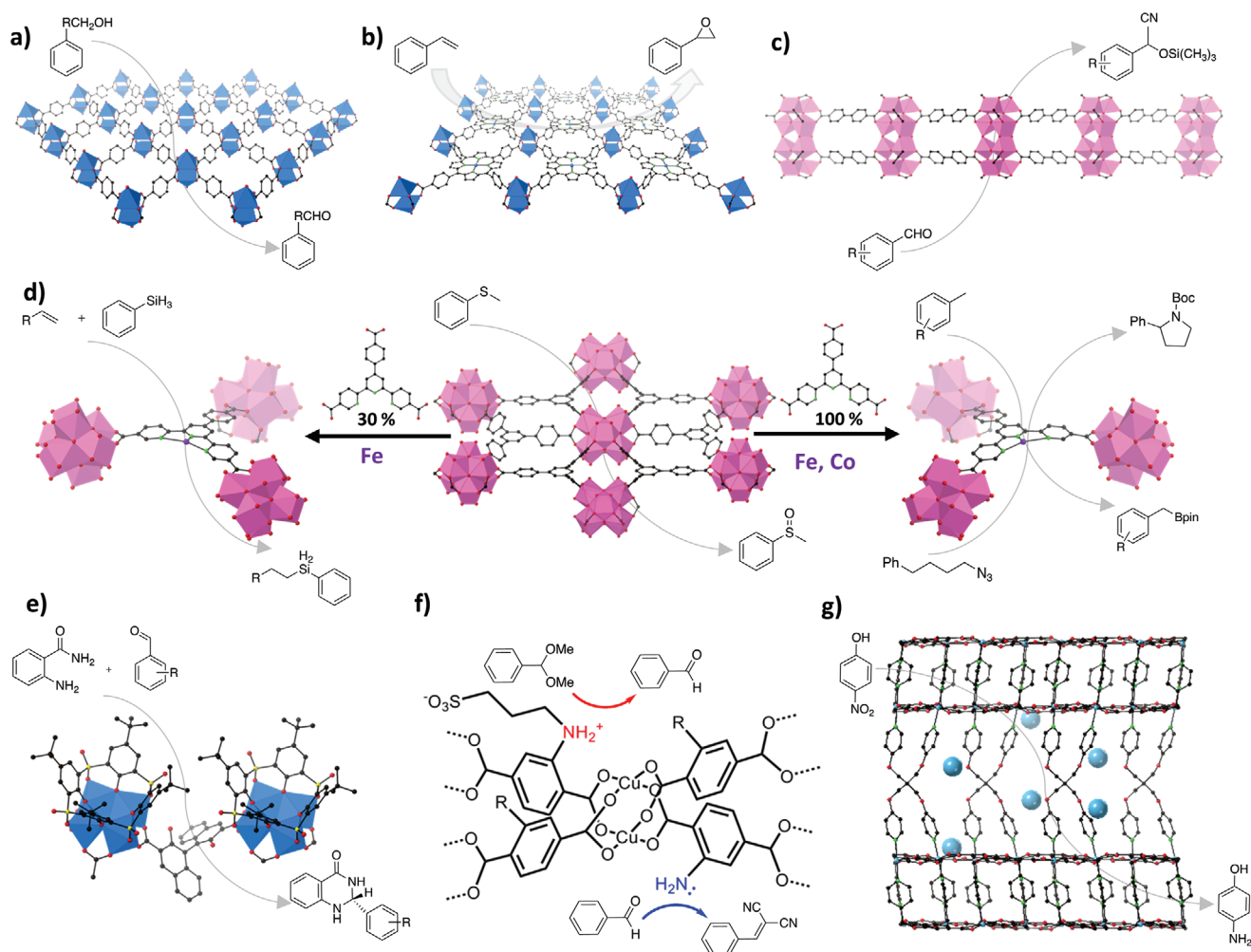
2.1. Heterogeneous Catalysis

2.1.1. Metal-Sites

Coordinatively unsaturated metal-sites present in the metal-clusters of MONs can act as Lewis acidic sites capable of promoting organic reactions. These active sites are usually generated via the removal of cluster coordinated solvent molecules after the MON synthesis. MONs based on the PW SBUs were some of the earliest examples of MON-based Lewis acidic catalysts. Fu and co-workers employed CoBDC (BDC = 1,4-benzene dicarboxylate) MONs with unsaturated Co^{2+} metal-sites in the cycloaddition of CO_2 with styrene epoxide.[45] They observed higher conversion and greater selectivity towards styrene carbonate compared to the bulk MOF. The CuBDC and NiBDC analogues have also been reported and shown to out-perform their bulk counterparts when catalyzing a variety of other reactions. CuBDC MONs catalyzed the aerobic oxidation of benzyl alcohols and epoxidation of cyclic and linear olefins (**Figure 2**a).[46,47] NiBDC MONs were used to promote the Knoevenagel condensation between propane dinitrile with various aromatic, as well as, aliphatic aldehydes.[48] Ultrathin NiBDC MONs on graphene oxide or graphitic carbon nitride composite materials also exhibited higher hydrogenation activity than the corresponding MOF-composite materials in the reduction of organic water pollutant 4-nitrophenol (4-NP) to the industrially useful precursor 4-aminophenol (4-AP) in H_2 atmosphere.[49] Surfactant-assisted synthesis of known MONs have been reported by multiple groups as a method to generate more accessible metal-sites via tuning their thickness and porosity. Polyvinylpyrrolidone (PVP) mediated CuTCPP (TCPP = Tetrakis(4-carboxyphenyl)porphyrin) synthesis yielded ultrathin MONs exhibiting higher efficiency and selectivity in styrene oxidation than bulk CuTCPP synthesized without PVP (Figure 2b).[50] Mesoporous CuBDC MONs obtained by cetyltrimethylammonium bromide (CTAB) assisted synthesis showed higher conversion in C-S coupling of bulk substituents than the microporous MOF.[51]

More recently MONs based on the more robust and Lewis acidic Zr and Hf clusters have been reported. 2D architectures were achieved by restricting the connectivity of the cluster to a plane via the addition of large amount of modulator (usually monocarboxylic acids) molecules. The cluster defects arising from this "restricted synthesis" can result in the formation of coordinatively unsaturated Zr or Hf sites promoting catalysis. The Zhao group reported that nanosheets obtained by the exfoliation of hxl-UiO-67 synthesized using this approach showed higher degrees of conversion in the cyanosilyation of aromatic aldehydes than the bulk MOF (Figure 2c).[52] Similarly, NUS-8(Zr) MONs obtained using modulator assisted synthesis that produced a high density of active sites facilitated the selective oxidation of thioethers (Figure 2d).[8] NUS-8(Zr) MONs showed >99% conversion and 100% selectivity towards sulfones at room temperature. In comparison to its 3D interpenetrated analogue, NUS-8(Zr) MONs exhibited higher reaction kinetics owing to their 2D structure enabling faster access across the active sites.

Ultrasonic exfoliation methods often used for MONs synthesis from bulk MOF systems can generate coordinatively unsaturated metal-sites due to the linker vacancies created during the procedure. Recently, Cheng and co-workers employed this method to produce ultrathin Ni-based MONs for ethylene dimerization.[53] The Ni-MONs promoted ethylene dimerization with a turnover frequency (TOF) of 5536 h⁻¹ and 75.6% selectivity towards 1-butene at 25 °C in the presence of alkylaluminium cocatalyst, Et_2AlCl. This activity was found to be twice of that shown by the bulk Ni-MOF with saturated

Figure 2. Various heterogeneous catalytic reactions promoted by different MONs: a) CuBDC catalyzed aerobic oxidation of benzyl alcohols, b) CuTCPP catalyzed styrene oxidation, c) UiO-67 MON catalyzed cyanosilylation of aromatic aldehydes, d) Reactions promoted by Zr/Hf-BTB MON and its isoreticular derivatives: (Middle) Coordinatively unsaturated Zr/Hf sites catalyzed selective oxidation of thioanisole, (left) hydrosilylation of terminal olefins catalyzed by Hf-BTB MON with 30% TPY loading post-metalated with Fe and (right) Hf-TPY MONs after post-metalation with Co and Fe catalyzed C—H borylation of methylarenes and intramolecular C_{sp^3}—H amination of alkyl azides, e) enantioselective 2,3-dihydroquinazolinones synthesis catalyzed by 1,1'-binaphthol moieties of Zn MON, f) post-synthetically functionalized CuABDC catalyzed tandem Knoevenagel condensation of benzaldehyde dimethyl acetal to benzylidene malononitrile, and g) Ni/MOF-Ni-0.4 catalyzed 4-NP to 4-AP reduction.

metal centers. AFM imaging of the MONs showed the thickness of nanosheets decreases in each catalytic run, implying further in situ exfoliation during catalysis. Further analysis proved that, although Ni leaching is accompanied in each exfoliation step, in situ generation of new active sites in a "snake's moulting" manner helped the catalyst to maintain its activity.

Another strategy that has been used to design MON catalysts for specific reactions is to incorporate metalloligands or organocatalysts known to be active under homogeneous conditions into the MON scaffold. The seminal works in this area was reported by the Lin group using Hf-BTB (BTB = benzene tribenzoate) MONs and its isoreticular derivatives (Figure 2). Hf-BTB MONs incorporated with 30% 4'-(4-benzoate-2,2',2''-terpyridine)-5,5''-dicarboxylate (TPY) linkers after post-metalation with FeBr$_2$ afforded Fe-TPY-MON precatalysts for the hydrosilylation of terminal olefins (Figure 2d).[27] After activation using NaBHEt$_3$, Fe-TPY-MON catalyzed complete hydrosilylation of styrene with

a turnover number (TON) > 5000 and 100% selectivity towards the anti-Markovnikov product. In contrast, the homogeneous catalyst (Fe-TPY) formed the Markovnikov product with significantly lower yields (30%). References run using the bulk layered MOF produced 30% yield whilst no detectable product was observed for the 3D interpenetrated MOF also used as a control.

In a concurrent study, Hf-TPY MONs after post-metalation with Co and Fe were activated with NaBHEt$_3$ to generate MON stabilized M^{II}-(TPY$^{·}$)$^{2-}$ active catalysts.[10] Activated CoCl$_2$.TPY-MON catalyzed the C—H borylation of m-xylene in the presence of bis(pinacolato)diboron, to afford borylated products in high yields (95%) with selectivity towards benzylic position (5.7:1) (Figure 2d). Similarly, FeBr$_2$.TPY-MON catalyzed intramolecular C_{sp^3}—H amination of 1-azido-4-phenylbutane to give Boc-protected α-phenyl pyrrolidine in the presence of di-*tert*-butyl dicarbonate in good yield (Figure 2d). The homogeneous

**ADVANCED
SCIENCE NEWS**

www.advancedsciencenews.com

**ADVANCED
FUNCTIONAL
MATERIALS**

www.afm-journal.de

analogues, CoCl$_2$.TPY and FeBr$_2$.TPY showed only negligible conversion due to catalyst disproportionation into nanoparticles under reaction conditions. This is an interesting example of MONs used to stabilize reactive sites. In a recent study, using 2-chloro-1,10-phenanthroline as the co-ligand, active Pd^{2+} center was incorporated to the Hf-TPY MONs by Chang and co-workers.[54] After treating with Selectfluor/H$_2$O, the active species, (N-fluoroxy)-(2-chloro)-phenanthrolinium, formed acts as a stoichiometric solid fluorination agent with varying regioselectivities and conversions comparable to homogeneous analogues.

2.1.2. Organic Ligands

In addition to catalysis taking place at post-synthetically coordinated metal-sites, functional groups of organic linkers on the MON surface can also promote catalytic reactions. In a pioneering contribution, Cui and co-workers showed how adding chiral organocatalytic groups to MONs can impart enantioselectivity to otherwise non-enantioselective organocatalysts.[55] They combined 1,1'-binaphthol/-biphenol dicarboxylic acids with zinc clusters to create layered MOFs which were then exfoliated to form the corresponding MONs. The resulting nanosheets were used for the asymmetric cascade reaction of aminobenzamide and aldehydes to produce 2,3-dihydroquinazolinones (Figure 2e). The MONs showed higher yields (56–90% for MOFs and 72–94% for MONs) and a higher ee (46–72% for MOFs and 64–82% for MONs) than the corresponding MOFs whilst the homogeneous linker exhibited no enantioselectivity.

In our own work we showed that covalent post-synthetic functionalization can be used to enhance the exfoliation of layered MOFs and add organic catalytic functionalities.[56] Layered Cu(ABDC) MOFs (ABDC = 2-amino benzenedicarboxylate) were partially functionalized (up to 25%) with 1,3-propanesultone and then exfoliated using ultrasound. The resulting nanosheets possessed both acidic and basic sites which enabled them to promote the one-pot, two-step tandem Knoevenagel condensation of benzaldehyde dimethyl acetal to benzylidene malononitrile in high yields (Figure 2f). Whilst the MONs showed 82% conversion towards desired benzylidene malononitrile, less than 5 % conversion was observed for the unexfoliated MOFs and unfunctionalized MONs. The MONs were also recovered from suspension and reused producing 86% yield.

2.1.3. Immobilized Species

In addition to functionalization with metal-ions and organic groups, another promising approach is to immobilize metal nanoparticles (MNPs) onto the surface of MONs.[57–59]

One of the most widely investigated reactions promoted by immobilized species is 4-NP to 4-AP reduction. The earliest example of this reaction was reported by Lu and co-workers who deposited AuNPs on a mixed-linker Ni MON to form Au-1@Ni-MON.[57] The MONs prevented aggregation of the AuNPs enabling efficient conversion of the 4-NP to 4-AP with a rate constant of 4.4×10^{-1} min^{-1}. Longer reaction times were observed for the reduction of a larger dye, Mordant green, indicating a size selectivity not observed in control studies using

pure AuNPs. In a similar study, the Zeng group deposited mono-, bi- and trimetallic MNPs onto Cu(HBTC)-MONs (BTC = 1,3,5-benzene tricarboxylate).[58] Among all the tested catalysts, Au$_{0.3}$Pt$_{0.3}$Pd$_{0.4}$ was found to be the most highly active with a rate constant of 0.478 min^{-1} for the conversion of 4-NP to 4-AP due to the synergistic activity of the MNPs. CuTCPP MONs with immobilized AuNPs generated via in situ hydrothermal growth showed nearly threefold enhancement (0.200 min^{-1}) in their activity for 4-NP to 4-AP reduction when compared to pure AuNPs (0.082 min^{-1}).[59] Ferrocenedicarboxylate (FDC) based Zr MONs decorated with AuNPs were also shown to catalyze the 4-NP to 4-AP reduction efficiently.[60] Recently, NiNPs deposited on Ni/NMOF-Ni-0.4 nanosheets obtained by the partial reduction of NMOF-Ni nanosheets catalyzed the 4-NP to 4-AP reduction with high efficiency than the unfunctionalized MON (Figure 2g).[61] The non-noble MNPs-MON composite showed a rate constant 7.92×10^{-3} s^{-1} and the authors suggested this could be an economically viable replacement to noble MNPs based catalysts.

Recently, the Han group deposited ultra-small RuNPs onto UiO-66 MONs synthesized using a bio-based surfactant-assisted method and investigated their use for the hydrogenation of levulinic acid to valerolactone.[62] The sub-2 nm RuNPs showed 10 times (349 h^{-1}) more activity when supported on the MONs than on the bulk UiO-66 (38 h^{-1}). The higher activity of MONs was attributed to the ease of accessing well-dispersed RuNPs on the MON surface than those confined within MOF pores. PdNPs loaded FDC-based Zr MONs obtained via in situ reduction of K$_2$PdCl$_4$ reported by Shea and co-workers showed very-high catalytic activity in styrene hydrogenation with a TOF of 7968 h^{-1} in comparison to the bulk Pd@UiO-66 (271 h^{-1}).[63] Furthermore, the Wang group recently showed how MONs can drastically improve the selectivity of PtNPs by even distribution of the latter on its surface. While Zr-2,2'-bipyridine-5,5'-dicarboxylate (ZrBPyDC) MONs exclusively yielded cinnamyl alcohol from cinnamaldehyde via transfer hydrogenation with NH$_3$BH$_3$, PtNPs alone produced a mixture of cinnamyl alcohol and phenyl propanol. In striking contrast to this, Pt@ZrBPyDC and NH$_3$BH$_3$ selectively formed phenyl propanol through a combination of transfer and catalytic hydrogenation reactions.[64] The reaction without any high-pressure hydrogen source was applicable to a range of α,β-unsaturated alcohols.

In an interesting study, Tan and co-workers reported the influence of MON structure in dictating the active Pd species formed.[65] The OX-1 MONs with (Et$_3$NH)$_2$Zn$_3$BDC repeating units favors the formation of atomic and small cluster Pd species that selectively resides on the benzene rings of the BDC linking units. The resulting Pd@OX-1 showed excellent catalytic activity in Suzuki coupling and Heck arylation under various reaction conditions. Pd@OX-1 shows the unique property of recapturing the active Pd species during the reaction, hence enabling the catalyst recycling.

2.2. Photocatalysis

2.2.1. Porphyrin-Based Metal-Organic Framework Nanosheets

Porphyrins are nature's light harvesters and M-TCPP have been widely used as a linker within MONs thanks to their planar
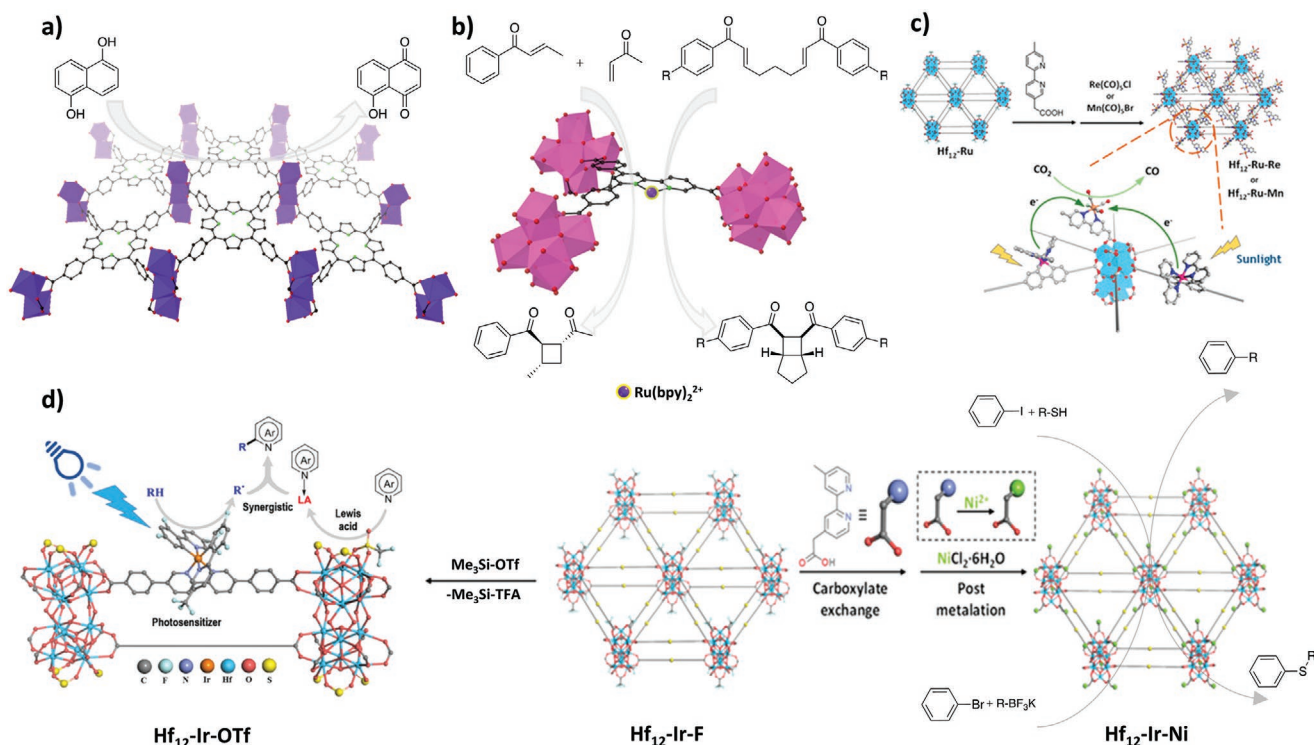
Figure 3. a) Ln MONs catalyzed photocatalytic conversion of 1,5-dihydroxynaphthalene to juglone. b) Zr-RuBPY MON catalyzed crossed [2+2] cycloadditions of acyclic enones and intramolecular cycloaddition of bisenones. c) Schematic representation of post-synthetic modification of Hf$_{12}$-Ru to access Hf$_{12}$-Ru-Re/Mn and Hf$_{12}$-Ru-Re mediated photocatalytic reduction of CO$_2$. Reproduced with permission.[72] Copyright 2018, American Chemical Society. d) (Middle) Schematic representation of post-synthetic modification of Hf$_{12}$-Ir-F to Hf$_{12}$-Ir-OTf and Hf$_{12}$-Ir-Ni, (Left) Hf$_{12}$-Ir-OTf catalyzed Minisci-type cross-coupling reactions of heteroarenes and (Right) Hf$_{12}$-Ir-Ni catalyzed C—S and C—C coupling reactions. Reproduced with permission.[74] Copyright 2019, American Chemical Society. Reproduced with permission.[75] Copyright 2020, American Chemical Society.

structure and high connectivity. M-TCPP MONs (M = Pd, Ni) have been used to promote photocatalytic oxidation of 1,5-dihydroxynapthalene (DHN) to juglone upon visible light irradiation.[26,66] Enhanced photocatalytic activity for DHN to juglone was recently reported for mixed-metal Ln MONs with TCPP linkers (**Figure 3a**).[67] The improved efficacy of the catalyst here is attributed to the energy and electron transfer between the linker and Yb^{3+} based metal-clusters. TCPP has also been added to Zr-BTB MONs to form ultrathin PCN-134 MONs by Zhou and co-workers.[68] The distance between the adjacent metal-clusters in Zr-BTB MONs matches the distance between the carboxylate groups of the TCPP linker enabling the functionalization of PCN-134 MONs. This system was found to be stable under adverse chemical conditions without any significant leaching problems compared to other porphyrin linkers employed. Moreover, under visible light irradiation, PCN-134(Ni) (NiTCPP functionalized) catalyzed the conversion of dihydroartemisinic acid to artemisinin in 64% yield. The catalyst was found to be significantly more active than its layer-pillar-type 3D analogue with limited accessibility to catalytic centers.

2.2.2. Post-Synthetic Modification of Zr/Hf-Based Metal-Organic Framework Nanosheets

Several exciting examples showing how post-synthetic modification can be used to create sophisticated photocatalysts have

been provided by Lin and co-workers. Hf-TPY MONs after post-metalation with FeBr$_2$ were examined in the photocatalytic oxidation of THF.[69] The hydrophilic-hydrophobic nature of the MONs were "tailored" via post-synthetic functionalization of the metal-clusters with various monocarboxylic acids prior to metalation. The functionalized Fe-TPY-MONs showed varying selectivity towards butyrolactone (BTL) and 2-hydroxytetrahydrofuran in the photocatalytic oxidation of tetrahydrofuran (under blue LED irradiation). However, the highly hydrophilic gluconic acid functionalized GA-Fe-TPY-MON showed 100% selectivity towards BTL, with a TON of $5.3 \pm 0.3 \times 10^2$ under identical reaction conditions. The enhanced catalytic activity of GA-Fe-TPY-MON was attributed to the optimal residence time of the reactive intermediates in the high hydrophilic MON environments.

The Lin group have also shown how the bipyridine sites of isoreticular Zr-4′6′-bis(4-benzoate-)2,2′-bipyridine)-5-carboxylate (Zr-BPY) can be post-metalated with Ru(bpy)$_2$Cl[2] to afford Zr-RuBPY MON photocatalyst (Figure 3b).[70] While Zr-RuBPY MON promoted the [2+2] intramolecular cycloaddition of bisenone upon irradiation with a blue LED (460 nm) to yielded mesodiastereomer of cyclobutene bicyclic dione in good yield, the reference UiO-67 MOF with Ru(bpy)$_3$ functionality exhibited only negligible conversion. Similar activities were observed for crossed [2+2] cycloadditions of acyclic enones and Meerwein reactions. In contrast to this, both MON and MOF showed very similar activity in the reductive cyclization

of bis(enones), which was attributed to the ease of accessing catalytic centers in the octahedral pores via tetrahedral pores of the MOF without any restrictions. This is a rare example in which both the MOF and MON exhibit the similar activity for a specific reaction. Upon examining the pore architecture of the MOF, the Ru(bpy)$_3$ functionality was found to be occupying the octahedral pores allowing the bis(enones) substrates to reach the active sites through tetrahedral pores without any interference, explaining the similar activity. Photopolymerization has also been catalyzed by isoreticular Hf-IrBPY MONs, obtained via post-metalation of Hf-BPY MONs with Ir$_2$(ppy)$_4$Cl$_2$. The MONs catalyzed the atom-transfer radical polymerization of methyl methacrylate to afford poly(methyl methacrylate) following irradiation with a blue LED (410 nm) in the presence of α-bromophenylacetate as a co-initiator.[71] The corresponding MOF failed to photopolymerize and exhibited low catalytic efficiency under identical conditions.

In the photocatalytic hydrogen evolution reaction (HER), Hf$_{12}$ cluster based UiO-67 MONs showed an 84-fold increase in photocatalytic efficiency than the bulk UiO-67. Furthermore, upon post-synthetic modification of clusters with Ti^{4+}, the activity again increased by a factor of 13 under same reaction conditions.[52] Remarkably sophisticated photocatalysts have also been created by Lin and co-workers using MONs consisting of Hf$_{12}$ clusters bridged by dicarboxylic acid linkers. In one example, MONs formed using bis(2,2′-bipyrdine)[5,5′-di(4-carboxyl-phenyl)-2,2′ bipyridine]ruthenium (II) dichloride linkers were further functionalized via post-metalation of the monodentate bipyridyl linkers incorporated on the Hf$_{12}$ clusters via modulator exchange with Re(CO)$_5$Cl/Mn(CO)$_5$Br clusters (Figure 3c).[72] This arrangement meant that each Re or Mn catalytic site was held in close proximity to six Ru-functionalised linkers, enabling multi-electron transfer which facilitated the photocatalytic reduction of CO$_2$. In contrast to other post-synthetically functionalized Zr/Hf systems,[73] Hf$_{12}$-Ru-Re MONs showed unprecedented efficiency with TON ≈670 in 6 h under sunlight irradiation and a cumulative TON of 8613 under artificial visible light.

Using similar synthetic strategy, an isoreticular Hf$_{12}$-Ir-F MON with Ir functionalized dicarboxylate linkers (Ir(DBB) [df(CF$_3$)ppy]$_2$$^+$ where DBB = 4,4′-di(4-benzoato)-2,2′-bipyridine, df(CF$_3$)ppy = 2,-(2,4-difluorophenyl)-5-(trifluoromethyl)pyridine referred as DBB-Ir-F), were post-metalated with NiCl$_2$.6H$_2$O to afford Hf$_{12}$-Ir-Ni MONs (Figure 3d).[74] In confined MON environment, upon irradiation with blue light (410–480 nm), the enhanced electron transfer from photoexcited DBB-Ir-F to Ni sites facilitated various photocatalytic reactions involving single-electron transfer to afford C—S, C—O, and C—C coupling products in excellent yields and high TONs. In a concurrent study based on the same system, trifluoroacetate groups in the metal-clusters were replaced with triflate (OTf) groups via metathesis reaction using trimethylsilyltriflate, to generate Hf$_{12}$-Ir-OTf with highly Lewis acidic metal-clusters (Figure 3d).[75] Hf$_{12}$-Ir-OTf MONs with Lewis acidic and photoredox centers working in synergy gave excellent to moderate yields (93–46%) with high TON (950–580) in the Minisci-type cross-coupling reactions of heteroarenes with ethers, amines and unactivated alkenes.

Solar fuels generated via photocatalysis are considered promising as a method for energy generation. MONs have the potential to play a role in the light absorption, charge funneling and redox reactions as part of these systems.[76] Qiao et al. used a 2D Ni-based MOF (NMF) [Ni(phen)(oba)]$_n$·0.5nH$_2$O (phen = 1,10-phenanthroline, oba = 4,4′-oxybis(benzoate)), as a platform to host cadmium sulphide (CdS) photocatalyst resulting in the best performing example (highest activity) of a noble-metal free photocatalytic H$_2$ generation of this kind (**Figure 4**a).[77] The authors demonstrated the formation of a staggering-type heterojunction between the MONs and CdS. Upon visible-light illumination, the photo-induced electrons transfer from the conduction band of CdS and migrate to active centers on the surface of the MONs that reduce protons to generate H$_2$ gas. The photo-induced holes remain on the valence band of CdS for the oxidation of lactic acid.

Duan et al. demonstrated the loading of plasmonic AuNPs on Co-PPF3 MONs (CoTCPP with bipyridine pillars prepared by surfactant-assisted method) for photocatalytic CO$_2$ generation.[78] The authors showed that the hot electrons generated by surface plasmon resonance excitation of the NPs have higher fermi levels and can easily be injected into the Co^{2+} centres of the MON leading to a higher photocatalytic efficiency. The plasmon resonance energy transfer effect was found to become weaker with increasing thickness of the MONs. Efficient photoelectrochemical reduction of CO$_2$ was demonstrated by Sun and co-workers using ZnTCPP MONs as semiconducting photosensitizers along with ZIF-67 as co-catalyst (Figure 4b).[79] Photoelectrochemical impedance measurements from the fabricated device and steady state PL measurements showed that MONs enabled better charge transport, efficient separation and longer lifetime of the photogenerated charge-carriers.

In all the previously described examples, the hybrid catalysts are assembled via physical/electrostatic interactions. Liu et al. show that the attachment of carbon nitride quantum dots (g-CNQDs) via coordination to the Co active sites in CoTCPP based photosensitizer improves directional transfer of the photogenerated electrons from the quantum dots to the Co sites for efficient photocatalytic reduction of CO$_2$ (Figure 4c).[80] The low dimensionality of both the components enabled spatial separation of the photoexcited charge carriers and acceleration of charge transfer.

2.3. Electrocatalysis

2.3.1. Oxygen Evolution Reaction

The oxygen evolution reaction (OER) is a two-step, four-electron transfer process which finds a wide range of applications in energy storage and conversion devices such as metal-air batteries and solar cells. Qiao and co-workers demonstrated the use of MONs to enhance the electrocatalytic behavior of Ni(OH)$_2$ nanosheets in OER.[81] Although Ni(OH)$_2$ nanosheets by themselves exhibit intrinsic water oxidation ability, high stability, and corrosion resistance, the low-oxidation state of Ni reduces its electrocatalytic activity. To address this drawback, a NiBDC/Ni(OH)$_2$ hybrid material was synthesized via sonication assisted growth of NiBDC MONs on Ni(OH)$_2$ nanosheets (Figure 4d). Co-ordination of BDC to the Ni sites on the Ni(OH)$_2$ nanosheets reduces the electron density around Ni atoms in
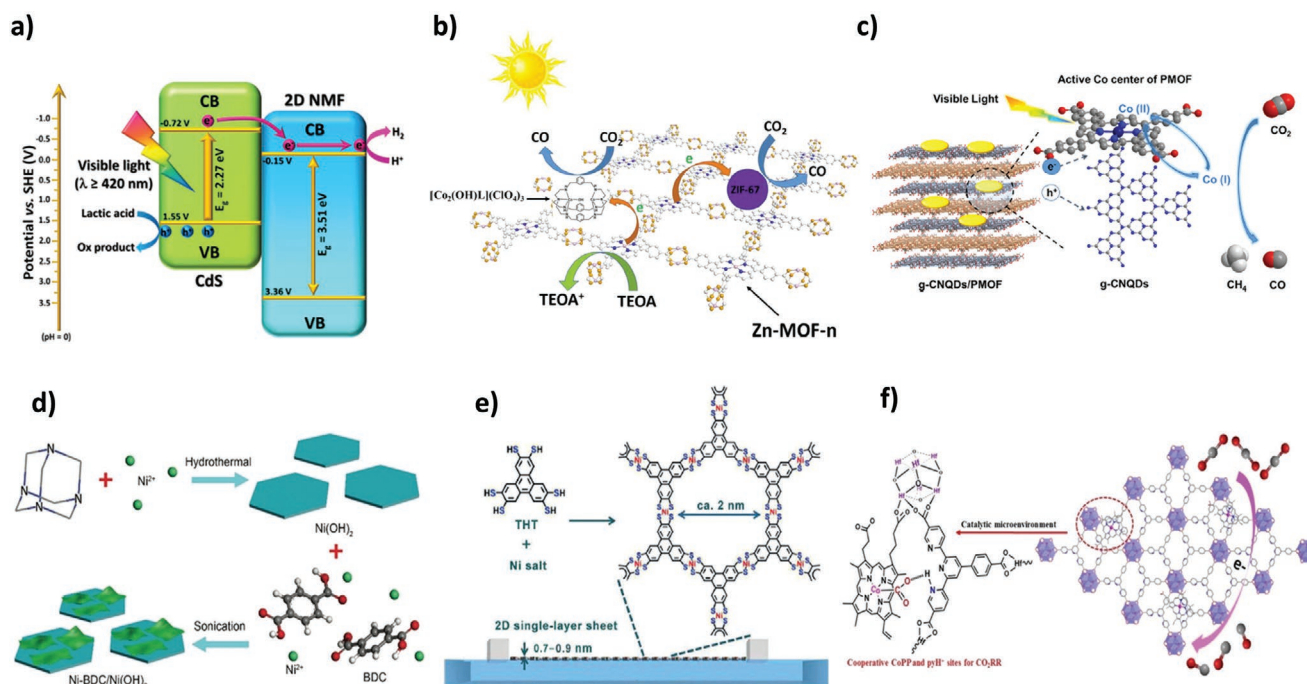
Figure 4. a) The excitons dissociation and transfer in the 2D NMF/CdS heterostructure under visible-light irradiation. The pink and blue spheres denote photoinduced electrons and holes, respectively. Reproduced with permission.[77] Copyright 2019, Wiley. b) A MON/complex or MON/ZIF system for CO_2 photoreduction with Zn-MOF nanosheets as the photosensitizer. Reproduced with permission.[79] Copyright 2018, Elsevier. c) Proposed mechanism for photocatalysis promoted by g-CNQDs/CoTCPP system. Reproduced with permission.[80] Copyright 2019, American Chemical Society. d) Schematic illustration of NiBDC/Ni(OH)$_2$ heterostructure on Ni(OH)$_2$ nanosheets. Reproduced with permission of the Royal Society of Chemistry.[81] e) Schematic showing the synthesis of Ni-THT MON by Langmuir–Blodgett method. Reproduced with permission.[97] Copyright 2015, Wiley. f) Schematic showing the cooperative action of multiple active-sites in CO_2RR. Reproduced with permission.[103] Copyright 2019, American Chemical Society.

Ni(OH)$_2$, increasing the oxidation state of Ni and so boosting the intrinsic activity of each site. Furthermore, the hybrid structure reduces the aggregation, increasing the number of exposed active sites whilst the porosity of the MONs enables rapid transport of electrolytes to the reaction site and the release of O$_2$ products. The combination of the effects results in the hybrid materials outperforming NiBDC (5.5 times), Ni(OH)$_2$ (20.6 times), and the benchmark commercial catalysts Ir/C (3.0 times).

MONs have also been used in combination with electrochemically active MNPs in order to enhance OER activity. He and co-workers recently reported the controlled calcination of Ni-MONs for the in situ generation of NiO NPs deposited MONs showing enhanced OER.[82] These NiO/Ni MONs demonstrated low overpotential and Tafel slope values in comparison with parent Ni-MONs and Ni-MONs calcined at 400 °C. The addition of NPs to lamellar MOFs has also been shown to enhance their exfoliation to generate efficient OER catalysts. Zhou and co-workers[83] showed that [Co$_2$(bim)$_4$] (bim = benzimidazolate) embedded with CoFeO$_X$ NPs weakened interlayer interactions resulting in ultrathin MONs in contrast to the layered MOFs without NPs. The CoFeO$_X$ NPs was proposed to consist of coordinatively saturated FeO$_6$ octahedral core with coordinatively unsaturated FeO$_5$/CoO$_5$ edges and highly active interfacial CoO$_2$N$_2$ sites for OER as predicted by theoretical calculations. The nanosheets coated on a carbon cloth showed higher current densities, lower over potentials and faster reaction kinetics than a range of reference samples. Post-catalysis

PXRD indicated retention of crystallinity for the MONs even after 1000 cycles indicating good stability.

In comparison with MONs based on single metals, enhanced OER activity are observed for bimetal MONs.[31,32,84–96] While direct synthesis of bimetal MON systems involves simultaneous use of different metal precursors or metal-doping, layered double hydroxides can also be used as starting materials. The improved intrinsic activity generated by the incorporation of the bimetallic sites in periodic arrangement was attributed to the enhancement OER activity in bimetal MONs. Tang and co-workers reported that Ni and Co-MONs showed high overpotential values of 321 and 371 mV, respectively.[90] Combining both metal centres to create bimetallic NiCo-MONs significantly reduced the over potential to 250 mV. Liu and co-workers showed similar enhancements in OER activity and reduction in overpotential for bimetal MONs based on NiCo and NiFe metal-clusters as well.[31] Their NiCoBDC arrays showed an overpotential of 230 mV compared with overpotential values of 308 and 289 mV for references using NiCo powder on layered double hydroxide nanosheets or NiCoBDC powder.

2.3.2. Hydrogen Evolution Reaction

HER is one of the most important reactions from an electrochemical perspective. In addition of being one of the simplest routes to access high purity hydrogen which is utilized as an energy carrier and fuel in electrochemical devices, it is other

half of water-splitting reaction together with OER. MONs based on MN_4, MS_4, and MS_2N_2 (M = Co, Ni) complexes have been recently examined for their electrocatalytic HER activity.[17,97,98] Generally, MONs of monolayer thickness possessing MN_4, MS_4, and MS_2N_2 complexes are obtained by the reaction of appropriate metal precursors with 2,3,6,7,10,11-triphenylenehexathiol or 2,3,6,7,10,11-triphenylhexamine linkers via interfacial synthesis methods (Figure 4e). The mixed-linker MS_2N_2 complex based MONs were found to be more active in comparison with those bearing MN_4 and MS_4 complexes. The higher activity was attributed to the easy accessibility to active sites. Furthermore, DFT studies revealed a protonation step preferentially occurs in the M-N sites of MS_2N_n complex of MONs.

In a recent study, Lin group reported Ce-BTB MONs with Ir and Ru photosensitizers post-synthetically anchored on the metal-clusters for photocatalytic HER.[99] Under visible light irradiation, the photosensitizers and Ce metal-clusters in close proximity promotes HER with high TONs, ≈8.7–9.3 times higher than the corresponding homogeneous analogues. Detailed characterization studies revealed a dual photoexcitation pathway where the photoreduced Ir and Ru photosensitizers facilitates the reduction of Ce^{IV} to Ce^{III}, which again on photoexcitation enables the HER. Under acidic conditions, Pt is the ideal electrocatalyst for HER. However, in alkaline condition, the sluggish dissociation kinetics arising from weak $OH^.$ absorption reduces its performance drastically. Sun and co-workers showed that the incorporation of Pt NPs on MON surfaces can impart HER activity to otherwise electrochemically inert Ni-MONs in both acidic and alkaline media.[100]

2.3.3. Carbon Dioxide Reduction Reaction

The electrochemical CO_2 reduction reaction (CO_2RR) can be used to produce high-energy density fuels and/or industrially relevant chemicals and is an attractive approach to reduce CO_2 emissions. Recently, Gu and co-workers showed cathodized MONs can acts as precursor materials for highly active CO_2RR catalysts.[101] The CO_2RR activity of $Cu_2(CuTCPP)$ MONs on a fluorine doped tin oxide electrode yielded formic and acetic acids with a cumulative Faradaic efficiency (FE) of ≈85.2% and high TOFs of 2037 and 138 h^{-1}. This compared favorably with the electrode by itself which generated a negligible amount of CO with an FE of <10%. Detailed structural analysis revealed the $Cu_2(CuTCPP)$ MONs restructured to form CuO, Cu_2O, and Cu_4O_3 under catalytic conditions and these species were speculated to be real active catalysts. Even though the crystalline nature of the MONs was not preserved during restructuring, the TCPP ligand was believed to remain anchored to the copper oxide catalysts.

The Gu group also showed how post-synthetic functionalization of ZrBTB can be used to enhance CO_2RR.[102] Zr-BTB MONs were unable to catalyze CO_2RR to form CO by themselves. However, addition of bridging CoTCPP functional groups onto the surface of the ZrBTB MONs resulted in CO production with a faradaic efficiency of 77.2%. This was further enhanced through functionalization of the missing linkers defects in the Zr clusters with *p*-sulfamidobenzoic acid resulting in an increased CO Faradaic efficiency of 85%

and much lower Tafel slope values. In a related study, Lin and co-workers showed how post-synthetic functionalization of the Hf_6 clusters of Hf-TPY MONs with monodentate cobalt centered porphyrin functionalities could be used to enhance CO_2RR (Figure 4f).[103] The authors propose that co-operative interactions stabilize a highly active pyridinium-CO_2-Co species formed between the Co of the coordinated porphyrin unit and the protonated TPY ligand. The authors highlight that key to enhancing CO_2RR activity, is suppressing the competing HER. Zr-TPY/CoPP MONs showed enhanced CO/H_2 selectivity of 11.8 in comparison to the 2.7 for Zr-BTB/CoPP. Zr-TPY/CoPP also exhibited high CO-FE of 92.2% with a TOF of 0.40 s^{-1}.

2.4. Perspective

The most clearly demonstrated advantage of MONs over MOFs in catalysis are the enhanced yields and TON shown throughout the examples thanks to increased external surface area and exposed active sites of MONs compared to bulk MOFs. Comparisons with the equivalent homogeneous catalysts are less common, although the high density of active sites and ease of recovery from solution shows some promise here too. Stability is often touted as the barrier to the industrial application of MOFs as catalysts and it might be expected to be all the more problematic for MONs as atomically thin nanosheets. Some examples do show that MONs can degrade under catalytic conditions and the active species may not be those of the MON, highlighting the importance of fully characterizing the MONs following catalysis. However, other impressive examples such as those of the Hf and Zr MONs show that MONs can remain robust even under relatively harsh thermo-, photo- and electro-catalytic conditions.

The diverse chemistry of MONs has enabled them to catalyze a wide variety of reactions. MONs have been shown to catalyze reactions through coordinatively unsaturated metal ions at the center of porphyrins, the axial positions of paddlewheels and in Zr or Hf based clusters. The optical and electronic properties of linkers and metal ions also allow them to be used directly for photo- and electrocatalysis. However, although a diverse range of different MONs have been reported, most examples are clustered around a handful of core structures which have previously been reported to form nanosheets. This is probably partially a reflection of this being a relatively new area of research in which a small number of groups have made significant contributions and partly due to the difficulty of optimizing the synthesis of new MONs. We anticipate that with time examples of many other catalytically active MON architectures will come to prominence offering different activities.

In the majority of examples, known catalytic functional groups are attached to the surface of MONs post-synthetically. A wide range of organic functional groups and co-ordination complexes have been added to different MONs through post-metalation, ligand exchange or covalent attachment. Furthermore, the MONs can be combined with MNPs, enzymes, other nanosheets, polymers, and nanotubes. In some cases, these functionalities directly catalyze the reactions, but they can also enable chiral selectivity, act as light harvesting groups, enhance conductivity or electrochemical activity. Indeed, to our taste,

ADVANCED
SCIENCE NEWS
www.advancedsciencenews.com

ADVANCED
FUNCTIONAL
MATERIALS
www.afm-journal.de

the most exciting aspect of MON chemistry is this potential to bring multiple functional groups onto the surface of MONs in well-defined positions in order to create sophisticated active sites. Beautiful examples of the levels of complexity that can be achieved through multiple levels of post-synthetic functionalization have already been demonstrated.

3. Accessible Binding Sites for Sensing Applications

New sensors, with enhanced selectivity and sensitivity are needed to address global challenges such as monitoring atmospheric and environmental pollutants, the early diagnosis of diseases and detection of explosives. MONs possess a number of features which make them ideal for use in sensing applications. Their high external surface areas are easily accessible to analytes allowing for more rapid and sensitive detection. Unlike most other 2D materials, the easily modifiable structures of MONs mean each system can potentially be tailored to facilitate interactions between the target analytes and metal nodes, ligand functionalities, or species adsorbed onto MON surfaces. MONs can be employed as sensors in suspension, as thin films or within membranes, and can produce a variety of different optical and electronic responses. In this section we discuss current examples of MONs used in the sensing of small molecules, biological molecules, and metal ions. Examples of integrated electronic sensors are discussed in Section 4.

3.1. Small Molecules

Numerous authors have demonstrated the use of molecular interactions between analytes and the metal nodes of MONs to facilitate chemosensing. PW-based MONs have proven particularly effective in this regard as the PW unit possesses Lewis acidic axial sites, typically occupied by weakly coordinating solvent molecules that can be exchanged for Lewis basic analytes. A simple approach based on this was demonstrated by Qiu et al., who used a ZnBDC system to sense ethylamine via a ratiometric fluorescence-quenching mechanism, in which the organic amine binds to the PW via the N-donor.[5] Zhang et al. then used similar CuBDC nanosheets to selectively bind larger organic dye molecules with electron donor moieties, such as methyl orange, to open PW-sites (**Figure 5**a).[105] The authors also observed weaker binding in solvents with higher basicity, owing to the stronger MON-solvent interactions. However, the significant adsorption and selectivity was still observed, indicating the suitability of PW MONs for sensing such analytes.

In our own work, we demonstrated the sensing of small N-heterocycles with analogous CuBDC systems, functionalised with alkyl-ether chains at the 2- and 5- positions of the aromatic linker intended to aid exfoliation and dispersion.[7,106] UV–vis titrations were used to quantify the binding and MONs functionalised with pentyl chains were found to bind more strongly than those with methoxy-propyl chains, which was attributed to intramolecular binding of the oxygen lone pair. In a follow-up
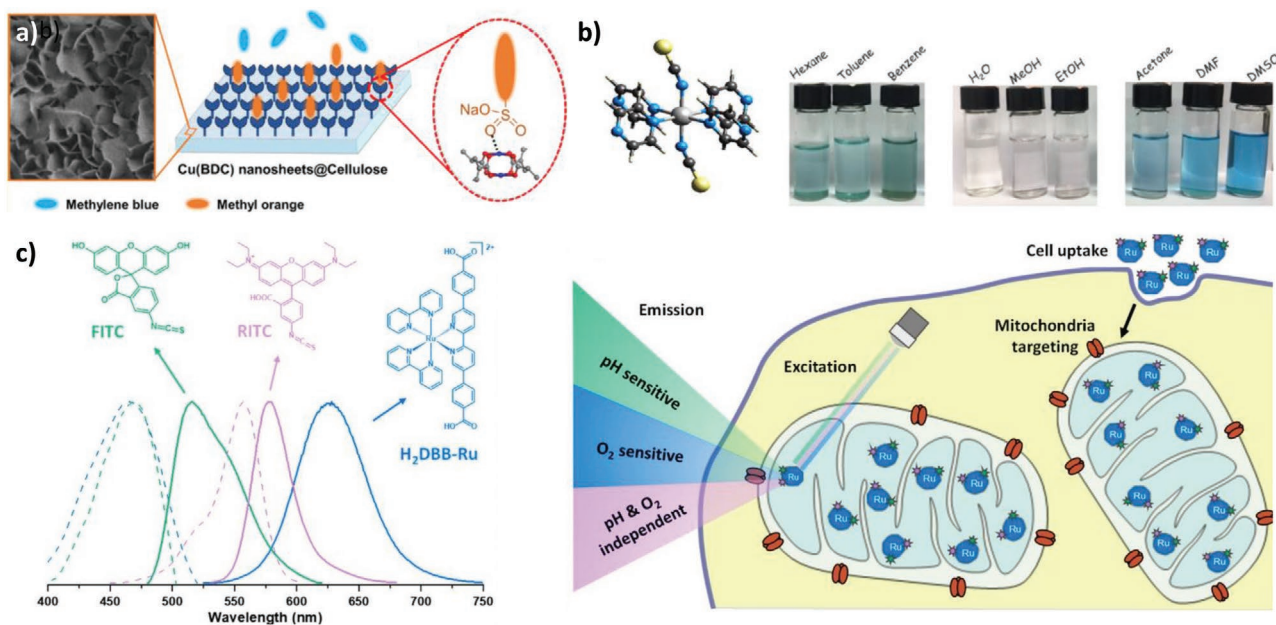
Figure 5. a) An illustration showing the preferred binding of methyl orange, via a pendant sulfonate group, over methylene blue to CuBDC nanosheets grown on cellulose by Zhang and co-workers. Reproduced with permission.[105] Copyright 2019, American Chemical Society. b) The chemical structure of the $Co(CNS)_2(pyz)_4$ unit used by Sun et al. to construct their MON system, and the color displays of colloidal suspensions of these MONs in selected nonpolar, protonic, and polar solvents. Reproduced with permission.[110] Copyright 2018, American Chemical Society. Further permissions related to this material excerpted should be directed to the ACS. c) Schematic showing the chemical structures and excitation/emission spectra of FITC, RITC, and H_2DBB-Ru. Used by Lin and co-workers, alongside an illustration demonstrating how positively charged Hf_{12}-Ru-F/R targets mitochondria and allows ratiometric sensing of intramitochondrial pH and oxygen via the luminescence ratios of pH-sensitive FITC to pH-independent RITC and O_2-sensitive DBB-Ru to O_2-independent RITC, respectively. Reproduced with permission.[112] Copyright 2019, American Chemical Society.

**ADVANCED
SCIENCE NEWS**

www.advancedsciencenews.com

**ADVANCED
FUNCTIONAL
MATERIALS**

www.afm-journal.de

study, we demonstrated that blending different linkers to create multivariate MONs could be used to fine tune their binding, as well as enhance their dispersion in different solvents.[107]

Other examples of small molecule sensing involve analytes interacting with linker functionalities rather than metal node sites. Several examples of fluorescent MONs which show enhancements or quenching of their fluorescence upon guest binding have been reported. Ma and co-workers created ultrathin MONs incorporating calix[4]arenes as fluorescent sensors for pesticides. The cavities of the calix[4]arene enabled host-guest interactions with glycophosphate leading to enhanced fluorescence with a detection limit of 0.38 ppm.[108] Cui and co-workers developed a MON system based on chiral 1,1′-binaphthol/-biphenol dicarboxylic acids, capable of enantioselective sensing.[55] The chiral —OH groups become exposed post-exfoliation, resulting in an enhanced fluorimetric sensing response for a series of chiral amino alcohols.

Moorthy and co-workers have demonstrated efficient sensing of nitroaromatics using a MON system based on a fluorescent 6-connecting hexa-acid linker.[109] Here, the fluorescence of the electron rich MON is quenched by increasingly electron deficient analytes, with trinitrotoluene the most deficient and most effective quencher. The coordination polymer only exhibits fluorescence when exfoliated, as the close-packed nature of the MOF causes self-quenching. The MON also demonstrates advantages over the free linker, both in quantum yield and quenching efficiency, which the authors attribute to the rigidification of the fluorophore linker, and to confinement of the analytes within the MON pores, indicating that the loss of three-dimensionality does not inhibit the use of host-guest pore chemistry.

Sun et al. developed a $Co(CNS)_2(pyz)_2$ (pyz = pyrazine) layered MOF, which when exfoliated, was capable of colorimetrically distinguishing between different classes of solvent (Figure 5b).[110] This was determined to be a result of the way that sulphur atoms on the coordinating thiocyanate groups exposed on the nanosheet surfaces interacted with solvents with different polarity and proton acidity. Tan and co-workers were able to use OX-1 nanosheets to distinguish between polar solvents with different sizes.[111] In this case the sensing mechanism was the disruption of host-guest interactions between the MON and a fluorescent zinc(II) bis(8-hydroxyquinoline) guest, leading to changes in emission. The MONs emission red-shifted in the presence of nonpolar aliphatic solvents and halogenated solvents which was attributed to differences in their mobility and size respectively.

Perhaps one of the most intricate examples of small molecule sensing with MONs to date came from Lin et al. in 2019, who demonstrated simultaneous and ratiometric sensing of pH and O_2 in live cells using a coordinatively post-synthetically modified MON.[112] The DBB ligand was modified with a Ru photosensitizing complex pre-synthetically and two different dyes, fluorescein (FITC) and rhodamine B (RITC), modified with isothiocyanate groups were introduced to the Hf_{12} clusters via a post-synthetic modification of the Hf_{12} capping groups (Figure 5c). Both FITC and the Ru complex are pH and O_2 sensitive, respectively, whereas the RITC dye is independent of the concentration of both. Thus, by comparing the emission intensities of FITC and Ru to RITC, the concentration of pH and O_2 in live cells could be determined.

Several authors have used MONs as horseradish peroxidase mimics to facilitate sensing of H_2O_2, glucose, and other small molecules. In these reports, the role played by the MONs is as a catalyst for the reduction of H_2O_2, which in turn induces an electro- or photochemical response that is then detected. A simple but effective example of this was reported by Zheng et al., who used hybrid CuTCPP nanosheet and carbon nanotube (CNT) films to electrocatalytically reduce H_2O_2, producing an amperometric response with an impressive detection limit of 5 nM.[113] In this case the nanosheets directly catalyze the reduction, but other authors have used embedded MNPs and complexes as additives to enhance the catalysis.[114,115] The reduction of H_2O_2 can also be coupled with the oxidation of glucose by glucose oxidase (GOx) to detect the simple sugar, as demonstrated by Li and co-workers using luminescent In(AIP) MONs.[116] However, the more typical approach has been to couple the peroxidase activity of MONs with an oxidation-sensitive chromophore, including 3,3″,5,5″-tetramethylbenzidine (TMB),[117–119] o-phenylenediamine,[120] thiamine,[121] or luminol.[122] This sensor setup allows one to generate a colorimetric response upon detection of H_2O_2 or a corresponding analyte through redox chemistry. For example, Wang et al. used a system shown in **Figure 6**, constructed of PtNP/CuTCPP(Fe) hybrid nanosheets, GOx and TMB to develop a cascade colorimetric method capable of detecting H_2O_2 and glucose with excellent sensitivity and selectivity.[117] Although this same peroxidase mechanism can be achieved using other 2D materials, such as transition metal dichalcogenides,[123] MONs have demonstrated higher sensitivities and selectivities, shown in **Table 1**.

3.2. Biological Molecules

A well-established mechanism is the adsorption of fluorophore-labelled single-strand DNA (ssDNA) which is quenched by
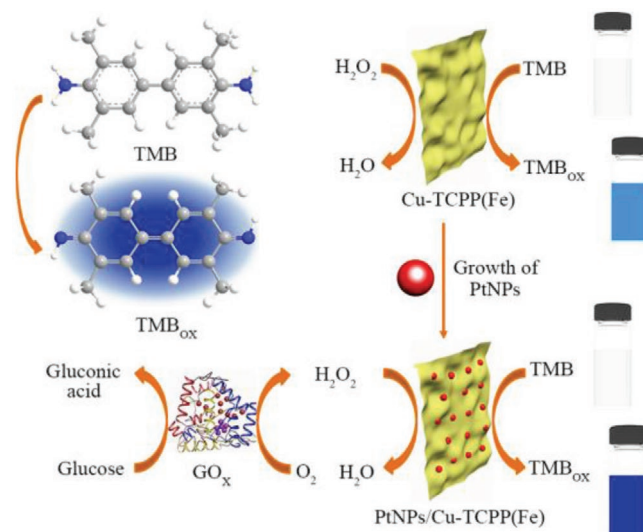
Figure 6. An illustration of the sensor developed by Ying and co-workers, using PtNPs/Cu-TCPP(Fe) hybrid nanosheets, GOx, and TMB and the mechanism by which it achieves colorimetric detection of both H_2O_2 and glucose. Reproduced with permission.[117] Copyright 2018, American Chemical Society.

Table 1. Horseradish peroxidase activities of reported MONs, alongside other selected high performing nanoparticles and MOFs.

MON system	Response type	Additives	Analyte(s)	Limit of detection/µM	Linear range/µM	Ref.
CuTCPP	Amperometric	CNTs	H_2O_2	0.005	0.01–3.75	[113]
CuTCPP	Amperometric	CNTs	H_2O_2	0.7	0.001–8.159	[124]
CuTCPP	Amperometric	Ag NPs	H_2O_2	1.2	0.0037–5.8	[114]
CuTCPP(Fe)	Colorimetric	Pt NPs, TMB, GOx	H_2O_2	0.357	2–100	[117]
			Glucose	0.994	2–200	
CoTCPP(Fe)	Chemiluminescence	Luminol, GOx	Glucose	0.06	0.18–30	[127]
NiBDC	Colorimetric	TMB	H_2O_2	0.008	0.04–160	[118]
NiBDC	Amperometric	Hemin	H_2O_2	0.2	1–400	[115]
InAIP	Fluorimetric	–	H_2O_2	0.87	0–160	[116]
Cu(HBTC)	Colorimetric	Fe_3O_4-AuNPs, TMB, ssDNA	H_2O_2	0.0011	0.00286–0.07143	[124]
			Glucose	12.2	12.86–257.14	
			Sulfadimethoxine	0.005	0.01–1.15	
CuABDC	Fluorimetric	TMB, xanthine oxidase, OPD	Hypoxanthine	3.93	10–2000	[120]
$Cu(BPY)_2(OTf)_2$	Fluorimetric	Thiamin, GOx	Glucose	0.41	10–100 and 100–1000	[121]
Other Systems						
Titania NPs	Colorimetric	–	H_2O_2	0.5	1–1000	[125]
MIL-68 / MIL-100	Colorimetric	TMB	H_2O_2	0.256/0.155	3.0–40	[126]

MON systems, initiating a signal-on response in the presence of its complimentary strand. Zhao and co-workers have shown that simple organic dyes, such as Rhodamine B, bind to MONs because of spontaneous and hydrophobic forces followed by a quenching of their emission, meaning this approach is broadly applicable to any ssDNA with a fluorescent tag.[127] This has been demonstrated numerous times as a simple and selective mechanism for the targeted detection of DNA, as shown in **Figure 7**a. Zhang et al. were the first to document this, exploiting the accessible and anisotropic structure of a CuTCPP system to efficiently quench the emission of Texas red-labelled ssDNA.[128] Several tests demonstrated that this fluorescence quenching was a direct result of the 2D nature of the MONs and their surface interactions, as both the H_6TCPP ligand and the bulk layered MOF had significantly reduced quenching efficiencies. The MON-based DNA bioassay was then used for the simultaneous detection of the Influenza A virus sub-type H5N1 gene and subtype H1N1 gene by using Texas Red-labelled ssDNA and tetrafluororescein-labelled ssDNA probes. The introduction of the target DNA selectively recovered the fluorescence of the respective probe.

Since these early studies, multiple authors have reported related studies which make use of MONs as a platform to quench the fluorescence of ssDNA based probes.[129–131] In particular, Lei and Zheng et al. identified coordination from electron donor groups on the DNA-fluorophores to open Fe^{2+} sites present in their Hofmann-type nanosheets leading to ligand to metal charge transfer which quenched the fluorescence (Figure 7b). The analogous 3D MOF showed a reduced quenching efficiency compared to the nanosheets as the majority of surface accessible metal sites are unaccessible.[132] Interactions between surface-accessible metal sites and the DNA-fluorophores have been highlighted by other authors as potentially key to explaining the increased quenching efficiency

of MONs compared to other 2D materials and 3D MOFs.[133] Xia and co-workers reported a two-color sensing platform for DNA by using two dye labels which interacted differently with their lanthanide-based (Ln) MONs.[134] The fluorescence of ssDNA labelled with fluorescein amidite (FAM), carrying negative charges, was only partially quenched by Ln-MONs. When hybridized with the complementary target DNA, the FAM-dsDNA detached from the surface of the nanosheets and reattached to the edge of the nanosheets via an electrostatic interaction between FAM and Ln^{3+}. In contrast, the ssDNA labelled with 5-carboxytetramethylrhodamine, carrying positive charges, showed the same quenching and recovery properties on MOF-Ln nanosheets as observed with traditional 2D materials. It was also observed that lanthanum-based MONs exhibited superior fluorescence quenching abilities to the neodymium, europium, and terbium-based MONs due to the lanthanide contraction.

Electrochemiluminescence (ECL) is often cited as a more sensitive response-type than fluorescence in the broader sensing literature, and multiple authors have exploited the redox chemistry of MONs to demonstrate this.[135] In particular, Dong-Rong Xiao and co-workers have used MONs based on aggregation induced emission (AIE) ligands to develop ECL platforms that are quenched by ferrocene-tagged ssDNA.[136,137] These systems are another example of how enhanced functionality can be built into MON systems through rational design. The AIE ligand MONs exhibit increased sensitivity and ECL intensity compared to the layered MOFs, ligand aggregates and ligand monomers. These systems are some of many reports in which current biosensing technologies are employed to increase the biosensors sensitivity. For example, to facilitate detection of the carcinoembryonic antigen down to 0.63 fg mL^{-1}, Xiao et al. use a rolling circle replication in order to produce duplicate DNA fragments which, form the complimentary ssDNA.
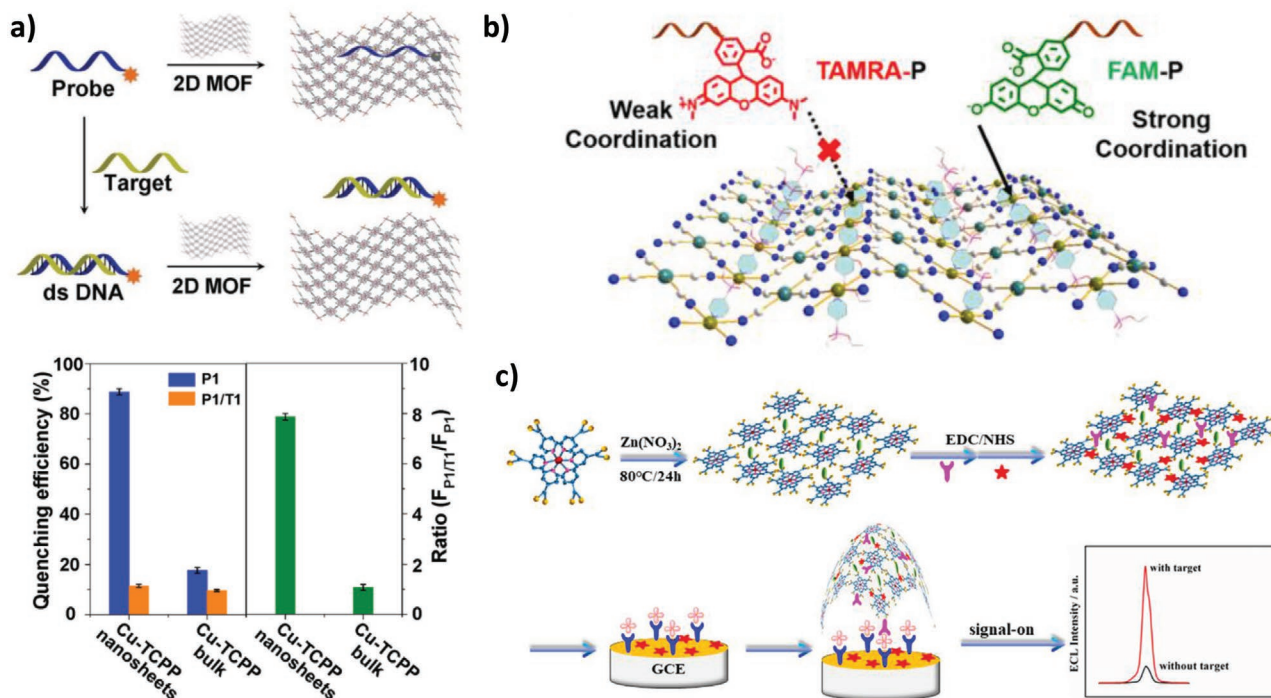
Figure 7. a) An illustration of a MON-based fluorescent DNA assay and bar chart showing Left: The quenching efficiency of CuTCPP nanosheets and bulk CuTCPP MOFs for P1 and P1/T1. Right: The fluorescence intensity ratio at 609 nm in the presence of CuTCPP nanosheets or bulk CuTCPP MOFs. $F_{P1/T1}$ is the fluorescence intensity of dsDNA (P1/T1) at 609 nm and F_{P1} is the fluorescence intensity of ssDNA (P1) at 609 nm. Reproduced with permission.[128] Copyright 2015, Wiley. b) A schematic illustration showing the differing interactions of nanosheets developed by Lei and co-workers with TAMRA-labelled and FAM-labelled ssDNA. Reproduced with permission.[132] Copyright 2019, American Chemical Society. c) An illustration depicting the construction and mechanism of the signal-on ECL immunosensor developed by Huang and Yang et al. for the detection of Cardiac Troponin I. Reproduced with permission.[138] Copyright 2019, American Chemical Society.

Although the immobilization of labelled-DNA strands is one of the most common bio-sensing mechanisms in the 2D materials literature, the use of antibody and enzyme-based biosensors can be significantly more selective and effective in the monitoring of some diseases. Yang and Huang et al. have demonstrated antibody-immobilization onto MONs, utilizing a Ru(DCBPY) system to construct a signal-on ECL immunosensor (Figure 7c).[138] In this case, the use of MONs allows the facile incorporation of redox-active species (in this case Ru), meaning signal-outputs such as ECL can be easily incorporated into the final sensor, a factor that has also been utilized by Xiao et al. in the detection of mucin 1 using a DNA assay.[139] A separate report by Xia et al. utilizes the high aspect ratios of CuTCPP(Fe) MONs to immobilize both PtNi nanoparticles and antibodies onto their surfaces, thus constructing a sandwich-type electrochemical immunosensor for calprotectin in serum. In this study, the nanoparticle/MON hybrid structure exhibits enhanced electrocatalytic activity towards H_2O_2 reduction, enabling them to act as signal amplifiers resulting in the highly sensitive detection of calprotectin down to 137.7 fg mL^{-1}.[140]

3.3. Ions

To date, the sensing of solution-phase ions with MONs is limited to a handful of examples, the majority of which have only explored the sensing of Fe^{3+} ions. The first example of

Fe^{3+} sensing with MONs was demonstrated by Qian et al. in 2016, who showed that $Ti_2(HDOBDC)_2(H_2DOBDC)$ nanosheets exhibited a fluorescence quenching response in the presence of Fe^{3+} ions.[141] This was attributed to competitive absorption in the UV–vis region, and potential electron transfer between Fe^{3+} and the MONs. The authors also demonstrated that the highly dispersive nature of the nanosheets allows close contact between them and the metal ions, leading to reduced limits of detection compared to bulky MOF sensors and other nanomaterials. The same fluorescence quenching mechanism of Fe^{3+} sensing has since been demonstrated with other nanosheets systems, also exhibiting improved detection limits.[142,143] However, although each of these systems has been demonstrated to be selective amongst a range of transition metal ions, this mechanism of detection is potentially hindered by the presence of other species present that absorb in the same region of the UV–vis spectrum. This is partially demonstrated by Ni and Sang et al., who observed that their $Zn_2(bim)_4$ system was capable of sensing Fe^{3+} via this mechanism, but Cr^{3+} also exhibited a similar but reduced quenching effect. Furthermore, Chen and co-workers observed that Zn(5-(4-pyridyl)-tetrazolyl) MONs can sense but cannot distinguish between both Fe^{3+} and Cu^{2+} ions.[144]

In 2019, Hmadeh et al. demonstrated a comparable turn-off probe for Pd^{2+} with isonicotinate-based AUBM-6 nanosheets.[107] In this case, it was shown that the unexfoliated layered MOF exhibits a significantly reduced fluorescence intensity, and thus
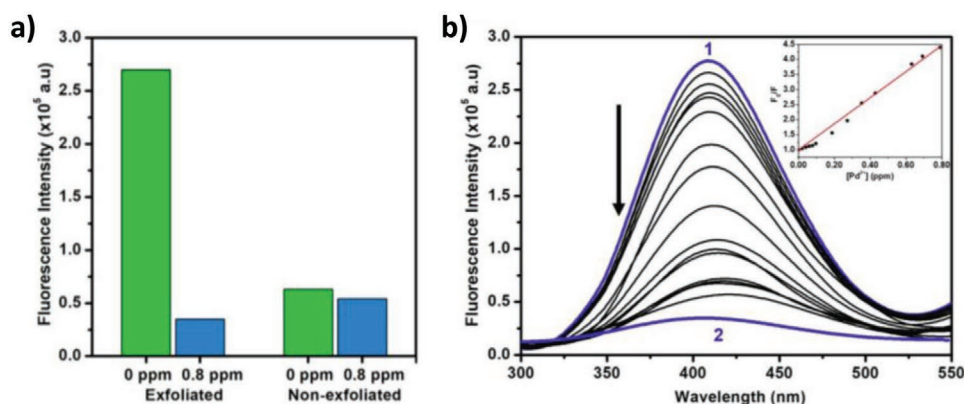
Figure 8. a) The effect of exfoliation of AUBM-6 MOF into nanosheets on the sensing of Pd^{2+} at 0.8 ppm. b) Photoluminescence spectra of AUBM-6 MONs. PL titrations of AUBM-6 at 1) 0 and 2) 0.8 ppm of Pd^{2+} ions at $\lambda_{ex} = 285$ nm. (inset) Stern–Volmer plot demonstrating gradual Pd^{2+} titrations. Reproduced with permission.[107] Copyright 2019, American Chemical Society.

is much less sensitive to changes in the concentration of Pd^{2+}, as shown in **Figure 8**. However, the fluorescence of this system is also sensitive to the presence of As^{3+}, Cu^{2+}, and Fe^{3+} ions, albeit to a lesser degree.

3.4. Perspective

The current literature on the use of MONs in the development of novel sensors broadly divides into one of two approaches. The first approach involves the design of MONs as the complete active sensor with analytes interacting directly with the MONs surface and so inducing observable changes in the MONs optical or electronic properties. The diverse chemistry of MONs mean that they can play many different roles within these interactions with open metal sites binding analytes, catalyzing reactions or acting as redox sites and ligands acting as hosts to quench or enhance fluorescence. The porosity of MONs can also be exploited by creating cavities to enhance guest binding. The outputs can be diverse with changes in color, fluorescence or an electrochemical response. The second approach uses MONs as just one component within often complex, well established, multicomponent sensor systems. In these examples, much of the sensitivity and selectivity often comes from other components within the system such as single-stranded DNA, enzymes or nanoparticles.

Multiple reports have demonstrated the enhanced sensitivity and response times of MONs compared to MOFs thanks to their increased accessibility of their binding sites. Although the higher surface area of MONs is advantageous in sensing, this must also be coupled with a highly sensitive method of detection such as fluorescence, ECL or electrochemistry to

create a competitive sensor. Another advantage is the potential for improved response times compared to bulk MOFs where access to binding sites can be diffusion limited, however this has not yet fully been demonstrated. The density of active metal and ligand binding sites on MONs is also a potential advantage compared to solution-based sensors, particularly for larger analytes where multiple interactions can occur. The selectivity introduced by the MONs in most of the examples above is limited to generic binding interactions such as co-ordination to metal sites or quenching of fluorophores. In our opinion, only a few examples so far demonstrate the full potential of MONs as a platform for creating specific binding sites within effective sensors.

4. Tunable Opto-Electronic Properties for Energy Storage, Light Harvesting, and Other Devices

The silicon-centered paradigm in electronics has recently been challenged by the commercialization of organic light emitting device (OLED) technology, rapid developments in hybrid perovskites for solar cells and new types of graphene based integrated photonics. The diverse chemistry and modular structure of MONs allows for ready tuning of a diverse range of useful electronic and optical properties including their dielectric constants,[145] electrical resistance,[146] redox activity and band gap.[40,147–149] Although most MONs are insulating, there are a growing number of 2D architectures which show semi-conducting and conducting behavior. The nanoscopic dimensions of MONs allow for integration within thin-film devices in a way not possible for bulk MOFs.[150] This section focuses on the progress that has been made in the use

Table 2. MON based metal-ion batteries and their performance parameters.

MON	Diffusion coefficient [$cm^2 s^{-1}$]	Rate capability [mAh g^{-1} at 2 A g^{-1}]	Reversible capacity [mAh g^{-1}]	Cycles tested	Ref.
Mn-UMOFNs	2.48×10^{-9}	701	1187	100	[159]
Ni-UMOFNs	3.77×10^{-9}	229	546	100	[159]
u-CoTDA MONs	Not reported	694	790	400	[158]
Zn-LMOFNs	Not reported	525	623	100	[160]

Table 3. MON based supercapacitors and their performance parameters.

MON	Specific capacitance [F g^{-1}]	Current density (A g^{-1})	Cycling capacity [%]	Cycles tested	Energy density	Power density	Ref.
NiCoMOF/rGO	1553	1	83.60	5000	44 Wh kg^{-1}	3168 W kg^{-1}	[167]
CuTCPP/PPy	163.34	0.2	n/a	n/a	2.27 µWh cm^{-2}	50 µW cm^{-2}	[168]
NiTCPP/CNT	2280	5	90.3	2000	n/a	n/a	[113]
NiCo-BDC	2230	1	68.5	6000	34.3 Wh kg^{-1}	375 W kg^{-1}	[164]
Co$_2$(OH)$_2$C$_8$H$_4$O$_4$	2564	1	95.8	3000	n/a	n/a	[163]
NiCo-MOF@PNTs	1109	0.5	79.10	10 000	41.2 Wh kg^{-1}	375 W kg^{-1}	[169]
Ni-Co BDC	1700.40	1	93.2	2000	n/a	n/a	[165]
CuBTC@MnO$_2$	340	1	95	6000	n/a	n/a	[170]
NiCo-PTA MON	1202.1	1	n/a	n/a	49.4	562.5	[166]

of MONs within electronic sensors, batteries, supercapacitors, light emitting diodes, and photovoltaics.

4.1. Device-Integrated Sensors

MONs have been cast as films onto interdigitated electrodes and used as chemresistive sensors to monitor analytes based on changes in their electrical resistance. Dinca and co-workers demonstrated the use of conductive MONs of Cu$_3$(HITP)$_2$ (HITP = hexaminotriphenylene) as ammonia sensors via potentiostatic measurements (**Figure 9**a).[154] These MONs with intrinsic pi-conjugation and charge de-localization within the plane, showed a conductivity of 0.2 S cm^{-1}. Similar chemresistive sensors developed using isomorphic Ni$_3$(HITP)$_2$ and Cu$_3$(HHTP)$_2$ MONs (HHTP = 2,3,6,7,10,11-hexahydroxytriphenylene) were shown to reliably distinguish between different categories of volatile organic compounds. The authors attributed either charge transfer or hydrogen bonding as

the possible mechanisms for the various sensing responses observed.[151]

Zhao and co-workers used first principles calculation to show that the selectivity of semiconducting MONs towards gas sensing arose from the increased electronic states near the fermi level due to adsorption of the gas molecules onto MONs (Figure 9c). The authors stated that the resulting up-shifted fermi level is expected to change the electronic property of the MONs from semi-conducting to metallic—leading to the chemresistive response.[152]

Non-conductive MONs have also been used in combination with conductive substrates to make electronic sensors. Hu and co-workers demonstrated the use of NiBDC MONs when composited with Ni/NiO/C as a non-enzymatic glucose sensor with high sensitivity of 367.45 mA M^{-1} cm^{-2} (Figure 9b).[153] Other notable examples include CoTCPP(Fe) MONs as amperometric sensors for H$_2$O$_2$ detection, AuNCs@521-MOF (where NC = nanocrystal) for detection of cocaine by electrochemical impedance spectroscopy and ZnTCPP MONs for amperometric sensing of nitrite.[154–156]
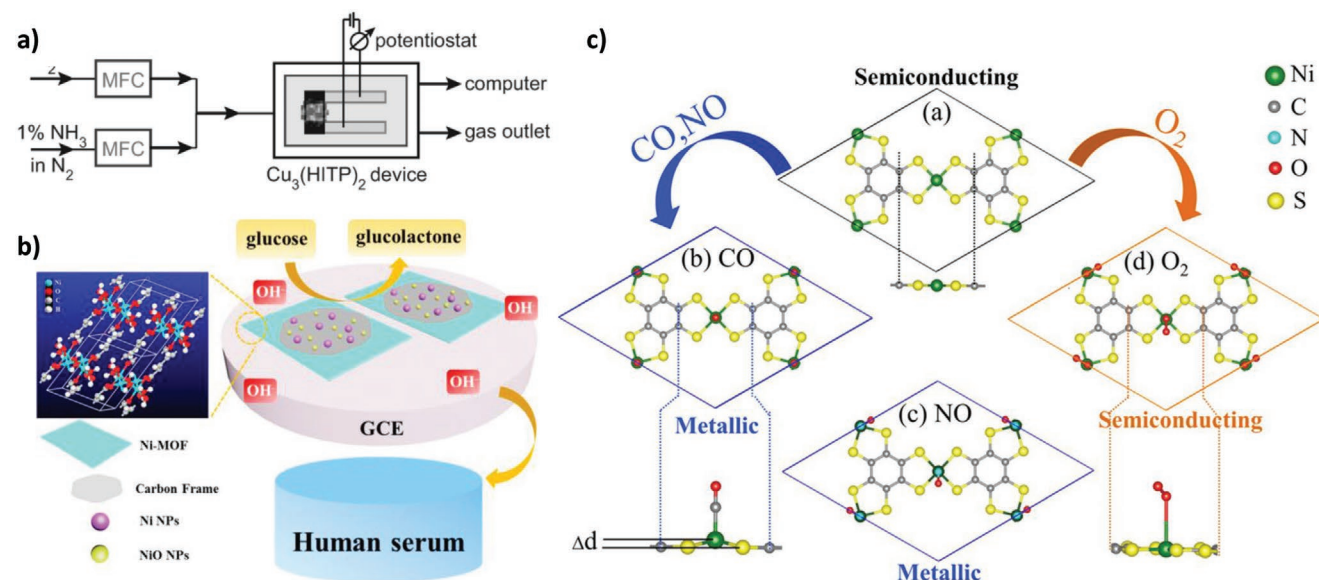
Figure 9. a) Scheme of a MON based chem-resistive device for ammonia sensing. Reproduced with permission.[154] Copyright 2015, Wiley. b) Schematic of the Ni-MOF/Ni/NiO/C nanocomposite glucose sensor for human serum samples. Reproduced with permission.[153] Copyright 2017, America Chemical Society. c) Schematic representation of change in electronic nature of MONs upon gas adsorption. Reproduced with permission.[153] Copyright 2016, American Chemical Society.

**ADVANCED
SCIENCE NEWS**

www.advancedsciencenews.com

**ADVANCED
FUNCTIONAL
MATERIALS**

www.afm-journal.de
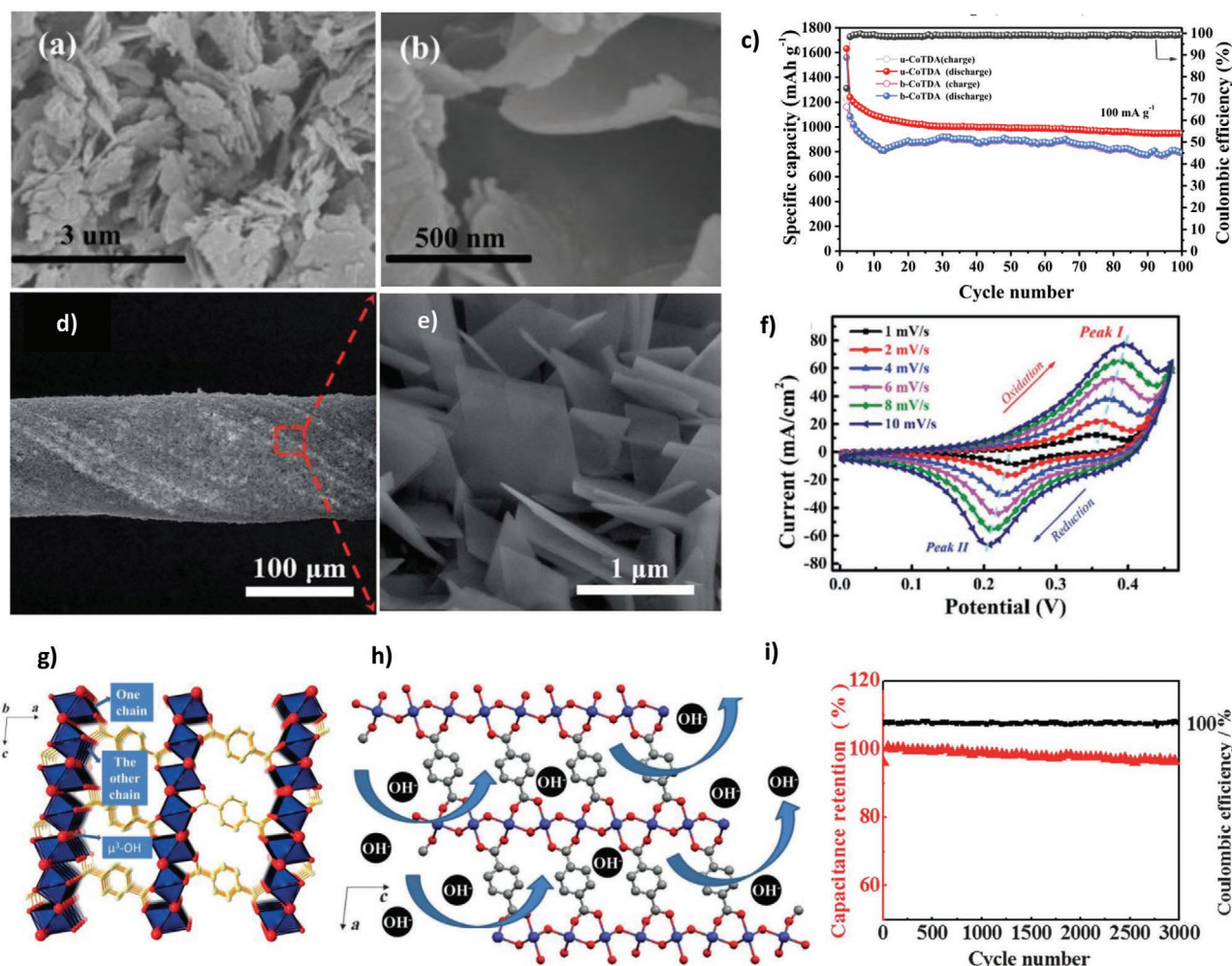
Figure 10. a,b) SEM images of Co-TDA MONs employed as anodes in lithium ion batteries. c) Cycling performance of CoTDA MONs (u-CoTDA) compared with the bulk MOF (b-CoTDA) at a current density of 100 mA g^{-1} versus Li+/Li with the corresponding coulombic efficiency. a–c) Reproduced with permission.[158] Copyright 2017, Wiley. d,e) SEM images of Ni-MOF/CNTF showing nanostructured hybrid composites of MONs. f) The cyclic voltammetry curve of the corresponding MON based FAR Ni-Zn battery. d–f) Reproduced with permission of the Royal Society of Chemistry.[161] g) Structure of the Co MON with a layered structure and a conductive network frame used as a supercapacitor electrode. h) Schematic representation of intercalation/de-intercalation process of OH^{-1} in the layered structure of the Co-MOF crystal. i) Charge–discharge profile (black line) and specific capacitance (red line) at a current density of 2 A g^{-1} of the Co-MOF electrode. Reproduced with permission.[163] Copyright 2016, Wiley.

Layered MOFs have also been assembled as a transducer device for molecular recognition via capacitive response. NH$_2$-MIL-53(Al) was synthesized as nanosheets and nanoparticles by Gascon et al. using surfactant-assisted arrested crystallization technique. The nanosheets were cast as films over p-doped silicon substrates to obtain planar capacitive electrodes.[157] The authors showed that anisotropic structure of the nanosheets orientated the 1D channels with respect to the electrodes resulting in shorter diffusion pathways and so better capacitive sensing with reduced response time.

4.2. Electrodes for Energy Storage

MONs have been explored as potential electrode materials in lithium-ion batteries (LIB). The accessible redox active centres in MONs offer enhanced Li$^+$ ion insertion/desertion when used

within the anodes of LIB. Hu and co-workers demonstrated this strategy with (Ni$_2$(OH)$_2$BDC) MONs, (Mn$_2$(OH)$_2$BDC) MONs, and cobalt thiophenedicarboxylic acid MONs (**Figure 10**a–c).[158,159] The authors proposed that the lithiation/de-lithiation mechanism in these systems showed the involvement of both the metal center and the chelating ligands in the reduction/oxidation process, thereby providing a high theoretical electron storage capacity for the electrode. The ultra-thin morphology of the MONs offered shorter ion diffusion distances to the internal electroactive sites. This effective ion transportation in the MON based anodes resulted in 100% coulombic efficiency, outstanding rate capability, and long-term cyclic performance—key performance parameters in LIBs.[158–160]

MONs have also been used in conjunction with conductive supports to form high performing hybrid electrodes. Yao et al. demonstrated the use of nickel 2,6-naphthalene dicarboxylic acid (Ni-2,6 NDC) MONs grown on CNT fibers as a barrier

**ADVANCED
SCIENCE NEWS**

www.advancedsciencenews.com

**ADVANCED
FUNCTIONAL
MATERIALS**

www.afm-journal.de

free cathode to form a fiber-aqueous rechargeable nickel-zinc (FAR Ni-Zn) battery (Figure 10d–f).[161] The prepared device displayed high rate capacity and stability with up to 89% retention in capacity after 600 cycles of operation. Zong and co-workers studied the use of bimetallic porphyrin MONs/reduced graphene oxide (CoNi-MON/rGO) composite as the air electrode in zinc-air batteries. The authors attributed the superior performance and stability of this electrode to the optimized electronic conductivity of the bifunctional MON/rGO composite.[162]

MONs with high electrical conductivity have been reported as high performing electrodes in supercapacitors. Wei et al. demonstrated the pseudocapacitive behavior of conductive Co-MOF nanosheets (Figure 10g–i).[163] The study showed that the large interlayer distance in the MON structure provided enough space for electrolyte storage and ensured efficient OH^- intercalation and de-intercalation. The conductive network frame acted as an electron transport channel. The authors demonstrated that with a conductivity of 3.75×10^{-3} S cm^{-1}, the MONs helped accelerate the transfer of electrons at the electrode-electrolyte interface. Bu and co-workers demonstrated faradaic properties in a Ni-Co bimetallic MOF electrode deposited on Ni foam. This electrode showed lower series resistance and faster electron transfer rate during the charge/discharge procedure.[164] The electrochemical performance was shown to be better than the single ion MOFs due to the improved conductivity. In another study by Li and group, Ni-Co BDC MONs displayed strong coupling between the Ni^{2+} and Co^{2+} species which facilitated charge transfer during electrochemical reaction leading to high pseudocapacitive behavior.[165] Ni-Co BDC MONs on activated carbon were used to create asymmetric supercapacitors in another similar work by Yang et al.[166]

With a vast number of MONs exhibiting limited electrical conductivity, compositing them with other conductive nanomaterials is also a typical approach in supercapacitors. Zheng and co-workers demonstrated that NiTCPP film/CNT composites exhibit 1.8 times and 14 times higher specific capacitance than pure NiTCPP and pure CNT electrodes respectively.[113] The authors showed that the hybrid nanostructures reduced the aggregation of individual components and provided a shorter route between each component thereby improving electron transfer. Liu and co-workers developed 2D NiCo-MOF ultrathin nanosheets/rGO hybrid electrode. The authors showed that the rGO facilitated the ionic and electronic conductive pathway while the redox active sites of the MONs provided an additional pseudocapacitive component.[167] Zhang et al. demonstrated electrostatically self-assembled TCPP/GO electrode as a flexible asymmetric supercapacitor. The electropositive TCPP MONs and electronegative GO sheets when composited together showed bending tolerance and good conductivity.[171]

MONs have also been employed as substrates to host electrode materials. Zhao et al. demonstrated the electrochemical polymerization of polypyrrole (PPy) onto wrinkled 2D ultrathin CuTCPP nanosheets to construct a flexible CuTCPP/PPy hybrid film. The authors attributed the enhanced supercapacitive performance to intense electronic interaction between the CuTCPP MONs and PPy and the porous film structure that facilitated sufficient immersion of the electrolyte.[168] Detailed mechanistic investigations showed that PPy offered a conductive network for fast electron transport and enhanced the electrochemical kinetics. In a similar work, PPy nanotubes have also shown

success when used in conjunction with MONs to impede aggregation, boost conductivity and enhance the pseudocapacitance behavior.[169] In another example, Pang and co-workers used the porous Cu-BTC MON as an inert host for pseudocapacitive MnO_2 NPs. The authors attributed the resulting superior charge–discharge performance to the film formation in the MON/NPs composite that favored the diffusion path of ions.[170]
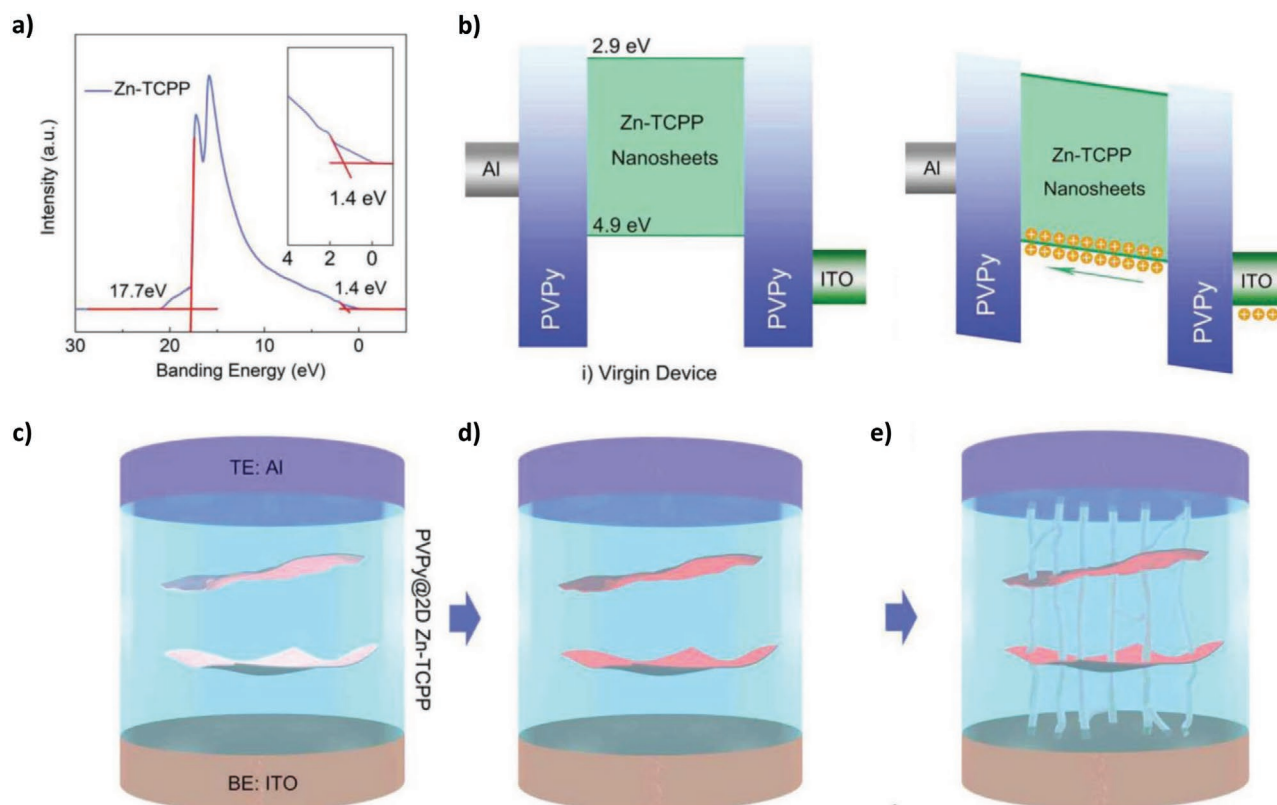
4.3. Memory Devices

Resistive random-access memory (R-RAM) devices are nonvolatile memory devices with a resistive-switching material as the active layer. Ding et al. showed how ZnTCPP MONs could be used to fabricate R-RAM devices which show bipolar resistive switching behaviour. In this work by ZnTCPP MONs are immobilized as guest in PVP polymer and cast as the resistive layer between two electrodes (**Figure 11**).[145] Differences in molecular orbital levels mean the MONs trap charge carriers within the insulating matrix. Once a high enough concentration of carriers is reached, charges can hop via the percolation pathways created by the MONs switching the device to a low-resistive state. Applying an electric field with reverse polarity leads to the collapse of the transport pathways and switches the device back to a high resistive state.

4.4. Metal-Organic Framework Nanosheets in Light Emitting Devices

In recent years, MONs have been used to create light emitting devices. In a work by Nishihara and co-workers, bis(dithiolato) nickel (NiDT) nanosheets on ITO were employed as the hole buffer layer within OLEDs. The devices showed comparable efficiencies to conventional OLEDs and nearly twofold enhancement in device lifetime compared to the standard PEDOT:PSS based devices.[172] Another promising example of MONs in emissive applications is by Lin et al. who used Zr-4′,4″,4‴,4⁗-(ethene-1,1,2,2-tetrayl)tetrakis([1,1′-biphenyl]-4-carboxylate-(TCBPE) based MONs to create visible light communication devices.[173] The bi-layered nanosheets display favorable photophysical properties, high quantum yields and restricted internal motion of the fluorescent struts owing to the network structure. However, there is a drop of 30% in output power following 168 h of operation, which the authors attribute to degradation of the linker upon light-exposure in the presence of oxygen.

4.5. Metal-Organic Framework Nanosheets in Photovoltaic Devices

The first example of MONs used in a functional solar cell was as a buffer layer in a paper by Huang and co-workers in 2018. Tellurophene based MON was mixed with a polymer surfactant PEIE (polyethylenimine ethoxylate) to form a hybrid ink that was integrated as an electron extraction layer along with ZnO into organic solar cells (**Figure 12**a).[174] Ultraviolet photoelectron spectroscopy measurements showed that the work function of ZnO decreased with the addition of PEIE,

Figure 11. a) UPS measurement of ZnTCPP MONs used as memory device; b) the corresponding energy band diagram; and c–e) an illustration of resistance switching mechanism based on charge trapping. Reproduced with permission.[145] Copyright 2018, Wiley.

whilst adding the MONs increased it to a medium work function that improved device performance. The study showed this as a widely applicable approach by employing this MON based electron extraction layer in two important types of solar cells—P3HT-PCBM the workhorse of semiconducting devices—the most well characterized and largely accepted standard organic photovoltaics (OPV);[175] and PBDB-T-ITIC the best performing non-fullerene OPV at the time.[176] MONs have also been used to form a liquid-junction solar cell. Jiang et al. showed that porphyrin-based MONs could be assembled onto ITO and embedded with fullerenes to form a functioning device. The high surface area and porous structure of the photoactive MONs enhanced charge transfer to the electron accepting fullerenes resulting in a quantum efficiency of <0.5% (Figure 12b).[177]

A study published by our group is the first example showing incorporation of MONs into the photoactive layer of OPV bulk heterojunctions (Figure 12c,d).[178] Porphyrin MONs as a ternary blend within the archetypal P3HT-PCBM architecture resulted in the formation of a ternary blend solar cell which showed a doubling in device power conversion efficiency (PCE).[178] Detailed investigations into the morphology of the active layer using AFM, wide angle X-ray, and dark injection measurements showed that the relative proportion of crystalline regions in the thin films is improved upon incorporation of MONs. Thus, MONs act as templates to increase the crystallinity of the otherwise semi-crystalline polymer P3HT leading to more balanced charge mobility and device performance metrics.

Recently, Jen and co-workers demonstrated the use of MONs as an electron extraction layer at the perovskite/cathode interface leading to a 22.02% efficient perovskite solar cell (Figure 12e–g).[179] The MONs enabled improved long-term operational stability with up to 90% retention in PCE under accelerated testing conditions. The thiol functionalized Zr-BTB MON formed intimate contact with the silver electrode to extract electrons efficiently from the perovskite solar cell. The authors also demonstrated that the thiol functionalization trapped the mobile Pb^{2+} ions at the perovskite/electrode interface—a major step to mitigate the potential impact of perovskites on environmental sustainability.

4.6. Perspective

The growing number of examples of 2D conducting and semiconducting MOFs offer significant opportunities for use within device-integrated sensors. The high surface area, inherent porosity, and ease of thin film formation of MONs offers advantages over other 2D materials and 3D frameworks. However, only a handful of conductive SBUs are so far known and the requirement to maintain extended conjugation limits the scope for enhancing the selectivity of these devices. The ultrathin nature of MONs allow for close contact between MONs and conductive supports opening up the use of a diverse array of insulating MONs within device integrated sensors.

MONs have already been shown to outperform their bulk counterparts when incorporated as electrodes in energy storage

ADVANCED
SCIENCE NEWS
www.advancedsciencenews.com

ADVANCED
FUNCTIONAL
MATERIALS
www.afm-journal.de
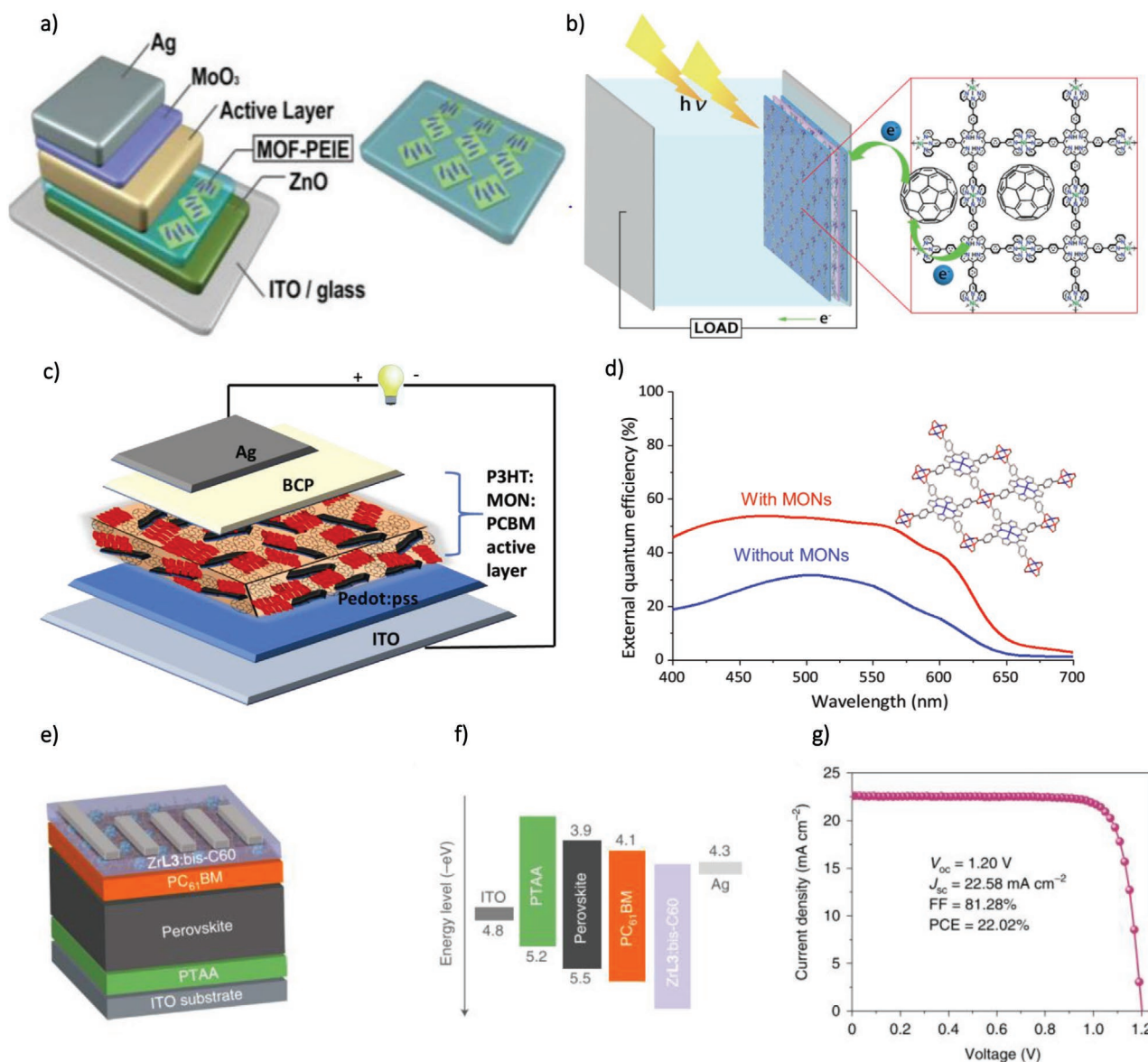
Figure 12. MONs in light harvesting devices. a) Device structure of solar cells investigated with a MON based electron extraction layer. Reproduced with permission.[174] Copyright 2018, Elsevier. b) Schematic representation of the porphyrin based liquid junction solar cell with incorporated fullerene. Reproduced with permission.[177] Copyright 2019, Wiley. c) device structure of solar cells with Zn_2(ZnTCPP) MONs in ternary bulk heterojunctions in our work. d) The external quantum efficiency curves showing enhanced device performance with MONs. c,d) Reproduced with permission.[178] Published by the Royal Society of Chemistry. e) Device structure of the inverted MON based perovskite solar cell; f) the energy level alignment of the used materials in (e); g) The *J–V* curve of the best performing perovskite solar cell with the MON electron extraction layer. e–g) Reproduced with permission.[179] Copyright 2020, Springer Nature.

devices. While not all MONs are electronically conducting, they are physically flexible enough to stick closely with conductive substrates allowing insulating MONs to be used high performing batteries and supercapacitors. As MONs approach monolayer thicknesses, they offer shorter diffusion paths for the electrons/ions and improve the rate performance. The higher surface area also increases the number of coordinatively unsaturated redox sites leading to higher capacity of the electrodes. The porous nature of MONs is advantageous in the transport of the electrolyte ions in battery applications. MONs also can provide an inert scaffold for psuedocapacitive materials in supercapacitors.

The optical properties of MONs can also be combined with their electronic properties to enable their use in light harvesting and emission applications. MONs have already shown tremendous success in a variety of roles ranging from use as electron extraction layers, to electron donors and light absorbers and emitters. The tunability of MONs also offers great potential for fine-tuning their band-gap in order to optimize overall device performance. The surface chemistry of MONs also allows them to impart morphological changes to devices as well as trap the release of toxic heavy metals and improve the environmental sustainability of devices.

5. Tuneable Porosity and High Anisotropy for Separation Applications

Membrane based separations are of critical importance to enabling a wide range of technologies needed to address the climate emergency including CO_2 capture, hydrogen generation and cleaning polluted water. The suitability of MONs for separation applications stems from the combination of their 2D anisotropic structure, large surface area for separation and inherent porosity provided by the metal-organic structure. MONs therefore possess two distinct routes for mass transport: 1) Through the intrinsic pores within the MON layers 2) by creating a tortuous path for molecules to travel around, differentially interacting with the MONs surfaces as they do so (through both external and interlayer channel mass transport).[180] The diverse and tunable surface chemistry of MONs can allow fine-tuning of interactions with specific molecules, as well as, other components within membranes. The anisotropic structure of MONs allows for their orientation within the membranes, enhancing the tortuous path. At present, it is difficult to compare the performance of different MON-based membranes across the literature, as authors use different feed-pressures, temperatures, substrates, fillers, membrane thickness, and MON loadings (**Table 4**). However, both 2D and MOF materials have already been extensively investigated for separation applications providing a rich literature to build on and compare with. Within this section we discuss how the porosity, anisotropy and tunability of MONs has led to their application in gas separation and water purification applications and highlight significant advances to the state-of-the-art.

5.1. Gas Separation

MON based membranes for gas separation can generally be split into two categories: MON films deposited onto a macroporous support such as α-Al_2O_3, and mixed-matrix membranes (MMMs) in which the MONs are dispersed within a polymer-containing medium and cast into solid membranes. A common problem with incorporating MOFs or other nanoparticle fillers into MMMs is filler agglomeration at relatively low loadings,[181,182] and decreased selectivity due to pathways around the filler because of poor polymer/filler blending.[183] A similar problem occurs for supported films of other 2D materials, in that inefficient packing/stacking of nanosheets exacerbates interlayer channel transport. To avoid this, Yang and co-workers used a hot- drop coating method to deposit a sub-10 µm MON film with disordered nanosheet stacking onto α-Al_2O_3 support instead of the simple filtration common for other 2D materials.[13] This prevented the ordered restacking of MONs into bulk MOF, which would result in blockage of the sieving pores. Jiang et al. took the idea of reducing the non-target diffusion pathway further by including flexible graphene oxide nanosheets into a CuBDC film to "repair" the junctions between MONs, resulting in increased H_2/CO_2 selectivity of 95.1.[184]

Table 4. Summary of data related to CO_2-based gas separations using MONs within the size-discriminative layer.

MON	Layer thickness /µm	s or f, substrate or filler	MON loading /wt%	[a]Gas pair	Feed conditions p/bar, T/°C	Max. permeance (gas) /GPU	/Barrer	Max. selectivity	Ref.
$[Zn_2(bim)_4]_n$	<0.01	s, α-Al_2O_3	N/A	H_2/CO_2	1, 25	3760 (H_2)	–	291	[13]
$[Zn_2(bim)_3(H_2O)(OH)]_n$	<0.01	s, α-Al_2O_3	N/A	H_2/CO_2	1, 120	2388 (H_2)	–	166	[185]
$[Cu_2(NDC)_2(DABCO)]_n$	40	f, PBI	N/A	H_2/CO_2	5, 35	–	6.13 (H_2)	26.7	[186]
$[Ni_8(5\text{-}BBDC)_6(\mu\text{-}OH)_4]_n$	0.04	s, AAO	N/A	H_2/CO_2	1, 20	553 (H_2)	–	235	[21]
					1, 100	36 (H_2)	–	<8	[21]
$[Cu(BDC)]_n$	47	f, PI	8.2	CO_2/CH_4	7.5, 25	–	2.78 (CO_2)	88.2	[6]
$[Cu(BDC)]_n$		f, PI	12	CO_2/CH_4	20	–	6 (CO_2)	32	[189]
$[Cu(BDC)]_n$	0.66	f, PIM-1	10	CO_2/CH_4	1, 25	407 (CO_2)	–	15.6	[187]
$[Cu(BDC)]_n$	70	f, PIM-1	2	CO_2/CH_4	1, 25	–	2030 (CO_2)	24	[190]
	50	f, 6FDA-DAM	4	CO_2/CH_4	1, 25	–	430 (CO_2)	43	[190]
NUS-8	66	f, PIM-1	2	CO_2/CH_4	1, 25	–	6462 (CO_2)	30.1	[188]
NH_2-MIL-53(Al)	86	f, PI	8	CO_2/CH_4	9, 25	–	11.73 (CO_2)	31.9	[157]
$[Zn(TCPP)]_n$[b]	0.025	s, PAN	N/A	CO_2/N_2	1, 35	1710 (CO_2)	–	34	[191]
$[Cu(BDC)]_n$[b]	<0.05	s, Polyactive	N/A	CO_2/N_2 (15/85)	2, 25	129 (CO_2)	–	35	[192]
$[Cu(BDC)]_n$	0.708	f, Polyactive	8	CO_2/N_2 (15/85)	2, 25	40 (CO_2)	–	77	[192]
ZIF-67	<100	f, Pebax	5	CO_2/N_2	1, 25	–	139.4 (CO_2)	73.2	[14]
NUS-8 [...]$_n$	66	f, PIM-1	2	CO_2/N_2	1, 25	–	6725 (CO_2)	26.8	[188]
ZIF-L	unknown	f, Pebax	20	CO_2/N_2 (10/90)	2, 25	–	387.2 (CO_2)	47.1	[193]

[a]Equimolar unless stated; [b]MONs are not the sole selective layer in the multilayered membrane; A discriminatory porous polymer layer was additionally present; Acronyms: bim = benzimidazole, NDC = 1,4-naphthalenedicarboxylate, DABCO = 1,4-diazabicyclo[2.2.2]octane, 5-BBDC = 5-tert-butyl-1,3-benzenedicarboxylate, MeIM = 5-methylimidazole, PBI = polybenzimidazole, AAO = anodic aluminum oxide, 6FDA-DAM = 4,4′-(hexafluoroisopropylidene)diphthalic anhydride (6FDA) and diaminomesitylene (DAM), PAN = polyacrylonitrile.

**ADVANCED
SCIENCE NEWS**

www.advancedsciencenews.com

**ADVANCED
FUNCTIONAL
MATERIALS**

www.afm-journal.de
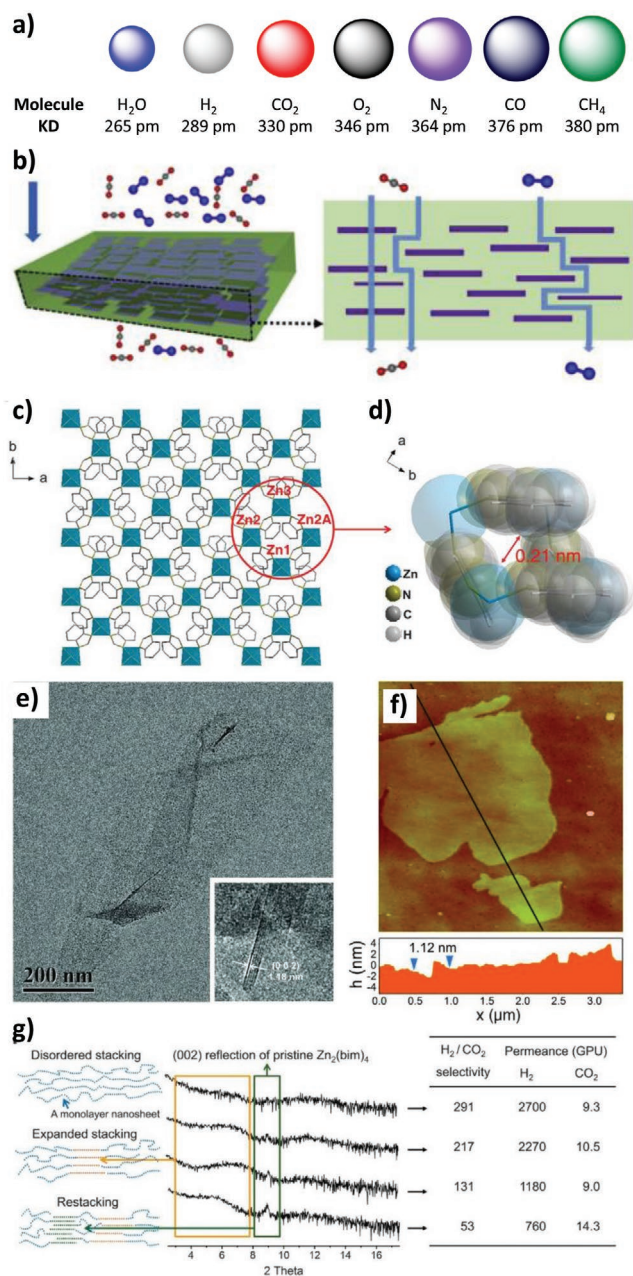
Figure 13. Schematic illustrations of a) different gas molecules' kinetic diameters (KD) and b) mass transport pathways through a MONs. Reproduced with permission.[14] Copyright 2020, Elsevier. c) Illustration of the porous grid-like structure and d) space-filling representation of a pore within a layer of $[Zn_2(bim)_4]_n$. e) TEM and f) AFM images of $[Zn_2(bim)_4]_n$ nanosheets. g) PXRD of membranes with different separation properties with (left) illustrations of microstructural features of the MON layers. c–g) Reproduced with permission.[13] Copyright 2014, AAAS.

For MMMs, Gascon et al. demonstrated that CuBDC nanosheets could be readily included within a polyimide (PI) matrix (**Figure 13**).[6] The high anisotropy of the MONs resulted in near parallel alignment of the MONs within the polymer matrix upon casting into membranes. This was perpendicular to the gas flow direction, readily exposing the pores for the desired gas transport. This led to higher CO_2/CH_4 selectivity

compared to the neat polymer, with difference increasing further upon increasing pressure- the opposite effect to that normally observed for MMMs. This was ascribed to the polymer swelling under increased pressure, reducing the undesirable interlayer channel transport and so increasing the effect of the size-discriminative pathway.

5.1.1. H_2/CO_2 Separations

Separating H_2 from CO_2 relies on the size exclusion of CO_2 (kinetic diameter, KD = 0.33 nm) from H_2 (KD = 0.29 nm) as well as the difference in polarity between the molecules. ZIF-based MONs with relatively small pore apertures are well suited to this separation. Yang's seminal work (**Figure 14**) in 2014 utilized $[Zn_2(bim)_4]_n$ MONs as building blocks for molecular sieving membranes and demonstrated good H_2/CO_2 selectivity of >200 for more than 400 h with a high H_2 permeance up to 3760 gas permeation units (GPU).[13] In practical use, flu gas contains appreciable amounts of H_2O, and so stability under humid conditions at elevated temperature is paramount for uptake of gas separation membranes. These MON films showed good stability over 120 h at 150 °C with a gas feed containing ≈4 mol% steam. Further work developed $[Zn_2(bim)_3(H_2O)(OH)]_n$ films with selectivity up to 166 at elevated temperature.[185]

The Zhao group demonstrated the importance of filler morphology on film separation performance and clearly depicted the importance of using lamellar MONs over bulk MOF crystals and nanoparticles, using polybenzimidazole as the macroporous support.[186] Excitingly, Zhao et al. have also demonstrated the first reversed thermo-switchable MON film, composed of 2D MAMS-1 nanosheets on an anodic aluminum oxide support (**Figure 15**).[21] Normally, gas permeance increases with increasing temperature. However, they found that increasing temperature from room to 100 °C resulted in H_2 permeance decreasing from 392 GPU to merely 14 GPU, and this effect was reversible and repeatable. MAMS-1 has a known thermo-response structure which was expected to increase permeance through increasing aperture size at elevated temperature. Instead, the kinetic opening of the aperture was governed by the rotation of a *tert*-butyl group. At increasing temperature, the free rotation is restricted due to increased steric hindrance resulting from the thermo-responsive structural change, which results in blocking of the pore aperture, and decreased H_2 permeance. This effect could find application in temperature-related gas separations.

5.1.2. CO_2/CH_4 Separations

Separation of CO_2 (KD = 0.33 nm) from CH_4 relies on the size exclusion of larger CH_4 molecules (KD = 0.38 nm). This has been achieved using MMMs of MON and polymers such as, PI, PIM-1, and Pebax. Gascon et al. first incorporated MONs into a MMM for CO_2/CH_4 separation (Figure 13).[6] An 8.2 wt% loading of CuBDC into a polyimide MMM resulted in up to an 80% increase in CO_2 selectivity compared to the control polyimide membrane, and up to an eightfold increase compared

**ADVANCED
SCIENCE NEWS**

www.advancedsciencenews.com

**ADVANCED
FUNCTIONAL
MATERIALS**

www.afm-journal.de
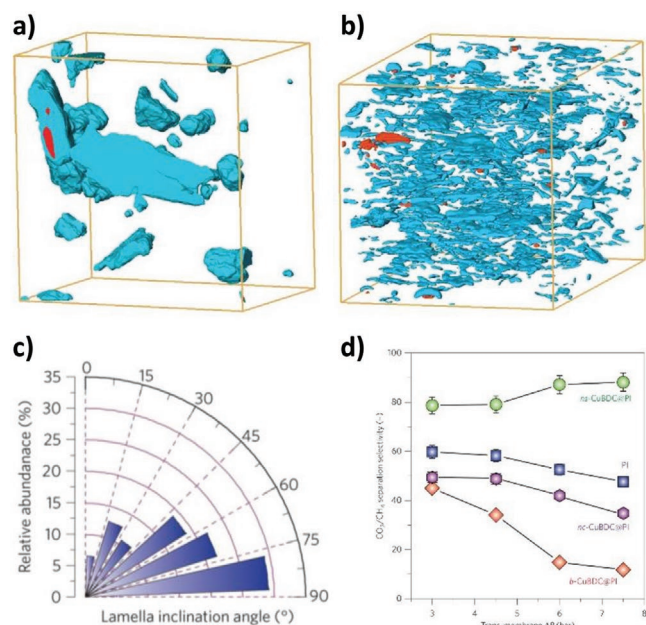
Figure 14. Surface-rendered views of segmented FIB-SEM for composite membranes containing a) bulk-type and b) nanosheet CuBDC embedded in PI. MOF particles are shown in blue, while voids are shown in red. Dimensions of box (x:y:z): 11.2:11.2:7.6 a) and 4.9:4.9:6.6 μm b), respectively. c) Angular histogram showing the orientation of MON lamellae with respect to the gas flux direction (y axis) for CuBDC:PI MMM. d) Separation selectivity as a function of the pressure difference over the CuBDC:PI MMM. Data corresponds to steady operation, after >8 h operation, of an equimolar feed of CO_2/CH_4 feed at 298 K. Reproduced with permission.[6] Copyright 2014, Springer Nature.

to bulk MOF MMM. Remarkably, selectivity increased upon increasing upstream pressure. This is contrary to classical polymeric or MOF-MMM membrane operation, due to the polymeric swelling and decreased interlayer transport pathway, discussed in Section 5.1.1.

Zhao and co-workers also used CuBDC but in PIM-1 MMM.[187] They optimized membrane thickness and filler content to achieve a selectivity of 15.6 and CO_2 permeance of 407 GPU, using 10 wt% nanosheet loading and spin coating an ultrathin 660 nm thick MMM (N.B. conventional solution casting typically produces membranes ≈50 μm thick). Increasing membrane thickness increased selectivity, while permeance decreased, consistent with PIM-1 membranes. Introduction of CuBDC nanosheets decreased permeance, and low loadings increased selectivity. MON wt% > 10 resulted in selectivity drop off. The same group also incorporated NUS-8 nanosheets to form a PIM1 MMM.[188] In this case, a 2 wt% loading of MONs was the maximum achievable before noticeable agglomeration within the MMM and subsequent negative property introduction. The authors demonstrated that there was good interaction between the large surface area of NUS-8 MONs and PIM-1, through π-π interactions and H-bonding. This led to an increase in polymer chain packing (i.e., increase in crystallinity) in the MMM, beneficial to gas separation through increasing the discriminative diffusion pathway through the MONs.

Tsapatsis et al. incorporated 12 wt% CuBDC MONs into a polyimide MMM which resulted in a 70% increase in selectivity compared to the pure PI membrane.[189] Interestingly, they applied a mathematical model for flake composites based on their own and Gascon's previous data,[6] to predict the performance of other literature MMMs. Model predictions for other fillers were an
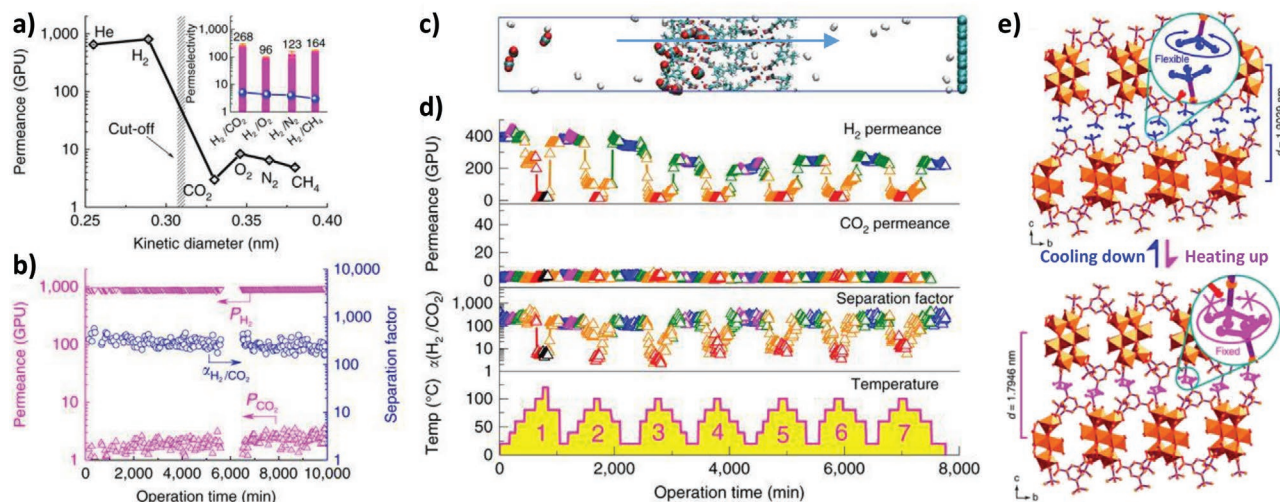
Figure 15. a) Single gas permeation of the membrane (blue line in insert figure indicates the Knudsen diffusion selectivity of H_2 over other gases). b) A 10 000 min continuous test of the membrane for the separation of equimolar H_2/CO_2 mixture at room temperature. c) A snapshot of molecular dynamics simulation for the separation of equimolar H_2/CO_2 mixture through a bilayered MAMS-1 membrane (after 80 ns of simulation). d) Gas permeance and H_2/CO_2 separation factors of the 40-nm membrane under seven heating/cooling cycles. Different colors represent various temperatures: Blue, 20 °C; magenta, 40 °C; olive, 60 °C; orange, 80 °C; red, 100 °C; and black, 120 °C. e) Illustration of shrinkage and expansion upon heating and cooling, respectively, on interlayer distance of MAMS-1, with freely rotating and "frozen" *tert*-butyl groups highlighted in blue and magenta, respectively. Adapted with permission.[21] Copyright 2017, Springer Nature.

**ADVANCED
SCIENCE NEWS**
www.advancedsciencenews.com

**ADVANCED
FUNCTIONAL
MATERIALS**
www.afm-journal.de

order of magnitude lower than the observed CO_2 permeability, which the authors ascribe to non-selective interlayer channel transport not considered in the model. Nonetheless, modelling of gas transport pathways is an interesting development in which there is scope for improvement as the blending of MONs and polymers become increasingly understood.

Gascon et al. more recently demonstrated a synthetic route to MONs of non-layered frameworks, using CTAB polymer surfactant to adsorb selectively to a crystal face within the MOF synthesis, resulting in free-standing lamellae of non-layered Al-based MONs, which have 1D channels.[157] Incorporating 8 wt% of these MONs into a polyimide MMM resulted in maintenance of the CO_2 selectivity, while nearly doubling the permeance.

5.1.3. CO_2/N_2 Separations

Separation of CO_2 (KD = 0.33 nm) from N_2 relies on the size exclusion of the larger N_2 (KD = 0.36 nm). Qiao et al. used relatively large pore ZnTCPP (pore size ≈1.27 nm) film as an intermediary highly permeable gutter layer in a composite membrane.[191] This layer can prevent the polymer solution penetrating into the porous support, which is a common problem with low concentrations of polymer used to make ultrathin membranes. The introduction of the MON gutter layer increased permeability to ≈2100 GPU whilst maintaining the selectivity of the membrane around 30, which satisfied the properties desired in for an economically viable post-combustion CO_2 capture membrane.

Kapteijn and co-workers incorporated CuBDC MONs as a gutter layer within a composite membrane and found that this was more beneficial to membrane performance than a classical poly(dimethylsiloxane) gutter layer.[192] The main role of the MONs was to cover the defects in the thin films. They also manufactured MMMs containing CuBDC MONs. Supporting these on polyacrylonitrile porous supports further increased the CO_2 selectivity (77 v 60 for free standing MMMs).

Water stability is an important factor to consider when using MONs within membranes for gas separation. Sun and co-workers incorporated ZIF-67, [Co(methylimidazole)]$_n$, pore size ≈0.34 nm) MONs in Pebax (polyether block amide MH 1657) MMMs.[14] ZIF-67 is a non-layered structure, but their synthetic method promoted growth in the [211] direction. The hydrothermal stability of ZIF-67 was improved through the morphology regulation, due to fewer exposed Co—N bonds per unit area on the exposed crystal faces. MON/Pebax MMM showed improved permeability (139.4 barrer, 50.7% increase) and ideal selectivity (73.2, 76% increase) with a 5 wt% loading compared to pure Pebax membranes.

5.2. Water Purification

5.2.1. Organics

The impending worldwide clean water crisis means that developing new water purification techniques is becoming increasingly pressing.[197] Ang and Hong published the first example of nanofiltration from aqueous solution in 2017.[28] They cross linked the terminal carboxylate groups of mixed metal TCPP-based

MONs with polycationic polymer to form the selective layer within a nanofiltration membrane. Water flux was 4243 L m^{-2} h^{-1} bar^{-1} at a low pressure of 0.01 bar, with good rejection rates (90%) for dyes (size ≈ 0.8 × 1.1 nm) and salt (20–40%). The separation performance at low pressure was a record at the time, and surpassed equivalent graphene or graphene-oxide based membranes. A GO membrane minimum operational pressure was 0.56 bar. The reduced pressure required for MON based membranes was explained by the transport pathway through the pores of the framework, which graphene-based nanosheets do not possess. Similarly, the water flux was double that of the control polymer-based membrane. Peng et al. have also crosslinked their $[Zn_2(bim)_3(OH)(H_2O)]_n$ MONs, with poly(amidoamine) dendrimers, to enhance the interlayer interactions and stabilize the nanosheet stacking in water (**Figure 16**b).[194] Crosslinking
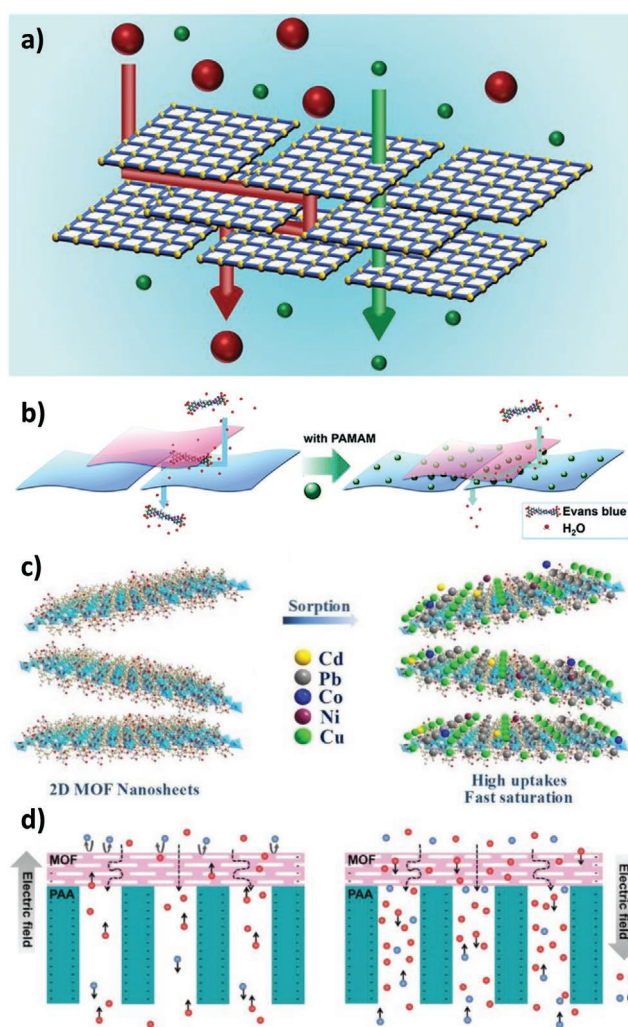
Figure 16. Schematics of methods of water purification: a) General scheme of mass transport pathway through a MON film membrane. Reproduced with permission.[41] Copyright 2019, Wiley. b) The improved selectivity when cross-linking nanosheets. Reproduced with permission.[194] Copyright 2019, Royal Society of Chemistry. c) Heavy metal ion adsorption to MON. Reproduced with permission.[195] Copyright 2020, Elsevier. d) Illustration of the "off" (left) state in the ion current rectification, which results from ion concentration depletion in the nanochannels, and "on" (right) state. Reproduced with permission.[196] Copyright 2019, Wiley.

endowed the membrane with antiswelling character when exposed to water, and resulted in markedly improved dye (Evans blue, 1.2×3.1 nm^2) rejection rate (99.4%) compared to a pristine non-crosslinked MON membrane.

Gao et al. used layered lanthanide-based [Eu(BTB)(H$_2$O)$_2$.solvent]$_n$ nanosheets (5 wt%) with 1D channel pores in a sodium alginate membrane for the dehydration of ethanol.[198] Both ethanol and water fit through the 1D channel (0.5–0.8 nm diameter), but the hydrophobic internal environment means there is a large energy barrier to ethanol transport. Water molecules are significantly smaller and so can pass through the channels much more easily, resulting in a large water flux (1996 g m^{-2} h^{-1}) and high selectivity for H$_2$O (1160) from a 10 wt% water in ethanol solution.

5.2.2. Oil/Water Separations

Deng et al. prepared hydrophobic MONs and demonstrated their use in separating oil from water.[199] A post-synthetic modification technique was used to exchange pillaring bipyridine in the 3D-connected MOF with monotopic substituted pyridine derivatives, which resulted in exfoliation to form MONs. The subsequent presentation of the hydrophobic groups of the substituted pyridine derivatives on the exposed surfaces of the MONs enabled the efficient separation of oils (cyclohexane or dichloroethane) from water using a column packed with MONs. When the original 3D-connected MOF was used, both oils and water readily passed through.

5.2.3. Desalination and Ion Separation

The reduced dimensions of MON based membranes holds particular promise in increasing the permeability of membranes in desalination applications. Wang and co-workers used CuBDC MONs (pore aperture 0.52 nm) to improve polyamide membrane performance in forward osmosis, increasing water permeability by 61% compared to the pristine membrane, while decreasing salt permeability by 24% (hydrated ion diameter = 0.42 and 0.66 nm for Na$^+$ and Cl$^-$, respectively). The inclusion of CuBDC nanosheets also contributed to increased antifouling behaviour using municipal wastewater. This was attributed to multiple effects including the increased hydrophilicity of the membrane surface, which facilitates the formation of a thin water film at the water-membrane interface and serves as a barrier against foulant adhesion. However, increased dead bacteria cells were observed for the CuBDC membrane, suggesting biocidal properties that may result from Cu^{2+} leaching from the membrane.[200]

Farimani et al. used molecular dynamic simulation to suggest that hexaaminobenzene-based MONs[18] of over two layers thick may successfully reject almost 100% of Na$^+$ and Cl$^-$ ions.[201] Peak water permeation of two-layer MONs was an order of magnitude larger than that of graphene or MoS$_2$, and was between 3 and 6 orders of magnitude larger permeation than commercially used membranes. This assumes a "perfect" crystalline membrane, which is not achievable in practise, nonetheless this work suggests that MON may have a good future within desalination membranes.

Recently, Wang et al. demonstrated that a layer of CuTCPP(Fe) grown over porous anodic aluminum could be used a nanochannel mimic for biological ion channel (K$^+$ and Cl$^-$).[196] A power density of 1.6 W m^2 was achieved by integrating this into a salinity-gradient-driven energy conversion device. Further improvements to such nanofluidic devices could be made through strategies such as surface modification and tuning MON film thickness.

5.2.4. Heavy Metal Adsorption

An alternative method of water remediation is chemical adsorption, typically using porous adsorbents. This is advantageous due to simplicity and cost efficiency.[202] New porous materials such as MOFs, COFs and porous organic polymers are emerging as a burgeoning class of adsorbents; however, buried chelating sites still limit full accessibility. Wang et al. used MONs containing thiocyanate groups for mercury chloride capture from aqueous solution.[203] The maximum uptake was 1698 mg g^{-1}, and the adsorption had very fast kinetics (reducing mercury concentration from 10 ppm to 1 ppb within 15 min), attributed to the total exposure of chelating sites on the surfaces of the MONs. Moreover, building blocks of 2D Hg-MON produced a new 3D framework with permanent porosity through stacking of layers with adsorbed Hg. Duan et al. showed that exposed C−N(H) and O−H groups could complex U^{6+} in a exothermic and spontaneous nature, in solution.[204] Similarly, Xu et al. used MONs with exposed imino and hydroxyl groups to selectively adsorb Pb^{2+} and Cu^{2+} ions, respectively, from a solution containing other heavy metals (Figure 16c).[195] Facile access to adsorbing sites on the MON surface resulted in fast adsorption kinetics, with saturation occurring within 90 and 30 min for Pb^{2+} and Cu^{2+} and maximum loadings of 253.8 and 335.6 mg g^{-1}, respectively. Metal sites are coordinatively saturated within this framework structure, therefore outer-sphere surface complexes dominated the metal adsorption mechanism.

5.2.5. Nanoparticle Sieving

The regular nanochannels presented by MONs could render them useful in nanoparticle sieving applications, where there is specific size requirements for the particles utilized. Ruoff and co-workers utilized [Cu$_3$(tri(β-diketone)$_2$)]$_n$ MONs with pore size = 0.45 nm (by N$_2$ adsorption) to form a 50 μm thick film supported on an Anodisc membrane support (pore size = 0.02 μm).[205] They demonstrated that this could effectively sieve Au NPs with diameter > 2.4 nm from a mixture with (average ± standard deviation) diameters 1.4 ± 0.8 nm. The transport pathway of the NPs in this study is unclear, however the effective use of MON frameworks with different effective pore sizes could allow this approach to be tailored towards the selection of different size distributions of NPs.

5.3. Perspective

Many of the earliest and highest profile applications of MONs are in the area of separation, likely because the use of MOFs

ADVANCED
SCIENCE NEWS
www.advancedsciencenews.com

ADVANCED
FUNCTIONAL
MATERIALS
www.afm-journal.de

for gas storage and separation is so well established. MONs have already demonstrated clear advantages over their bulk counter parts, with several examples showing how the nanoscopic dimensions of MONs can reduce membrane thickness leading to increased permeability and selectivity. MONs have been used to separate species across a range of length scales from hydrogen molecules to nanoparticles. This is in part because MONs have well defined, crystalline structures, which allows their pore size and chemistry to be precisely tuned. Judicial combination of ligand and SBU allow control over aperture sizes, for example, ≈0.21 nm for benzimidazole based $[Zn_2(bim)_4]_n$,[13] and ≈2.3 nm for quaterphenyldicarboxylate based MONs.[117] MOFs with apertures up to ≈10 nm have previously been synthesized indicating the potential to extend this range even further. The tunable chemistry of the MONs pores is equally important in determining selectivity as shown, for example, by the ability of hydrophobic pores to pass larger oil molecules but not water. It is likely that many of the systems and techniques that have been developed for gas storage and separation in MOFs will apply equally in enhancing the selectivity of MON based membranes. Similarly, there are a number of industrially relevant gas-pair separations that have received attention using MOFs, such as H_2/C_3H_8, C_2H_4/C_2H_6, and $C_3H_6/C_3H_8$217 and therefore there is significant scope for developing MONs towards these applications.[206] However, there are also likely to be significant differences in the mechanisms by which molecules diffuse through MON based membranes due to the ultrashort through pore distances and detailed experimental and theoretical studies to understand this would be of great interest.

Like other 2D materials, the anisotropic structure of MONs means they create a tortuous path forcing molecules to interact with functional groups on their surfaces. The size of the nanosheets used in the studies varies considerably from a few hundred nanometers to microns wide and from a single layer to more than 50 layers thick. At this stage, it is not clear what the optimal size of nanosheet is and studies comparing the same nanosheets with different aspect ratios would be highly beneficial. All of the MONs investigated to date have a relatively simple structure and there is plenty of scope for designing ligands, metal-clusters, and post-synthetic functionalization to create more targeted interactions with specific analytes. Compared to bulk fillers, 2D materials have very large external surfaces that exacerbate the importance of interactions between the MONs and other components present. Optimizing MON-polymer interaction is therefore equally important and indeed the effect of the MONs are sometimes amplified through ordering the surrounding polymer, leading to increased selectivity. The antifouling properties of MONs due to the release of metal ions is another potential benefit of using MONs in water-separation applications, although it also raises questions regarding their long-term stability and potential for use in, for example, generating potable water where the potential release of metal-ions and ligands raises potential health or environmental concerns. Overall, although further optimization and understanding is required before uptake for large-scale separations, MONs have great promise for utilization across separation applications.

6. Overall Perspective and Outlook

The growing body of research on MONs has already demonstrated how the distinct combination of properties they offer allow them to be exploited in a diverse range of applications. The high external surface area and periodic structure of MONs creates a high density of accessible active sites. This has been exploited extensively in catalysis with MONs showing increased rates of reaction compared to their bulk counterparts, as well as, to a lesser degree in sensing to enhance sensitivity and response times. The anisotropic structure of MONs helps orientate MONs within membranes and combined with their high surface area create "tortuous paths" for separation applications. Their ultrathin dimensions and intrinsic porosity also open a second route by which some molecules, but not others, can pass through MONs. This combination of high external surface area and intrinsic porosity is also central to their success in many electronics applications where close contact with electrolytes and ion mobility are key.

It is the diverse chemistry and programmable structures of MONs that most distinguishes them from other 2D materials and has enabled their use in such a range of applications. Metal ions and clusters have been used as Lewis acidic sites in catalytic, sensing and separation applications. Metals can also provide MONs with advantageous optical and electronic properties such as long-lived fluorescence, metal-to-ligand charge transfer, semi-conducting behaviour, magnetism, and redox activity, which have been extensively exploited. The molecular nature of MONs allows for fine-tuning of their structure and properties and for new functionalities to be added without disrupting their 2D connectivity.

Of the >88 000 crystal structures contained in the MOF subset of the Cambridge Structural Database (MOF-CSD), one third are estimated to be layered providing a wealth of materials that could be exfoliated to form MONs.[207] However, despite the almost infinite number of potential MONs that could be made, most application papers draw on a handful of previously reported structures. This is presumably testament to the challenges in optimizing new MON systems with those working on applications preferring (not unreasonably) to make use of established systems. It is interesting to note that many of the structures that appear repeatedly in this review have close analogues to the 3D architectures that dominate much of the MOF literature, particularly HKUST-1, UIO-66, and ZIF-8. Clearly these robust, accessible, neutral architectures work well but at this early stage it is far from clear that the rules that govern the design of 3D MOFs will be optimal for 2D materials. There is therefore considerable work still to be done in understanding the fundamental design principles behind MONs in order to create new architectures with potentially improved dimensions and properties. In particular, MONs with conducting, semi-conducting and redox active SBU's would be valuable for use in variety of catalytic, sensing and electronics applications.

In addition to the properties of the ligands and metal ions that make up the structural backbone of the MONs, active components have been added to the surface of MONs through post-synthetic modification. This approach overcomes many of

the challenges of developing new systems and allows for the introduction of active components not compatible with the synthetic conditions or that would disrupt nanosheet formation. In contrast to most other 2D materials, the periodic structure of MONs means that groups are introduced in well-defined positions with respect to each other. The potential of this approach is perhaps best demonstrated in some of the sophisticated photocatalytic systems developed by Lin, Wang and co-workers where Zr/Hf MONs are used as scaffolds to co-ordinate multiple different light absorbing and catalytic groups with respect to each other.

Another trend that repeats across this review is the use of MONs as just one component within often complex mixtures that form a functional system. Examples range from the use of MONs as fluorescence quenchers in enzyme-based glucose sensors, as a scaffold to separate faradaic nanoparticles within supercapacitors, and as additives with solar cells or mixed matrix membranes. Here the other components can make up for potential deficiencies in the MONs properties such as a lack of selectivity, conductivity or structural stability. The high surface area of MONs enables them to interact strongly with other components within the mixtures and even small quantities can have a templating effect on surrounding components amplifying their properties. The monolayer dimensions of ultrathin MONs allow for efficient transfer of excited states and charges to-and-from other components within blends.

The scalable synthesis of ultrathin MONs with high aspect ratios in good yields is an outstanding problem in the field. Other reviews provide a good discussion of the range of methods that have so far been used to synthesis MONs and the relative advantages and disadvantages of each approach. It is worth highlighting here that the optimal method will vary for each application depending on the desired characteristics of the MONs. For example, surfactant-assisted synthesis routes can offer improved aspect ratios and yields, but the surfactants can be difficult to remove and potentially block active sites on the surfaces of MONs inhibiting their use in catalysis or sensing applications. Monolayer thickness and well-defined lateral dimensions may be essential for some applications, but in others it might be more economic to accept a broader particle size distribution in order to achieve a higher yield of material. Fabricating nanosheets with large lateral dimensions is typically more challenging and having micron-sized nanosheets may be beneficial in, for example, forming free standing membranes. However, large lateral dimensions may be undesirable in other applications such as thin films, composite blends or where stable suspensions need to be formed. Systematic studies are required to understand the effect of different particle size distribution on performance and compare the same MONs prepared using different methods to identify the best approach for each application.

In comparison to many inorganic 2D materials formed using covalent or ionic bonds, the molecular nature and relatively labile co-ordination bonds of MONs mean they typically have lower thermal stabilities and are less resistant to attack by reactive chemical species. The potential for decomposition or structural rearrangements highlights the importance of fully characterizing systems before and after function. However, the articles in this review indicate that despite their apparent fragility,

MONs can be designed which are remarkably robust and survive in a wide range of solvents, biological fluids, when irradiated with light, strong electric fields and high ionic concentrations. Showing the stability and recyclability of MONs persists during long-term testing under real world conditions is a key them finding use in real-world applications.

The intense academic and industrial interest in both 2D and MOF materials over the last two decades highlights the potential for MONs as a class of materials which combines the properties of both. This review highlights the inroads that have already been made over just the last five years in exploring the potential of MONs for use within catalysis, sensing, electronics and separation applications. We anticipate that next five years will continue to see an exponential growth in research on MONs as new materials and methods are developed, existing systems are further functionalised and optimized, the role of MONs within existing applications is better understood and new opportunities investigated.

Conflict of Interest

The authors declare no conflict of interest.

Author Contributions

R.R.R.P., K.S. and D.J.A. were lead authors of sections 2, 4 and 5 respectively. JN was the lead author of section 3 and edited the whole manuscript together. J.A.F. contributed to all sections and editing of the manuscript.

[1] M. Zhao, Y. Huang, Y. Peng, Z. Huang, Q. Ma, H. Zhang, *Chem. Soc. Rev.* **2018**, *47*, 6267.

[2] D. J. Ashworth, J. A. Foster, *J. Mater. Chem. A* **2018**, *6*, 16292.

[3] S. R. Batten, N. R. Champness, X. M. Chen, J. Garcia-Martinez, S. Kitagawa, L. Öhrström, M. O'Keeffe, M. P. Suh, J. Reedijk, *CrystEngComm* **2012**, *14*, 3001.

[4] M. J. Kalmutzki, N. Hanikel, O. M. Yaghi, *Sci. Adv.* **2018**, *4*, eaat9180.

[5] Z. Q. Li, L. G. Qiu, W. Wang, T. Xu, Y. Wu, X. Jiang, *Inorg. Chem. Commun.* **2008**, *11*, 1375.

[6] T. Rodenas, I. Luz, G. Prieto, B. Seoane, H. Miro, A. Corma, F. Kapteijn, F. X. L. I. Xamena, J. Gascon, *Nat. Mater.* **2015**, *14*, 48.

**ADVANCED
SCIENCE NEWS**

www.advancedsciencenews.com

**ADVANCED
FUNCTIONAL
MATERIALS**

www.afm-journal.de

[7] J. A. Foster, S. Henke, A. Schneemann, R. A. Fischer, A. K. Cheetham, *Chem. Commun.* **2016**, *52*, 10474.

[8] Z. Hu, E. M. Mahdi, Y. Peng, Y. Qian, B. Zhang, N. Yan, D. Yuan, J. C. Tan, D. Zhao, *J. Mater. Chem. A* **2017**, *5*, 8954.

[9] L. Cao, Z. Lin, W. Shi, Z. Wang, C. Zhang, X. Hu, C. Wang, W. Lin, *J. Am. Chem. Soc.* **2017**, *139*, 7020.

[10] Z. Lin, N. C. Thacker, T. Sawano, T. Drake, P. Ji, G. Lan, L. Cao, S. Liu, C. Wang, W. Lin, *Chem. Sci.* **2017**, *9*, 143.

[11] M. J. Cliffe, E. Castillo-Martínez, Y. Wu, J. Lee, A. C. Forse, F. C. N. Firth, P. Z. Moghadam, D. Fairen-Jimenez, M. W. Gaultois, J. A. Hill, O. V. Magdysyuk, B. Slater, A. L. Goodwin, C. P. Grey, *J. Am. Chem. Soc.* **2017**, *139*, 5397.

[12] S. C. Junggeburth, L. Diehl, S. Werner, V. Duppel, W. Sigle, B. V. Lotsch, *J. Am. Chem. Soc.* **2013**, *135*, 6157.

[13] Y. Peng, Y. Li, Y. Ban, H. Jin, W. Jiao, X. Liu, W. Yang, Y. Peng, Y. Li, Y. Ban, H. Jin, W. Jiao, X. Liu, W. Yang, Y. Peng, Y. Li, B. Yujie, H. Jin, W. Jiao, X. Liu, W. Yang, *Science* **2014**, *346*, 1356.

[14] S. Feng, M. Bu, J. Pang, W. Fan, L. Fan, H. Zhao, G. Yang, H. Guo, G. Kong, H. Sun, Z. Kang, D. Sun, *J. Membr. Sci.* **2020**, *593*, 117404.

[15] T. Kambe, R. Sakamoto, K. Hoshiko, K. Takada, M. Miyachi, J. H. Ryu, S. Sasaki, J. Kim, K. Nakazato, M. Takata, H. Nishihara, *J. Am. Chem. Soc.* **2013**, *135*, 2462.

[16] D. Sheberla, L. Sun, M. A. Blood-Forsythe, S. Er, C. R. Wade, C. K. Brozek, A. Aspuru-Guzik, M. Dincă, *J. Am. Chem. Soc.* **2014**, *136*, 8859.

[17] A. J. Clough, J. W. Yoo, M. H. Mecklenburg, S. C. Marinescu, *J. Am. Chem. Soc.* **2015**, *137*, 118.

[18] N. Lahiri, N. Lotfizadeh, R. Tsuchikawa, V. V. Deshpande, J. Louie, *J. Am. Chem. Soc.* **2017**, *139*, 19.

[19] P.-Z. Li, Y. Maeda, Q. Xu, *Chem. Commun.* **2011**, *47*, 8436.

[20] Q. Qiu, H. Chen, Z. You, Y. Feng, X. Wang, Y. Wang, Y. Ying, *ACS Appl. Mater. Interfaces* **2020**, *12*, 5429.

[21] X. Wang, C. Chi, K. Zhang, Y. Qian, K. M. Gupta, Z. Kang, J. Jiang, D. Zhao, *Nat. Commun.* **2017**, *8*, 14460.

[22] A. Abhervé, S. Mañas-Valero, M. Clemente-León, E. Coronado, *Chem. Sci.* **2015**, *6*, 4665.

[23] J. López-Cabrelles, S. Mañas-Valero, I. J. Vitórica-Yrezábal, P. J. Bereciartua, J. A. Rodríguez-Velamazán, J. C. Waerenborgh, B. J. C. Vieira, D. Davidovikj, P. G. Steeneken, H. S. J. van der Zant, G. M. Espallargas, E. Coronado, *Nat. Chem.* **2018**, *10*, 1001.

[24] J. Xie, Y. Wang, D. Zhang, C. Liang, W. Liu, Y. Chong, X. Yin, Y. Zhang, D. Gui, L. Chen, W. Tong, Z. Liu, J. Diwu, Z. Chai, S. Wang, *Chem. Commun.* **2019**, *55*, 11715.

[25] J. Huang, Y. Li, R. K. Huang, C. T. He, L. Gong, Q. Hu, L. Wang, Y. T. Xu, X. Y. Tian, S. Y. Liu, Z. M. Ye, F. Wang, D. D. Zhou, W. X. Zhang, J. P. Zhang, *Angew. Chem., Int. Ed.* **2018**, *57*, 4632.

[26] Y. Ding, Y. P. Chen, X. Zhang, L. Chen, Z. Dong, H. L. Jiang, H. Xu, H. C. Zhou, *J. Am. Chem. Soc.* **2017**, *139*, 9136.

[27] L. Cao, Z. Lin, F. Peng, W. Wang, R. Huang, C. Wang, J. Yan, J. Liang, Z. Zhang, T. Zhang, L. Long, J. Sun, W. Lin, *Angew. Chem., Int. Ed.* **2016**, *55*, 4962.

[28] H. Ang, L. Hong, *ACS Appl. Mater. Interfaces* **2017**, *9*, 28079.

[29] G. Xu, K. Otsubo, T. Yamada, S. Sakaida, H. Kitagawa, *J. Am. Chem. Soc.* **2013**, *135*, 7438.

[30] R. Sakamoto, K. Hoshiko, Q. Liu, T. Yagi, T. Nagayama, S. Kusaka, M. Tsuchiya, Y. Kitagawa, W. Y. Wong, H. Nishihara, *Nat. Commun.* **2015**, *6*, 6713.

[31] B. Wang, J. Shang, C. Guo, J. Zhang, F. Zhu, A. Han, J. Liu, *Small* **2019**, *15*, e1804761.

[32] L. Zhuang, L. Ge, H. Liu, Z. Jiang, Y. Jia, Z. Li, D. Yang, R. K. Hocking, M. Li, L. Zhang, X. Wang, X. Yao, Z. Zhu, *Angew. Chem.* **2019**, *131*, 13699.

[33] R. Sakamoto, K. Takada, T. Pal, H. Maeda, T. Kambe, H. Nishihara, *Chem. Commun.* **2017**, *53*, 5781.

[34] J. Duan, Y. Li, Y. Pan, N. Behera, W. Jin, *Coord. Chem. Rev.* **2019**, *395*, 25.

[35] C. Tan, X. Cao, X. J. Wu, Q. He, J. Yang, X. Zhang, J. Chen, W. Zhao, S. Han, G. H. Nam, M. Sindoro, H. Zhang, *Chem. Rev.* **2017**, *117*, 6225.

[36] T. Hyun, J. Jeong, A. Chae, Y. K. Kim, D.-Y. Koh, *BMC Chem. Eng.* **2019**, *1*, 12.

[37] M. A. Solomos, F. J. Claire, T. J. Kempa, *J. Mater. Chem. A* **2019**, *7*, 23537.

[38] S. Kim, H. Wang, Y. M. Lee, *Angew. Chem., Int. Ed.* **2019**, *58*, 2.

[39] G. Chakraborty, I.-H. Park, R. Medishetty, J. J. Vittal, *Chem. Rev.* **2021**, *121*, 3751.

[40] W. Zhao, J. Peng, W. Wang, S. Liu, Q. Zhao, W. Huang, *Coord. Chem. Rev.* **2018**, *377*, 44.

[41] Y. Peng, W. Yang, *Adv. Mater. Interfaces* **2019**, *7*, 1901514.

[42] A. Dhakshinamoorthy, A. M. Asiri, H. Garcia, *Adv. Mater.* **2019**, *31*, 1900617.

[43] M. Xu, S. S. Yang, Z.-Y. Gu, *Chem. – Eur. J.* **2018**, *24*, 15131.

[44] D. Zhu, M. Qiao, J. Liu, T. Tao, C. Guo, *J. Mater. Chem. A* **2020**, *8*, 8143.

[45] Y. N. Li, S. Wang, Y. Zhou, X. J. Bai, G. S. Song, X. Y. Zhao, T. Q. Wang, X. Qi, X. M. Zhang, Y. Fu, *Langmuir* **2017**, *33*, 1060.

[46] B. Wang, J. Jin, B. Ding, X. Han, A. Han, J. Liu, *Front. Mater.* **2020**, *7*, 37.

[47] F. Zhang, J. Zhang, B. Zhang, L. Zheng, X. Cheng, Q. Wan, B. Han, J. Zhang, *Nat. Commun.* **2020**, *11*, 1431.

[48] X. Zhang, L. Chang, Z. Yang, Y. Shi, C. Long, J. Han, B. Zhang, X. Qiu, G. Li, Z. Tang, *Nano Res.* **2019**, *12*, 437.

[49] X. Yang, R. Xiong, X. Chang, S. Wang, Z. Ding, Q. Li, *ChemistrySelect* **2019**, *4*, 14300.

[50] Y. Xiao, W. Guo, H. Chen, H. Li, X. Xu, P. Wu, Y. Shen, B. Zheng, F. Huo, W. D. Wei, *Mater. Chem. Front.* **2019**, *3*, 1580.

[51] S. Wang, T. Wang, H. Zheng, F. Fan, Z. Gu, W. He, B. Zhang, L. Shao, H. Chen, Y. Li, X. Zhang, L. Zhang, Y. Fu, W. Qi, *Microporous Mesoporous Mater.* **2020**, *303*, 110254.

[52] J. Wang, J. Zhang, S. B. Peh, L. Zhai, Y. Ying, G. Liu, Y. Cheng, D. Zhao, *ACS Appl. Energy Mater.* **2019**, *2*, 298.

[53] Y. Hu, Y. Zhang, Y. Han, D. Sheng, D. Shan, X. Liu, A. Cheng, *ACS Appl. Nano Mater.* **2019**, *2*, 136.

[54] W. Shi, L. Zeng, L. Cao, Y. Huang, C. Wang, W. Lin, *Nano Res.* **2020**, *14*, 473.

[55] C. Tan, K. Yang, J. Dong, Y. Liu, Y. Liu, J. Jiang, Y. Cui, *J. Am. Chem. Soc.* **2019**, *141*, 17685.

[56] J. Nicks, J. Zhang, J. A. Foster, *Chem. Commun.* **2019**, *55*, 8788.

[57] R. Yan, Y. Zhao, H. Yang, X. J. Kang, C. Wang, L. L. Wen, Z. D. Lu, *Adv. Funct. Mater.* **2018**, *28*, 1802021.

[58] G. Zhan, H. C. Zeng, *Adv. Funct. Mater.* **2016**, *26*, 3268.

[59] J. Liu, H. Yu, L. Wang, *Appl. Catal., A* **2020**, *599*, 117605.

[60] S. Wu, L. Qin, K. Zhang, Z. Xin, S. Zhao, *RSC Adv.* **2019**, *9*, 9386.

[61] T. Guo, C. Wang, N. Zhang, Y. Zhang, T. Chen, X. Xing, Z. Lu, L. Wen, *Cryst. Growth Des.* **2020**, *20*, 6217.

[62] X. Zhang, P. Zhang, C. Chen, J. Zhang, G. Yang, L. Zheng, J. Zhang, B. Han, *Green Chem.* **2019**, *21*, 54.

[63] Z. Deng, H. Yu, L. Wang, J. Liu, K. J. Shea, *J. Mater. Chem. A* **2019**, *7*, 15975.

[64] Y. Zhou, Z. Li, Y. Liu, J. Huo, C. Chen, Q. Li, S. Niu, S. Wang, *ChemSusChem* **2020**, *13*, 1746.

[65] K. Titov, D. B. Eremin, A. S. Kashin, R. Boada, B. E. Souza, C. S. Kelley, M. D. Frogley, G. Cinque, D. Gianolio, G. Cibin, S. Rudić, V. P. Ananikov, J. C. Tan, *ACS Sustainable Chem. Eng.* **2019**, *7*, 5875.

[66] T. He, B. Ni, S. Zhang, Y. Gong, H. Wang, L. Gu, J. Zhuang, W. Hu, X. Wang, *Small* **2018**, *14*, e1703929.

2103723 (27 of 31)

[67] Z. W. Jiang, Y. C. Zou, T. T. Zhao, S. J. Zhen, Y. F. Li, C. Z. Huang, *Angew. Chem., Int. Ed.* **2020**, *621900*, 3300.

[68] Y. Wang, L. Feng, J. Pang, J. Li, N. Huang, G. S. Day, L. Cheng, H. F. Drake, Y. Wang, C. Lollar, J. Qin, Z. Gu, T. Lu, S. Yuan, H. C. Zhou, *Adv. Sci.* **2019**, *6*, 2.

[69] W. Shi, L. Cao, H. Zhang, X. Zhou, B. An, Z. Lin, R. Dai, J. Li, C. Wang, W. Lin, *Angew. Chem., Int. Ed.* **2017**, *56*, 9704.

[70] R. Xu, T. Drake, G. Lan, W. Lin, *Chem. – Eur. J.* **2018**, *24*, 15772.

[71] R. Xu, Z. Cai, G. Lan, W. Lin, *Inorg. Chem.* **2018**, *57*, 10489.

[72] G. Lan, Z. Li, S. S. Veroneau, Y.-Y. Zhu, Z. Xu, C. Wang, W. Lin, *J. Am. Chem. Soc.* **2018**, *140*, 12369.

[73] X. Hu, P. Chen, C. Zhang, Z. Wang, C. Wang, *Chem. Commun.* **2019**, *55*, 9657.

[74] G. Lan, Y. Quan, M. Wang, G. T. Nash, E. You, Y. Song, S. S. Veroneau, X. Jiang, W. Lin, *J. Am. Chem. Soc.* **2019**, *141*, 15767.

[75] Y. Quan, G. Lan, Y. Fan, W. Shi, E. You, W. Lin, Y. Quan, G. Lan, Y. Fan, W. Shi, E. You, W. Lin, *J. Am. Chem. Soc.* **2020**, *142*, 1746.

[76] H. Wang, L. Zhang, Z. Chen, J. Hu, S. Li, Z. Wang, J. Liu, X. Wang, *Chem. Soc. Rev.* **2014**, *43*, 5234.

[77] J. Ran, J. Qu, H. Zhang, T. Wen, H. Wang, S. Chen, L. Song, X. Zhang, L. Jing, R. Zheng, S.-Z. Qiao, *Adv. Energy Mater.* **2019**, *9*, 1803402.

[78] L. Chen, Y. Wang, F. Yu, X. Shen, C. Duan, *J. Mater. Chem. A* **2019**, *7*, 11355.

[79] L. Ye, Y. Gao, S. Cao, H. Chen, Y. Yao, J. Hou, L. Sun, *Appl. Catal., B* **2018**, *227*, 54.

[80] C. Zheng, X. Qiu, J. Han, Y. Wu, S. Liu, *ACS Appl. Mater. Interfaces* **2019**, *11*, 42243.

[81] D. Zhu, J. Liu, L. Wang, Y. Du, Y. Zheng, K. Davey, S. Z. Qiao, *Nanoscale* **2019**, *11*, 3599.

[82] Q. Hu, X. Huang, Z. Wang, G. Li, Z. Han, H. Yang, X. Ren, Q. Zhang, J. Liu, C. He, *J. Mater. Chem. A* **2020**, *8*, 2140.

[83] W. Zhang, Y. Wange, H. Zheng, R. Li, Y. Tang, C. Li, Z. Boyuan, L. You, M.-R. Gao, Z. Liu, S.-H. Yu, K. Zhou, *ACS Nano* **2020**, *14*, 1971.

[84] R. J. Li, Y. F. Qi, Q. Wang, J. J. Wang, Z. Y. Liu, X. G. Wang, X. J. Zhao, E. C. Yang, *J. Inorg. Gen. Chem.* **2020**, *646*, 1412.

[85] W. Cheng, X. F. Lu, D. Luan, X. W. Lou, *Angew. Chem., Int. Ed.* **2020**, *59*, 18234.

[86] C. Pan, Z. Liu, M. Huang, *Appl. Surf. Sci.* **2020**, *529*, 147201.

[87] S. W. Luo, R. Gu, P. Shi, J. Fan, Q. J. Xu, Y. L. Min, *J. Power Sources* **2020**, *448*, 227406.

[88] J. Huang, J.-Q. Wu, B. Shao, B.-L. Lan, F.-J. Yang, Y. Sun, X.-Q. Tan, C.-T. He, Z. Zhang, *ACS Sustainable Chem. Eng.* **2020**, *8*, 10554.

[89] P. Thangasamy, S. Shanmuganathan, V. Subramanian, *Nanoscale Adv.* **2020**, *2*, 2073.

[90] S. Zhao, Y. Wang, J. Dong, C. T. He, H. Yin, P. An, K. Zhao, X. Zhang, C. Gao, L. Zhang, J. Lv, J. Wang, J. Zhang, A. M. Khattak, N. A. Khan, Z. Wei, J. Zhang, S. Liu, H. Zhao, Z. Tang, *Nat. Energy* **2016**, *1*, 16184.

[91] W. Ye, Y. Yang, X. Fang, M. Arif, X. Chen, D. Yan, *ACS Sustainable Chem. Eng.* **2019**, *7*, 18085.

[92] J. Cui, J. Liu, C. Wang, F. Rong, L. He, Y. Song, Z. Zhang, S. Fang, *Electrochim. Acta* **2020**, *334*, 135577.

[93] M. Cai, Q. Liu, X. Zue, Y. Li, Y. Fan, A. Huang, M.-R. Li, M. Croft, T. A. Tyson, Z. Ke, G. Li, *J. Mater. Chem. A* **2020**, *8*, 190.

[94] W. Li, W. Fang, W. Chen, K. N. Dinh, H. Ren, L. Zhao, C. Liu, Q. Yan, *J. Mater. Chem. A* **2020**, *8*, 3658.

[95] L. Zhao, B. Dong, S. Li, L. Zhou, L. Lai, Z. Wang, S. Zhao, M. Han, K. Gao, M. Lu, X. Xie, B. Chen, Z. Liu, X. Wang, H. Zhang, H. Li, J. Liu, H. Zhang, X. Huang, W. Huang, *ACS Nano* **2017**, *11*, 5800.

[96] W. Pang, B. Shao, X.-Q. Tan, C. Tang, Z. Zhang, J. Huang, *Nanoscale* **2020**, *12*, 3623.

[97] R. Dong, M. Pfeffermann, H. Liang, Z. Zheng, X. Zhu, J. Zhang, X. Feng, *Angew. Chem., Int. Ed.* **2015**, *54*, 12058.

[98] R. Dong, Z. Zheng, D. C. Tranca, J. Zhang, N. Chandrasekhar, S. Liu, X. Zhuang, G. Seifert, X. Feng, *Chem. – Eur. J.* **2017**, *23*, 2255.

[99] Y. Song, Y. PI, X. Feng, K. Ni, Z. Xu, J. S. Chen, Z. Li, W. Lin, *J. Am. Chem. Soc.* **2020**, *142*, 6866.

[100] K. Rui, G. Zhao, M. Lao, P. Cui, X. Zheng, X. Zheng, J. Zhu, W. Huang, S. X. Dou, W. Sun, *Nano Lett.* **2019**, *19*, 8447.

[101] J.-X. Wu, S.-Z. Hou, X.-D. Zhang, M. Xu, H.-F. Yang, P.-S. Cao, Z.-Y. Gu, *Chem. Sci.* **2019**, *10*, 2199.

[102] X.-D. Zhang, S.-Z. Hou, J.-X. Wu, Z.-Y. Gu, *Chem. – Eur. J.* **2019**, *26*, 1604.

[103] Y. Guo, W. Shi, H. Yang, Q. He, Z. Zeng, J. Y. Ye, X. He, R. Huang, C. Wang, W. Lin, *J. Am. Chem. Soc.* **2019**, *141*, 17875.

[104] R. Al Natour, Z. K. Ali, A. Assoud, M. Hmadeh, *Inorg. Chem.* **2019**, *58*, 10912.

[105] J. Zha, X. Yin, J. R. Baltzegar, X. Zhang, *Langmuir* **2019**, *35*, 12908.

[106] D. J. Ashworth, A. Cooper, M. Trueman, R. W. M. Al-Saedi, S. D. Liam, A. J. Meijer, J. A. Foster, *Chem. – Eur. J.* **2018**, *24*, 17986.

[107] D. J. Ashworth, J. A. Foster, *Nanoscale* **2020**, *12*, 7986.

[108] C. X. Yu, F. L. Hu, J. G. Song, J. L. Zhang, S. Liu, B. X. Wang, H. Meng, L. L. Liu, L. F. Ma, *Sens. Actuators, B* **2020**, *310*, 127819.

[109] V. K. Maka, A. Mukhopadhyay, G. Savitha, J. N. Moorthy, *Nanoscale* **2018**, *10*, 22389.

[110] Y. H. Luo, C. Chen, C. He, Y. Y. Zhu, D. L. Hong, X. T. He, P. J. An, H. S. Wu, B. W. Sun, *ACS Appl. Mater. Interfaces* **2018**, *10*, 28860.

[111] A. K. Chaudhari, H. J. Kim, I. Han, J. C. Tan, *Adv. Mater.* **2017**, *29*, 1701463.

[112] G. Lan, K. Ni, E. You, M. Wang, A. Culbert, X. Jiang, W. Lin, *J. Am. Chem. Soc.* **2019**, *141*, 18964.

[113] W. Bai, S. Li, J. Ma, W. Cao, J. Zheng, *J. Mater. Chem. A* **2019**, *7*, 9086.

[114] J. Ma, W. Bai, J. Zheng, *Microchim. Acta* **2019**, *186*, 482.

[115] Y. Shu, J. Chen, Z. Xu, D. Jin, Q. Xu, X. Hu, *J. Electroanal. Chem.* **2019**, *845*, 137.

[116] D. Ning, Q. Liu, Q. Wang, X. M. Du, W. J. Ruan, Y. Li, *Sens. Actuators, B* **2019**, *282*, 443.

[117] H. Chen, Q. Qiu, S. Sharif, S. Ying, Y. Wang, Y. Ying, *ACS Appl. Mater. Interfaces* **2018**, *10*, 24108.

[118] J. Chen, Y. Shu, H. Li, Q. Xu, X. Hu, *Talanta* **2018**, *189*, 254.

[119] B. Tan, H. Zhao, W. Wu, X. Liu, Y. Zhang, X. Quan, *Nanoscale* **2017**, *9*, 18699.

[120] S. Hu, J. Yan, X. Huang, L. Guo, Z. Lin, F. Luo, B. Qiu, K. Y. Wong, G. Chen, *Sens. Actuators, B* **2018**, *267*, 312.

[121] M. Y. Shi, M. Xu, Z. Y. Gu, *Anal. Chim. Acta* **2019**, *1079*, 164.

[122] N. Zhu, L. Gu, J. Wang, X. Li, G. Liang, J. Zhou, Z. Zhang, *J. Phys. Chem. C* **2019**, *123*, 9388.

[123] T. M. Chen, X. J. Wu, J. X. Wang, G. W. Yang, *Nanoscale* **2017**, *9*, 11806.

[124] C. Wang, S. Huang, L. Luo, Y. Zhou, X. Lu, G. Zhang, H. Ye, J. Gu, F. Cao, *J. Electroanal. Chem.* **2019**, *835*, 178.

[125] S. S. Pan, W. Lu, Y. H. Zhao, W. Tong, M. Li, L. M. Jin, J. Y. Choi, F. Qi, S. G. Chen, L. F. Fei, S. F. Yu, *ACS Appl. Mater. Interfaces* **2013**, *5*, 12784.

[126] J. W. Zhang, H. T. Zhang, Z. Y. Du, X. Wang, S. H. Yu, H. L. Jiang, *Chem. Commun.* **2014**, *50*, 1092.

[127] L. Zhao, Y. Zhao, R. Li, D. Wu, X. Xie, H. Ye, Y. Zhang, Q. Xin, *Chem. Phys.* **2020**, *534*, 110743.

[128] M. Zhao, Y. Wang, Q. Ma, Y. Huang, X. Zhang, J. Ping, Z. Zhang, Q. Lu, Y. Yu, H. Xu, Y. Zhao, H. Zhang, *Adv. Mater.* **2015**, *27*, 7372.

[129] C. Liu, T. Wang, J. Ji, C. Wang, H. Wang, P. Jin, W. Zhou, J. Jiang, *J. Mater. Chem. C* **2019**, *7*, 10240.

[130] Q. Qiu, H. Chen, S. Ying, S. Sharif, Z. You, Y. Wang, Y. Ying, *Microchim. Acta* **2019**, *186*, 93.

[131] W.-J. J. Song, *Talanta* **2017**, *170*, 74.

**ADVANCED
SCIENCE NEWS**

www.advancedsciencenews.com

**ADVANCED
FUNCTIONAL
MATERIALS**

www.afm-journal.de

[132] B. J. C. Wong, D. M. Xu, S. S. Bao, L. M. Zheng, J. Lei, *ACS Appl. Mater. Interfaces* **2019**, *11*, 12986.

[133] Q. Yang, J. Hong, Y.-X. Wu, Y. Cao, D. Wu, F. Hu, N. Gan, *ACS Appl. Mater. Interfaces* **2019**, *11*, 41506.

[134] H. S. Wang, J. Li, J. Y. Li, K. Wang, Y. Ding, X. H. Xia, *NPG Asia Mater* **2017**, *9*, e354.

[135] S. Wang, M. Wang, C. Li, H. Li, C. Ge, X. Zhang, Y. Jin, *Sens. Actuators, B* **2020**, *311*, 127919.

[136] L. Y. Yao, F. Yang, G. B. Hu, Y. Yang, W. Huang, W. B. Liang, R. Yuan, D. R. Xiao, *Biosens. Bioelectron.* **2020**, *155*, 112099.

[137] Y. Yang, G.-B. Hu, W.-B. Liang, L.-Y. Yao, W. Huang, Y.-J. Zhang, J.-L. Zhang, J.-M. Wang, R. Yuan, D.-R. Xiao, *Nanoscale* **2020**, *12*, 5932.

[138] M. Yan, J. Ye, Q. Zhu, L. Zhu, J. Huang, X. Yang, *Anal. Chem.* **2019**, *91*, 10156.

[139] G. B. Hu, C. Y. Xiong, W. B. Liang, Y. Yang, L. Y. Yao, W. Huang, W. Luo, R. Yuan, D. R. Xiao, *Biosens. Bioelectron.* **2019**, *135*, 95.

[140] L. Dong, L. Yin, G. Tian, Y. Wang, H. Pei, Q. Wu, W. Cheng, S. Ding, Q. Xia, *Sens. Actuators, B* **2020**, *308*, 127687.

[141] H. Xu, J. Gao, X. Qian, J. Wang, H. He, Y. Cui, Y. Yang, Z. Wang, G. Qian, *J. Mater. Chem. A* **2016**, *4*, 10900.

[142] L. J. Han, D. Zheng, S. G. Chen, H. G. Zheng, J. Ma, *Small* **2018**, *14*, 1703873.

[143] D. Liu, B. Liu, C. Wang, W. Jin, Q. Zha, G. Shi, D. Wang, X. Sang, *ACS Sustainable Chem. Eng.* **2020**, *8*, 2167.

[144] X. Qian, S. Deng, X. Chen, Q. Gao, Y. L. Hou, A. Wang, L. Chen, *Chin. Chem. Lett.* **2020**, *31*, 2211.

[145] G. Ding, Y. Wang, G. Zhang, K. Zhou, K. Zeng, Z. Li, Y. Zhou, C. Zhang, X. Chen, S. T. Han, *Adv. Funct. Mater.* **2019**, *29*, 1806637.

[146] M. G. Campbell, D. Sheberla, S. F. Liu, T. M. Swager, M. Dincǎ, *Angew. Chem., Int. Ed.* **2015**, *54*, 4349.

[147] M. D. Allendorf, A. Schwartzberg, V. Stavila, A. A. Talin, *Chem. – Eur. J.* **2011**, *17*, 11372.

[148] I. Stassen, N. Burtch, A. Talin, P. Falcaro, M. Allendorf, R. Ameloot, *Chem. Soc. Rev.* **2017**, *46*, 3185.

[149] M. Yuan, R. Wang, W. Fu, L. Lin, Z. Sun, X. Long, S. Zhang, C. Nan, G. Sun, H. Li, S. Ma, *ACS Appl. Mater. Interfaces* **2019**, *11*, 11403.

[150] J. F. Liao, W. Q. Wu, Y. Jiang, J. X. Zhong, L. Wang, D. B. Kuang, *Chem. Soc. Rev.* **2020**, *49*, 354.

[151] M. G. Campbell, S. F. Liu, T. M. Swager, M. Dincǎ, *J. Am. Chem. Soc.* **2015**, *137*, 13780.

[152] H. Liu, X. Li, L. Chen, X. Wang, H. Pan, X. Zhang, M. Zhao, *J. Phys. Chem. C* **2016**, *120*, 3846.

[153] Y. Shu, Y. Yan, J. Chen, Q. Xu, H. Pang, X. Hu, *ACS Appl. Mater. Interfaces* **2017**, *9*, 22342.

[154] Y. Zhao, L. Jiang, L. Shangguan, L. Mi, A. Liu, S. Liu, *J. Mater. Chem. A* **2018**, *6*, 2828.

[155] F. Su, S. Zhang, H. Ji, H. Zhao, J. Y. Tian, C. Sen Liu, Z. Zhang, S. Fang, X. Zhu, M. Du, *ACS Sens.* **2017**, *2*, 998.

[156] Y. Wang, M. Zhao, J. Ping, B. Chen, X. Cao, Y. Huang, C. Tan, Q. Ma, S. Wu, Y. Yu, Q. Lu, J. Chen, W. Zhao, Y. Ying, H. Zhang, *Adv. Mater.* **2016**, *28*, 4149.

[157] A. Pustovarenko, M. G. Goesten, S. Sachdeva, M. Shan, Z. Amghouz, Y. Belmabkhout, A. Dikhtiarenko, T. Rodenas, D. Keskin, I. K. Voets, B. M. Weckhuysen, M. Eddaoudi, L. C. P. M. de Smet, E. J. R. Sudhölter, F. Kapteijn, B. Seoane, J. Gascon, *Adv. Mater.* **2018**, *30*, 1707234.

[158] Y. Ning, X. Lou, C. Li, X. Hu, B. Hu, *Chem. – Eur. J.* **2017**, *23*, 15984.

[159] C. Li, X. Hu, W. Tong, W. Yan, X. Lou, M. Shen, B. Hu, *ACS Appl. Mater. Interfaces* **2017**, *9*, 29829.

[160] C. Shi, Y. Gao, L. Liu, Y. Song, X. Wang, H. J. Liu, Q. Liu, *J. Nanopart. Res.* **2016**, *18*, 3.

[161] C. Li, Q. Zhang, T. Li, B. He, P. Man, Z. Zhu, Z. Zhou, L. Wei, K. Zhang, G. Hong, Y. Yao, *J. Mater. Chem. A* **2020**, *8*, 3262.

[162] X. Zheng, Y. Cao, D. Liu, M. Cai, J. Ding, X. Liu, J. Wang, W. Hu, C. Zhong, *ACS Appl. Mater. Interfaces* **2019**, *11*, 15662.

[163] J. Yang, Z. Ma, W. Gao, M. Wei, *Chem. – Eur. J.* **2017**, *23*, 631.

[164] J. Wang, Q. Zhong, Y. Zeng, D. Cheng, Y. Xiong, Y. Bu, *J. Colloid Interface Sci.* **2019**, *555*, 42.

[165] H. M. Ma, J. W. Yi, S. Li, C. Jiang, J. H. Wei, Y. P. Wu, J. Zhao, D. S. Li, *Inorg. Chem.* **2019**, *58*, 9543.

[166] Y. Wang, Y. Liu, H. Wang, W. Liu, Y. Li, J. Zhang, H. Hou, J. Yang, *ACS Appl. Energy Mater.* **2019**, *2*, 2063.

[167] L. G. Beka, X. Bu, X. Li, X. Wang, C. Han, W. Liu, *RSC Adv.* **2019**, *9*, 36123.

[168] W. Zhao, W. Wang, J. Peng, T. Chen, B. Jin, S. Liu, W. Huang, Q. Zhao, *Dalton Trans.* **2019**, *48*, 9631.

[169] Y. Liu, Y. Wang, Y. Chen, C. Wang, L. Guo, *Appl. Surf. Sci.* **2020**, *507*, 145089.

[170] J. Xu, Y. Wang, S. Cao, J. Zhang, G. Zhang, H. Xue, Q. Xu, H. Pang, *J. Mater. Chem. A* **2018**, *6*, 17329.

[171] J. Cheng, S. Chen, D. Chen, L. Dong, J. Wang, T. Zhang, T. Jiao, B. Liu, H. Wang, J. J. Kai, D. Zhang, G. Zheng, L. Zhi, F. Kang, W. Zhang, *J. Mater. Chem. A* **2018**, *6*, 20254.

[172] S. Liu, Y.-C. Wang, C.-M. Chang, T. Yasuda, N. Fukui, H. Maeda, P. Long, K. Nakazato, W.-B. Jian, W. Xie, K. Tsukagoshi, H. Nishihara, *Nanoscale* **2020**, *12*, 6983.

[173] X. Hu, Z. Wang, B. Lin, C. Zhang, L. Cao, T. Wang, J. Zhang, C. Wang, W. Lin, *Chem. – Eur. J.* **2017**, *23*, 8390.

[174] W. Xing, P. Ye, J. Lu, X. Wu, Y. Chen, T. Zhu, A. Peng, H. Huang, *J. Power Sources* **2018**, *401*, 13.

[175] G. Li, R. Zhu, Y. Yang, *Nat. Photonics* **2012**, *6*, 153.

[176] P. Cheng, G. Li, X. Zhan, Y. Yang, *Nat. Photonics* **2018**, *12*, 131.

[177] C. Liu, C. Wang, H. Wang, T. Wang, J. Jiang, *Eur. J. Inorg. Chem.* **2019**, *2019*, 4815.

[178] K. Sasitharan, D. G. Bossanyi, N. Vaenas, A. J. Parnell, J. Clark, A. Iraqi, D. G. Lidzey, J. A. Foster, *J. Mater. Chem. A* **2020**, *8*, 6067.

[179] S. Wu, Z. Li, M. Li, Y. Diao, F. Lin, T. Liu, J. Zhang, P. Tieu, W. Gao, F. Qi, X. Pan, Z. Xu, Z. Zhu, A. K. Jen, *Nat. Nanotechnol.* **2020**, *15*, 934.

[180] M. G. Buonomenna, W. Yave, G. Golemme, *RSC Adv.* **2012**, *2*, 10745.

[181] J. Sánchez-Laínez, B. Zornoza, S. Friebe, J. Caro, S. Cao, A. Sabetghadam, B. Seoane, J. Gascon, F. Kapteijn, C. L. Guillouzer, G. Clet, M. Daturi, C. Téllez, J. Coronas, *J. Membr. Sci.* **2016**, *515*, 45.

[182] S. Japip, Y. Xiao, T. S. Chung, *Ind. Eng. Chem. Res.* **2016**, *55*, 9507.

[183] E. V. Perez, K. J. Balkus, J. P. Ferraris, I. H. Musselman, *J. Membr. Sci.* **2009**, *328*, 165.

[184] F. Yang, M. Wu, Y. Wang, S. Ashtiani, H. Jiang, *ACS Appl. Mater. Interfaces* **2019**, *11*, 990.

[185] Y. Peng, Y. Li, Y. Ban, W. Yang, *Angew. Chem., Int. Ed.* **2017**, *56*, 9757.

[186] Z. Kang, Y. Peng, Z. Hu, Y. Qian, C. Chi, L. Y. Yeo, L. Tee, D. Zhao, *J. Mater. Chem. A* **2015**, *3*, 20801.

[187] Y. Cheng, X. Wang, C. Jia, Y. Wang, L. Zhai, Q. Wang, D. Zhao, *J. Membr. Sci.* **2017**, *539*, 213.

[188] Y. Cheng, S. R. Tavares, C. M. Doherty, Y. Ying, E. Sarnello, G. Maurin, M. R. Hill, T. Li, D. Zhao, *ACS Appl. Mater. Interfaces* **2018**, *10*, 43095.

[189] M. Shete, P. Kumar, J. E. Bachman, X. Ma, Z. P. Smith, W. Xu, K. A. Mkhoyan, J. R. Long, M. Tsapatsis, *J. Membr. Sci.* **2018**, *549*, 312.

[190] Y. Yang, K. Goh, R. Wang, T. H. Bae, *Chem. Commun.* **2017**, *53*, 4254.

[191] M. Liu, K. Xie, M. D. Nothling, P. A. Gurr, S. S. L. Tan, Q. Fu, P. A. Webley, G. G. Qiao, *ACS Nano* **2018**, *12*, 11591.

[192] A. Sabetghadam, X. Liu, S. Gottmer, L. Chu, J. Gascon, F. Kapteijn, *J. Membr. Sci.* **2019**, *570–571*, 226.

[193] J. Deng, Z. Dai, J. Hou, L. Deng, *Chem. Mater.* **2020**, *32*, 4174.

[194] Y. Peng, R. Yao, W. Yang, *Chem. Commun.* **2019**, *55*, 3935.

[195] R. Xu, M. Jian, Q. Ji, C. Hu, C. Tang, R. Liu, X. Zhang, J. Qu, *Chem. Eng. J.* **2020**, *382*, 122658.

[196] C. Wang, F. Liu, Z. Tan, Y. Chen, W. Hu, X. Xia, *Adv. Funct. Mater.* **2019**, *30*, 1908804.

[197] M. A. Shannon, P. W. Bohn, M. Elimelech, J. G. Georgiadis, B. J. Marĩas, A. M. Mayes, *Nature* **2008**, *452*, 301.

[198] B. Gao, Z. Jiang, M. Zhao, H. Wu, F. Pan, J. Q. Mayta, Z. Chang, X. Bu, *J. Membr. Sci.* **2018**, *546*, 31.

[199] J.-H. Deng, Y.-Q. Wen, J. Willman, W.-J. Liu, Y.-N. Gong, D.-C. Zhong, T.-B. Lu, H.-C. Zhou, *Inorg. Chem.* **2019**, *58*, 11020.

[200] R. Dai, X. Zhang, M. Liu, Z. Wu, Z. Wang, *J. Membr. Sci.* **2019**, *573*, 46.

[201] Z. Cao, V. Liu, A. B. Farimani, *Nano Lett.* **2019**, *19*, 8638.

[202] S. J. Tesh, T. B. Scott, *Adv. Mater.* **2014**, *26*, 6056.

[203] C. Wang, C. He, Y.-H. Luo, S. Su, J.-Y. Wang, D.-L. Hong, X.-T. He, C. Chen, B.-W. Sun, *Chem. Eng. J.* **2020**, *379*, 122337.

[204] S. Duan, L. Wu, J. Li, Y. Huang, X. Tan, T. Wen, T. Hayat, A. Alsaedi, X. Wang, *J. Hazard. Mater.* **2019**, *373*, 580.

[205] Y. Jiang, G. H. Ryu, S. H. Joo, X. Chen, S. H. Lee, X. Chen, M. Huang, X. Wu, D. Luo, Y. Huang, J. H. Lee, B. Wang, X. Zhang, S. K. Kwak, Z. Lee, R. S. Ruoff, *ACS Appl. Mater. Interfaces* **2017**, *9*, 28107.

[206] X. Zhao, Y. Wang, D. S. Li, X. Bu, P. Feng, *Adv. Mater.* **2018**, *30*, 1705189.

[207] P. Z. Moghadam, A. Li, X. W. Liu, R. Bueno-Perez, S. D. Wang, S. B. Wiggin, P. A. Wood, D. Fairen-Jimenez, *Chem. Sci.* **2020**, *11*, 8373.
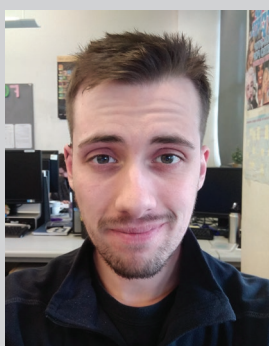
Joshua Nicks was awarded his MChem degree in 2017 from the University of Sheffield, under the supervision of Dr. Peter Portius. He is currently studying for his Ph.D. in chemistry at the same institution, under the supervision of Dr. Jonathan A. Foster. His research involves exploring the programmability of 2D metal-organic framework nanosheets and their applications.

Kezia Sasitharan completed her MSc in Chemistry at Christ University, India in 2017. She was awarded a Ph.D. in Chemistry in 2021 by The University of Sheffield, UK, under the supervision of Dr. Jonathan Foster. During her Ph.D. she researched the use of porphyrin MONs for enhanced performance of organic photovoltaic devices. She moved to Czech Technical University, Prague in 2021 after being awarded the Centre for Advanced Photovoltaics Postdoctoral Fellowship where she is currently exploring the role of low dimensional materials as additives for perovskite solar cells.

Ram R. R. Prasad obtained his master's from National Institute of Technology Trichy, where he completed a final year project under the guidance of Dr. S. Anandan. He went on to complete his Ph.D. at the University of St Andrews under the joint supervision of Prof. Paul Wright and Prof. Matt Clarke, where he investigated the use of metal-organic frameworks for tandem catalytic applications. Now in the Foster group, he is working on designing and functionalizing novel MONs for catalysis.

**ADVANCED
SCIENCE NEWS**

www.advancedsciencenews.com

**ADVANCED
FUNCTIONAL
MATERIALS**

www.afm-journal.de

David J. Ashworth completed his MChem with study in industry at the University of Sheffield in 2016. He was awarded a Ph.D. in chemistry from the same institution in 2019 under the supervision of Dr. Jonathan Foster, researching the design and synthesis of functional MONs. He was then awarded an EPSRC Doctoral Prize Fellowship towards developing scalable routes of MON syntheses, in additional collaboration with Prof. Siddharth Patwardhan. Dave currently holds an EPSRC funded post-doctoral position at the University of Strathclyde, developing flexible, responsive MOFs with particular interest in gas adsorption properties.

Jonathan A. Foster completed his Ph.D. in the groups of Prof. Jonathan Steed and Prof. Judith Howard at the University of Durham before moving to the University of Cambridge with Prof. Jonathan Nitschke and Prof. Anthony Cheetham. In 2015 he was awarded a Ramsay Memorial Fellowship and the position of Vice Chancellors Fellow with the goal to develop metal-organic framework nanosheets (MONs) as a distinct class of 2D materials. He was appointed as lecturer in 2019 and his group continue to work with academic and industrial collaborators to develop MONs for a diverse range of applications.

Chapter 3

Tandem Catalysis by Ultrathin Metal–Organic Nanosheets Formed through Post-Synthetic Functionalisation of a Layered Framework

Chapter 3

Tandem Catalysis by Ultrathin Metal–Organic Nanosheets Formed through Post-Synthetic Functionalisation of a Layered Framework

Joshua Nicks, Jiawen Zhang, and Jonathan A. Foster

Author Contributions

Joshua Nicks	Performed all experiments and collected all data. Drafted manuscript and SI and created all figures. Assisted in editing of manuscript.
Jiawen Zhang	MSc student supervised by JAF, who performed initial investigations into MOF synthesis.
Jonathan A. Foster	Supervised JN and JZ, coordinated body of work, assisted in editing of manuscript.

Check for updates

Tandem catalysis by ultrathin metal–organic nanosheets formed through post-synthetic functionalisation of a layered framework†

Joshua Nicks, Jiawen Zhang and Jonathan A. Foster ![ORCID] *

Covalent post-synthetic functionalisation of layered metal–organic frameworks is demonstrated as a new approach to forming ultrathin nanosheets for use in catalysis. An aminoterephthalate framework was partially functionalised with sulfonate chains and exfoliated to form predominantly monolayer nanosheets able to catalyse a two-step acid–base reaction in one pot.

Metal–organic nanosheets (MONs) are an exciting new class of two-dimensional (2D) nanomaterial with tunable, periodic structures that lend themselves to numerous applications, including: molecular separation, sensing and electronics.[1–5] In particular, their high external surface areas, exposed active sites and ease of recovery make them ideal candidates for use as catalysts and MONs have been shown to outperform their bulk counterparts, metal–organic frameworks (MOFs), in a range of reactions.[6–14]

MONs can be fabricated directly from their molecular building blocks or by exfoliation of a layered MOF, described as bottom-up and top-down approaches respectively. In the latter, energy is added to overcome weak interlayer interactions and exfoliate the nanosheets whilst minimising disruption to the in-plane bonding which leads to fragmentation. Liquid-assisted ultrasonication has become the most commonly used top-down method due to its ease of setup and scalability,[15–19] though other techniques have also been used to produce few-layer sheets.[20–23] A number of groups have also demonstrated enhanced exfoliation by intercalating groups between layers to further weaken these inter-layer interactions.[13,24,25]

Post-synthetic functionalisation (PSF), in which new functionalities are introduced following assembly of the metal–organic material, provides an attractive pathway to tuning the structure and properties of MONs.[26,27] Examples of MON PSF through coordination of ligand, solvent molecules or metal-ions have been demonstrated.[28,29] However, to our knowledge, no studies have been undertaken into the effect of covalent PSF on MONs.

Department of Chemistry, University of Sheffield, Sheffield, UK.
E-mail: jona.foster@sheffield.ac.uk

† Electronic supplementary information (ESI) available: Full experimental details, synthetic procedures, exfoliation studies and catalytic data. See DOI: 10.1039/c9cc02061f

Covalent functionalisation offers the advantages of a stable covalent bond rather than a more labile dative bond, meaning functionalisation is typically more robust.[30,31] A range of covalent PSF chemistries have already been developed and used to introduce functionalities to other metal–organic materials.[27] In particular, covalent PSF of amino functionalised MOFs has been thoroughly studied, due to the variety of reactions in which amines serve as nucleophiles.[31]

We hypothesised that covalent PSF of a layered MOF could be used to enhance exfoliation and introduce new catalytically active functionalities onto the surface of the resulting MON. In particular, we predicted that functionalisation of copper 2-amino-benzenedicarboxylate, Cu(ABDC)(DMF), with 1,3-propanesultone would introduce repulsive charges between the layers, aiding exfoliation and creating acidic and basic active sites for catalysis (Fig. 1).

Copper acetate monohydrate and 2-aminobenzene-1,4-dicarboxylic acid (ABDC) were heated in DMF at 100 °C for 18 h in a sealed reaction vial. Elemental and thermogravimetric analysis of the resulting green microcrystalline powder (96% yield) confirmed the materials composition to be consistent with the expected formula, Cu(ABDC)(DMF) (Fig. S1–S4, ESI†). Pawley refinement of the powder X-ray diffraction pattern (Fig. S5, ESI†) obtained from the material showed the structure is isostructural with the known crystal structure of MOF-46 (Zn(ABDC)(DMF)). Cu (ABDC)(DMF) therefore has a layered structure in which four ABDC linkers coordinate to the M_2-paddlewheel (PW) and interconnect these units in the 2D **sql** topology, while DMF coordinates to the PW axial sites. Hence, the lamellar structure features strong metal-carboxylate bonding within the layers, with disordered amine groups providing weak interlayer hydrogen bonding.

Cu(ABDC)(DMF) was post-synthetically functionalised by treating a suspension of the MOF in chloroform with a 10 molar excess of 1,3-propanesultone and stirring at 55 °C. Cu(ABDC-PS)(DMF) was obtained as a lighter green powder after 1 week (Fig. 1a). Comparison of experimental PXRD patterns confirmed the layered structure had been maintained and no change in the

a)

b)
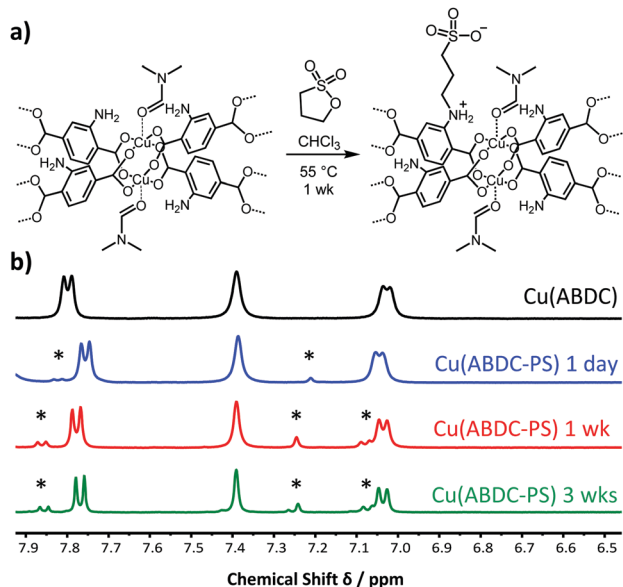
Fig. 1 (a) Reaction scheme showing the conditions in which Cu(ABDC)(DMF) was functionalised with 1,3-propanesultone to obtain Cu(ABDC-PS)(DMF). (b) Comparison between the aromatic regions of ^{1}H NMR spectra of digested samples of [from top to bottom] Cu(ABDC)(DMF) (black) and Cu(ABDC-PS)(DMF) after functionalisation for 1 day (blue), 1 week (red) and 3 weeks (green). Asterisks indicate peaks associated with the functionalised linker. Full spectra can be seen in the ESI,† Section S2.

interlayer distance was observed (Fig. S9, ESI†). Multiple analytical methods evidenced that PSF had taken place. FT-IR measurements of Cu(ABDC)(DMF) and Cu(ABDC-PS)(DMF) gave similar spectra, though the latter possessed peaks at 1212 cm^{-1} and 1040 cm^{-1} associated with the sulfonate group introduced (Fig. S7, ESI†).[32–34] Weak bands were also observed in the region of 3300–3000 cm^{-1}, associated with introduced C–H stretches. Mass spectrometry of the MOF after acid digestion indicated the presence of both the functionalised ([M]$^-$ = 302.0, [M + Na]$^-$ = 324.0) and unfunctionalised linker ([M]$^-$ = 180.0).

The degree of conversion was determined using ^{1}H NMR spectroscopy, in which the functionalised and unfunctionalised MOFs were digested with DCl/d_6-DMSO solution (Fig. 1b). Integration of the aromatic protons indicated 17% conversion of the secondary amines. PSF was also performed under the same conditions for 1 day and for 3 weeks, giving 6% and 20% conversion respectively. The MOFs were also first desolvated by soaking in acetonitrile for 3 days followed by PSF for 1 day or 1 week, which resulted in 21% and 25% functionalisation respectively (Fig. S10, ESI†). The relatively low degrees of conversion are attributed to the lack of void space within this relatively dense MOF (Fig. S11, ESI†). The samples following PSF of Cu(ABDC)(DMF) for 1 week were used for all remaining studies.

Mass spectrometry also indicates the formation of a difunctionalised species ([M]$^-$ = 424.0, 11% wrt 302.0), which is thought to be due to the reaction of 1,3-propanesultone with the terminal carboxylic acids of the MOF. Peaks associated with this product were not observed directly in ^{1}H NMR spectra, however aliphatic protons consistent with 3-hydroxypropane-1-sulfonic acid were

observed and thought to be formed due to partial hydrolysis of the ester in the acidic NMR solvent system. These sites integrate to approximately 6% of total amine sites.

In order to compare the effect of PSF on exfoliation, the functionalised and unfunctionalised MOFs were each suspended in acetonitrile and subject to 80 kHz ultrasound for 12 hours at ~18 °C (see ESI,† S3.1). Samples were then centrifuged for 1 hour at 1500 rpm to remove larger fragments and leave only nanosheets in suspension. Our initial intention was to exfoliate the material into water. Unfortunately, unlike other Cu-PW MONs we've developed, Cu(ABDC) dissolved in water. Acetonitrile was therefore chosen as the exfoliation medium, as previous studies have demonstrated it to be a good candidate for copper benzenedicarboxylate-based systems.[18,19]

Both Cu(ABDC)(DMF) and Cu(ABDC-PS)(DMF) exfoliated well into acetonitrile. Each suspension exhibited strong Tyndall scattering indicating the presence of nanoparticles (Fig. S12, ESI†). The functionalised suspensions appeared more transparent and this was reflected by weaker absorption in the UV-Vis spectra with extinction coefficients of 4285 and 1451 dm^3 mol^{-1} cm^{-1} for Cu(ABDC)(DMF) and Cu(ABDC-PS)(DMF) respectively. UV-Vis spectroscopy was also used to estimate the concentration of the two suspensions which were both calculated to be 0.4 mg mL^{-1} (Fig. S16–S18, ESI†), corresponding to ~50% of the dispersed material remaining in suspension following centrifugation.

The suspensions were drop-cast onto hot mica sheets for AFM imaging (Fig. 2). Cu(ABDC)(DMF) nanosheets had rectangular morphologies and a broad particle size distribution, with an average
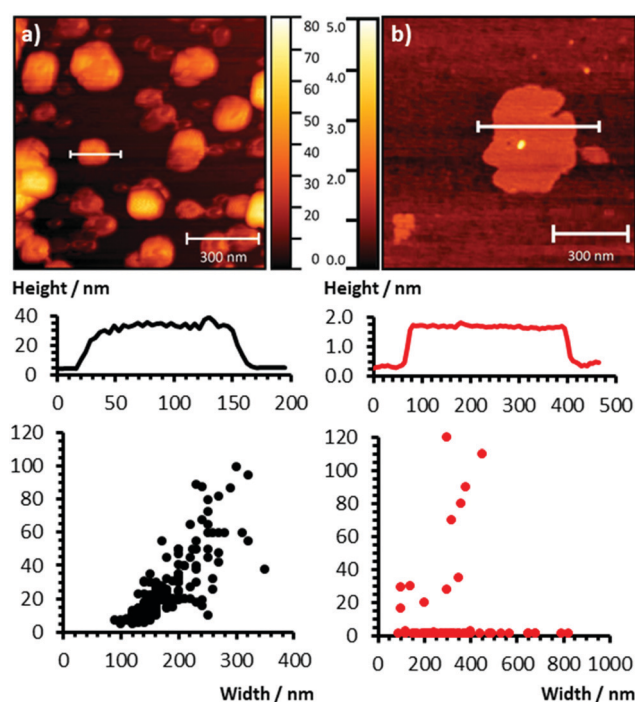
Fig. 2 AFM topographical images, associated height profiles and respective size distribution scatter plots of (a) Cu(ABDC)(DMF) nanosheets and (b) Cu(ABDC-PS)(DMF) nanosheets. Further imaging data can be found in the ESI,† Fig. S19–S22.

thickness of 25 nm (SD ±19) and average lateral size of 175 nm (SD ±48). In contrast, Cu(ABDC-PS)(DMF) predominantly yielded nanosheets which were consistently ~1.4 nm thick, corresponding to a single layer. A few fragments of partially exfoliated material were observed ranging between 15 and 120 nm. The functionalised nanosheets were typically larger and had a broader size distribution than those of the unfunctionalised MOFs, with an average lateral size of 344 nm (±205). The shapes of the functionalised nanosheets also appear less geometric, most likely a result of the increased fragility of the structures as they approach monolayer thickness.

This trend in size distribution was also observed in DLS data (Fig. S15, ESI†), wherein the Cu(ABDC-PS)(DMF) MON exhibited a larger average size with a broader distribution than the Cu(ABDC)(DMF) MON. Although the DLS data indicates smaller average nanosheet sizes than those observed via AFM for both systems, this is consistent with previous studies which have shown that DLS underestimates particle sizes of materials with sheet morphologies.[35]

The functionalised nanosheets were isolated from suspension by centrifugation at 4500 rpm for 3 hours. The FT-IR spectrum indicated no chemical change in comparison to the functionalised MOF (Fig. S23, ESI†), and PXRD analysis of the nanosheets indicated that the layered framework had been maintained (Fig. S14, ESI†). It is interesting to note that despite monolayer formation, well defined peaks are observed which indicates repacking is taking place upon sedimentation. Minor additional peaks at 6, 8 and 50° are also observed in XRPD patterns of the PSF-MONs following exfoliation in acetonitrile. Soaking of the MONs in DMF removes these peaks which are attributed to a desolvated phase as has previously been observed for related systems (Fig. S13 and S14, ESI†).[18,19] Proton NMR spectroscopy of the digested MONs showed an increased conversion from 17 to ~23% (Fig. S23, ESI†), suggesting the more functionalised layers of the MOF had preferentially exfoliated and retained better in suspension.

Zeta potential analysis of both Cu(ABDC)(DMF) and Cu(ABDC-PS) MONs gave values of −23.0 mV and −39.6 mV respectively (also see Table S2, ESI†). This indicates that addition of the sulfonate groups produces nanosheets with a larger negative surface charge. In the MOF, this excess of negative charge could lead to repulsive interlayer interactions aiding exfoliation during sonication resulting in the thinner nanosheets observed by AFM. Contact angle measurements for drops of acetonitrile on a mica sheet coated with Cu(ABDC-PS) or Cu(ABDC)(DMF) were 7.0° and 12.5° respectively. This suggesting the surface energy of the PSF-MON matches more closely with acetonitrile, which could further drive the formation of observed ultrathin nanosheets and improve the stability of larger sheets in suspension.

The use of catalysts for tandem reactions in which multiple distinct active sites catalyse sequential steps in a reaction has recently received considerable attention as a means of producing greener catalysts. There has been growing interest in the use of MOFs for tandem catalysis[36–38] with recent reports of MONs being used alongside nanoparticles and enzymes to facilitate multistep reactions.[9,10,39] As Cu(ABDC-PS) is partially functionalised with sulfonic acid groups, with basic amine sites remaining, we decided

Table 1 Reaction scheme and catalytic data for the acid hydrolysis of benzaldehyde dimethyl acetal (1) to benzaldehyde (2), followed by base-catalysed Knoevenagel condensation of benzaldehyde with malononitrile (3) to form nitrostyrene. All experiments were performed at 60 °C in d₃-acetonitrile for 24 hours
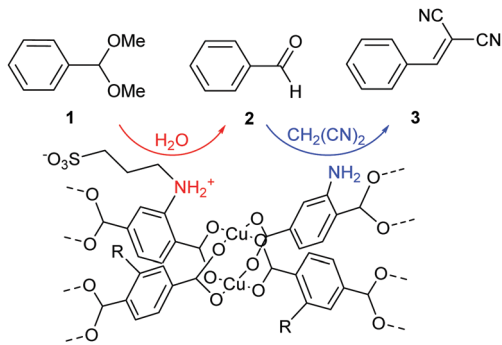
Catalyst	Type	[Cat.]/mol%	Product/%		
			1	**2**	**3**
No catalyst	—	0	78	21	1
Cu(ABDC)	MOF	0.2	70	28	2
Cu(ABDC)	MON	0.1	56	42	2
Cu(ABDC-PS)	MOF	0.2	62	35	3
Cu(ABDC-PS)	MON	0.1	0	18	82
Cu(ABDC-PS) post-filtration	MON	0.1[a]	65	32	3
Cu(ABDC-PS), recycled	MON	1.5	0	14	86
			0	21	79

[a] 0.1 mol% added before filtration (Fig. S25–S31, ESI).

to investigate their ability to catalyse a well-known acid–base tandem reaction.[34,40,41]

Cu(ABDC-PS) was tested as a catalyst for the acid hydrolysis of benzaldehyde dimethyl acetal (1) to benzaldehyde (2), followed by a Knoevenagel condensation to form benzylidene malononitrile (3). The results of the catalytic experiments after 24 h at 60 °C and those of the corresponding PSF-MOF, and unfunctionalised MOF and MON are shown in Table 1. Only Cu(ABDC-PS) was able to catalyse both acid and base reactions to any significant degree, with conversion to 82% of **3** after 24 hours with the remaining material being the intermediate **2**. In contrast, unexfoliated PSF-MOF produced only 3% conversion to **3** demonstrating the rate enhancement caused by the vastly higher surface area following exfoliation to nanosheets. The unfunctionalised MOF and MON produced less than 2% of this product demonstrating the role of the PSF group in facilitating the reaction.

A detailed analysis is beyond the scope of this paper but previous studies indicate that, as highlighted in the scheme above Table 1, the ligand is zwitterionic with the secondary and primary amines acting as acid and base respectively.[34] The acid catalysed reaction had a relatively high background rate with 21% conversion to **2** over the reaction period. Interestingly this step is enhanced by the presence of all of the references, including the unfunctionalised MOF (35%) and MON (42%), which could indicate a role for the Lewis acidic axial sites in facilitating this reaction.[42]

The heterogeneous nature of the catalyst and its recyclability were tested. The reaction mixture including the nanosheet

suspension was filtered through a 0.2 μm GHP filter before heating for 24 hours. UV-Vis spectroscopy indicated a concentration of <0.01 mg mL^{-1} after filtration with no Tyndall scattering observed (Fig. S27, ESI†). Analysis of the reaction mixture after 24 h indicates a significantly reduced yield of 3% for **3** and 32% of **2** confirming that the catalyst is heterogeneous. In order to demonstrate recyclability, the concentration of MONs was increased to 1.5 mol% to allow the nanosheets to be washed during recovery. The initial reaction proceeded as previously giving 86% conversion to **3**. The mixture was then centrifuged for 3 h at 4500 rpm and washed with acetonitrile. The nanosheets were redispersed in fresh reaction mixture, allowed to proceed and gave conversion to **3** of 79% (Fig. S28, ESI†) showing the nanosheets can be reused.

In conclusion, we have demonstrated that covalent post-synthetic functionalisation of layered MOFs can be used to enhance their top-down exfoliation into monolayer nanosheets and to impart catalytic activity. The layered MOF, Cu(ABDC)(DMF) was reacted with 1,3-propanesultone resulting in 17% functionalisation after 1 week due to its relatively dense structure. Ultrasonic exfoliation in acetonitrile produced larger, predominantly monolayer (1.4 nm) nanosheets, in contrast to the broad thickness distribution (25 nm ±19) and smaller lateral dimensions observed for the unfunctionalised system. The higher aspect ratio of the PSF MON is attributed to electrostatic repulsion between the negatively charged sulfonate groups, weakening interlayer interactions leading to enhanced exfoliation during sonication and improved solvent-MON interactions reducing the loss of larger nanosheets from suspension during centrifugation. The partially functionalised MONs were found to catalyse the acid–base deacetylation-Knoevenagel condensation reaction in contrast to their unfunctionalised and unexfoliated counterparts. We anticipate that covalent PSF will be broadly applicable to enhancing the exfoliation of a range of layered MOFs and for introducing 'active' functional groups onto the surface of MONs to enable catalysis, sensing, separation and electronic applications.

Conflicts of interest

There are no conflicts to declare.

Notes and references

1 D. J. Ashworth and J. A. Foster, *J. Mater. Chem. A*, 2018, **6**, 16292–16307.
2 M. Zhao, Y. Huang, Y. Peng, Z. Huang, Q. Ma and H. Zhang, *Chem. Soc. Rev.*, 2018, **47**, 6267–6295.
3 M. Xu, S. S. Yang and Z. Y. Gu, *Chem. – Eur. J.*, 2018, 15131.
4 W. Zhao, J. Peng, W. Wang, S. Liu, Q. Zhao and W. Huang, *Coord. Chem. Rev.*, 2018, **377**, 44–63.
5 A. Mukhopadhyay, V. K. Maka, G. Savitha and J. N. Moorthy, *Chem*, 2018, **4**, 1059–1079.
6 L. Cao, Z. Lin, F. Peng, W. Wang, R. Huang, C. Wang, J. Yan, J. Liang, Z. Zhang, T. Zhang, L. Long, J. Sun and W. Lin, *Angew. Chem., Int. Ed.*, 2016, **55**, 4962–4966.
7 Y. Wang, M. Zhao, J. Ping, B. Chen, X. Cao, Y. Huang, C. Tan, Q. Ma, S. Wu, Y. Yu, Q. Lu, J. Chen, W. Zhao, Y. Ying and H. Zhang, *Adv. Mater.*, 2016, **28**, 4149–4155.
8 R. Dong, Z. Zheng, D. C. Tranca, J. Zhang, N. Chandrasekhar, S. Liu, X. Zhuang, G. Seifert and X. Feng, *Chem. – Eur. J.*, 2017, **23**, 2255–2260.
9 P. Ling, C. Qian, F. Gao and J. Lei, *Chem. Commun.*, 2018, **54**, 11176–11179.
10 Y. Wang, M. Zhao, S. Han, Z. Lai, J. Yang, C. Tan, Q. Ma, Q. Lu, J. Chen, X. Zhang, Z. Zhang, B. Li, B. Chen, Y. Zong and H. Zhang, *Adv. Mater.*, 2017, **29**, 1–5.
11 J.-X. Wu, S.-Z. Hou, X.-D. Zhang, M. Xu, H.-F. Yang, P.-S. Cao and Z.-Y. Gu, *Chem. Sci.*, 2019, **10**, 2199–2205.
12 Z. Xia, J. Fang, X. Zhang, L. Fan, A. J. Barlow, T. Lin, S. Wang, G. G. Wallace, G. Sun and X. Wang, *Appl. Catal., B*, 2019, **245**, 389–398.
13 J. Huang, Y. Li, R. K. Huang, C. T. He, L. Gong, Q. Hu, L. Wang, Y. T. Xu, X. Y. Tian, S. Y. Liu, Z. M. Ye, F. Wang, D. D. Zhou, W. X. Zhang and J. P. Zhang, *Angew. Chem., Int. Ed.*, 2018, **57**, 4632–4636.
14 T. He, B. Ni, S. Zhang, Y. Gong, H. Wang, L. Gu, J. Zhuang, W. Hu and X. Wang, *Small*, 2018, **14**, 1–6.
15 Z. Q. Li, L. G. Qiu, W. Wang, T. Xu, Y. Wu and X. Jiang, *Inorg. Chem. Commun.*, 2008, **11**, 1375–1377.
16 P.-Z. Li, Y. Maeda and Q. Xu, *Chem. Commun.*, 2011, **47**, 8436.
17 H. Xu, J. Gao, X. Qian, J. Wang, H. He, Y. Cui, Y. Yang, Z. Wang and G. Qian, *J. Mater. Chem. A*, 2016, **4**, 10900–10905.
18 J. A. Foster, S. Henke, A. Schneemann, R. A. Fischer and A. K. Cheetham, *Chem. Commun.*, 2016, **52**, 10474–10477.
19 L. D. Smith, J. A. Foster, R. W. M. Al-Saedi, A. J. H. M. Meijer, A. Cooper, M. Trueman and D. J. Ashworth, *Chem. – Eur. J.*, 2018, **24**, 17986–17996.
20 X. Wang, C. Chi, K. Zhang, Y. Qian, K. M. Gupta, Z. Kang, J. Jiang and D. Zhao, *Nat. Commun.*, 2017, **8**, 14460.
21 Y. Peng, Y. Li, Y. Ban and W. Yang, *Angew. Chem., Int. Ed.*, 2017, **56**, 9757–9761.
22 Y. Zhou, M. Zhang, Z. Guo, L. Miao, S. T. Han, Z. Wang, X. Zhang, H. Zhang and Z. Peng, *Mater. Horiz.*, 2017, **4**, 997.
23 A. Abhervé, S. Mañas-Valero, M. Clemente-León and E. Coronado, *Chem. Sci.*, 2015, **6**, 4665–4673.
24 Y. Ding, Y. P. Chen, X. Zhang, L. Chen, Z. Dong, H. L. Jiang, H. Xu and H. C. Zhou, *J. Am. Chem. Soc.*, 2017, **139**, 9136–9139.
25 W. J. Song, *Talanta*, 2017, **170**, 74–80.
26 Z. Wang and S. M. Cohen, *Chem. Soc. Rev.*, 2009, **38**, 1315.
27 K. K. Tanabe and S. M. Cohen, *Chem. Soc. Rev.*, 2011, **40**, 498–519.
28 G. Lan, Z. Li, S. S. Veroneau, Y. Y. Zhu, Z. Xu, C. Wang and W. Lin, *J. Am. Chem. Soc.*, 2018, **140**, 12369–12373.
29 W. Shi, L. Cao, H. Zhang, X. Zhou, B. An, Z. Lin, R. Dai, J. Li, C. Wang and W. Lin, *Angew. Chem., Int. Ed.*, 2017, **56**, 9704–9709.
30 Y. F. Song and L. Cronin, *Angew. Chem., Int. Ed.*, 2008, **47**, 4635–4637.
31 S. M. Cohen, *Chem. Rev.*, 2012, **112**, 970–1000.
32 R. S. Andriamitantsoa, J. Wang, W. Dong, H. Gao and G. Wang, *RSC Adv.*, 2016, **6**, 35135–35143.
33 M. Köppen, O. Beyer, S. Wuttke, U. Lüning and N. Stock, *Dalton Trans.*, 2017, **46**, 8658–8663.
34 H. Liu, F. G. Xi, W. Sun, N. N. Yang and E. Q. Gao, *Inorg. Chem.*, 2016, **55**, 5753–5755.
35 M. Lotya, A. Rakovich, J. F. Donegan and J. N. Coleman, *Nanotechnology*, 2013, **24**, 265703.
36 Y. B. Huang, J. Liang, X. S. Wang and R. Cao, *Chem. Soc. Rev.*, 2017, **46**, 126–157.
37 S. M. J. Rogge, A. Bavykina, J. Hajek, H. Garcia, A. I. Olivos-Suarez, A. Sepúlveda-Escribano, A. Vimont, G. Clet, P. Bazin, F. Kapteijn, M. Daturi, E. V. Ramos-Fernandez, F. X. I. Llabrés Xamena, V. Van Speybroeck and J. Gascon, *Chem. Soc. Rev.*, 2017, **46**, 3134–3184.
38 A. H. Chughtai, N. Ahmad, H. A. Younus, A. Laypkov and F. Verpoort, *Chem. Soc. Rev.*, 2015, **44**, 6804–6849.
39 L. Ye, L. Gao, S. Cao, H. Chen, Y. Yao, J. Hou and L. Sun, *Appl. Catal., B*, 2018, **227**, 54–60.
40 H. He, F. Sun, B. Aguila, J. A. Perman, S. Ma and G. Zhu, *J. Mater. Chem. A*, 2016, **4**, 15240–15246.
41 J. Park, J. R. Li, Y. P. Chen, J. Yu, A. A. Yakovenko, Z. U. Wang, L. B. Sun, P. B. Balbuena and H. C. Zhou, *Chem. Commun.*, 2012, **48**, 9995–9997.
42 R. Natarajan, M. Yoon, Y. Ho Ko, K. Kim, R. Srirambalaji, S. Hong, Y. Kim and R. Hota, *Chem. Commun.*, 2012, **48**, 11650.

Tandem catalysis by ultrathin metal-organic nanosheets formed through post-synthetic functionalisation of a layered framework

Supplementary Information (SI)

Joshua Nicks, Zhang Jiawen and Jonathan A. Foster*

University of Sheffield, Department of Chemistry, Sheffield, S3 7HF, UK

Contents

S1. General Details

S1.1. Materials

Commercial solvents, reagents and spectroscopic grade deuterated solvents were used as purchased without further purification. Solvothermal synthesis of Cu(ABDC)(DMF) was carried out using borosilicate vials with Teflon-lined caps in a Carbolite Gero PF 60 Oven. Post-synthetic functionalisations were carried out in dry glassware with a nitrogen overpressure.

S1.2. Analytical Procedures

Elemental analyses were performed by the microanalytical service at the Department of Chemistry, University of Sheffield using a Vario MICRO Cube in an atmosphere of pure O_2. Elemental contents are determined to a tolerance of ± 0.5 % for organometallics.

FT-IR spectra were recorded using a Perkin Elmer Spectrum 100 FT-IR spectrophotometer, equipped with a SenseIR diamond ATR module. Samples were analysed without further preparation, and spectra were obtained in reflectance mode between 4000 – 600 cm^{-1}, using 12 scans with a spectral resolution of 1 cm^{-1}.

NMR spectra were recorded at 300 K using a Bruker Avance III HD 400 spectrometer equipped with a standard geometry 5mm BBFO probe with a single z-gradient at 400 MHz (^1H). Supramolecular frameworks were digested prior to submission, using DCl (23 μL) and DMSO-d_6 (1 mL). Mass spectra were recorded directly from NMR solutions using an Agilent 6530 QTOF LC-MS in negative ionization mode.

UV-vis absorption spectra were obtained on a Varian Cary 50 Bio spectrophotometer using standard 1 cm width quartz cells and Perkin Elmer Spectrum One software. Spectral data was formatted using Excel.

Powder X-ray diffraction data were collected using a Bruker-AXS D8 diffractometer using Cu K_α (λ=1.5418 Å) radiation and a LynxEye position sensitive detector in Bragg Brentano parafocussing geometry using a packed glass capillary or a flat silicon plate.

Thermogravimetric analyses were performed using a Perkin-Elmer Pyris 1 instrument. Approximately 4 mg of sample was weighed into a ceramic pan, held under nitrogen flow of 20 cm^3 min^{-1} at 25 °C for 10 minutes to purge the sample and allow for equilibration, then

ramped to varying end temperatures (see individual traces for details) at 1 °C min^{-1}. The samples were then held at the final temperature for 10 minutes to allow sample burn off.

DLS data were collected using a Malvern Zetasizer Nano Series particle size analyser, using a He-Ne laser at 633 nm, operating in backscatter mode (173 °). Samples were equilibrated at 298 K for 60 s prior to analysis. Zeta potential data were collected using the same instrument in zeta potential mode, using disposable polycarbonate capillary electrophoresis cells and according to the Smoluchowski method. Contact angle measurements were obtained using a Ramé-Hart Goniometer and coated mica surfaces.

Atomic force microscopy images were recorded using a Bruker Multimode 5 Atomic Force Microscope, operating in soft-tapping mode in air under standard ambient temperature and pressure, fitted with Bruker OTESPA-R3 silicon cantilevers operated with a drive amplitude of ~18.70 mV and resonance frequency of ~236 kHz. Samples were prepared by drop-casting 10 µL drops of suspension onto the centre of freshly cleaved mica sheets heated to 100 °C on a hot plate. These sheets were stuck to stainless steel, magnetic Agar scanning probe microscopy specimen discs. Images were processed using Gwyddion software.

S2. Synthetic Procedures

S2.1 Synthesis of Cu(ABDC)(DMF)
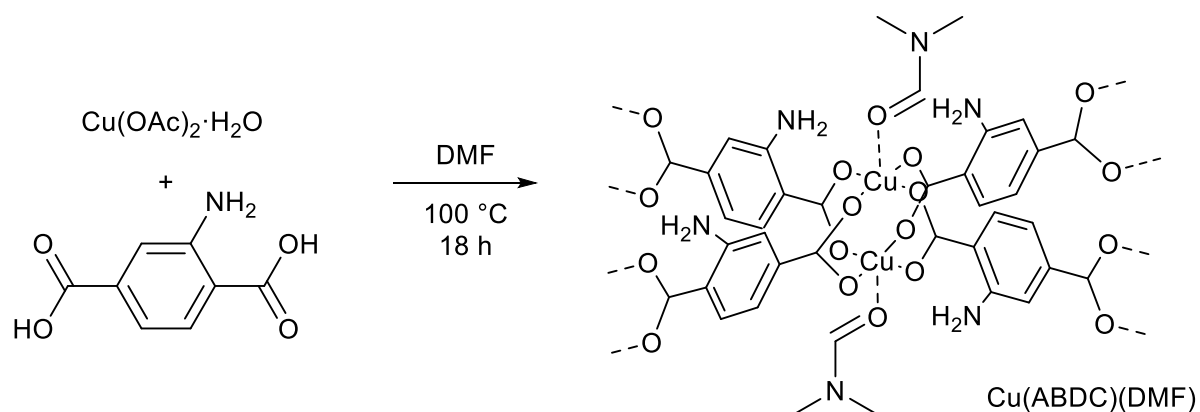
Copper acetate monohydrate (250.1 mg, 1.25 mmol) and 2-aminoterepthallic acid (229.1 mg, 1.26 mmol) were each dissolved in DMF (50 mL) and added in equal aliquots to 10 reaction vials. Reaction vials were then heated in a reaction oven to 100 °C at a rate of 1.0 °C min^{-1}, maintained for 18 hours, then cooled to 25 °C at a rate of 0.1 °C min^{-1}. Reaction mixtures were combined and centrifuged (4500 rpm, 30 mins), after which the supernatant was pipetted off and the wet solid washed with DMF (2 x 15 mL) and diethyl ether (2 x 10 mL). The sample was dried in air giving copper 2-aminoterephthalate (Cu(ABDC)(DMF) (382.3 mg, 1.20 mmol, 96 %) as a green powder. Elemental analysis: calculated mass for CuC$_{11}$H$_{12}$O$_5$N$_2$ %: C 41.82; H 3.83; N 8.87; Found mass %: C 41.46; H 4.02 N 8.79; MS (ESI-NEG): 180.0 [M]$^-$, 136.0 [M - CO$_2$]$^-$, 92.1 [M - 2(CO$_2$)]$^-$; phase purity was confirmed by PXRD (capillary) comparison to MOF-46.
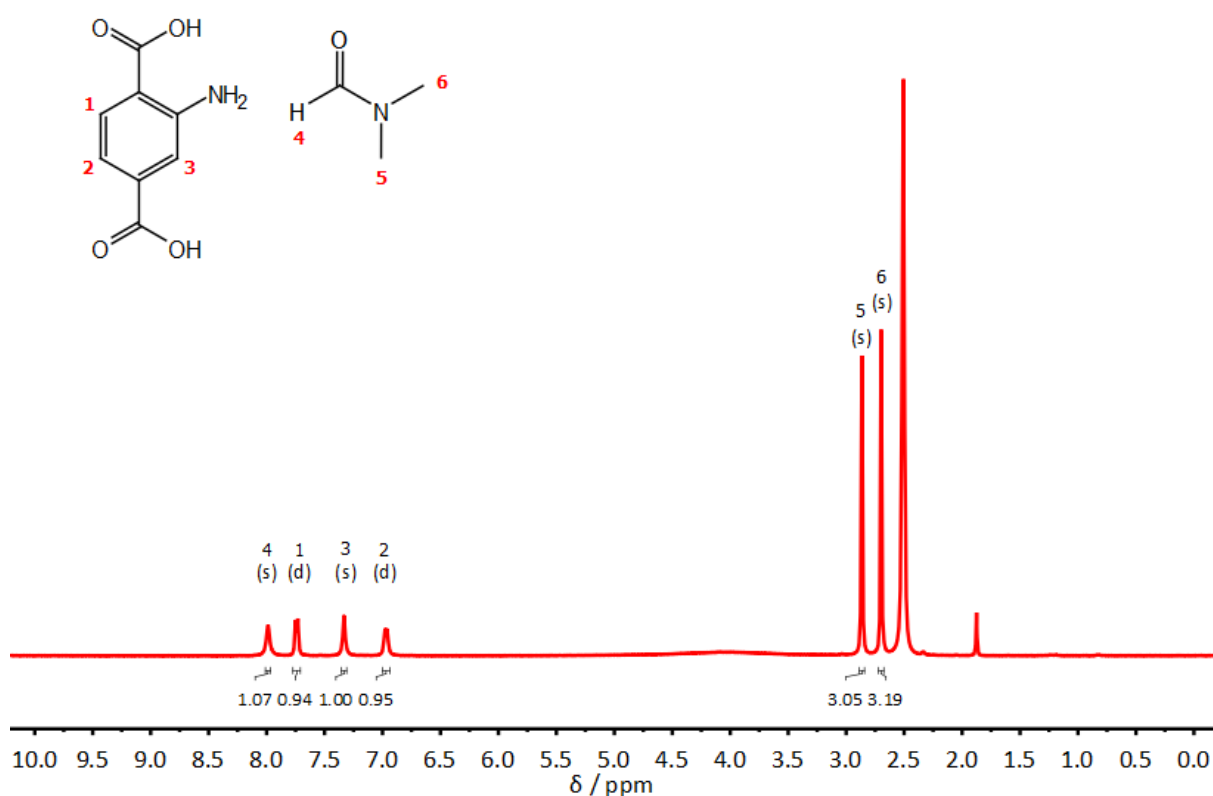
Figure S1. ^{1}H NMR spectrum of Cu(ABDC)(DMF) digested with DCl/DMSO-d$_6$, with peaks assigned according to the inset molecular structures. The unassigned peak at 1.90 ppm corresponds to residual acetate.
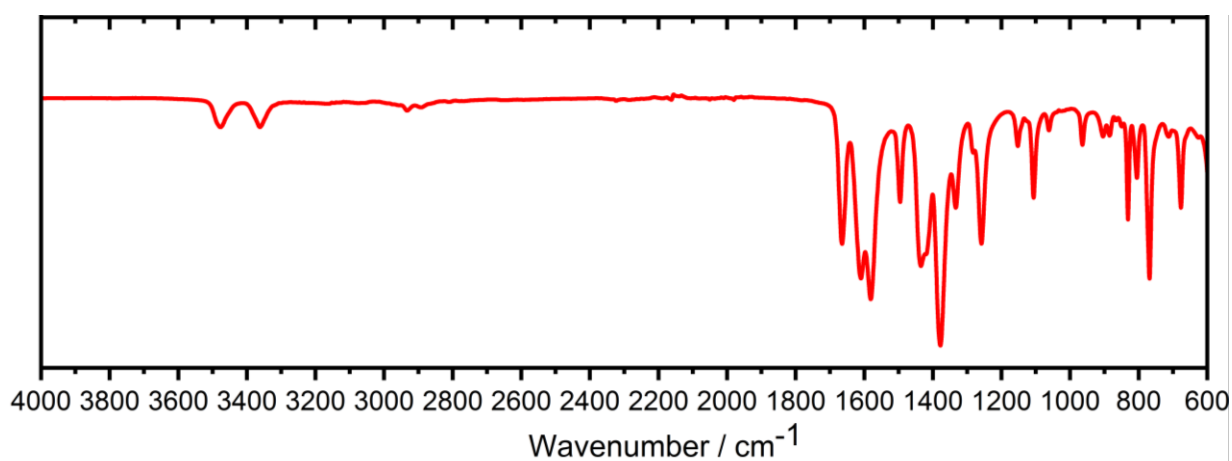
Figure S2. ATR-IR spectrum of Cu(ABDC)(DMF).
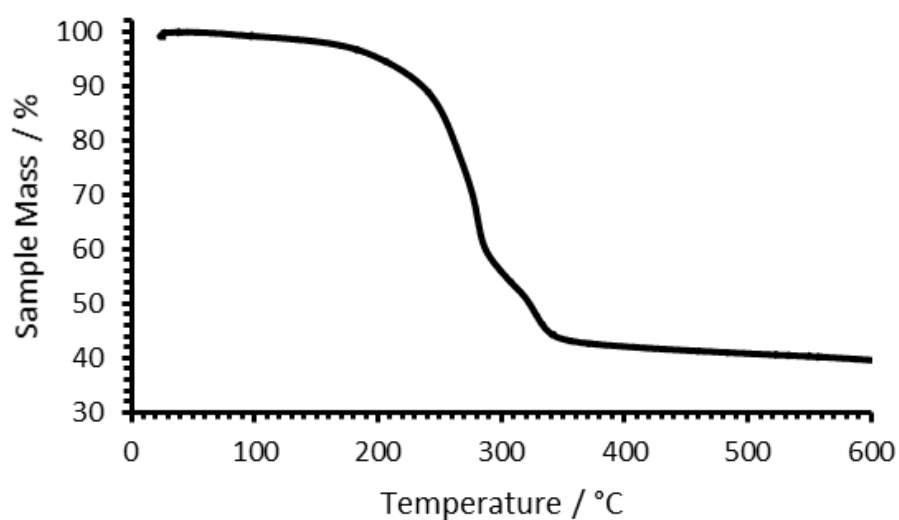
Figure S3. TGA plot for Cu(ABDC)(DMF).
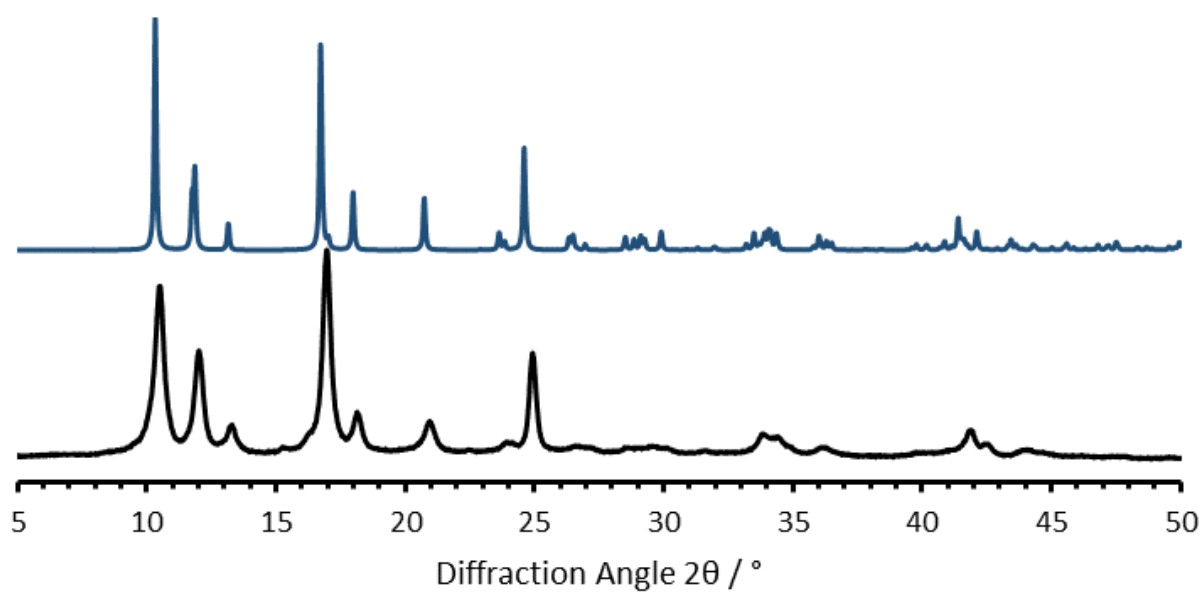
Figure S4. PXRD pattern obtained from Cu(ABDC)(DMF) (recorded in capillary mode) compared to a pattern calculated from the analogous Zn(ABDC)(DMF), MOF-46.[1]
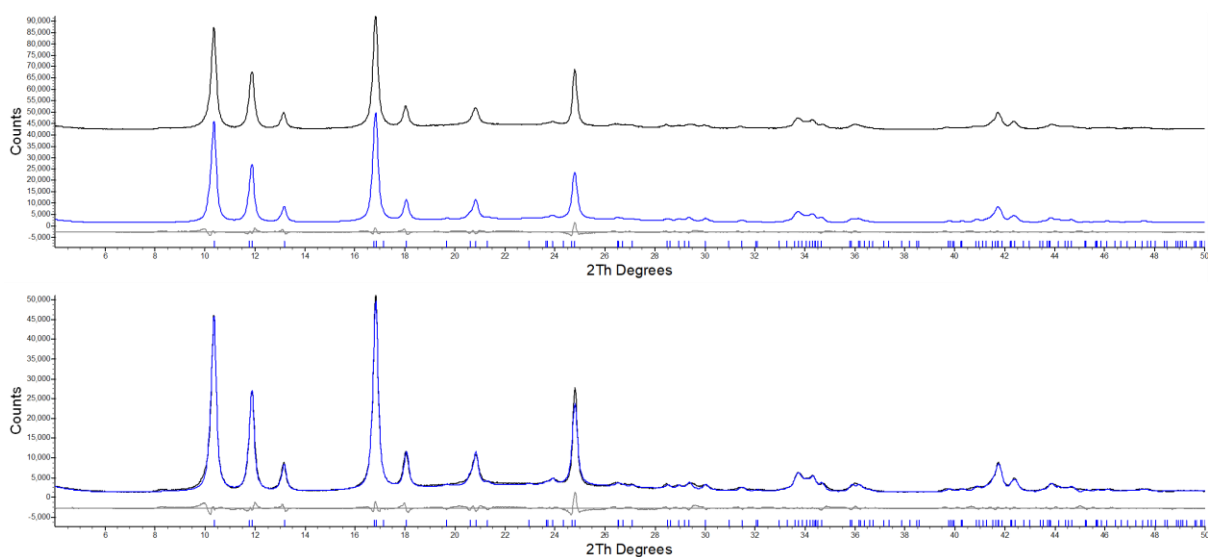
Figure S5. Pawley fit of the X-ray diffraction pattern of Cu(ABDC)(DMF) to MOF-46, stacked (top) and superimposed (bottom). Blue, black and grey lines represent calculated, experimental and difference profiles respectively. Tick marks indicate positions of allowed Bragg reflections in the space group C2/m.

Table S1. Crystallographic data of the Cu(ABDC)(DMF) MOF determined by Pawley refinement of PXRD data. Reference data for MOF-46 is also included.

	MOF-46 [1]	Cu(ABDC)(DMF)
Space Group	C2/m	C2/m
a / Å	11.2043(9)	11.1420(6)
b / Å	15.0516(12)	15.0305(4)
c / Å	8.0275(7)	8.0132(8)
β / °	111.7060(10)	111.8223(7)
R_{wp}		7.264
R_{exp}		1.635

S2.2. Post-synthetic functionalisation of Cu(ABDC)(DMF) with 1,3-propanesultone – Cu(ABDC-PS)(DMF)

Cu(ABDC)(DMF) (99.9 mg, 0.32 mmol) was suspended in chloroform (10 mL) and treated with 1,3-propanesultone (391.0 mg, 3.20 mmol, 280 µL) under a N_2 atmosphere. The suspension

was then heated under reflux at 55 °C for one week. The resulting suspension was centrifuged (4500 rpm, 1 hour) and the supernatant was pipetted off. The wet solid was then washed with chloroform (10 mL x3) and centrifuged (4500 rpm, 30 mins), after which the supernatant was removed. The sample was then washed with DMF (10 mL x 3) and diethyl ether (10 mL x 2) in the same way and left to dry in air, giving Cu(ABDC-PS)(DMF) as a light green powder (109.8 mg, 17 % conversion). Elemental analysis: Calculated mass for [0.17 Cu(ABDC-PS) + 0.83 Cu(ABDC) + 1.1 DMF + 0.08 $C_3H_6SO_3$] calc. from ^{1}H NMR] %: C 40.66; H 4.07; N 8.12; S 2.83; Found mass %: C 37.85; H 4.12 N 7.35; S 3.99; 1H NMR (DCl/DMSO-d_6): 7.97 (s, 1H, **DMF**), 7.84 (d, 1H, ArC*H* (**ABDC-PS**), *J* 8.0 Hz), 7.77 (d, 1H, ArC*H* (**ABDC**), *J* 8.0 Hz), 7.37 (s, 1H, ArC*H* (**ABDC**)), 7.23 (s, 1H, ArC*H* (**ABDC-PS**)), 7.06 (d, 1H, ArC*H* (**ABDC-PS**), *J* 8.0 Hz), 7.02 (d, 1H, ArC*H* (**ABDC**), *J* 8.0 Hz), 3.28 (m, 2H, C*H₂* (**ABDC-PS**)), 2.87 (s, 3H, **DMF**), 2.71 (s, 3H, **DMF**), 1.87 (m, 2H, C*H₂* (**ABDC-PS**)) ppm; MS (NEG-ESI): 424.0 [M + SO$_3$H]$^-$, 302.0 [M]$^-$, 180.0 [ABDC]$^-$.
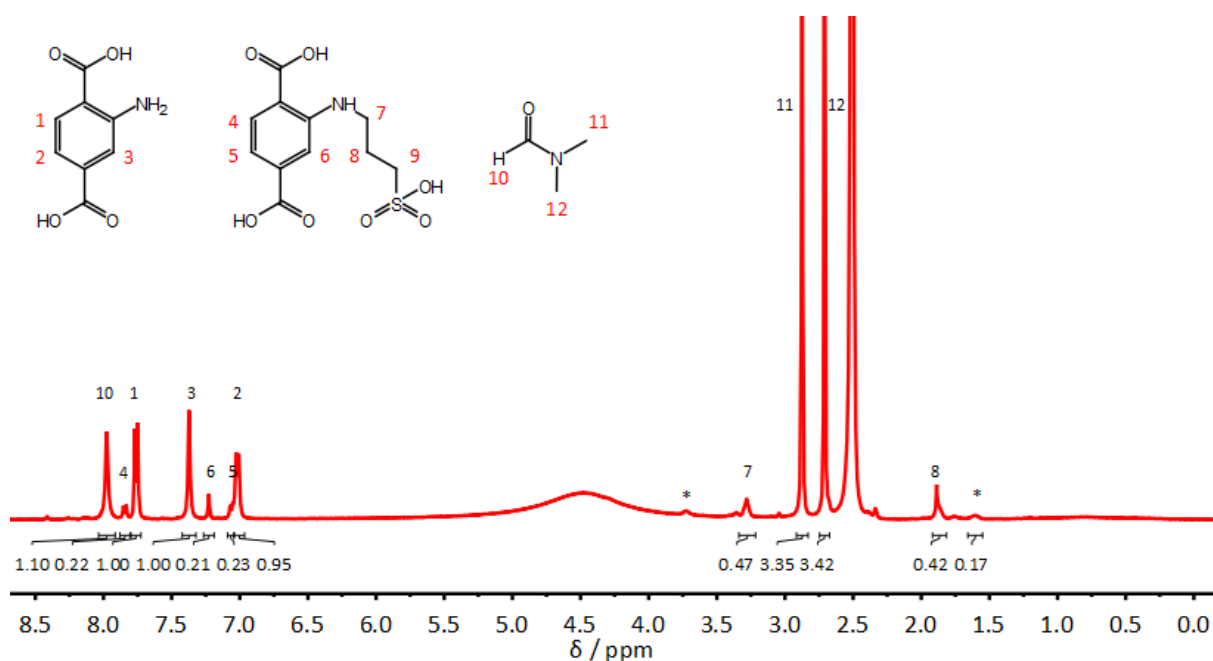
Figure S6. ^{1}H NMR spectrum of Cu(ABDC-PS)(DMF) digested with DCl/DMSO-d_6, showing a 17:83 ratio of the functionalised ligand to ABDC. A peak for the proton environment labelled 9 could not be assigned as it is masked by the residual solvent peak. Peaks marked with an * indicate small amounts of 3-hydroxypropane-1-sulfonic acid, which forms in the NMR solvent system due to hydrolysis of terminal acids which have reacted with 1,3-propanesultone.
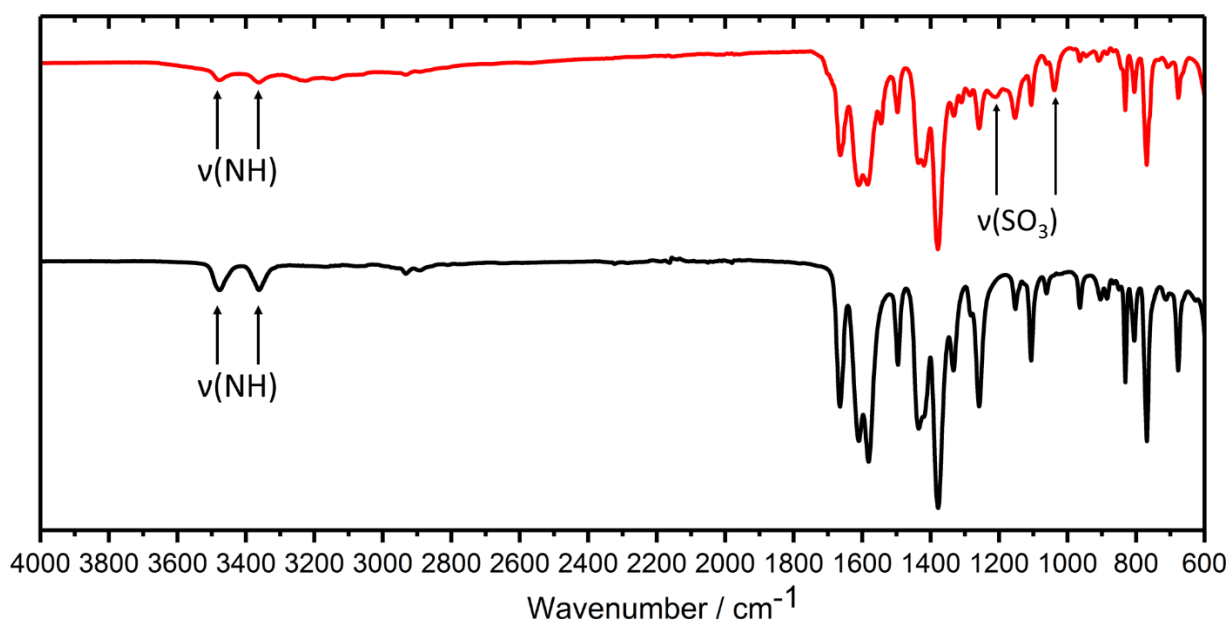
Figure S7. Infra-red spectrum of Cu(ABDC-PS)(DMF) (red) compared to Cu(ABDC)(DMF) (black), including two new bands associated with sulfonic acid stretches, as well as weak stretches in the 3200-3000 cm^{-1} region associated with the introduced C-H bonds.[2–4]
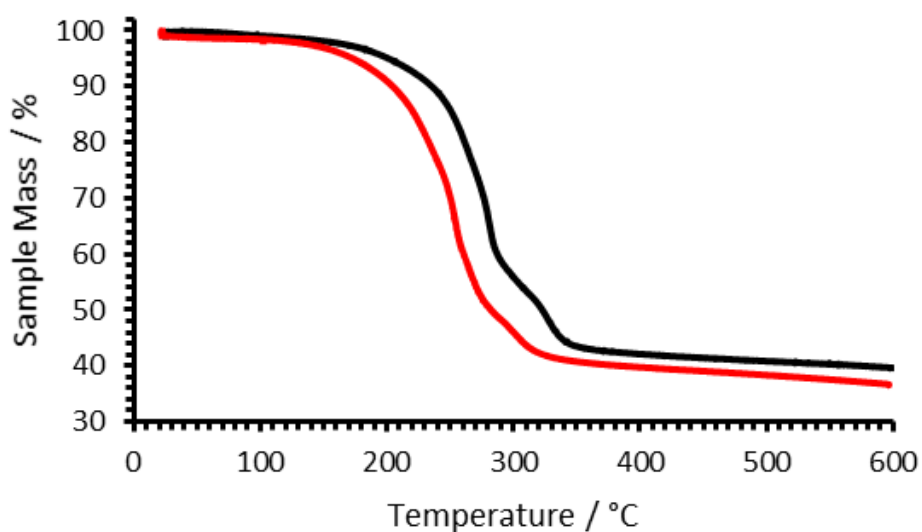
Figure S8. TGA plot of Cu(ABDC-PS)(DMF) (red) compared to Cu(ABDC)(DMF) (black).
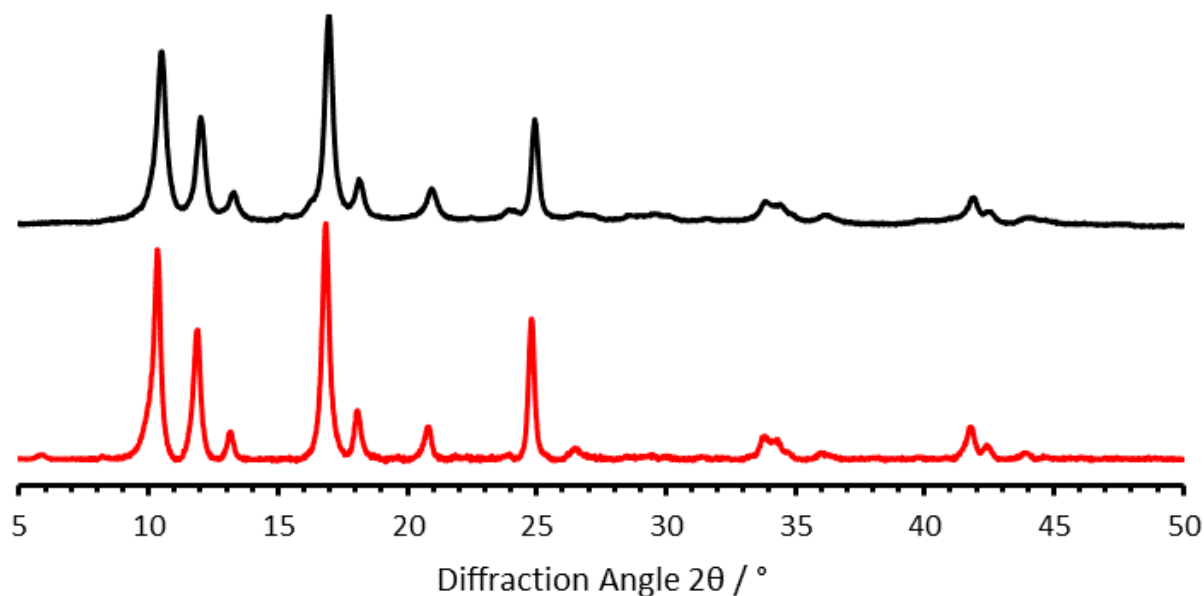
Figure S9. PXRD pattern obtained from Cu(ABDC-PS)(DMF) (red) (recorded in capillary mode) compared to the pattern obtained from Cu(ABDC)(DMF) (black), which indicates that phase and phase purity have been maintained.
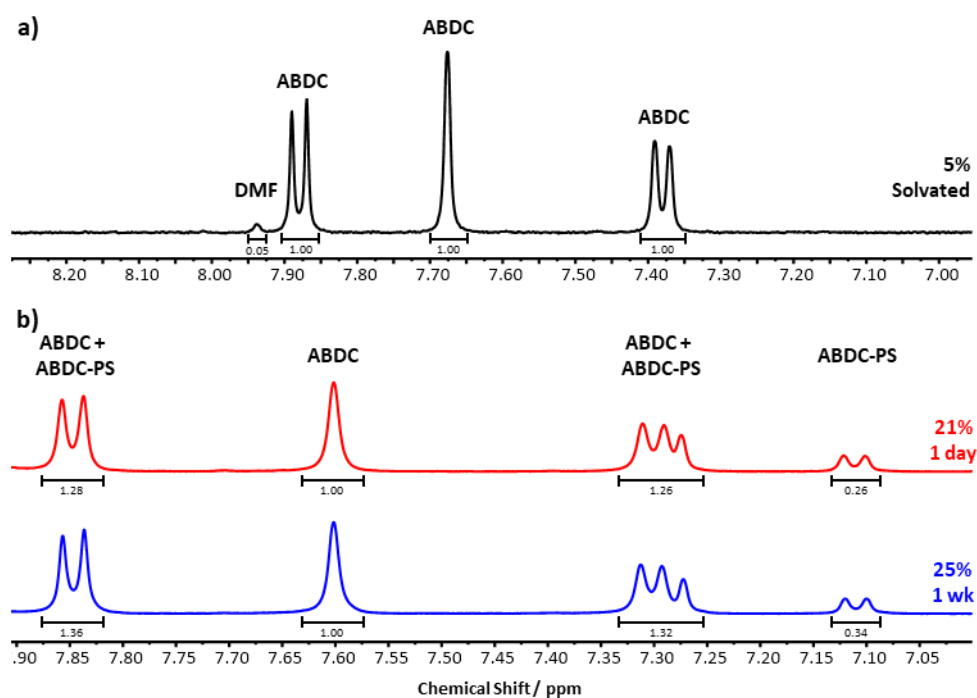
Figure S10. 1H NMR spectra of: a) desolvated Cu(ABDC) MOF which indicates only 5% solvation after soaking in acetonitrile for 3 days, b) products obtained from PSF of desolvated Cu(ABDC) for 1 day (red) and 1 week (blue), indicating 21 and 25 % functionalisation respectively.
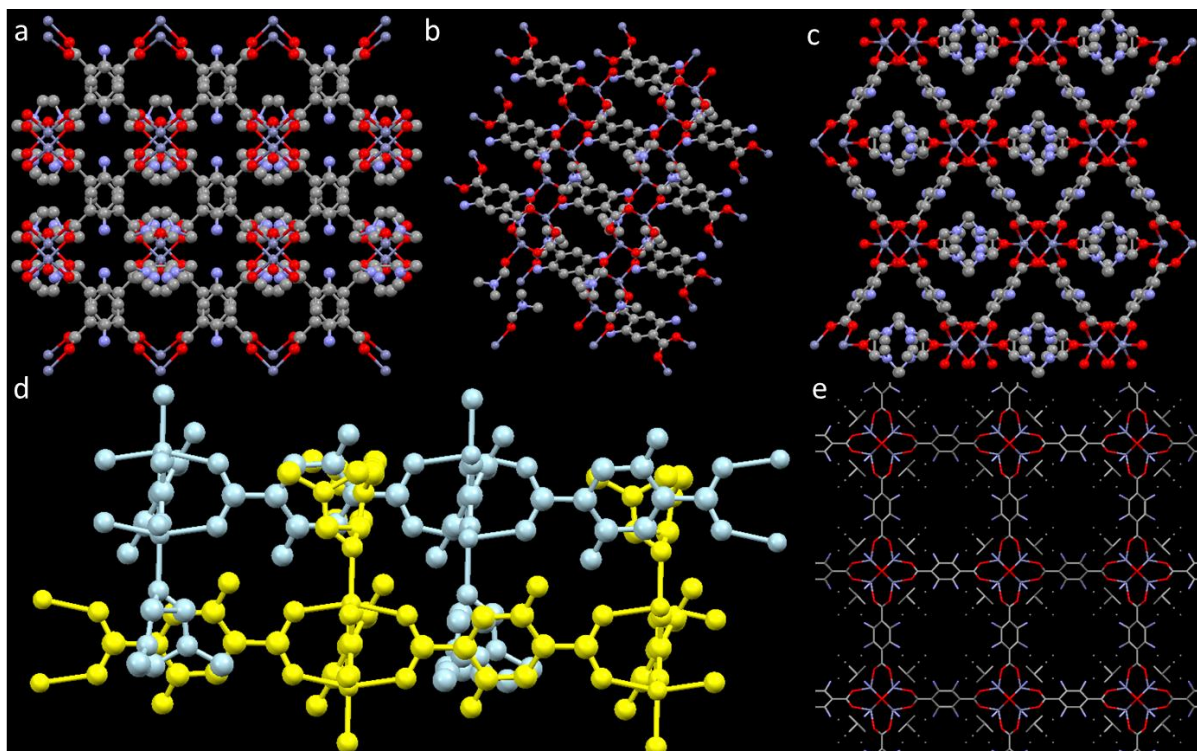
Figure S11. Ball and stick representations of single crystal structure of Zn(ABDC)(DMF) viewed along the hkl planes a) 100, b) 010 c) 001,[1] and d) through the layers, with adjacent layers highlighted in blue and yellow.[1] e) IRMOF-3, a Zn-O-C cluster based MOF with aminoterepthalate linkers that extend in 3D showing larger accessible pores in these systems, viewed from the hkl plane 100.[5]

S3. Exfoliation Studies

S3.1. Ultrasonic Exfoliation Method

Liquid-assisted ultrasonic exfoliations were carried out by suspension of 5 mg of MOF in 6 mL of acetonitrile inside a 10 mL reaction vial. The sample was mixed in a vortex mixer for 30 seconds to disperse the sediment. The samples were sonicated using a Fisherbrand Elmasonic P 30H ultrasonic bath (2.75 L, 380/350 W, UNSPSC 42281712) filled with water. Samples were sonicated for 12 hours at a frequency of 80 kHz with 100% power and the temperature was thermostatically maintained at 16-20°C using a steel cooling coil. Sonication was applied using a sweep mode and samples were rotated through the water using an overhead stirrer to minimise variation due to ultrasound "hot-spots" in accordance with a previously reported set-up.[6] Suspensions of nanosheets were obtained by centrifugation at 1500 rpm for 1 hour, followed by removal of the suspension from the isolated bulk powder.

S3.2. Tyndall Scattering

After sonication and exfoliation, samples of both Cu(ABDC)(DMF) and Cu(ABDC-PS)(DMF) exhibited Tyndall scattering effects, as shown in figure S11.
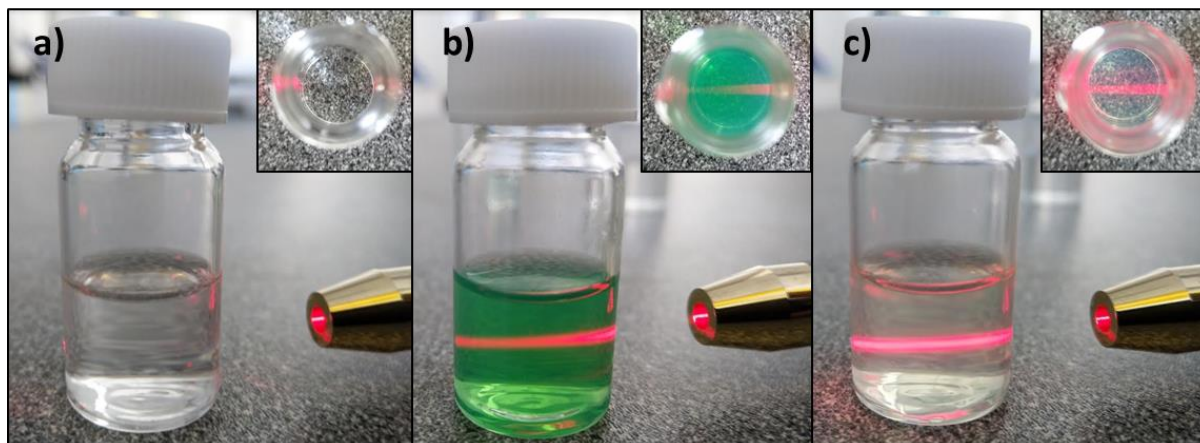
Figure S12. From left to right: profile and inset top-down images showing Tyndall scattering effects of a) acetonitrile and suspensions of b) Cu(ABDC)(DMF) and c) Cu(ABDC-PS)(DMF) following exfoliation in acetonitrile.

S3.3. Post-Exfoliation PXRD

In order to confirm that the supramolecular structure had been maintained post-exfoliation, powder X-ray diffraction patterns were obtained of nanosheet samples after exfoliation. Both patterns were recorded in flat plate mode due to the low mass obtained.
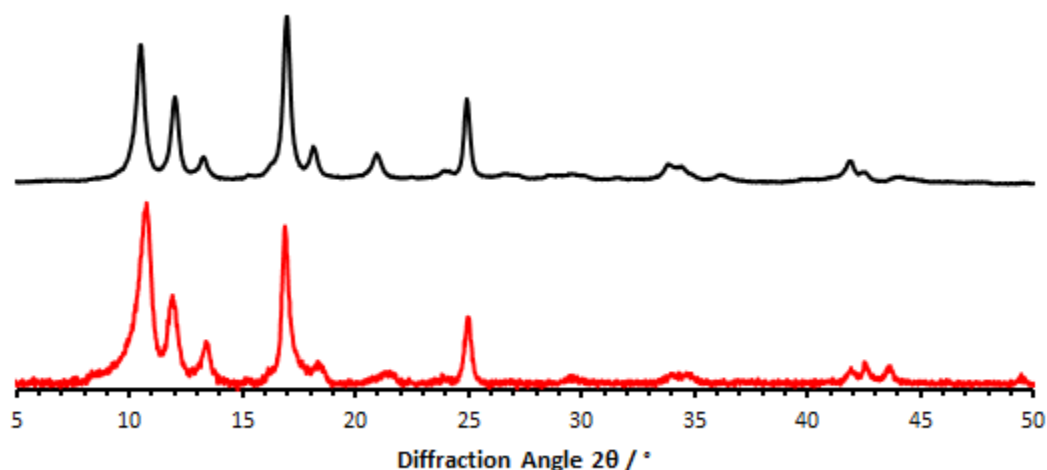
Figure S13. PXRD of Cu(ABDC)(DMF) before (black), after exfoliation (red) in acetonitrile. Sample obtained by centrifugation of nanosheet suspension at 4500 rpm for 3 hours.
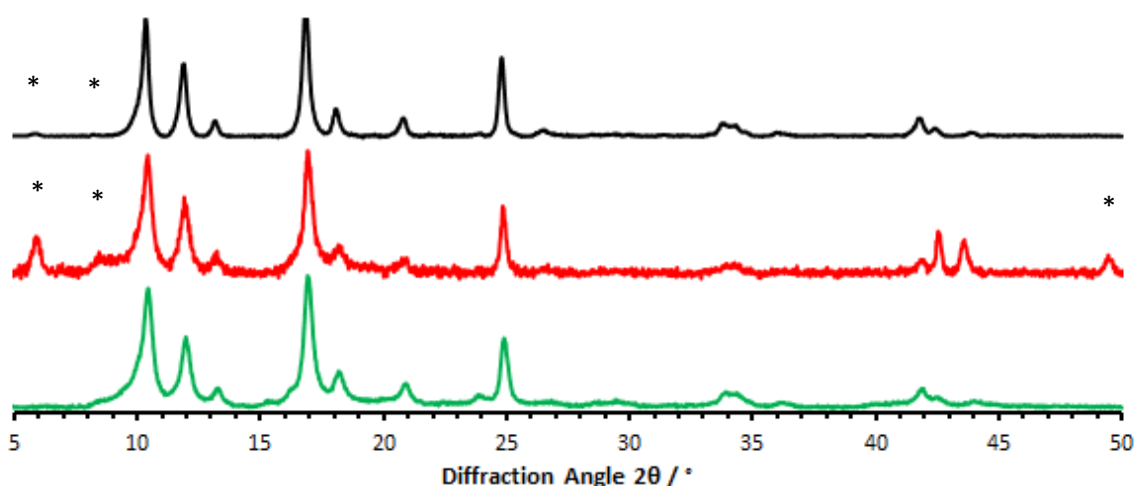
Figure S14. PXRD of Cu(ABDC-PS)(DMF) before (black), after exfoliation (red) in acetonitrile. Sample obtained by centrifugation of nanosheet suspension at 4500 rpm for 3 hours. * Peaks belonging to a minor phase were observed at 6, 8 and 50°, most prominently in the red exfoliated pattern. Trace amounts of this phase are also observed in the unexfoliated and unfunctionalised material. The MONs were redispersed in DMF (6 mL) using a vortex mixer for 30 seconds, and soaked for 18 h, centrifuged at 4500 rpm for 30 min, washed with diethyl ether. The resulting XRPD pattern (green) no-longer shows this minor phase which is attributed to a desolvated phase caused by loss of DMF from the axial sites of the MON as seen in related materials.[6,7] This is consistent with NMR data shown in Figure S23 which shows lower than expected DMF concentrations in the MONs which are restored in the material which has been soaked in DMF.

S3.4. Dynamic Light Scattering
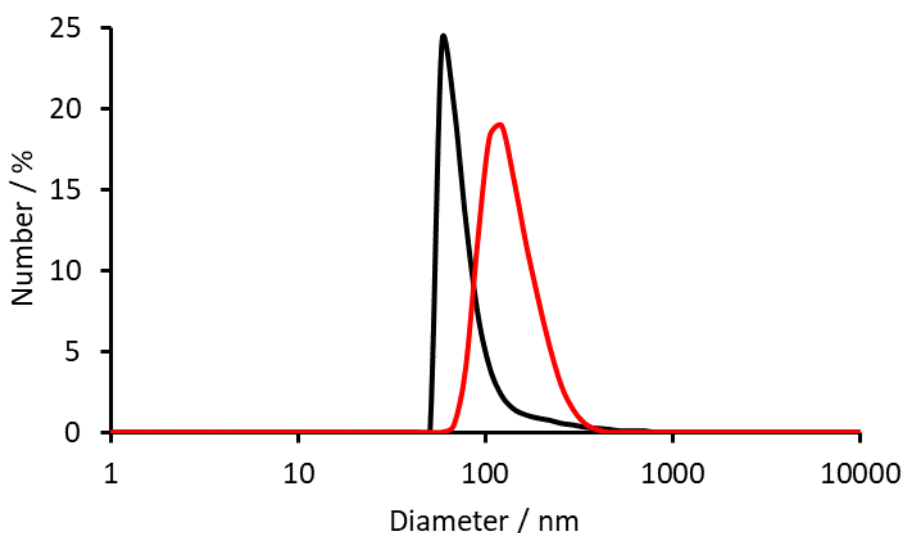
Figure S15. DLS number plot for MON suspensions of Cu(ABDC)(DMF) (black) and Cu(ABDC-PS)(DMF) (red). Suspensions were each diluted by a factor of 10 before analysis.

Table S2. Zeta potential data obtained using the Smoluchowski method.

Sample Name	T (°C)	ZP (mV)	Standard Deviation Frequency (Hz)	Zeta Deviation (mV)	Mobility (μmcm/Vs)	Mobility Deviation (μmcm/Vs)	Derived Count Rate (kcps)
Cu(ABDC) 1	20	-23.0	4.10	17.8	-0.4129	0.3184	1159.8
Cu(ABDC) 2	20	-23.3	3.52	15.3	-0.4175	0.2735	778.5
Cu(ABDC) 3	20	-22.3	3.95	17.1	-0.3991	0.3065	1241.2
Cu(ABDC) 4	20	-22.5	3.88	16.8	-0.4042	0.3018	2015.3
Cu(ABDC) 5	20	-24.0	4.46	19.3	-0.4302	0.3461	1374.4
	Avg	-23.0					
Cu(ABDC-PS) 1	20	-40.9	4.72	20.4	-0.7324	0.3666	1212.9
Cu(ABDC-PS) 2	20	-40.1	4.54	19.7	-0.7192	0.3526	1351.6
Cu(ABDC-PS) 3	20	-40.3	3.22	14.0	-0.723	0.2502	1125.3
Cu(ABDC-PS) 4	20	-40.2	3.85	16.7	-0.7206	0.2994	1041.6
Cu(ABDC-PS) 5	20	-36.7	3.47	15.0	-0.6575	0.2692	1778.1
	Avg	-39.6					

S3.5. UV-Vis Concentration Studies

λ_{max}=256 nm

λ_{max}=352 nm
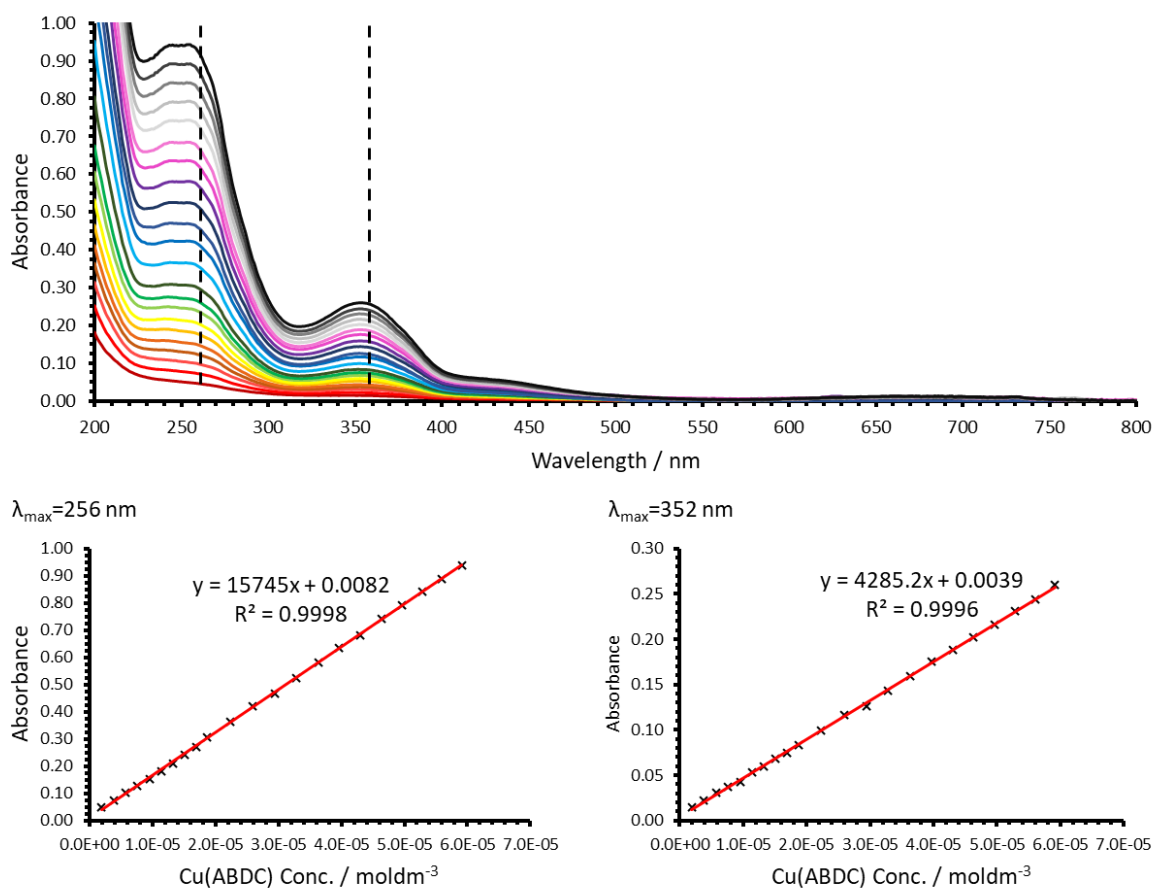
Figure S16. UV-Vis stack plot and extinction coefficient calculation graphs for Cu(ABDC)(DMF) in acetonitrile.
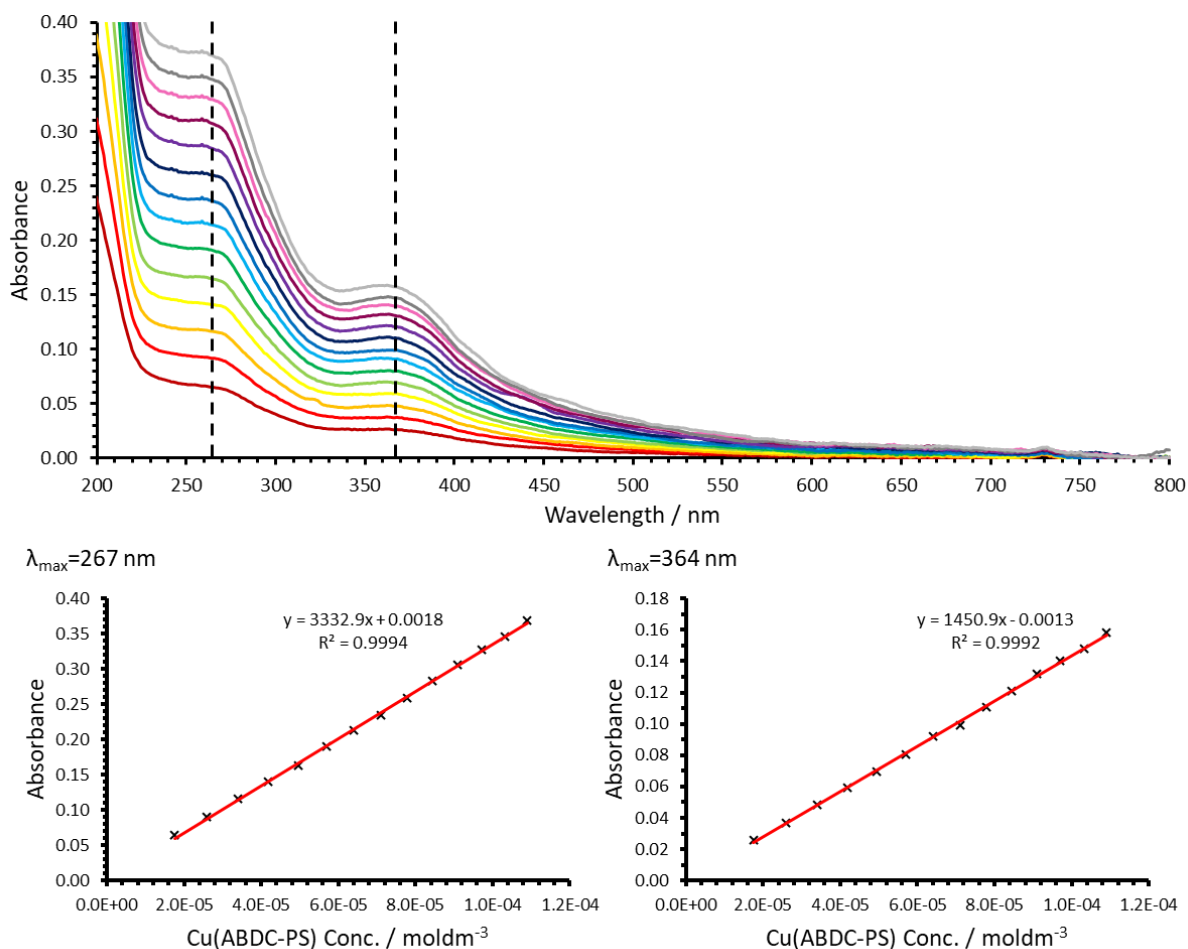
Figure S17. UV-Vis stack plot and extinction coefficient calculation graphs for Cu(ABDC-PS)(DMF) in acetonitrile.
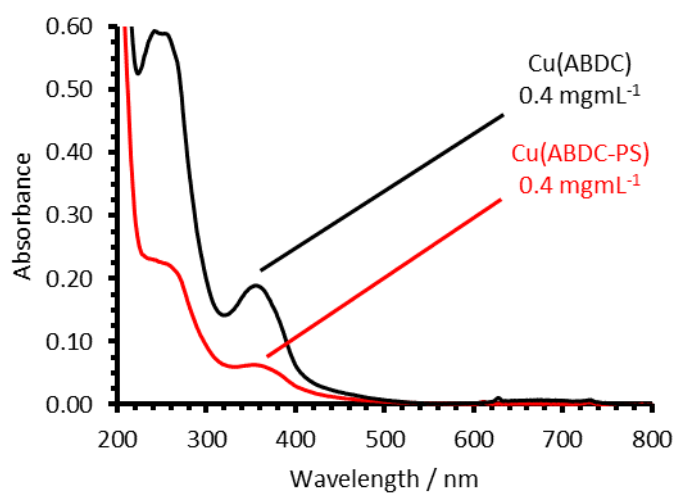
Figure S18. UV-Vis spectra of MON suspensions of Cu(ABDC)(DMF) (black) and Cu(ABDC-PS)(DMF) red, with concentrations highlighted as according the above extinction coefficients.

S3.6. Atomic Force Microscopy

S3.6.1. Exfoliation of Cu(ABDC)(DMF)

Shown in figure S19, nanosheets obtained from ultrasonic exfoliation of Cu(ABDC)(DMF) had a thickness distribution of 25 nm ±19 and a lateral size distribution of 175 nm ±48.
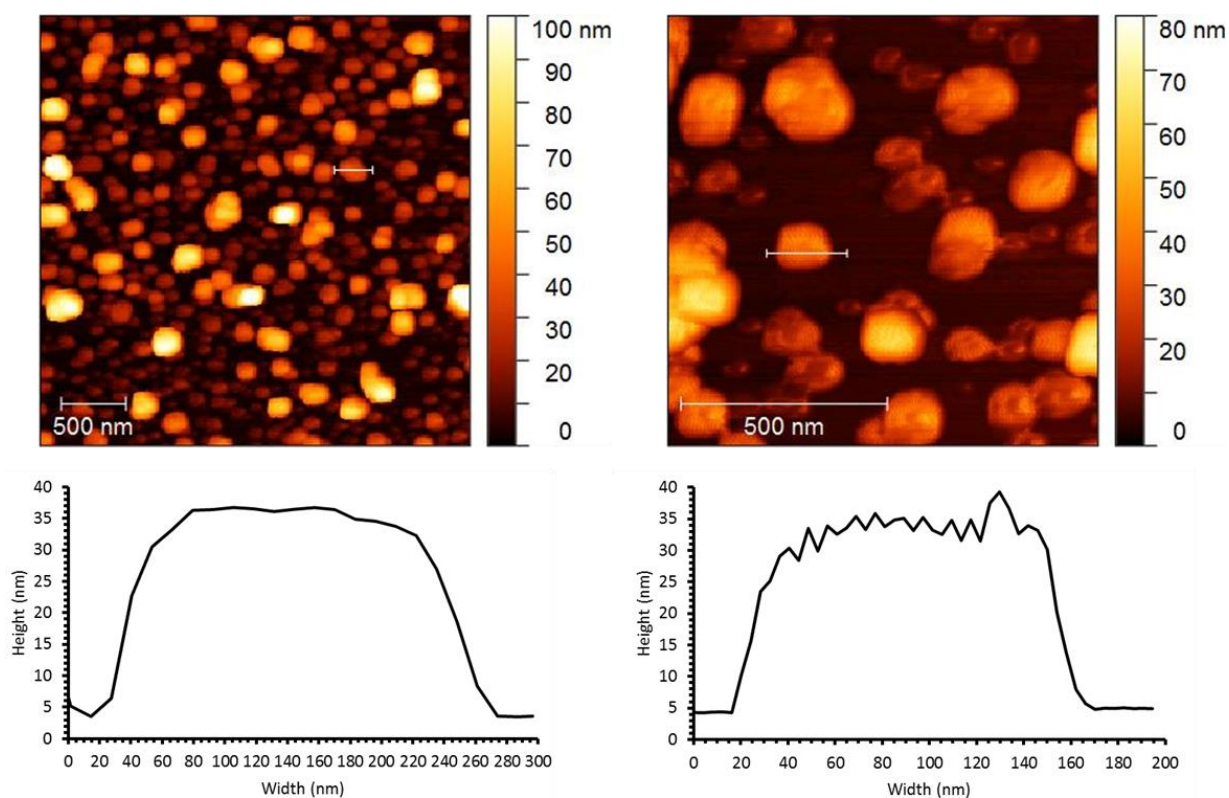
Figure S19. Atomic force microscopy images of exfoliated nanosheets of Cu(ABDC)(DMF) and associated height profiles.
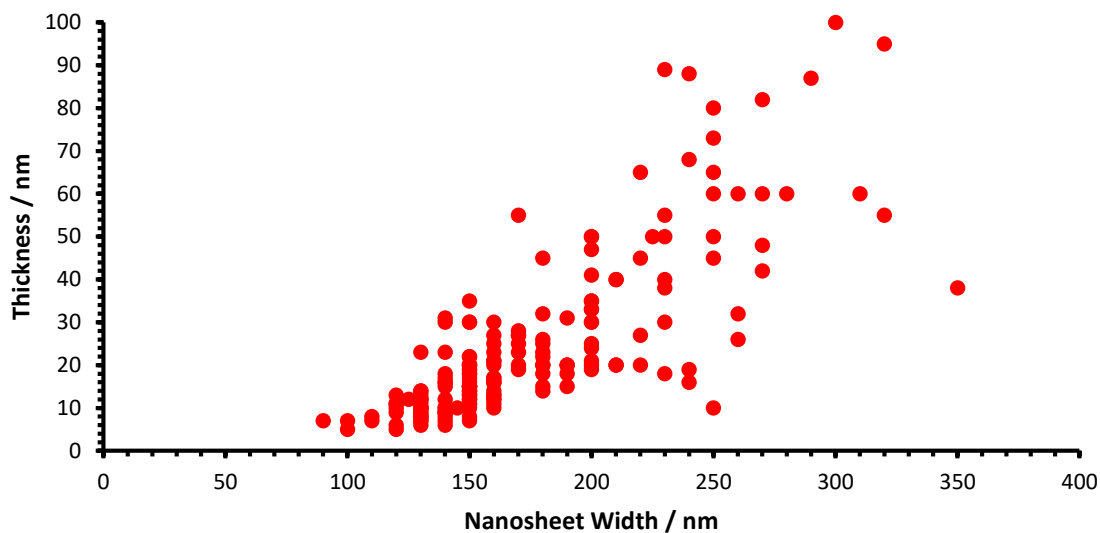
Figure S20. Size distribution scatter graph of Cu(ABDC)(DMF) nanosheets calculated from the above images.

3.6.2. Exfoliation of Cu(ABDC-PS)(DMF)

Nanosheets obtained from ultrasonic exfoliation of Cu(ABDC-PS)(DMF) were all consistently ~1.4 nm in thickness, with some exceptions that appeared to exhibit restacking or adsorption of particulates to the surfaces and some small amounts of unexfoliated material. Lateral sizes ranged typically from 100-400 nm, and nanosheets had irregular morphologies due to fracturing.
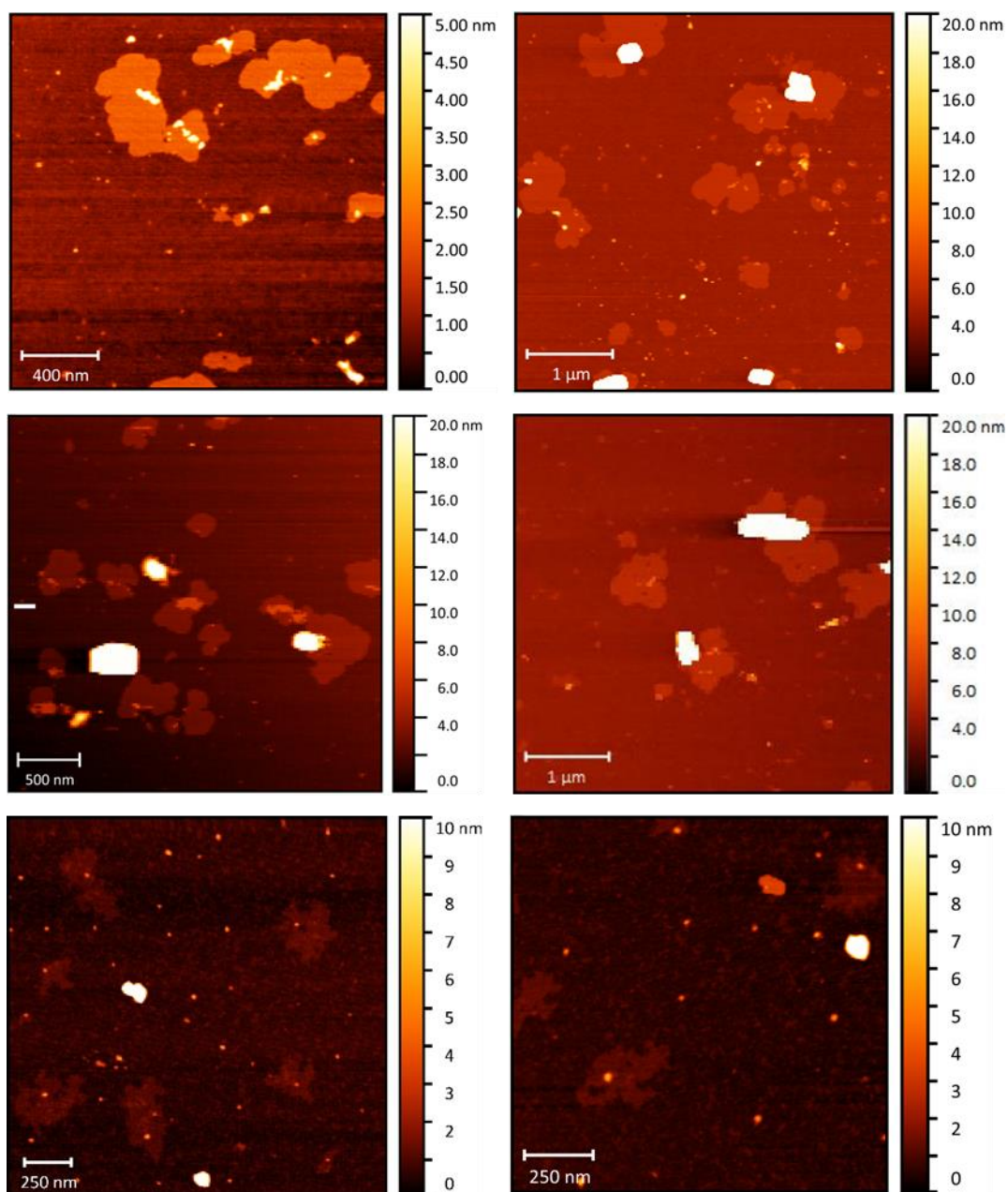
Figure S21. Atomic force microscopy images of exfoliated nanosheets of Cu(ABDC-PS)(DMF).
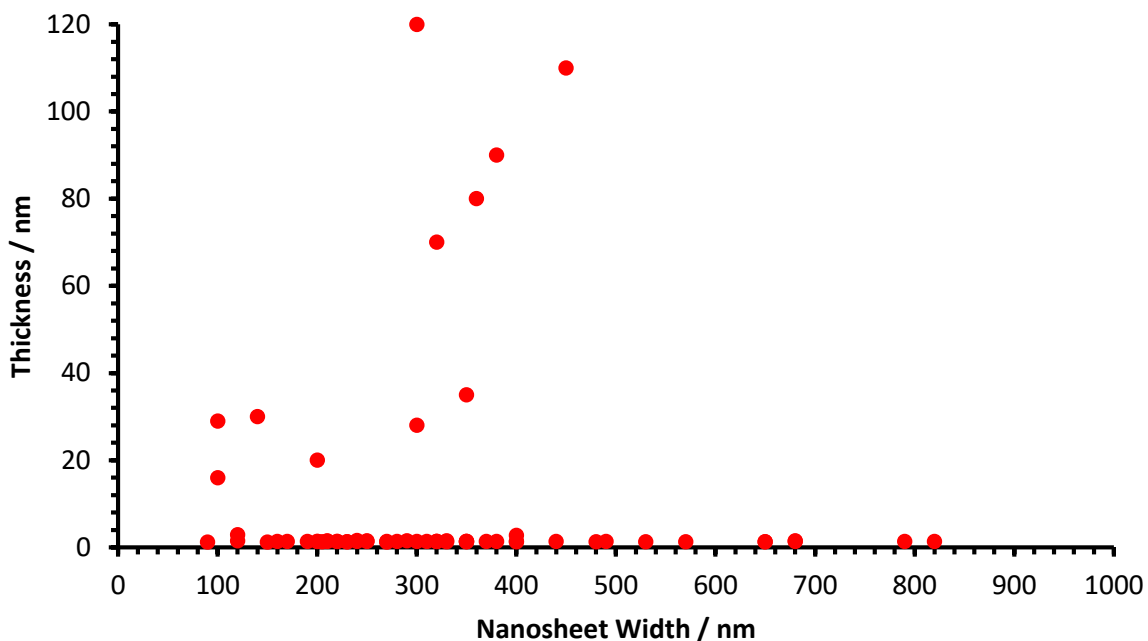
Figure S22. Size distribution scatter graph of Cu(ABDC-PS)(DMF) nanosheets calculated from the above images. The nanosheets consist of predominantly monolayer nanosheets (1.4 nm) alongside occasional poorly exfoliated fragments.

S3.7. Further Analysis of PSF MONs

S3.7.1. FT-IR Spectroscopy
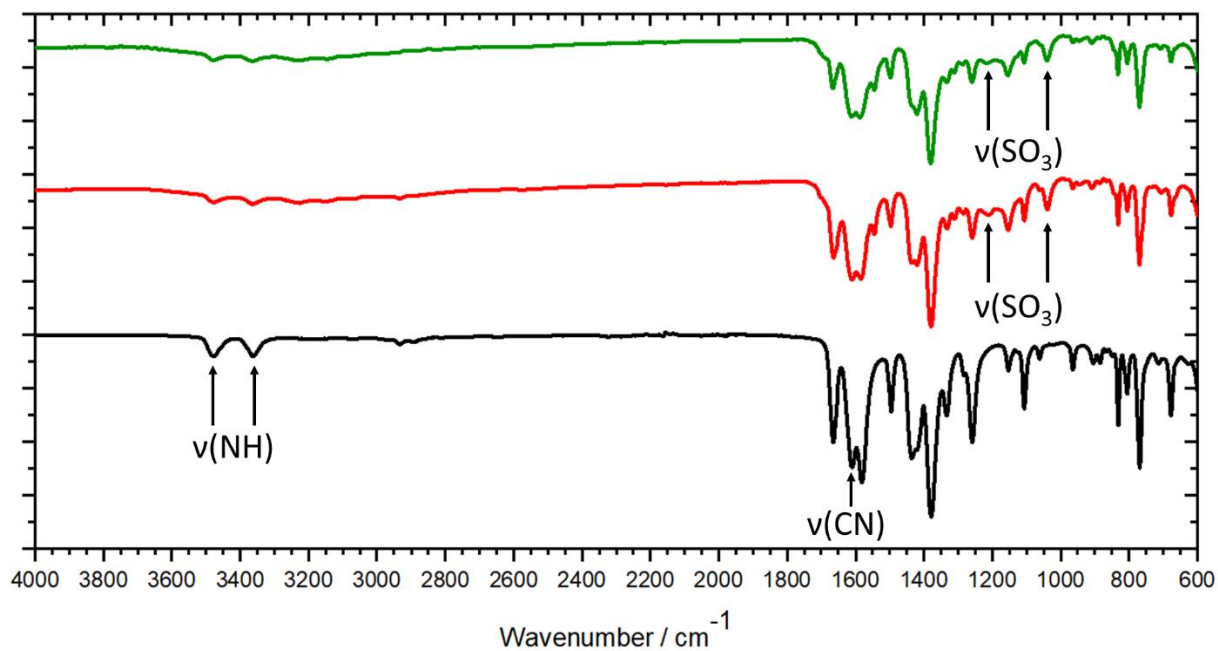
Figure S23. FT-IR spectra of as synthesised Cu(ABDC)(DMF) (black), Cu(ABDC-PS)(DMF) MOF (red) and Cu(ABDC-PS)(DMF) MONs (green), indicating the presence of sulfonic acid stretches in the latter two systems, as according to previous reports.[2–4]

S3.7.2. ¹H NMR Spectroscopy
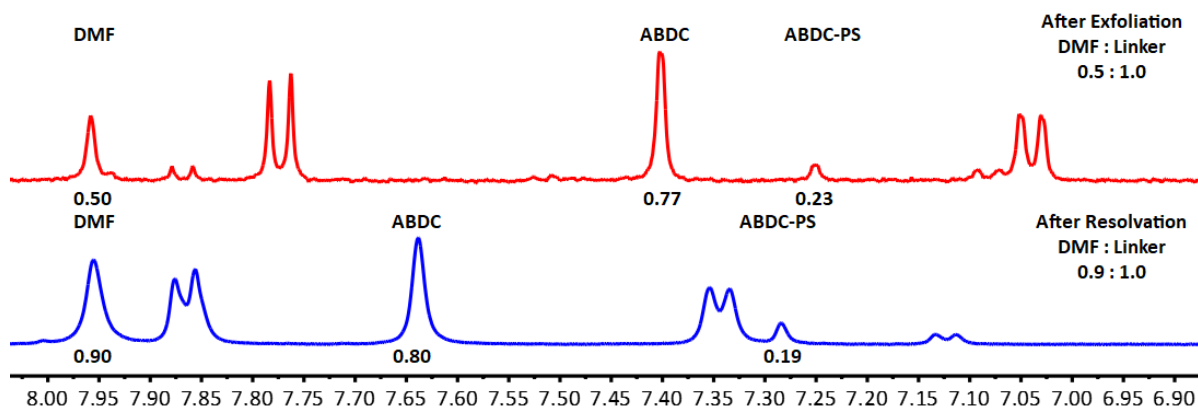
Figure S24. ¹H NMR spectrum of digested Cu(ABDC-PS)(DMF) nanosheets (red), indicating approximately 23% functionalisation. The ratio of DMF to MONs is lower than expected (50%) indicating partial desolvation of the MONs during exfoliation. The ¹H NMR spectrum of the nanosheets after resolvation with DMF (blue) shows almost full resolvation (90 %). Note that chemical shifts are altered due to the differing amounts of DCl present.

S4. Tandem Catalysis Studies

S4.1. Experimental Details

All catalytic experiments were performed using the same following conditions. Benzaldehyde dimethyl acetal (0.15 mmol), malononitrile (0.40 mmol) and water (0.20 mmol) were each dissolved in d_3-acetonitrile (0.6 mL), treated with catalyst and heated to 60 °C for 24 hours in sealed reaction vials.

S4.2. Catalysis Yields

Table S3. Yields of each reactant/product for different catalysts using the reaction conditions in S4.1.

Catalyst	Type	[Cat.] / mol%	Yields		
			1	2	3
-	-	0	78	21	1
Cu(ABDC)	MOF	0.2	70	28	1
Cu(ABDC)	MONs	0.1	56	42	2
Cu(ABDC-PS)	MOF	0.2	62	35	3
Cu(ABDC-PS)	MONs	0.1	0	18	82
Cu(ABDC-PS) (and recycled)	MONs	1.5	0 (0)	14 (21)	86 (79)
Cu(ABDC-PS) post-filtration	MONs	0.1	65	32	3

S4.3. 1H NMR Spectra
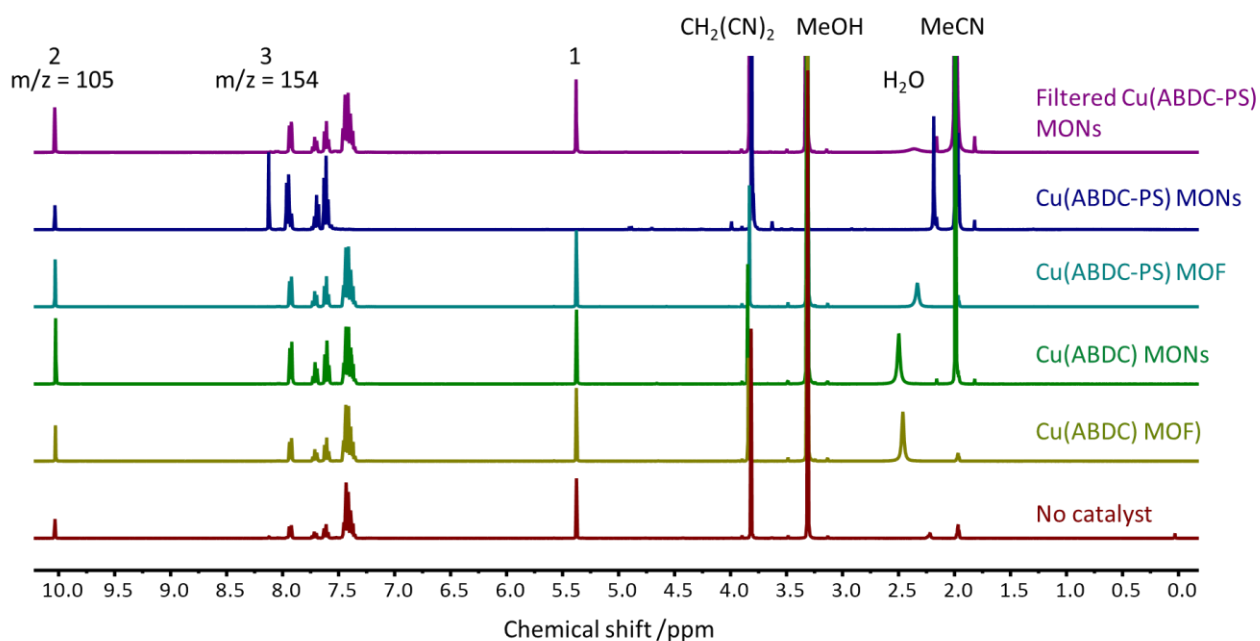
Figure S25. Stacked NMR spectra for each catalytic reaction and control, with characteristic peaks for benzaldehyde dimethyl acetal (1), benzaldehyde (2) and benzylidene malononitrile (3) indicated.
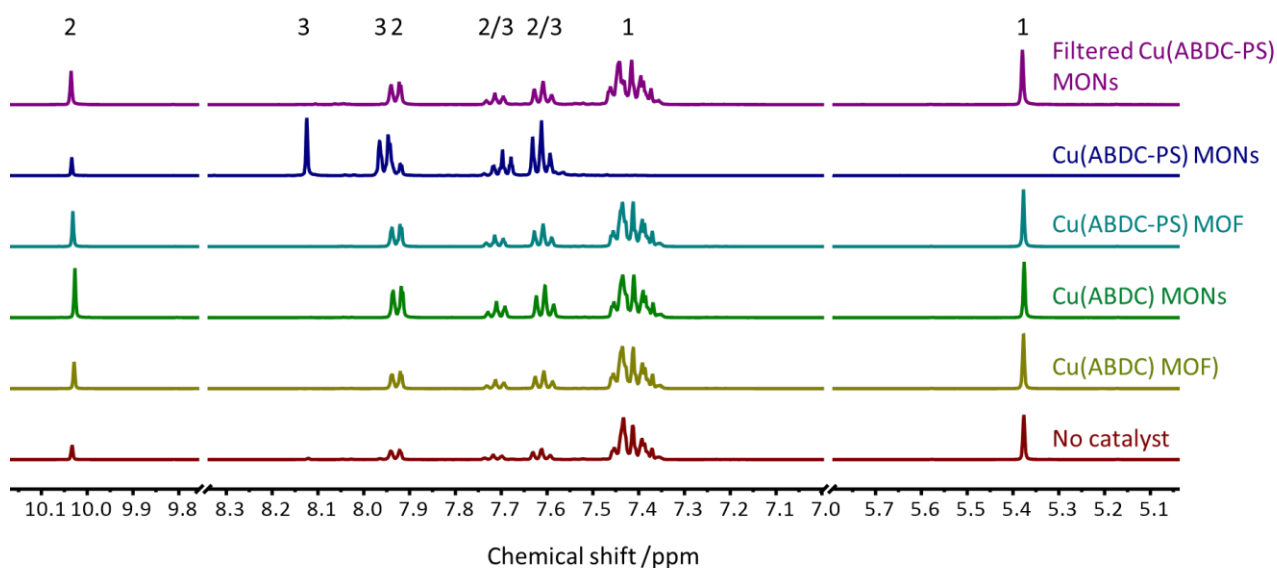
Figure S26. Stacked NMR spectra for each catalytic reaction and control, zoomed in on the region with characteristic peaks for benzaldehyde dimethyl acetal (1), benzaldehyde (2) and benzylidene malononitrile (3).

A suspension of Cu(ABDC-PS)(DMF) nanosheets was filtered through a 0.2 μm Pall® Acrodisc PSF GxF GHP membrane syringe filter three times, leaving a clear solution which exhibited no Tyndall scattering. Without prior dilution, the solution was subject to UV-Vis spectroscopy to determine the concentration of any remaining material (figure S4.4.1). This indicated an approximate concentration of 0.01 mgmL^{-1}. There was also an observed redshift in both peaks, perhaps suggesting that the remaining material is actually dissolved material. This sample was

then added to the reaction mixture as for the other catalyst samples to form the Cu(ABDC)(DMF) post-filtration reference.
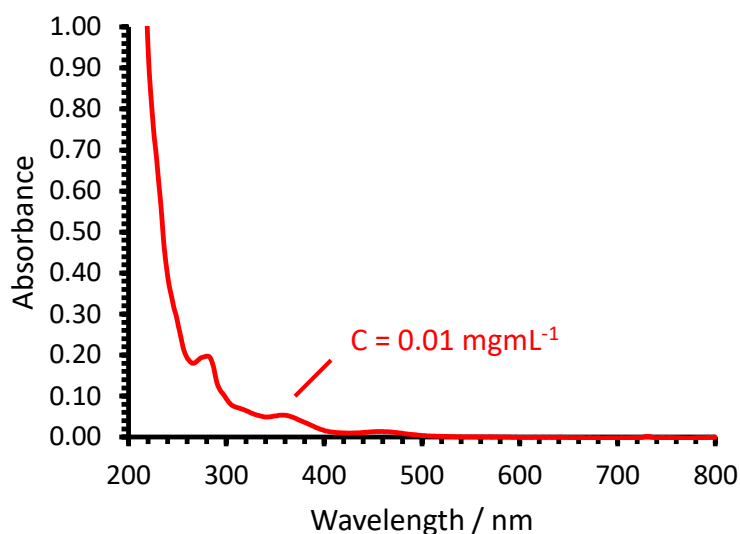
Figure S27. UV-Vis spectrum of the solution obtained from filtration of the Cu(ABDC-PS) nanosheet suspension through a 0.2 µm Pall® Acrodisc PSF GxF GHP membrane syringe filter three times.

S4.4. Recycling Experiments

A catalytic experiment was performed using Cu(ABDC-PS) MONs (1.5 mol%) and otherwise identical conditions to the previous experiments. After 24 hours, the suspension was centrifuged at 4500 rpm to separate the nanosheets, which were washed with acetonitrile and then used again in another catalytic test. The first and second experiments gave 86 and 79 % yields for benzylidene malononitrile respectively, indicating negligible loss of performance upon recycling of the catalyst. NMR spectra are shown in figure S27.
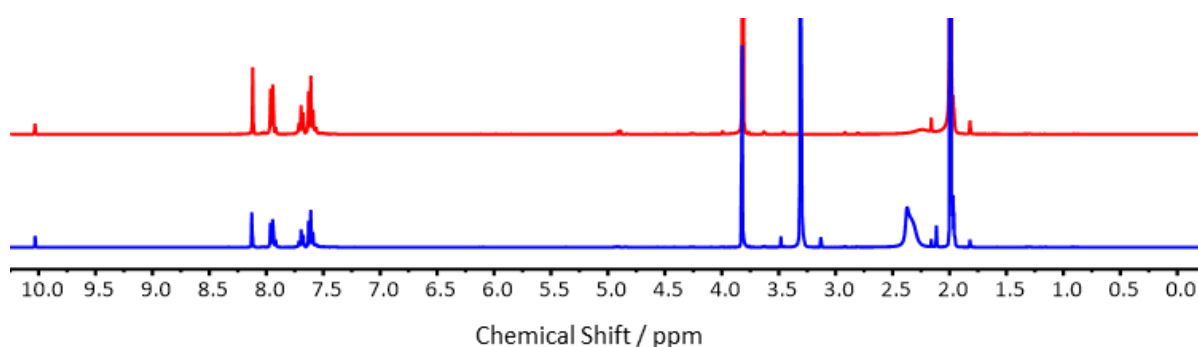
Figure S28. Stacked NMR spectra for mixtures obtained from Cu(ABDC-PS) MONs (1.5 mol%, red), and the same recycled MONs (obtained from centrifugation, blue), under the same conditions, giving 86 and 79 % yields respectively.
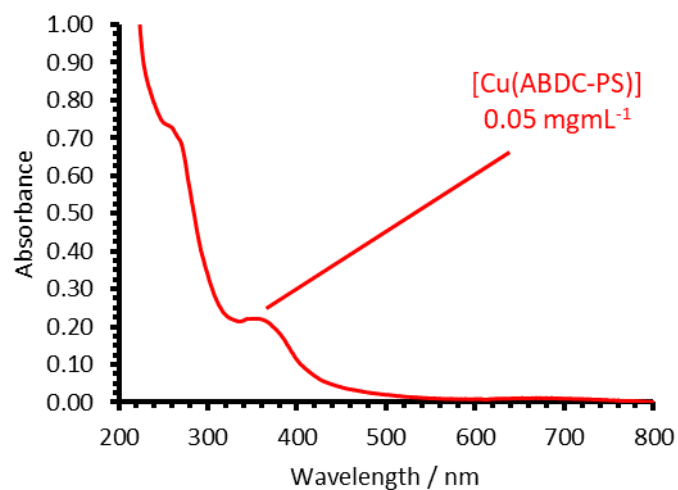
Figure S29. UV-Vis spectrum of material remaining in suspension following centrifugation at 4500 rpm for 3 hours of 1.25 mgmL^{-1} (1.5 mol%) suspension of Cu(ABDC-PS) MONs. The results indicate the majority fo MONs can be recovered by this method with a significantly reduced concentration of 0.05 mg mL^{-1} (no dilution was required).
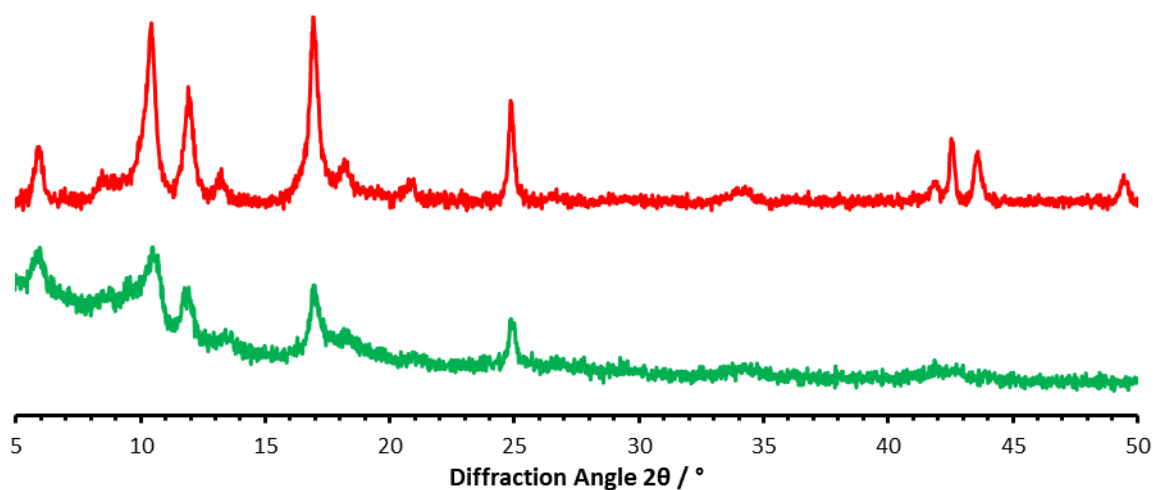
Figure S30. XRPD pattern of Cu(ABDC-PS) MOF (red) and MONs post-catalysis (green), indicating that the structure has been maintained.
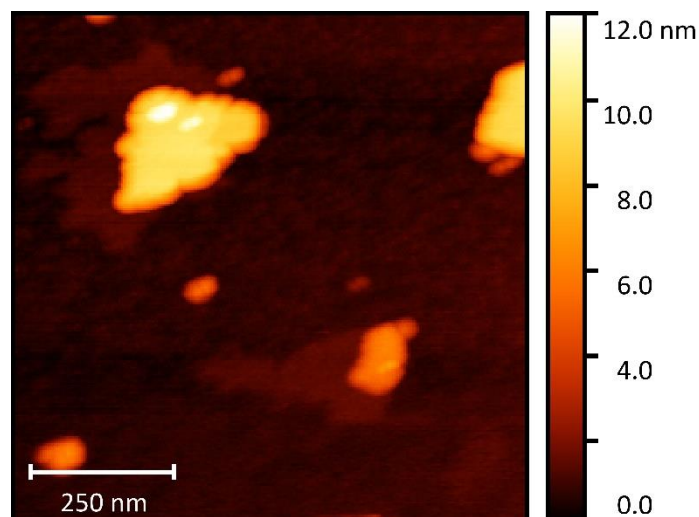
Figure S31. AFM image of Cu(ABDC-PS) MONs post-catalysis.

S5. References

1   M. E. Braun, C. D. Steffek, J. Kim, P. G. Rasmussen and O. M. Yaghi, *Chem. Commun.*, 2001, **2**, 2532–2533.

2   R. S. Andriamitantsoa, J. Wang, W. Dong, H. Gao and G. Wang, *RSC Adv.*, 2016, **6**, 35135–35143.

3   M. Köppen, O. Beyer, S. Wuttke, U. Lüning and N. Stock, *Dalt. Trans.*, 2017, **46**, 8658–8663.

4   H. Liu, F. G. Xi, W. Sun, N. N. Yang and E. Q. Gao, *Inorg. Chem.*, 2016, **55**, 5753–5755.

5   M. Eddaoudi, J. Kim, N. Rosi, D. Vodak, J. Wachter, M. O'Keeffe and O. M. Yaghi, *Science (80)*, 2002, **295**, 469–472.

6   D. J. Ashworth, A. Cooper, M. Trueman, R. W. M. Al-Saedi, S. D. Liam, A. J. Meijer and J. A. Foster, *Chem. - A Eur. J.*, **24**, 68, 17986-17996

7   J. A. Foster, *Chem. Commun.*, 2016, **52**, 10474–10477.

8   J. A. Foster, S. Henke, A. Schneemann, R. A. Fischer and A. K. Cheetham, *Chem. Commun.*, 2016, **52**, 10474–10477.

Chapter 4

Post-Exfoliation Functionalisation of Metal-Organic Framework Nanosheets *via* Click Chemistry
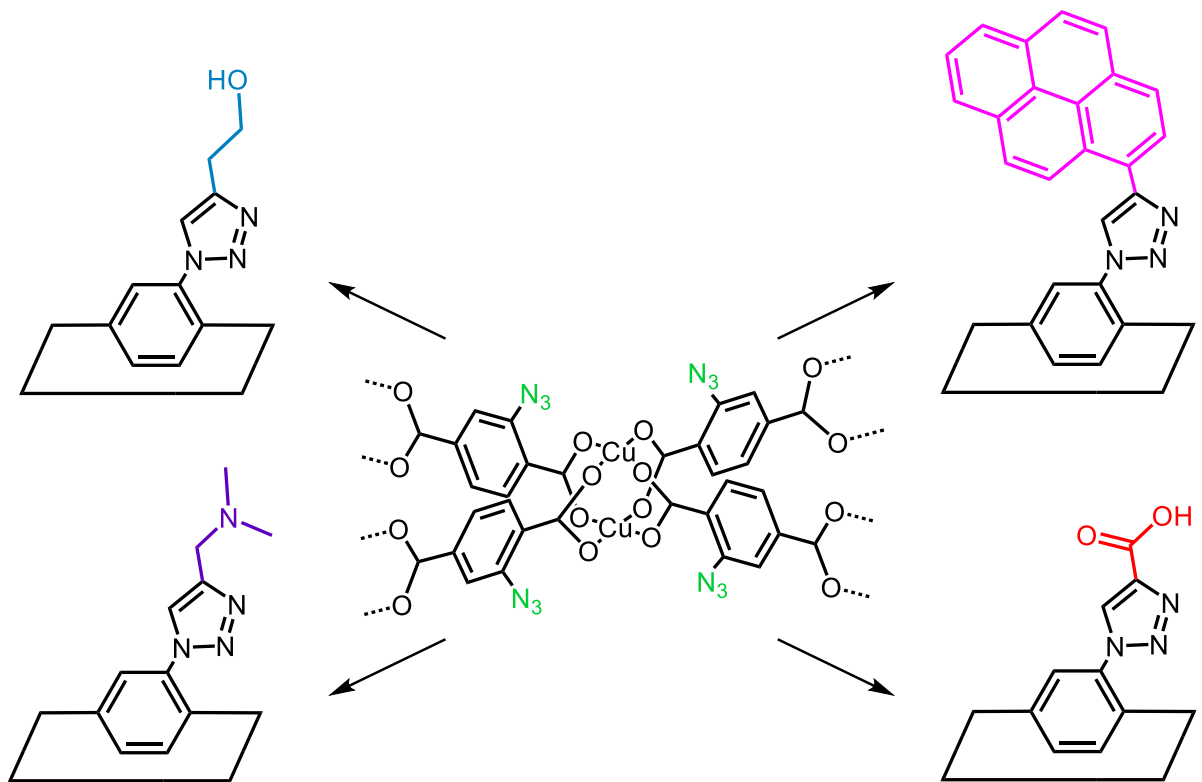
Chapter 4

Post-Exfoliation Functionalisation of Metal-Organic Framework Nanosheets via Click Chemistry

Unpublished paper (full article)

Joshua Nicks and Jonathan A. Foster

Author Contributions

Joshua Nicks	Performed all experiments and collected all data. Drafted manuscript and SI and created all figures. Assisted in editing of manuscript.
Jonathan A. Foster	Supervised JN, assisted in editing of manuscript.

Post-Exfoliation Functionalisation of Metal-Organic Framework Nanosheets via Click Chemistry

Joshua Nicks and Jonathan A. Foster[*]

The liquid exfoliation of layered metal-organic frameworks (MOFs) to form nanosheets (MONs) exposes buried functional groups making them useful in a range of sensing and catalytic applications. Here we show how high yielding click reactions can be used post-exfoliation to systematically modify the surface chemistry of MONs allowing for tuning of their surface properties and their use in new applications. A layered amino-functionalised framework is converted through conventional post-synthetic functionalisation of the bulk MOF to form azide functionalised frameworks of up to >99% yield. Ultrasonic liquid exfoliation is then used to form few-layer nanosheets, which are further functionalised through post exfoliation functionalisation using Cu(I)-catalysed azide-alkyne cycloaddition reactions. Here we demonstrate the advantages of post-exfoliation functionalisation (PEF) in enabling: (1) a range of functional groups to be incorporated in high yields (2) tuning of nanosheets surface properties without the need for extensive recharacterisation (3) the addition of fluorescent functional groups to enable their use in the sensing of hazardous nitrobenzene. We anticipate that the versatility of different functional groups that can be introduced through high yielding click reactions will lead to advances in the use of MONs and other 2D materials for a variety of applications.

Introduction

The liquid exfoliation of layered materials to form two-dimensional nanosheets results in dramatically increased surface area and so greater accessibility of functional groups compared to the bulk material.[1] This approach requires materials with strong intra-layer interactions but weak inter-layer interactions, creating free-standing single and few-layer nanosheets with high aspect ratios. This technique has been extensively applied to classically structured two-dimensional materials such as graphene,[2] hexagonal boron nitride,[3] and transition metal dichalcogenides.[4] However, the surfaces of most of these simple inorganic nanosheets can be difficult to modify without impacting the unique properties that arise from their reduced dimensionality. For example, covalent modification of graphene changes the hybridisation of the carbon atoms from sp[2] to sp[3], disrupting the planarity to the detriment of these properties.[5] For 2D materials incorporating metals, modifications are commonly performed by doping, a harsh process which typically creates defects in the nanosheets, again impacting these desired properties.[6] Though non-covalent functionalisation circumvents these issues, these methods often resultant in relatively weak composite materials.[7] A potential solution to these issues is the use of modular 2D materials formed from molecular building blocks such as covalent-organic (CONs),[8,9] hydrogen-bonded organic

(HONs),[10] and most prolifically metal-organic nanosheets (MONs).[11,12] These materials have a modular structure which allows different functional groups to be introduced easily without changing the underlying structure. Their crystalline nature also mean functional groups are presented on the surface in a well-defined, periodic way in contrast to the functional groups of most 2D materials.[13–15] This tunability and predictability makes MONs ideal for a diverse range of sensing, catalysis, electronic and separation applications.[16] However, the scope of these pre-synthetic approaches to modification are limited in terms of the size and functionality of groups that can be introduced, as they must not impede or interfere with the formation of the supramolecular structure.[17]

Covalent post-synthetic functionalisation (PSF) is a widely used approach for introducing new functional groups incompatible with synthesis conditions to metal-organic frameworks (MOFs).[17,18] PSF of MOFs is inherently limited by the pore size, with large functional groups not able to diffuse through small pore sites and reacted groups blocking further functionalisation. This is not a problem for MONs, as reactive groups are instead presented on the surface, potentially allowing for a much more diverse range of functionalisation options. Beyond our own work, to our knowledge there is only one other example of the covalent PSF of a MON system which is by Lin *et al.* in which amino-benzenetribenzoate ligands in a Zr_6-based MON are functionalised with two thiocyanate-tagged dyes to enable ratiometric sensing of glutathione and pH. Other forms of PSF such as coordinative modification of SBU's or post-synthetic metalation have also been exploited in these UiO-type MONs. In particular, elegant work by Lan and Lin *et al.* shows how capping groups of Hf_{12} clusters can be exchanged with

Department of Chemistry, University of Sheffield, Sheffield, UK.
E-mail: jona.foster@sheffield.ac.uk
† Electronic Supplementary Information (ESI) available: Full experimental details, synthetic procedures and exfoliation studies.

triflate groups for tandem Lewis acidic and photoredox catalysis,[19] and catalytically active metal ions can be added to co-ordinating ligand sites in order to facilitate multistep catalytic and photocatalytic reactions.[20,21]

In our previous work we have used liquid exfoliation to obtain a wide range of paddlewheel-based (PW) MOFs which we have used in sensing and solar cell applications.[22–24] We recently demonstrated that reaction of 1,3-propansultone with a layered amino-functionalised Cu-PW MOF can simultaneously aid exfoliation into thinner nanosheets and introduce new functionalities for catalysis. PSF occurred on the bulk MOF and the degree of functionalisation was limited to 25% by the small pore size of the MOF.[25] In this case, we took advantage of the mixed functionalities on the surface to facilitate a two-step, one-pot tandem reaction. However, coverage and the size of functional groups that can be introduced using this approach is inherently limited by pore size which is detrimental to many applications. This motivated us to develop versatile and high yielding chemistry that would enable us to offer a toolkit to systematically functionalise the surface of the MONs with a diverse range of groups and higher coverage.

In this work, we use click chemistry to modify the surface of MONs post-exfoliation in order to tune their surface properties and impart new functionality. Specifically, we employ Cu(I) catalysed azide-alkyne cycloaddition click chemistry, chosen due to the regioselectivity, versatility, high yield of the reaction under mild conditions, and the lack of side products, such as acids or water, that could impair the coordination bonds of the framework.[26] We show that the surface functionalities and properties of these materials can be programmed using this technique for target applications, by creating photo-functional nanosheets capable of sensing nitrobenzene by a fluorescence quenching mechanism.

Results and Discussion

Synthesis of Cu(N₃-BDC)(DMF) MOF *via* PSF

A layered amino- MOF, Cu(NH₂-BDC)(DMF), was prepared according to our previously published solvothermal method.[27] Cu(NH₂-BDC)(DMF) was then post-synthetically functionalised by treatment with *t*-butyl nitrite (t-BuONO) and up to 10.5 equivalents of azido-trimethylsilane (TMS-N₃) in THF to obtain Cu(N₃-BDC)(DMF) shown in Figure 1a. This is a common route to azide-functionalised coordination polymers, which utilises more mild conditions than typical diazonium salt conversions.[28–30]

^{1}H NMR spectroscopy of the digested MOF samples confirmed the conversion of the amino- into the azido- terephthalate linker. These spectra are comparable to those in other reports where this method has been used and of the as synthesised linker (Figure S1). FT-IR spectroscopy and mass spectrometry further confirmed PSF had occurred. A comparison between the FT-IR spectra of the amino- and azido- MOFs clearly showed the formation of the asymmetric ν(N=N=N) stretch at 2100 cm^{-1} and the loss of the two ν(N-H) stretching bands in the 3500-3350 cm^{-1} region (Figure S6). Mass spectrometry of the digested azido- MOF also indicates the presence of the functionalised linker, [M]$^{-}$ = 206.0, as well as its distinctive fragmentation pattern, shown in Figure S7. Furthermore, the degree of functionalisation could be controlled in a linear fashion by varying the number of equivalents of TMS-N₃ added, as shown in Figures 1b-d.
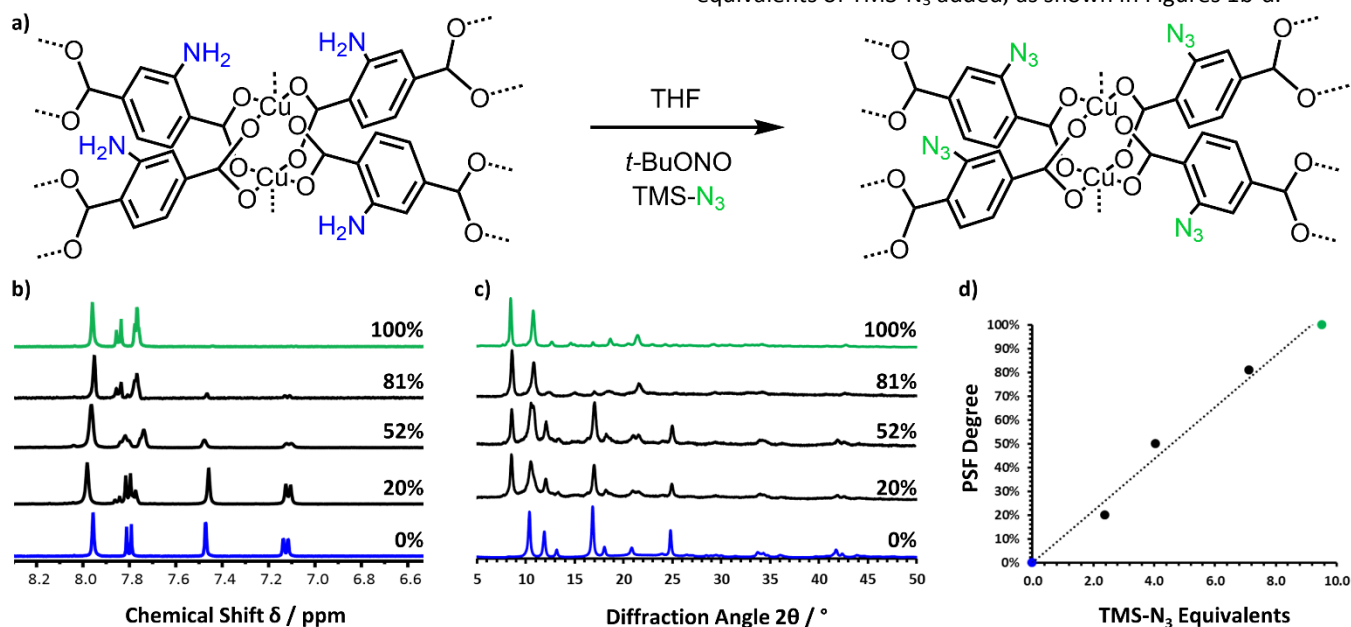
Figure 1. a) Scheme showing the post-synthetic functionalisation of the amino- functionalised layered MOF, Cu(NH₂-BDC)(DMF), into the azido- functionalised MOF, Cu(N₃-BDC)(DMF). **b)** Plot showing the tunable degree of conversion from the amino- MOF to the azido- MOF by altering the equivalents of TMS-N₃ used. **c)** Stack plot of ^{1}H NMR spectra showing the increasing degree of PSF with increasing equivalents of TMS-N₃ added, with Cu(NH₂-BDC)(DMF) shown in blue, mixed ligand MOFs in black and Cu(N₃-BDC)(DMF) in green. **d)** Stack plot of XRD patterns showing the phase change between the fully amino- functionalised MOF (blue) and the fully azido- functionalised MOF (green). Higher zoom figures are shown in Figures S3-5.

X-ray powder diffraction studies (Figure 1c) of the 100% converted sample show a new pattern. This is to be expected, as the parent amino- framework consists of densely packed layers, and it clear that full conversion to azides cannot proceed without a change in unit cell parameters. Pawley refinement of the 100% functionalised pattern confirmed changes in the unit cell volume (Figure S8 and Table S2). Remnants of the amino phase are seen in patterns with 20-52% functionalisation but the dominance of the azido-pattern indicates that functionalisation, and thus expansion, is taking place relatively uniformly throughout the sample. Interestingly, our previous studies functionalising Cu(NH$_2$-BDC) with 1,3-propansultone resulted in no change in unit-cell dimensions however the degree of functionalisation was limited to 25%. We attributed this to the functional group occupying pore space but in this case 100% functionalisation was achieved with a corresponding increase in unit cell parameters.

SEM images of both the amino- and azido- MOFs provided confirmation that there were no significant changes in crystallite size or morphology observed following conversion (Figure S9), with both samples forming aggregates <1–15 μm in size.

Attempts to incorporate the azide linker pre-synthetically were unsuccessful. Under identical solvothermal conditions to the Cu(NH$_2$-BDC)(DMF) synthesis, which is performed at 100 °C, a black solid was obtained, which we attribute to thermal decomposition of the azide moiety. When performed at room temperature, a similarly black amorphous solids was formed. Not only does this post-synthetic route give access to the azido-functionalised MOF, it also grants the ability to control the amine-azide ratio on the MOF surfaces, allowing for unique control over the surface functionalities of the resulting nanosheets obtained from exfoliation. As this study focuses on post-exfoliation functionalisation *via* click chemistry, all further experiments were performed using ≥ 99% azido- functionalised samples.

Exfoliation of Cu(N$_3$-BDC)(DMF) into MONs

Exfoliation of the layered azido- MOF was performed using a previously reported setup (shown in Figure S10) designed to regulate temperature and minimise hot-spots.[31] Cu(N$_3$-BDC)(DMF) was suspended in acetonitrile, and sonicated at 80 kHz for 12 hours, followed by centrifugation for 1 hour at 362 xG (1500 rpm) to remove unexfoliated material and larger fragments.

Suspensions of both the amino- and azido- MON systems exhibit strong Tyndall scattering indicating the presence of nanomaterial in colloidal suspension (Figure 2e). AFM imaging shows azido- analogue exfoliates into thinner nanosheets than those of the amino- MOF (Figures 2a and b, and S11). Size distribution analysis gives an average thickness of 25 ±19 nm for the amino- nanosheets, and a significantly thinner 8 ±7 nm
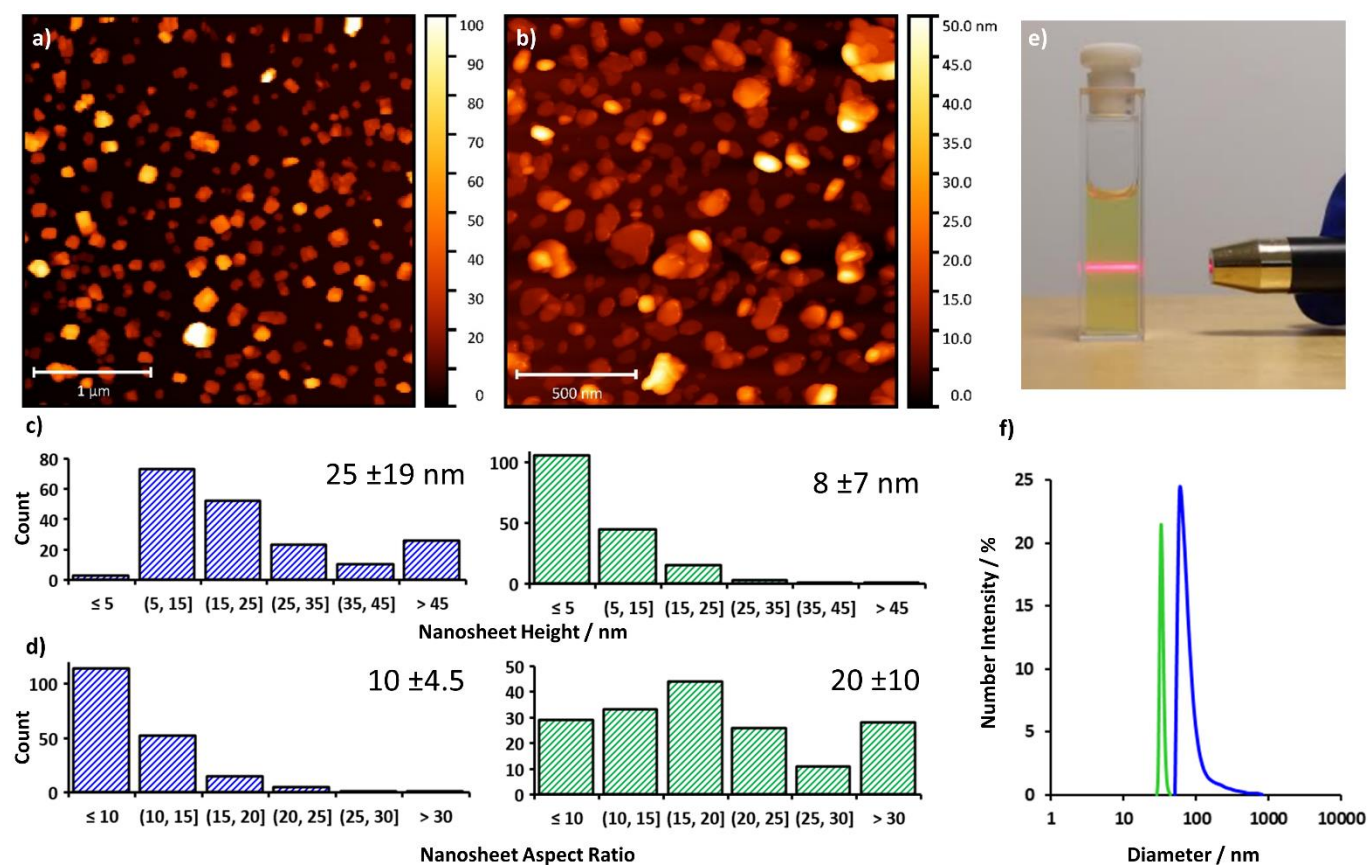
Figure 2. AFM topographical images of **a)** Cu(NH$_2$-BDC) and **b)** Cu(N$_3$-BDC) nanosheets exfoliated in acetonitrile. **c)** Nanosheet thickness histograms for Cu(NH$_2$-BDC) (blue) and Cu(N$_3$-BDC)(DMF) nanosheets (green), with inset values for average thickness and standard deviation. **d)** Nanosheet aspect ratio histograms for Cu(NH$_2$-BDC) (blue) and Cu(N$_3$-BDC) nanosheets (green), with inset values for average aspect ratio and standard deviation. **e)** Tyndall scattering images of Cu(N$_3$-BDC) nanosheets. **f)** Particle size distribution data obtained from DLS for Cu(NH$_2$-BDC) nanosheets (blue) and Cu(N$_3$-BDC) nanosheets (green).

thickness for the azido- MONs (Figures 2c and d, S12 and S13). Analysis of the aspect ratios (the ratio between a nanosheets thickness and its largest lateral dimension) also suggests that the azido MONs are much more "sheet"-like, with an average aspect ratio of 20 ±10, significantly higher than the 10 ±4.5 value observed for the unfunctionalised sheets. It is also noteworthy that the azido nanosheets are significantly less angular, something we have observed previously with few-layer nanosheets, suggesting that a reduction in thickness can also lead to increased fragmentation during exfoliation.[10,27] The size distribution analysis also indicates a reduction in the lateral size of the nanosheets obtained upon azidification, with the amino-MONs demonstrating an average largest lateral size of 175 ±48 nm, with 100 ±33 nm for the azido MONs. This trend is further supported by dynamic light scattering particle sizing, which indicates a smaller average size for the azido- MONs, with a narrower size distribution, shown in Figure S14. It should be noted that the average lateral sizes given by DLS are smaller than those obtained from AFM analysis, consistent with previous reports that implicate the assumption of spherical particles reduces the obtained sizes.[32]

Nanosheets suspensions had strong colloidal stability, with no aggregation-induced precipitation observed after two weeks. The concentrations of the nanosheet suspensions were determined by absorption spectroscopy, which indicated concentrations of 0.4 and 0.5 mg mL^{-1} for the amino- and azido-nanosheets respectively (Figures S15-17), which is further corroborated by mass yields of the dried suspensions (~2.3 mg and 2.9 mg respectively). Zeta potential measurements of the two suspensions indicated values of -23.0 and -35.8 mV for Cu(NH$_2$-BDC) and Cu(N$_3$-BDC) nanosheets respectively, indicating stronger colloidal stability and more favourable nanosheet-solvent interactions for the Cu(N$_3$-BDC) MON suspension. These results suggest that expansion of the inter-layer distance as a result of PSF has aided the exfoliation of the layered system into thinner nanosheets, alongside enhanced

nanosheet-solvent interactions associated with the azide moiety.

In order to confirm the phase purity of the material had been maintained post-exfoliation, XRD analysis of the nanosheets was performed after removal of the solvent by evaporation. Peaks in the diffraction pattern of the MONs are observed to be much broader and some reflections are absent (Figure S18). This is attributed to the reduction in long-range order associated with exfoliation of the layered framework. ^{1}H NMR spectroscopy of the digest nanosheets (Figure S19) indicates a loss of the coordinated DMF solvent, which is consistent with our previous results for PW-based MOFs exfoliated in acetonitrile.[27,33]

The data obtained suggest that a combination of increased surface charge and an expansion in inter-layer distance is aiding the exfoliation of the azido- MOF into significantly thinner nanosheets. These nanosheets are ideal candidates for exploring post-exfoliation functionalisation, as the majority of their azide groups are exposed and should, therefore, be easily accessed for functionalisation.

Post-Exfoliation Functionalisation of MONs *via* Click Chemistry

In order to demonstrate the versatility of our click chemistry approach, four different functional groups were introduced using a generalised method: a carboxylic acid, a tertiary amine, an alcohol, and a fluorescent pyrene group. These groups possess a variety of different chemistries, but are also difficult to introduce pre-synthetically, due to both their size and their likelihood to interfere with the formation of the secondary building unit. Cu(N$_3$-BDC) nanosheets suspended in acetonitrile, were treated with a Cu(I) catalyst, Cu(CH$_3$CN)$_4$PF$_6$, and an alkyne-tagged functional group, then stirred at 60 °C for 24 hours. Extensive washings were carried out with THF and diethyl ether to remove excess catalyst and reagent.

Degrees of conversion of ≥80% were obtained for the carboxylic acid (91%), tertiary amine (82%), and alcohol groups
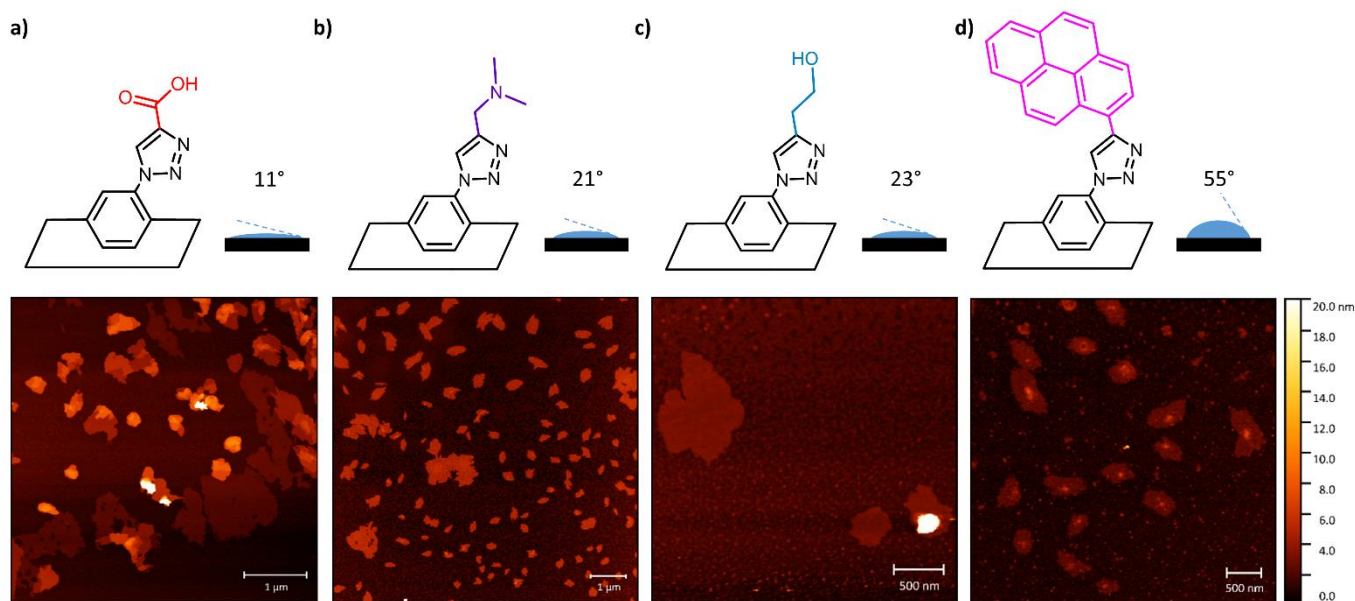
Figure 3. Structural representations, contact angles with water, and AFM topographical images of the obtained **a)** Cu(BDC-trz-CO$_2$H), **b)** Cu(BDC-trz-NMe$_2$), **c)** Cu(BDC-trz-OH), and **d)** Cu(BDC-trz-pyr) nanosheets.

(91%), and ~50% for the pyrene group, as determined by ^{1}H NMR spectroscopy of the digested nanosheets (Figures S20-23). The reduced degree of functionalisation using the pyrene group is attributed to the significant steric bulk and cone angle of the pyrene moiety inhibiting reactions at adjacent azide sites. FT-IR spectroscopy further confirms the extent of functionalisation, with a significant reduction in the intensity of the asymmetric (N=N=N) stretch at 2100 cm^{-1} observed for each system, shown in Figure S21. Furthermore, the emergence of broad peaks centred around 1050 and 730 cm^{-1} are consistent with previous reports, and are assigned to the introduced triazole group.[28,34–36]

Powder X-ray diffractometry studies show significant peak broadening and reductions in peak intensity for the clicked nanosheets compared to the bulk framework (Figure S25). This is an expected consequence of the nanoscopic dimensions of the nanosheets and their lack of three-dimensional extended crystallinity and has been observed by many other authors investigating such nanomaterials.[37–40] However, the peaks that can be identified still align with those of the as-synthesised layered framework or azido- nanosheets, particularly the most intense peak at ~8.6°, indicating that the coordination structure was maintained.

The functionalised nanosheets resuspended well into acetonitrile with an additional 30 seconds of sonication and these suspensions exhibit strong Tyndall scattering (Figure S26). AFM imaging of these suspensions confirmed that the nanosheet morphology was maintained post-functionalisation. As shown in Figure 3 (further imaging in S27-30), the functionalised nanosheets maintain their few-layer thickness across each system. Thicknesses range between 1.8 – 8 nm, with a much narrower distribution than observed for the Cu(N$_3$-BDC)(DMF) nanosheets (Figures S31-34), indicating that the click reaction may have further exfoliated the material. Furthermore, there appears to be no decrease in the lateral size. of the nanosheets, attributed to the mild nature of the functionalisation method.

The change in surface properties upon functionalisation was investigated using contact angle goniometry. Equal amounts of each nanosheet system were drop-cast onto identical hot mica plates to form a film, after which the contact angle with a drop of water was investigated. As represented in Figure 3, there is a clear correlation between the contact angle of the droplet and the hydrophilicity/hydrophobicity or polarity of the group introduced during functionalisation, with the acid functionalised nanosheets resulting in an almost completely flat droplet, and the pyrene functionalised nanosheets resulting in a significantly more spherical droplet.

This procedure of post-exfoliation functionalisation offers several advantages for the patterning of MON surfaces. The versatility of click chemistry means that a range of reactive functional groups (such as acids and amines) can be introduced, and at different ratios. The method uses mild conditions and reagents, meaning this could be extended to other MON systems which have pendant amino functionalities, such as those reported by Liu et al.[41] and Zhao et al.[14] Furthermore, the lack of pore size constraints in the context of using nanosheets means larger groups, such as polyaromatics or polymers, can be more easily introduced than is often the case for 3D MOFs or unexfoliated layered MOFs.

Sensing Experiments

The click-functionalisation of the azido- nanosheets with 1-ethynylpyrene afforded a fluorescent system with high surface area. As pyrene-based MOFs have been frequently targeted for use as sensors,[42] we sought to utilise these electron rich nanosheets for use as sensors in the detection of electron deficient nitrobenzene.

The unfunctionalized azido- nanosheets exhibit absorption maxima at 261 and 332 nm, though neither of these produce an emission upon excitation, thus the unfunctionalized nanosheets are non-fluorescent. Upon ~50% functionalisation with 1-ethynylpyrene, three new absorption maxima appear, at 244, 280 and 351 nm, corresponding to the introduced pyrene group (Figure S35). This fluorescence can be observed by the naked eye by application of a UV lamp to the sample (Figure 4 inset, Figure S36). Each of these maxima produce a broad emission spectrum with maxima at 389 and 410 nm. Excitation at 351 nm produces the most intense emission and was thus used for sensing experiments. No excimer formation was observed, which we attribute to the organised and periodic spatial separation of the pyrene groups on the surface of the nanosheets, which prevent the groups from approaching within ~10 Å to form the complex.

Fluorescence quenching titrations were carried by incremental addition of nitrobenzene to a known concentration of the pyrene-functionalised MONs in acetonitrile. As shown in Figure 4, at increasing concentrations of nitrobenzene, significant decreases in the emission intensity of the Cu(BDC-trz-pyr) MONs were observed. At concentrations of 100 µM, emission intensity was ~99% quenched. This a common mechanism for the sensing of nitroaromatic molecules, a result of charge-transfer between the electrons of photoexcited nanosheets and the LUMO of nitroaromatics, resulting in the quenching of fluorescence.[42] Thus, the electron deficient
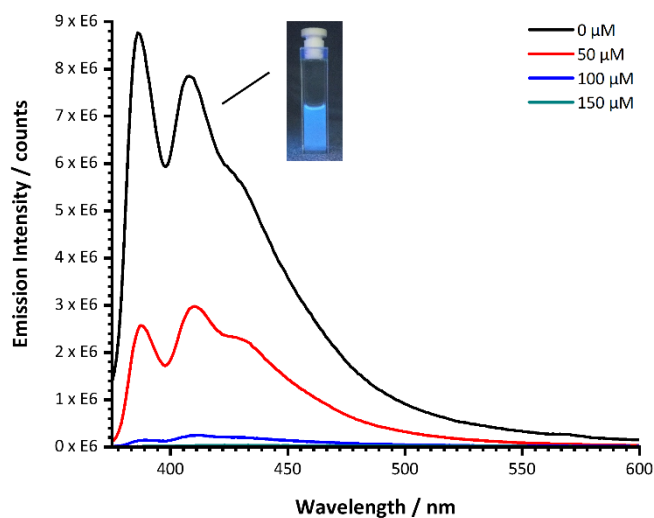
Figure 4. Emission spectra of Cu(BDC-trz-pyr) MONs in acetonitrile with increasing concentrations of nitrobenzene (λ_{ex} = 351 nm). Inset shows an image of the suspension under a UV lamp.

aromatics introduced here could be extended to the sensing of more energetic and explosive nitroaromatics, such as trinitrotoluene or picric acid.

Conclusion

We have demonstrated a post-synthetic process for the modification of the surfaces of two-dimensional metal-organic framework nanosheets. The first step is the post-synthetic functionalisation of a layered amino- MOF into its azido-form, and subsequent exfoliation into few-layer nanosheets, aided by the increased inter-layer distance afforded by PSF. The second step, post-exfoliation functionalisation of the nanosheets using click chemistry, allows for tuning of both surface functionality and interactions in one step. As a proof of concept, we introduced a photoactive pyrene moiety to the surface of these ultrathin nanosheets and used them for the sensing of nitrobenzene in solution by efficient quenching of the pyrene's fluorescence.

This technique of post-exfoliation functionalisation of metal-organic framework nanosheets using click chemistry represents a novel, versatile, and robust method for the modification of the surfaces of two-dimensional materials. We anticipate that the straightforward addition of new chemical groups using this approach will allow for fine tuning of the surface properties of nanosheets and addition of new functionalities to enable a wide range of sensing, catalysis, electronics and separation applications.

Experimental

Materials and Analytical Methods.
Materials and reagents were obtained from multiple different commercial suppliers and used without further purification. Chemical sources and all analytical methods are described in S1 of the supporting information.

Post-Synthetic Functionalisation of Cu(NH₂-BDC)(DMF).
Cu(NH₂-BDC)(DMF) was first prepared according to our previously reported method.[27] The layered amino- MOF (50 mg) was then suspended in THF (5 mL) in a 12 mL reaction vial, then treated with t-butyl nitrite (t-BuONO) and azidotrimethylsilane (TMS-N₃) in varying equivalents, as outlined in Table S1. The reaction mixture was gently stirred overnight, with the product MOF obtained by centrifugation (4500 rpm, 10 min). The product was washed with DMF (5 x 10 mL) and diethyl ether (4 x 10 mL), before being left to dry in air, affording Cu(NH₂-BDC)ₓ(N₃-BDC)ᵧ(DMF) with varying x:y ratios.

Liquid Exfoliation.
Cu(N₃-BDC)(DMF) (5 mg) was suspended in acetonitrile (6 mL) in reaction vials with Teflon-lined caps. Samples were sonicated at 80 kHz for 12 hours at 100% power, at a temperature <19 °C and with stirring of the vials to prevent hot-spots. Sonication was followed by centrifugation for 1 hour at 362 xG (1500 rpm) to remove unexfoliated material, followed by separation of the supernatant to obtain a green suspension of Cu(N₃-BDC) MONs.

Post-Exfoliation Functionalisation of Cu(N₃-BDC) Nanosheets.
Freshly exfoliated Cu(N₃-BDC) nanosheets in acetonitrile (0.5 mg mL⁻¹, 5 mL) were treated with Cu(CH₃CN)₄PF₆ (40 mmol) and acetylene derivatives in varying equivalents, as described in Table S3. Samples were then heated to 60 °C for 24 hours under a N₂ atmosphere, followed by washes with THF (5 x 10 mL) and diethyl ether (2 x 10 mL), before being left to dry in air, affording click-functionalised nanosheets.

Sensing of Nitrobenzene.
The fluorescent MONs prepared by the method above were used for sensing studies. A colloidal suspension of Cu(BDC-trz-pyr) nanosheets in acetonitrile (5 mg mL⁻¹) was treated with incremental amounts of nitrobenzene, with emission spectra recorded upon each addition (λ_{ex} = 351 nm). Uniform suspension was assured through use of a vortex mixer before each acquisition.

Conflicts of interest

There are no conflicts to declare.

Acknowledgements

References

1   J. N. Coleman, M. Lotya, A. O. Neill, S. D. Bergin, P. J. King, U. Khan, K. Young, A. Gaucher, S. De, R. J. Smith, I. V Shvets, S. K. Arora, G. Stanton, H. Kim, K. Lee, G. T. Kim, G. S. Duesberg, T. Hallam, J. J. Boland, J. J. Wang, J. F. Donegan, J. C. Grunlan, G. Moriarty, A. Shmeliov, R. J. Nicholls, J. M. Perkins, E. M. Grieveson, K. Theuwissen, D. W. Mccomb, P. D. Nellist and V. Nicolosi, *Science*, 2011, **331**, 568–572.

2   J. N. Coleman, *Acc. Chem. Res.*, 2013, **46**, 14–22.

3   L. H. Li and Y. Chen, *Adv. Funct. Mater.*, 2016, **26**, 2594–2608.

4   S. Manzeli, D. Ovchinnikov, D. Pasquier, O. V Yazyev and A. Kis, *Nat. Rev. Mater.*, 2017, **2**, 17033.

5   J. Liu, J. Tang and J. J. Gooding, *J. Mater. Chem.*, 2012, **22**, 12435–12452.

6   Y. Zhao, K. Xu, F. Pan, C. Zhou, F. Zhou and Y. Chai, *Adv. Funct. Mater.*, 2017, **27**, 1603484.

7   L. Daukiya, J. Seibel and S. De Feyter, *Adv. Phys. X*, 2019, **4**, 1625723.

8   D. Rodríguez-San-Miguel, C. Montoro and F. Zamora, *Chem. Soc. Rev.*, 2020, **49**, 2291–2302.

9   W. Wang, W. Zhao, H. Xu, S. Liu, W. Huang and Q. Zhao, *Coord. Chem. Rev.*, 2020, 213616.

10   J. Nicks, S. A. Boer, J. A. Foster and N. G. White, *Chem. Sci.*, 2021, **12**, 3322-3327.

11   D. J. Ashworth and J. A. Foster, *J. Mater. Chem. A*, 2018, **6**,

16292–16307.

12   M. Zhao, Y. Huang, Y. Peng, Z. Huang and Q. Ma, *Chem. Soc. Rev.*, 2018, **47**, 6267–6295.

13   J. López-Cabrelles, S. Mañas-Valero, I. J. Vitórica-Yrezábal, P. J. Bereciartua, J. A. Rodríguez-Velamazán, J. C. Waerenborgh, B. J. C. Vieira, D. Davidovikj, P. G. Steeneken, H. S. J. van der Zant, G. Mínguez Espallargas and E. Coronado, *Nat. Chem.*, 2018, **10**, 1001–1007.

14   H. Yuan, G. Liu, Z. Qiao, N. Li, P. J. S. Buenconsejo, S. Xi, A. Karmakar, M. Li, H. Cai, S. J. Pennycook and D. Zhao, *Adv. Mater.*, 2021, **2101257**, 2101257.

15   C. Tan, K. Yang, J. Dong, Y. Liu, Y. Liu, J. Jiang and Y. Cui, *J. Am. Chem. Soc.*, 2019, **141**, 17685–17695.

16   J. Nicks, K. Sasitharan, R. R. R. Prasad, D. J. Ashworth and J. A. Foster, *Adv. Funct. Mater. Mater.*, 2021, **31**, 2103723.

17   S. M. Cohen, *Chem. Rev.*, 2012, **112**, 970–1000.

18   M. Kalaj and S. M. Cohen, *ACS Cent. Sci.*, 2020, **6**, 1046–1057.

19   Y. Quan, G. Lan, Y. Fan, W. Shi, E. You and W. Lin, *J. Am. Chem. Soc.*, 2020, **142**, 1746–1751.

20   L. Cao, Z. Lin, F. Peng, W. Wang, R. Huang, C. Wang, J. Yan, J. Liang, Z. Zhang, T. Zhang, L. Long, J. Sun and W. Lin, *Angew. Chemie Int. Ed.*, 2016, **55**, 4962–4966.

21   G. Lan, Z. Li, S. S. Veroneau, Y.-Y. Zhu, Z. Xu, C. Wang and W. Lin, *J. Am. Chem. Soc.*, 2018, **140**, 12369–12373.

22   J. A. Foster, S. Henke, A. Schneemann, R. A. Fischer and A. K. Cheetham, *Chem. Commun.*, 2016, **52**, 10474–10477.

23   D. J. Ashworth, T. M. Roseveare, A. Schneemann, M. Flint, I. D. Bernáldes, P. Vervoorts, R. A. Fischer, L. Brammer and J. A. Foster, *Inorg. Chem.*, 2019, **58**, 10837–10845.

24   K. Sasitharan, D. G. Bossanyi, N. Vaenas, A. J. Parnell, J. Clark, A. Iraqi, D. G. Lidzey and J. A. Foster, *J. Mater. Chem. A*, 2020, **8**, 6067–6075.

25   J. Nicks, J. Zhang and J. A. Foster, *Chem. Commun.*, 2019, **55**, 8788–8791.

26   J. E. Moses, A. D. Moorhouse, J. E. Moses and K. B. Sharpless, *Chem. Soc. Rev.*, 2007, **8**, 1249–1262.

27   J. Nicks, J. Zhang and J. A. Foster, *Chem. Commun.*, 2019, **55**, 8788–8791.

28   M. Savonnet, E. Kockrick, A. Camarata, D. Bazer-Bachi, N. Bats, V. Lecocq, C. Pinel and D. Farrusseng, *New J. Chem.*, 2011, **35**, 1892.

29   M. Savonnet, D. Bazer-bachi, N. Bats, E. Jeanneau, V. Lecocq, C. Pinel and D. Farrusseng, *J. Am. Chem. Soc.*, 2010, **68**, 4518–4519.

30   X. Zhang, T. Xia, K. Jiang, Y. Cui, Y. Yang and G. Qian, *J. Solid State Chem.*, 2017, **253**, 277–281.

31   D. J. Ashworth, T. M. Roseveare, A. Schneemann, M. Flint, I. Dominguez Bernáldes, P. Vervoorts, R. A. Fischer, L. Brammer and J. A. Foster, *Inorg. Chem.*, 2019, 58, 16, 10837-10845.

32   M. Lotya, A. Rakovich, J. F. Donegan and J. N. Coleman, *Nanotechnology*, 2013, **24**, 265703.

33   D. J. Ashworth, A. Cooper, M. Trueman, R. W. M. Al-Saedi, S. D. Liam, A. J. Meijer and J. A. Foster, *Chem. Eur. J.*, 2018, **24**, 17986–17996.

34   M. Savonnet, D. Bazer-Bachi, N. Bats, J. Perez-Pellitero, E. Jeanneau, V. Lecocq, C. Pinel and D. Farrusseng, *J. Am. Chem. Soc.*, 2010, **132**, 4518–4519.

35   E. Borello, A. Zechina and E. Guglielminotti, *J. Chem. Soc.*, 1969, 307–311.

36   Y. Tanaka, S. R. Velen and S. I. Miller, *Tetrahedron*, 1973, **29**, 3271–3283.

37   C. F. Holder and R. E. Schaak, *ACS Nano*, 2019, **13**, 7359–7365.

38   S. Gutiérrez-Tarriño, J. L. Olloqui-Sariego, J. J. Calvente, G. M. Espallargas, F. Rey, A. Corma and P. Oña-Burgos, *J. Am. Chem. Soc.*, 2020, **142**, 19198–19208.

39   Y. Liu, L. Liu, X. Chen, Y. Liu, Y. Han and Y. Cui, *J. Am. Chem. Soc.*, 2021, 143, 9, 3509-3518.

40   G. Ding, Y. Wang, G. Zhang, K. Zhou, K. Zeng, Z. Li, Y. Zhou, C. Zhang, X. Chen and S. T. Han, *Adv. Funct. Mater.*, 2019, **29**, 1–11.

41   Z. Li, D. Zhan, A. Saeed, N. Zhao, J. Wang, W. Xu and J. Liu, *Dalton Trans.*, 2021, **2**, 8540–8548.

42   F. P. Kinik, A. Ortega-Guerrero, D. Ongari, C. P. Ireland and B. Smit, *Chem. Soc. Rev.*, 2021, **50**, 3143–3177.

Supplementary Information

Post-Exfoliation Functionalisation of Metal-Organic Framework Nanosheets via Click Chemistry

Joshua Nicks, and Jonathan A. Foster*

University of Sheffield, Department of Chemistry, Sheffield, S3 7HF, UK

Table of Contents

S1. General Details

S1.1. Materials

Commercial solvents, reagents and spectroscopic grade deuterated solvents were used as purchased without further purification, as listed: copper acetate monohydrate (98+%, Alfa Aesar), 2-aminoterephthalic acid (99%, Alfa Aesar), t-butyl nitrate (≥90%, Sigma-Aldrich), trimethylsilyl azide (94%, Alfa Aesar), tetrakis(acetonitrile)copper(I) hexafluorophosphate (97%, Sigma-Aldrich), propiolic acid (98+%, Alfa Aesar), 3-butyn-1-ol (97%, Fluorochem), 3-dimethylamino-1-propyne (97%, Sigma-Aldrich), 1-ethynylpyrene (98+%, Alfa Aesar), acetonitrile (≥99%, Fisher), dimethylformamide (≥99%, Fischer), diethyl ether (≥99.8%, Sigma-Aldrich), tetrahydrofuran (≥99%, VWR), nitrobenzene (≥99.0%, Merck), dimethyl sulfoxide-d_6 (99.5 atom % D, Sigma-Aldrich), deuterium chloride solution (35 wt. % in D_2O, ⩾99 atom % D, Sigma-Aldrich).

S1.2. Details of Analytical Procedures

Elemental analysis was performed by the microanalytical service at the Department of Chemistry, University of Sheffield using a Vario MICRO Cube in an atmosphere of pure O_2. Elemental CHN contents are determined to a tolerance of ± 0.5 % for organometallics.

FT-IR spectra were recorded using a Perkin Elmer Spectrum 100 FT-IR spectrophotometer, equipped with a SenseIR diamond ATR module. Samples were analysed without further preparation, and spectra were obtained in reflectance mode between 4000 – 600 cm^{-1}, using 12 scans with a spectral resolution of 1 cm^{-1}.

NMR spectra were recorded at 300 K using a Bruker Avance III HD 400 spectrometer equipped with a standard geometry 5mm BBFO probe with a single z-gradient at 400 MHz (^1H), or using a Bruker AV 400 spectrometer with a 5mm solution state probe at 400 MHz (^1H). Frameworks were digested prior to submission, using DCl (5 μL) and DMSO-d_6 (1 mL). NMR spectra were processed using MestreNova. Mass spectra were recorded directly from NMR solutions using an Agilent 6530 QTOF LC-MS in negative ionisation mode.

UV-visible absorption (UV-Vis) spectra were obtained using a Varian Cary 50 Bio spectrophotometer using standard 1 cm width quartz cells and Perkin Elmer Spectrum One

software. Spectral data was formatted using Microsoft Excel. Emission spectra were recorded using a Horiba Jobin Yvon Fluoromax-4-Spectrofluorimeter and were corrected using correction files included within the FluorEssence™ software. Data was formatted using Origin Pro.

Powder X-ray diffraction (XRD) data were collected using a Bruker-AXS D8 diffractometer using Cu K$_\alpha$ (λ=1.5418 Å) radiation and a LynxEye position sensitive detector in Bragg Brentano parafocussing geometry using a packed glass capillary or a flat silicon plate.

Thermogravimetric analyses (TGA) were performed using a Perkin-Elmer Pyris 1 instrument. Approximately 4 mg of sample was weighed into a ceramic pan, held under nitrogen flow of 20 cm^3 min^{-1} at 25 °C for 10 minutes to purge the sample and allow for equilibration, then ramped to varying end temperatures (see individual traces for details) at 1 °C min^{-1}. The samples were then held at the final temperature for 10 minutes.

Dynamic light scattering (DLS) data were collected using a Malvern Zetasizer Nano Series particle size analyser, using a He-Ne laser at 633 nm, operating in backscatter mode (173 °). Samples were equilibrated at 298 K for 60 s prior to analysis. Zeta potential data were collected using the same instrument in zeta potential mode, using disposable polycarbonate capillary electrophoresis cells and according to the Smoluchowski method. Contact angle measurements were obtained using a Ramé-Hart Goniometer.

Atomic force microscopy (AFM) images were recorded using a Bruker Multimode 5 Atomic Force Microscope, operating in soft-tapping mode in air under standard ambient temperature and pressure, fitted with Bruker OTESPA-R3 silicon cantilevers operated with a drive amplitude of ~18.70 mV and resonance frequency of ~236 kHz. Samples were prepared by drop-casting 10 μL drops of suspension onto the centre of freshly cleaved mica sheets heated to 100 °C on a hot plate. These sheets were stuck to stainless steel, magnetic Agar scanning probe microscopy specimen discs. Images were processed using Gwyddion software.

Scanning electron microscopy (SEM) samples were prepared by loading powdered samples onto carbon sticky tabs placed on aluminium SEM sample stubs, coated with approximately 20 nm gold using an Edwards S150B sputter coater and loaded into a TESCAN VEGA3 LMU SEM, operated at 15 keV. Images were collected at 10,000x magnification using the secondary electron detector.

S2. Preparation and Characterisation of Cu(N₃-BDC)(DMF) Layered MOF

S2.1. Details of Preparation

An attempt was made to synthesise the Cu(N$_3$-BDC)(DMF) in an analogous fashion to our previously published for Cu(NH$_2$-BDC)(DMF) using 2-azidoterephthalic acid, synthesised according to a previously published procedure by Wöll *et al.* The ^{1}H NMR spectrum of this linker is shown below in figure S1. This procedure afforded only a black amorphous solid under both solvothermal conditions and reaction at room temperature.
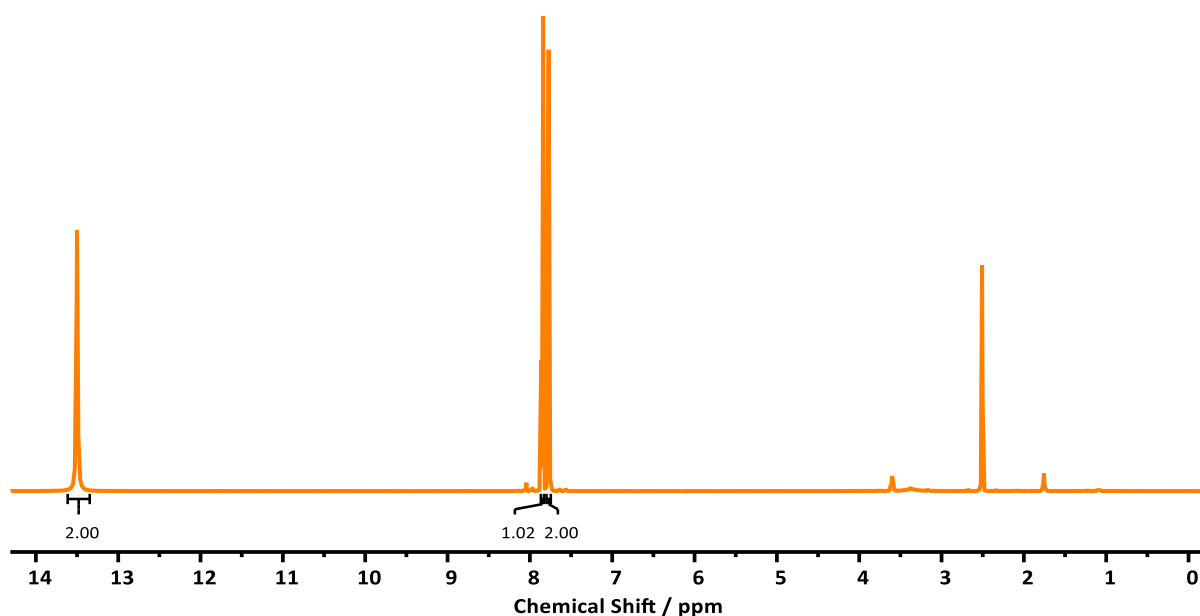
Figure S1. The ^{1}H NMR spectrum of as synthesised 2-azidoterephthalic acid.

Table S1. A table of the equivalents of t-butyl nitrite (*t*-BuONO) and azidotrimethylsilane (TMS-N$_3$) used to obtain varying degrees of conversion from the amino- layered MOF to the azido- layered MOF, Cu(N$_3$-BDC)(DMF).

t-BuONO Equivalents	TMS-N$_3$ Equivalents	Conversion / %
0.0	0.0	0
2.6	2.4	21
4.5	4.0	52
7.9	7.1	81
11.0	9.5	100
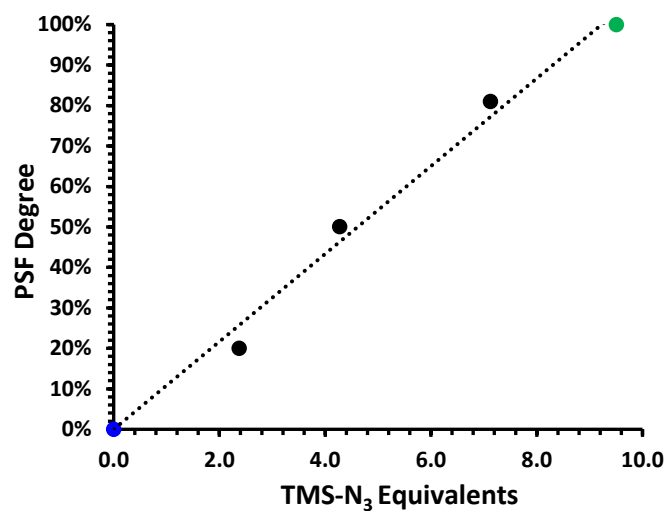
Figure S2. Plot of the values from table 1, demonstrating the tunable nature of the azidification process.
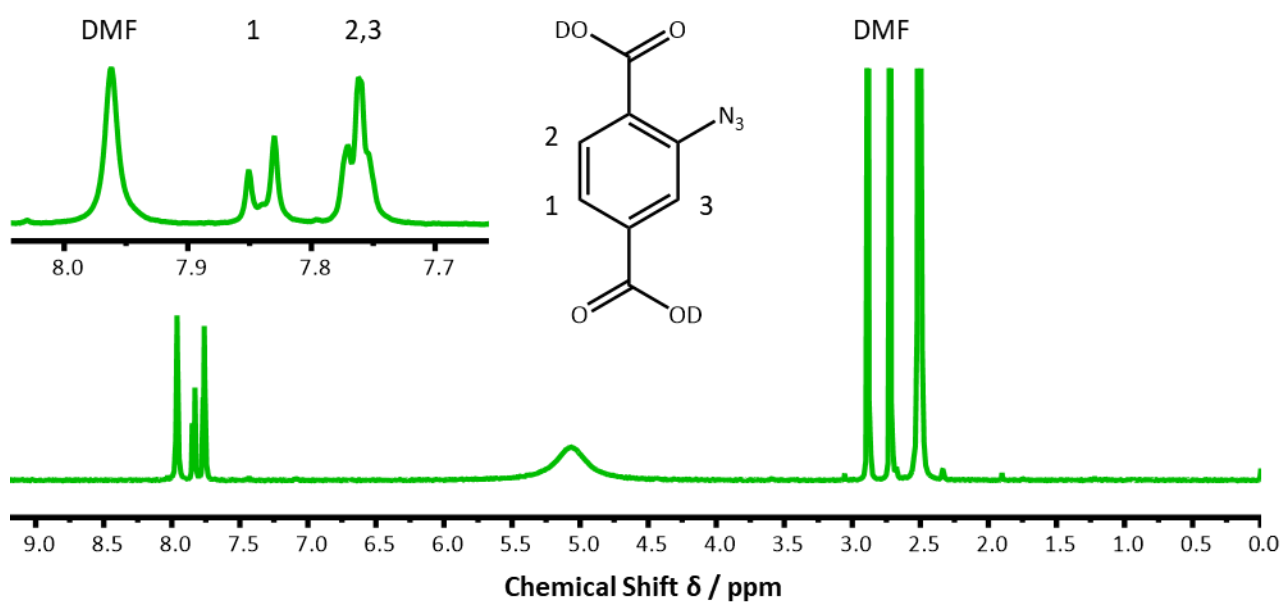
Figure S3. Annotated d6-DMSO ^{1}H NMR spectrum of digested Cu(N$_3$-BDC)(DMF).
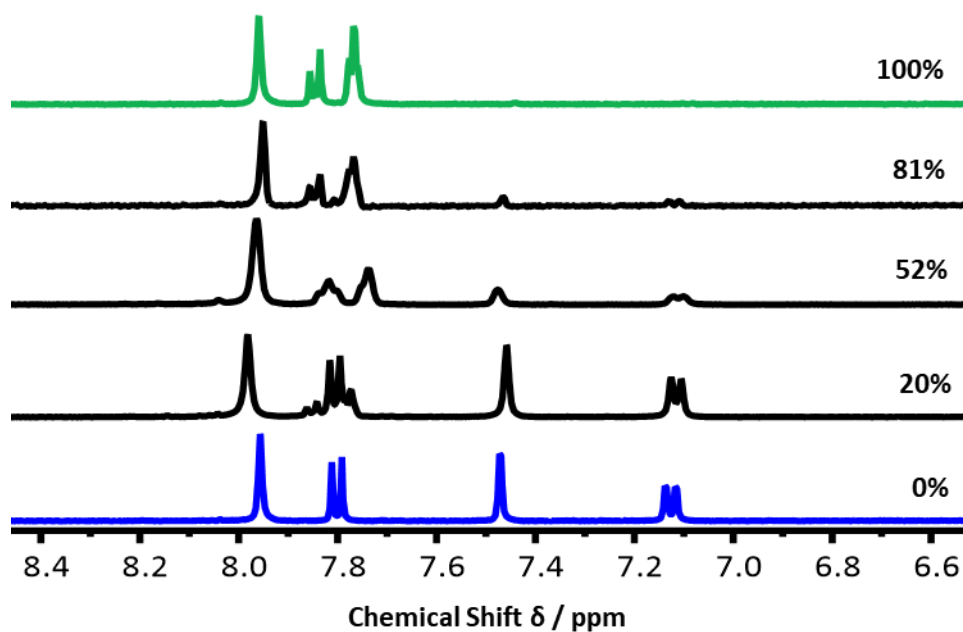
Figure S4. Stack plot of digested ^{1}H NMR spectra showing the conversion of Cu(ABDC)(DMF) into Cu(N_3-BDC)(DMF) with increasing equivalents of *t*-BuONO and TMS-N_3. Slight discrepancies in chemical shifts are a result of minor changes in DCl concentration.
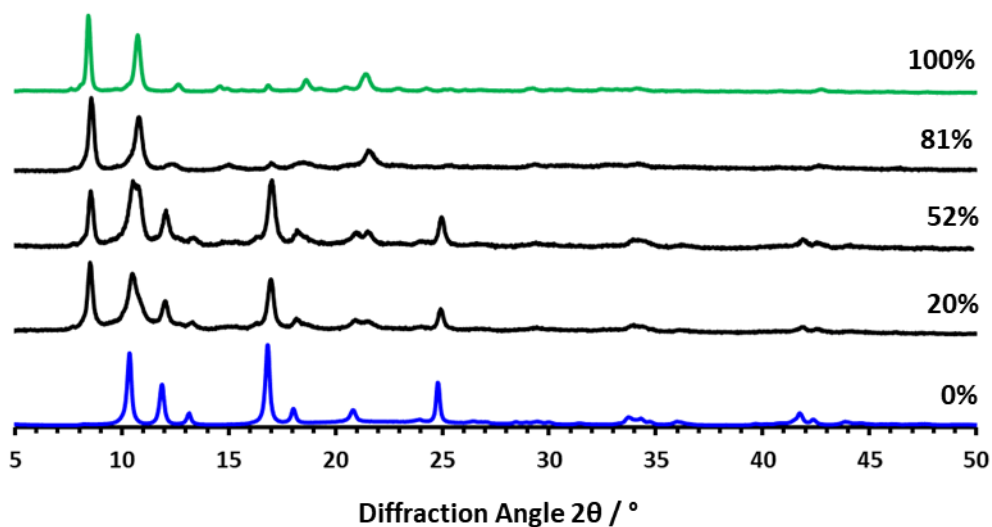
Figure S5. Stack plot of XRD powder patterns (recorded in flat plate stage), showing the conversion of Cu(ABDC)(DMF) into Cu(N_3-BDC)(DMF).
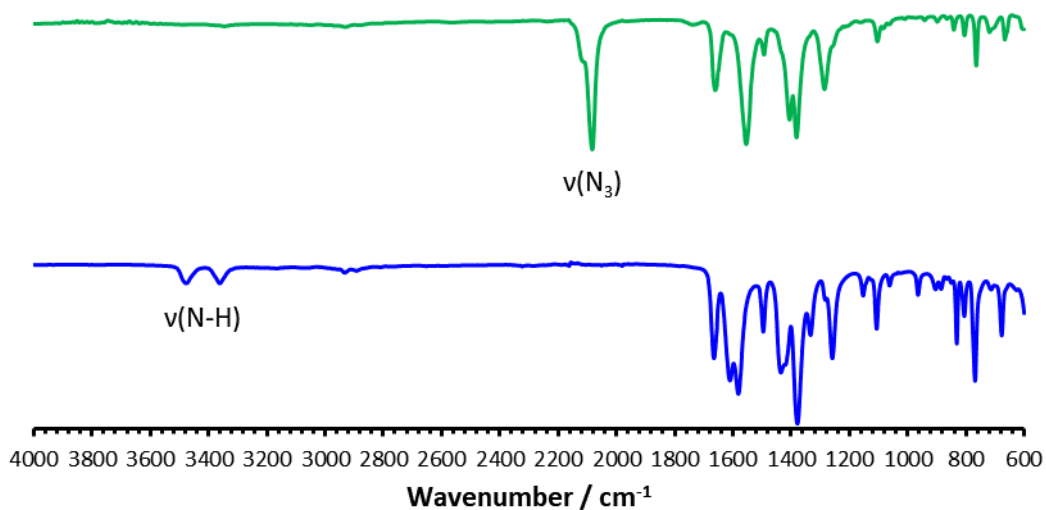
Figure S6. A comparison between the FT-IR spectra of Cu(ABDC)(DMF) (blue) and Cu(N_3-BDC)(DMF) (green), with the respective characteristic v(N-H) and v(N_3) peaks indicated.
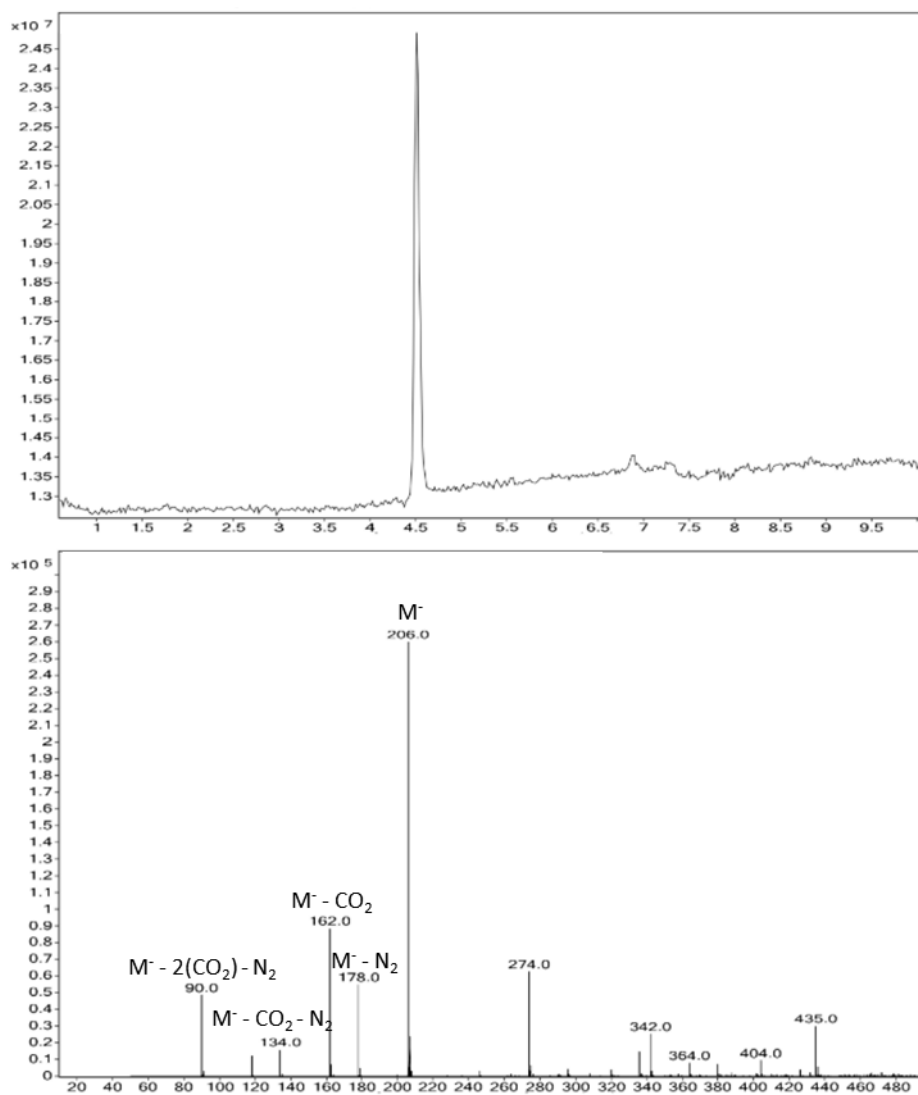
Figure S7. Assigned LC chromatograph and NEG-ESI mass spectrum of digested Cu(N_3-BDC)(DMF).
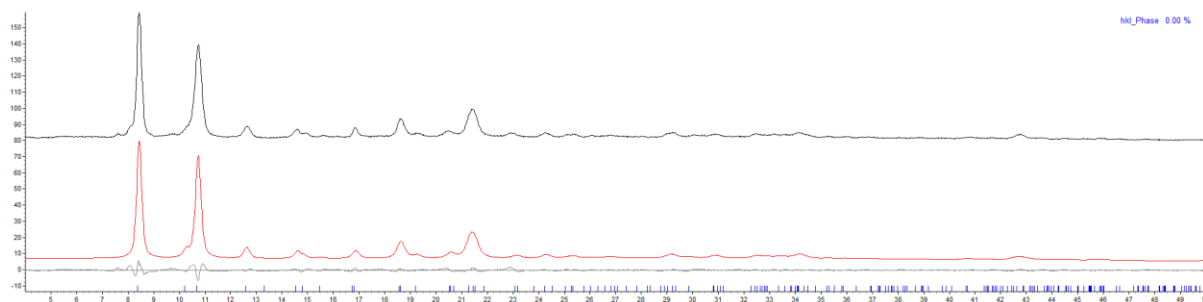
Figure S8. Fitted Pawley refinement of the Cu(N$_3$-BDC)(DMF) XRD pattern to the unit cell with dimensions outlined in table S2.

Table S2. The unit cell parameters obtained from Pawley refinement of the XRD pattern obtained from Cu(N$_3$-BDC)(DMF), compared to the unit cell parameters of MOF-46 (Zn analogue of Cu(NH$_2$-BDC)(DMF).[2]

MOF	Crystal System	Space Group	a / Å	b / Å	c / Å	β / °	Cell Vol. / Å³	R$_{wp}$	R$_{exp}$
MOF-46	Monoclinic	C2/m	11.2043(9)	15.0516(12)	8.0275(7)	111.7060(10)	1257.79(18)	-	-
Cu(N$_3$-BDC)(DMF)	Monoclinic	C2	13.41769)	17.1225	8.3632	100.3478	1890.14	5.269	1.831
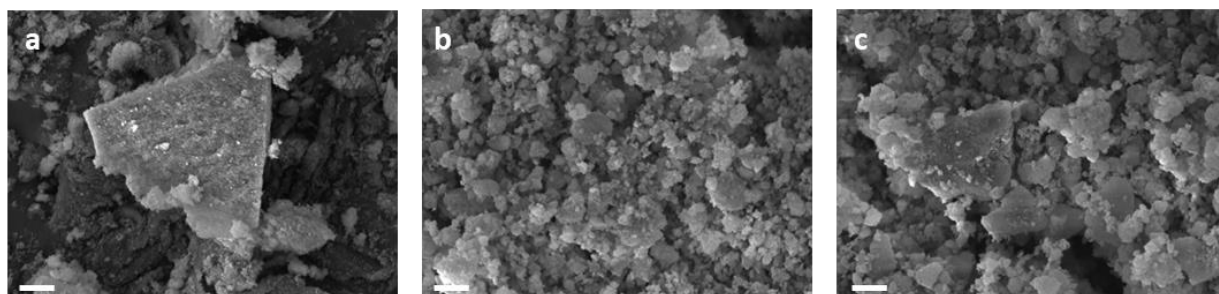
Figure S9. SEM images of **a)** Cu(ABDC)(DMF), and **b)** and **c)** Cu(N$_3$-BDC)(DMF). Inset scale bars represent 5 μm.

S3. Exfoliation and Characterisation of Cu(N₃-BDC)(DMF) MONs

S3.1. Exfoliation of Cu(N₃-BDC)(DMF)

Liquid-assisted ultrasonic exfoliations were carried out by suspension of 5 mg of MOF in 6 mL of acetonitrile inside a 10 mL reaction vial. The sample was mixed in a vortex mixer for 30 seconds to disperse the sediment. The samples were sonicated using a Fisherbrand Elmasonic P 30H ultrasonic bath (2.75 L, 380/350 W, UNSPSC 42281712) filled with water. Samples were sonicated for 12 hours at a frequency of 80 kHz with 100% power and the temperature was thermostatically maintained at 16-20°C using a steel cooling coil. Sonication was applied using a sweep mode and samples were rotated through the water using an overhead stirrer to minimise variation due to ultrasound "hot-spots". Suspensions of nanosheets were obtained by centrifugation at 362 xg (1500 rpm) for 1 hour, followed by removal of the suspension from the isolated bulk powder.
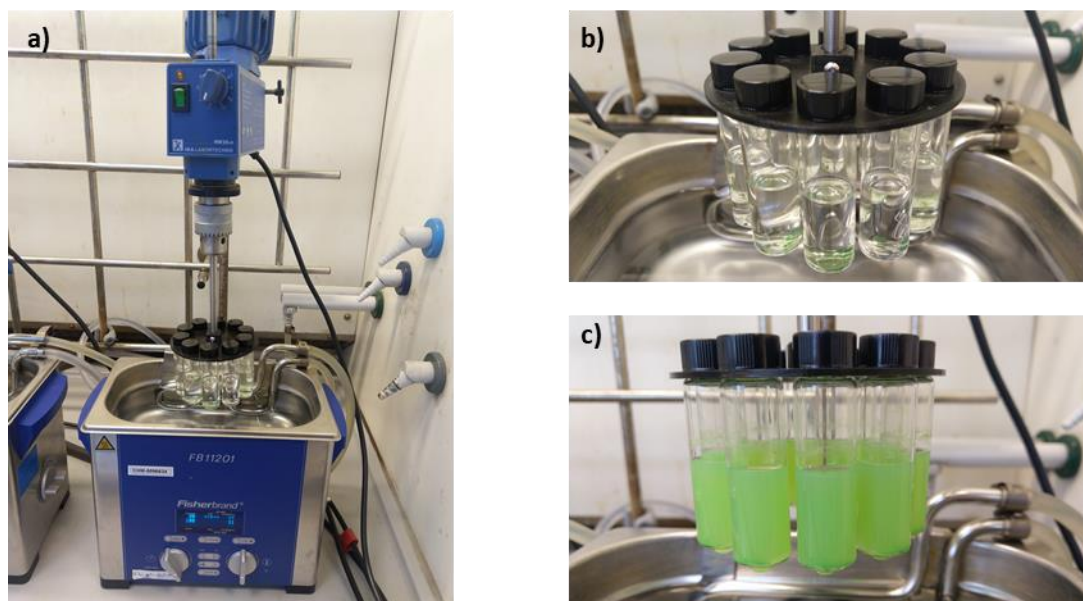
Figure S10. a) The setup used for liquid exfoliation of the Cu(N₃-BDC)(DMF) framework, **b)** and **c)** images of the samples pre- and post-exfoliation respectively.

S3.2. Characterisation of Cu(N₃-BDC) Nanosheets
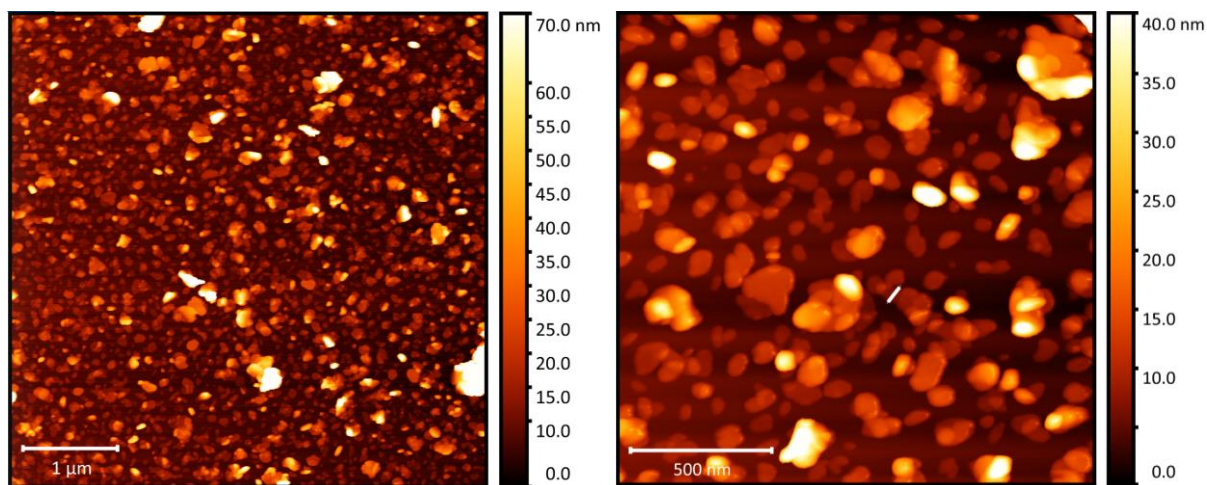
Figure S11. AFM images of the Cu(N₃-BDC) MONs obtained from ultrasonic exfoliation of the layered Cu(N₃-BDC)(DMF) MOF.
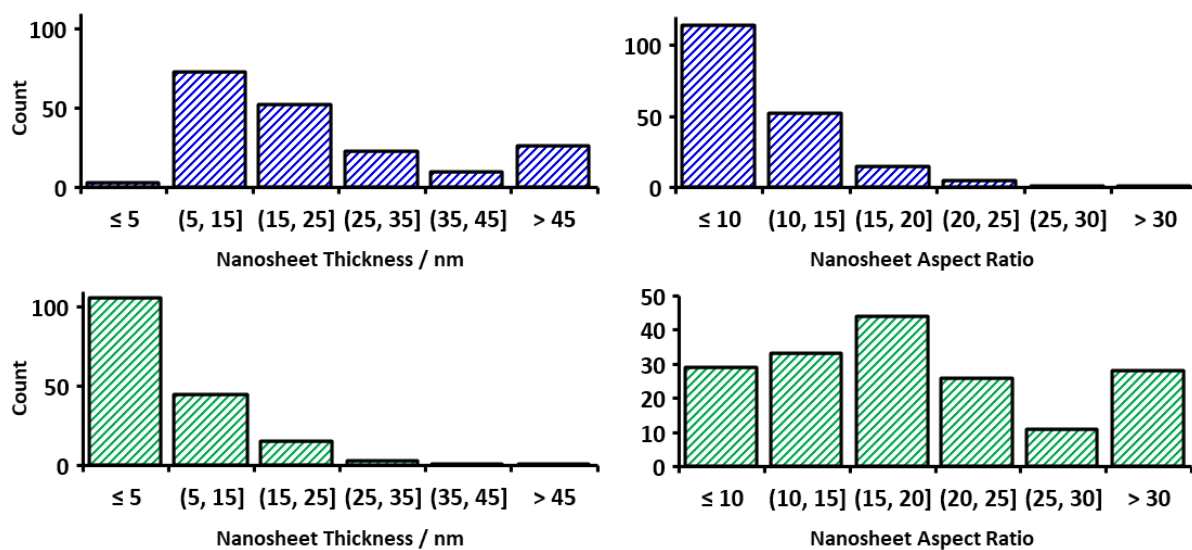
Figure S12. Size distribution histograms of both Cu(ABDC) and Cu(N₃-BDC) MONs, showing both nanosheet thickness and aspect ratio data.
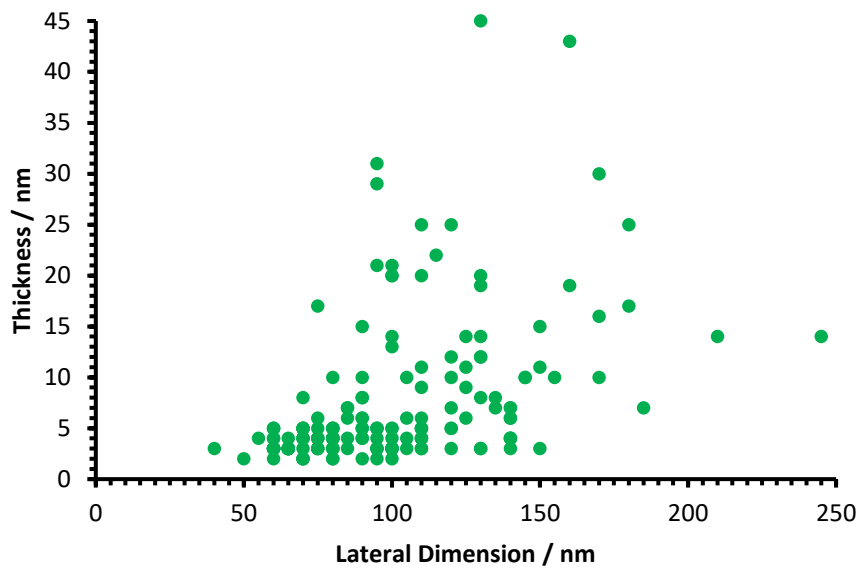
Figure S13. Size distribution scatter plot of Cu(N$_3$-BDC) MONs.
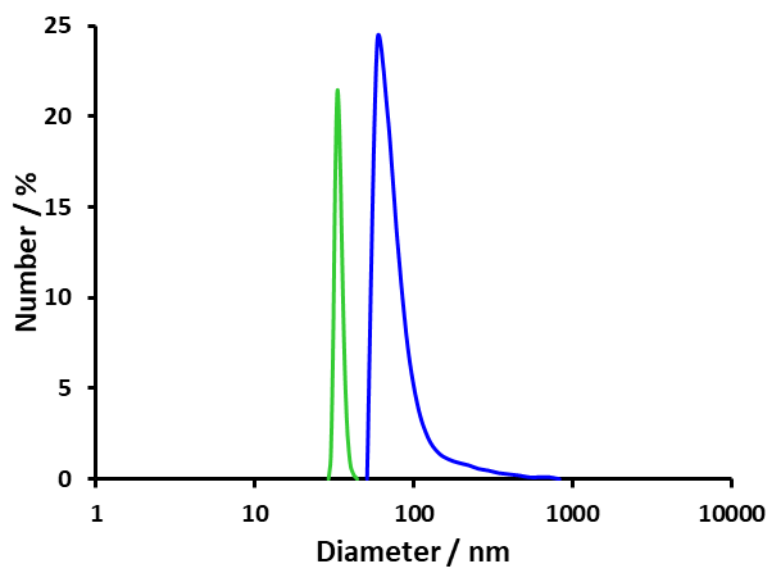
Figure S14. DLS plots of Cu(ABDC) (blue) and Cu(N$_3$-BDC) (green) nanosheets.
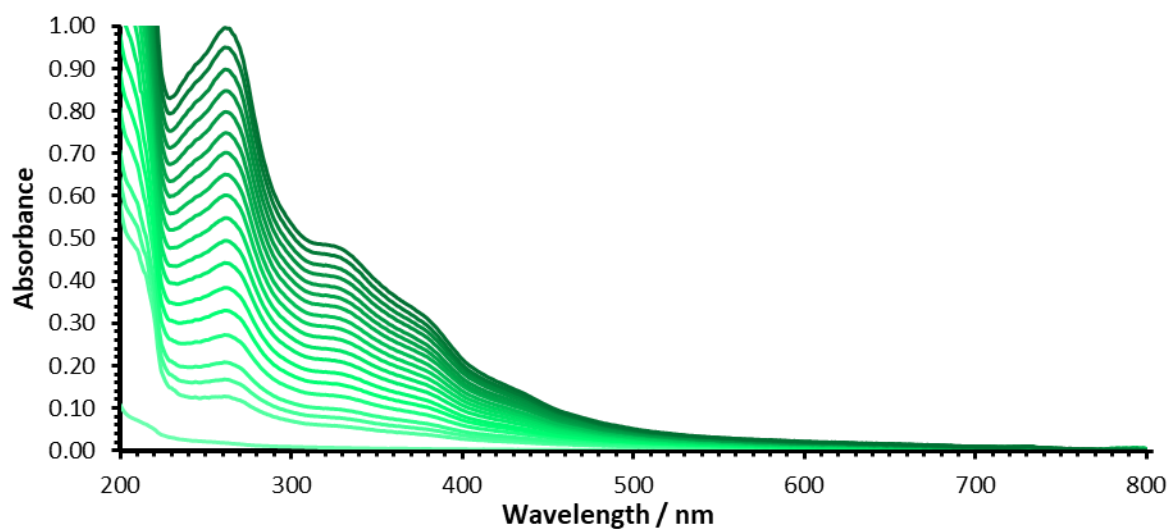
Figure S15. A series of UV-Vis spectra recorded for known concentrations of Cu(N$_3$-BDC) MONs used to calculate the extinction coefficient of the system.

$y = 12,841x + 0.05$
$R^2 = 1.00$
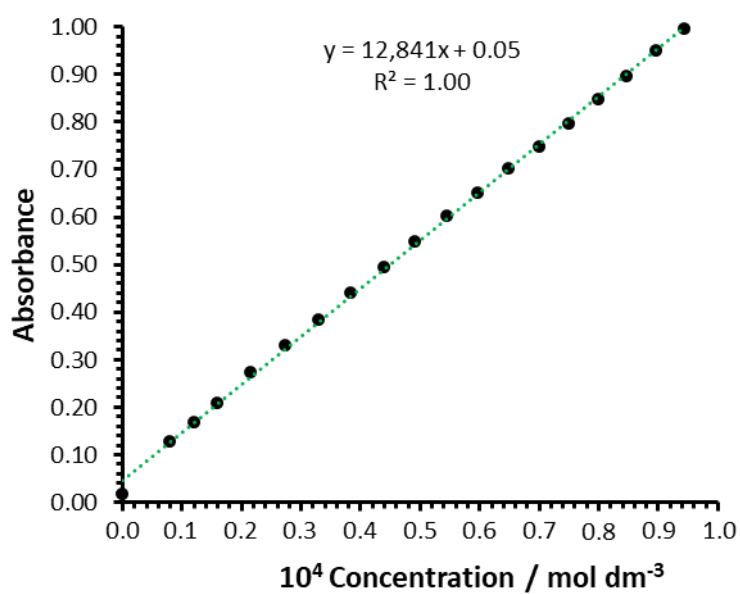
Figure S16. Plot used to calculate the extinction coefficient of the band at λ=261 nm, giving a value of 12,841 dm^3 mol^{-1} cm^{-1}.
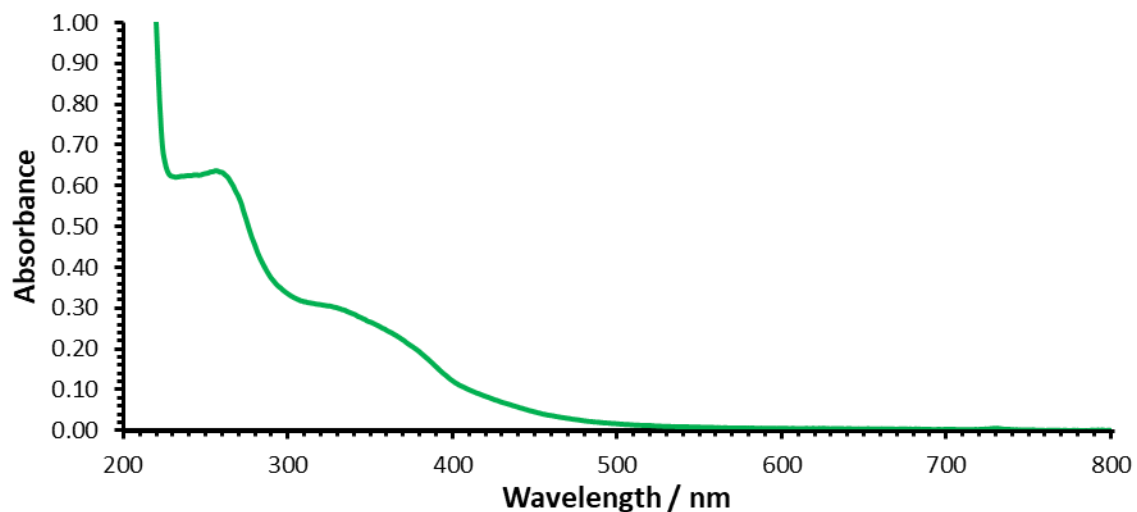
Figure S17. UV-Vis spectrum of the as exfoliated Cu(N$_3$-BDC) nanosheets, following centrifugation at 1500 rpm for 1 hour and dilution by a factor of 100.
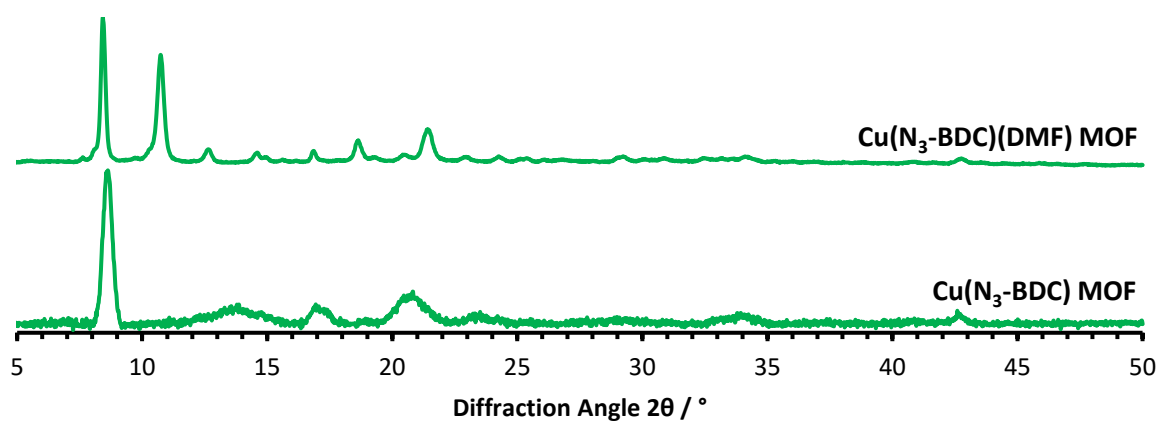
Figure S18. XRD pattern of Cu(N$_3$-BDC) nanosheets and Cu(N$_3$-BDC) layered MOF desolvated by repeated stirring in acetonitrile.
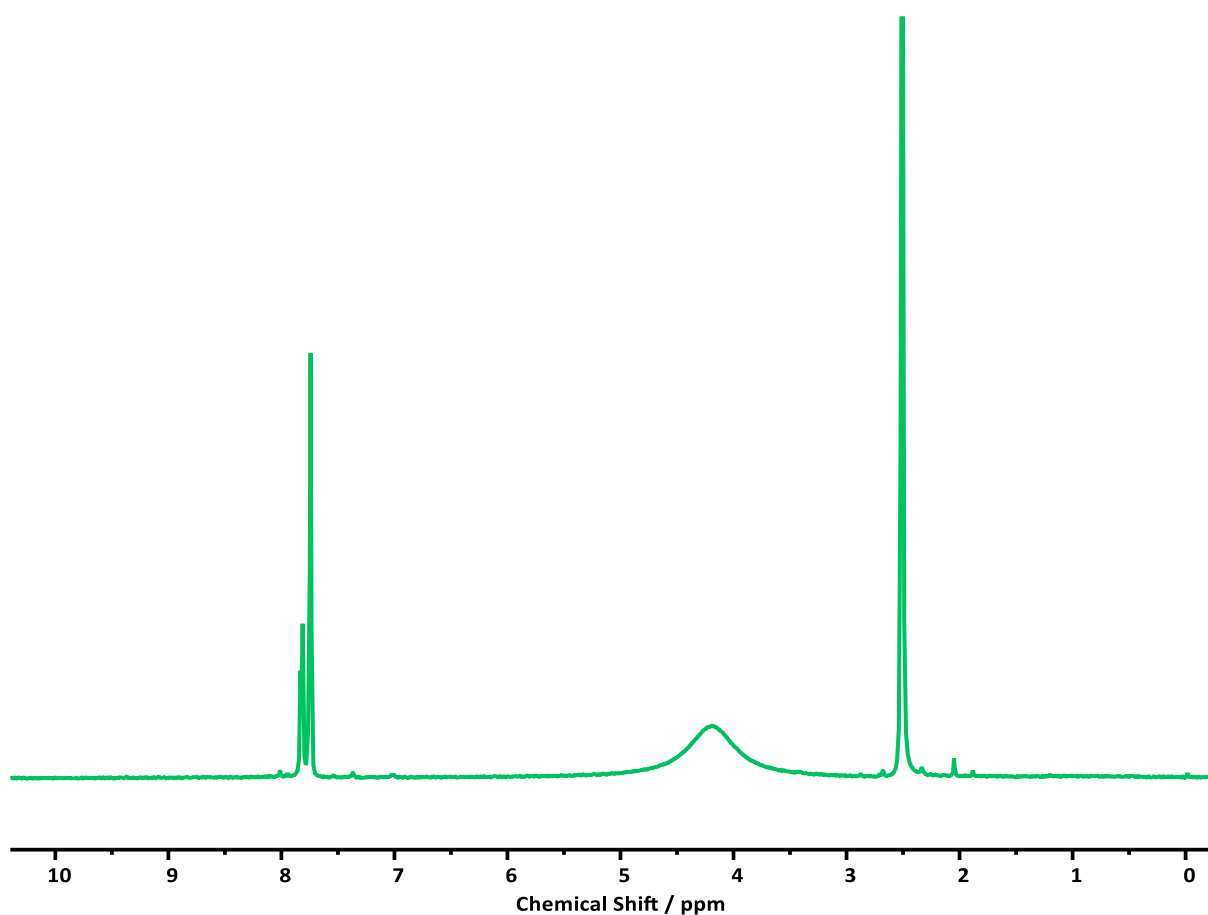
Figure S19. ^{1}H NMR spectrum of digested Cu(N$_3$-BDC) nanosheets, indicating desolvation of coordinated DMF by exfoliation in acetonitrile.

S4. Post-Exfoliation Functionalisation Data

S4.1. Experimental Conditions

Table S3. Experimental conditions for the click reactions performed using Cu(N$_3$-BDC) nanosheets.

	Cu(BDC-trz-CO$_2$H)	Cu(BDC-trz-NMe$_2$)	Cu(BDC-trz-OH)	Cu(BDC-trz-Pyr)
Cu(I)PF$_6$(MeCN)$_4$ / mg	15 (0.04 mmol)			
Acetylene derivative / mmol	0.04 (4 eq.)	0.40 (50 eq.)	1.00 (100 eq.)	(20 eq.)
Acetylene derivative / mg	2.80	33.3	70.1	45.2
Acetylene derivative / µL	3	55	75	-

S4.2. Characterisation of the Functionalised MONs

Due to the small quantity of MONs obtained from each experiment, some ^{1}H NMR spectra and PXRD patterns have poor signal to noise ratios.
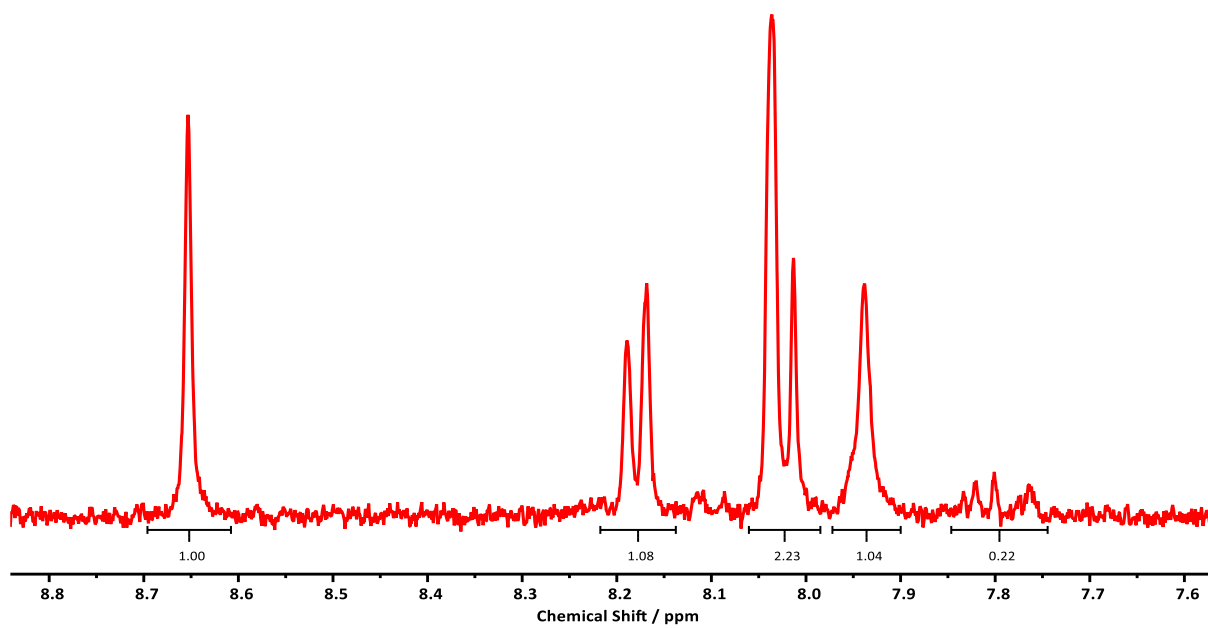
Figure S20. ^{1}H NMR spectrum of digested Cu(BDC-trz-CO$_2$H) MONs.
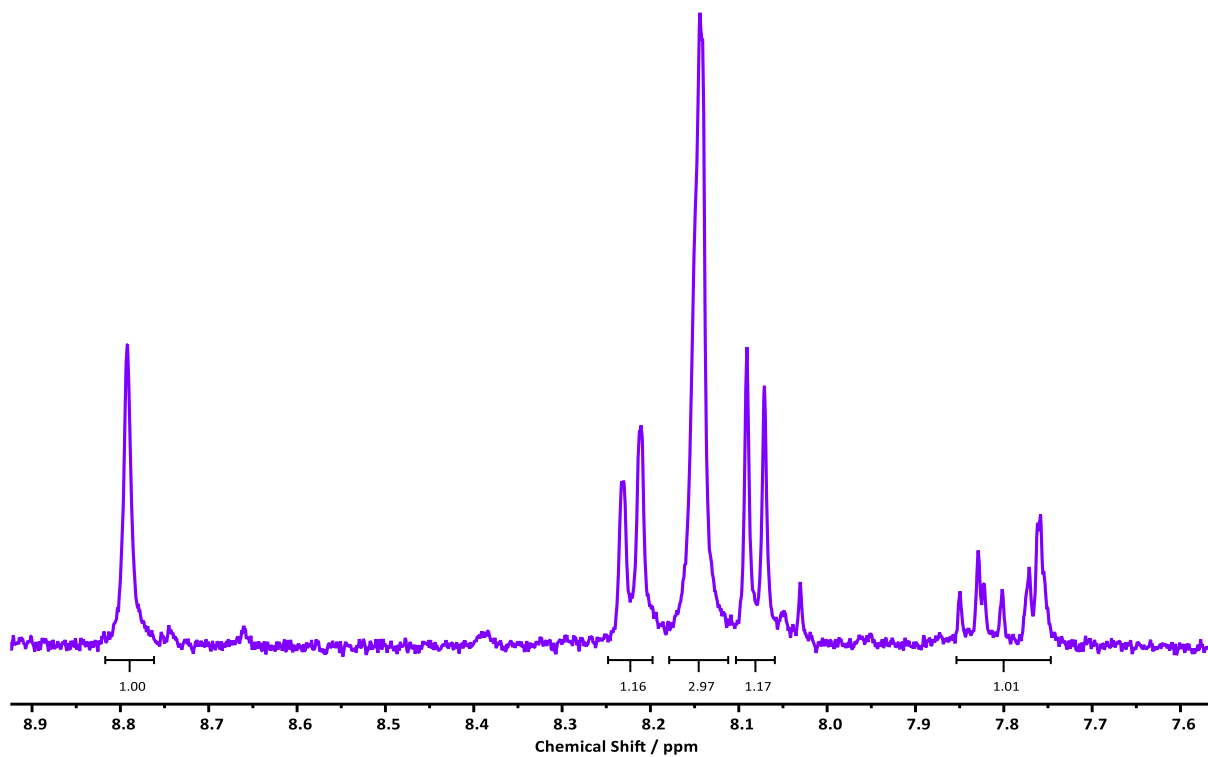
Figure S21. ^{1}H NMR spectrum of digested Cu(BDC-trz-NMe$_2$) MONs.
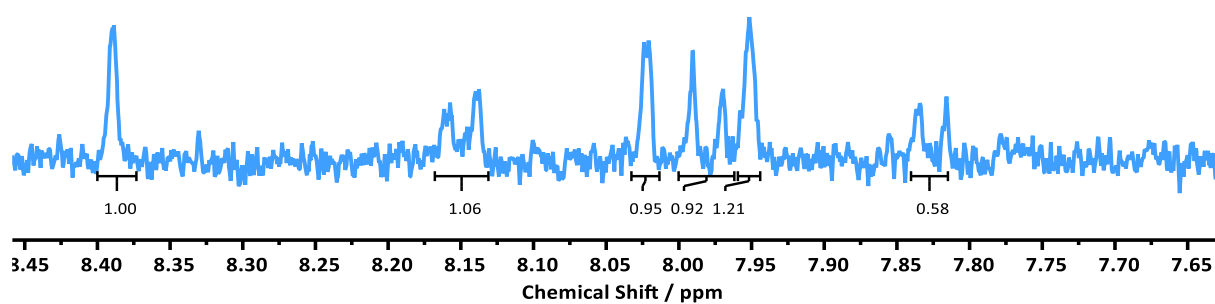
Figure S22. ^{1}H NMR spectrum of digested Cu(BDC-trz-OH) MONs.
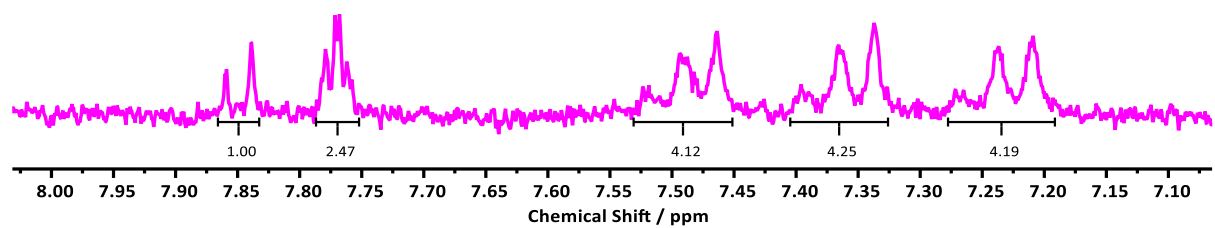
Figure S23. ^{1}H NMR spectrum of digested Cu(BDC-trz-pyr) MONs.
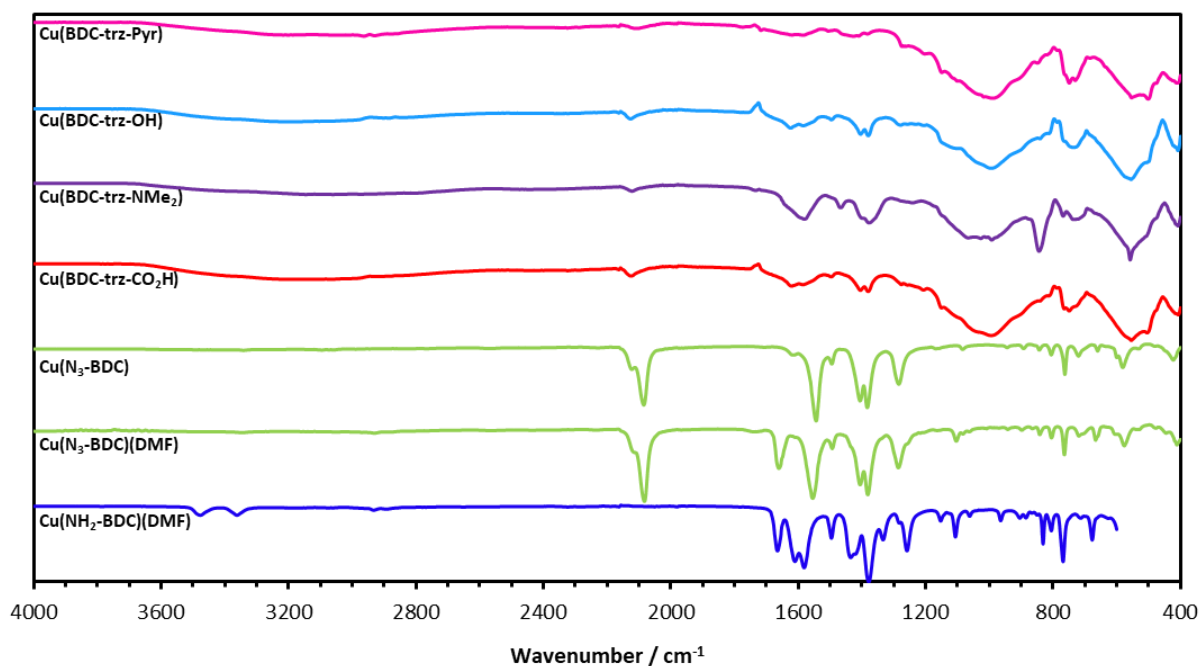
Figure S24. From bottom to top, FT-IR Spectra of: Cu(NH$_2$-BDC)(DMF) (dark blue), Cu(N$_3$-BDC)(DMF), desolvated Cu(N$_3$-BDC) (green), Cu(BDC-trz-CO$_2$H) nanosheets (red), Cu(BDC-trz-NMe$_2$) nanosheets (purple), Cu(BDC-trz-OH) nanosheets (light blue), and Cu(BDC-trz-pyr) nanosheets (pink).
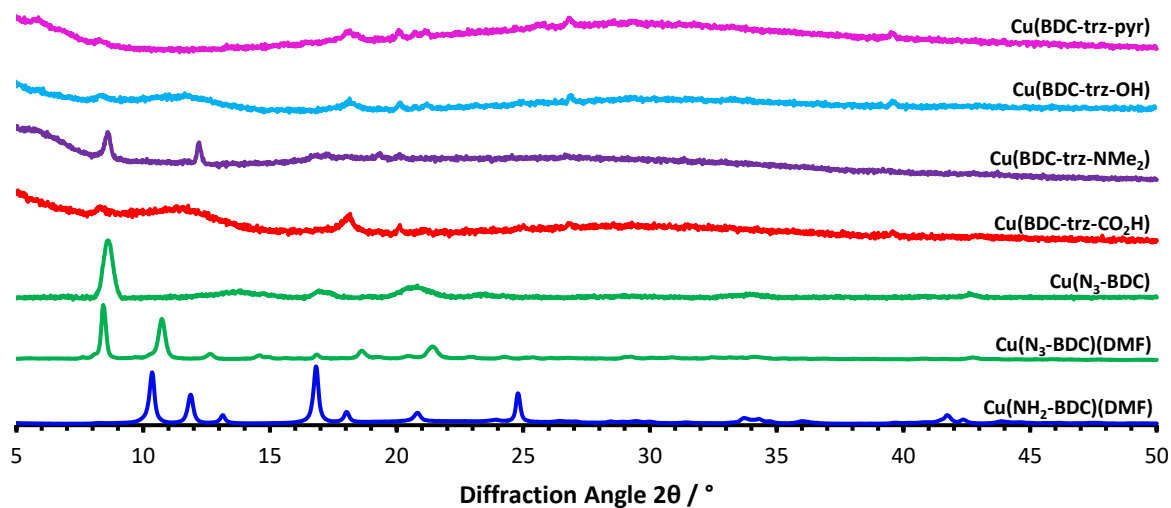
Figure S25. From bottom to top, X-ray powder diffraction patterns of: Cu(NH$_2$-BDC)(DMF) (dark blue), Cu(N$_3$-BDC)(DMF), desolvated Cu(N$_3$-BDC) (green), Cu(BDC-trz-CO$_2$H) nanosheets (red), Cu(BDC-trz-NMe$_2$) nanosheets (purple), Cu(BDC-trz-OH) nanosheets (light blue), and Cu(BDC-trz-pyr) nanosheets (pink).
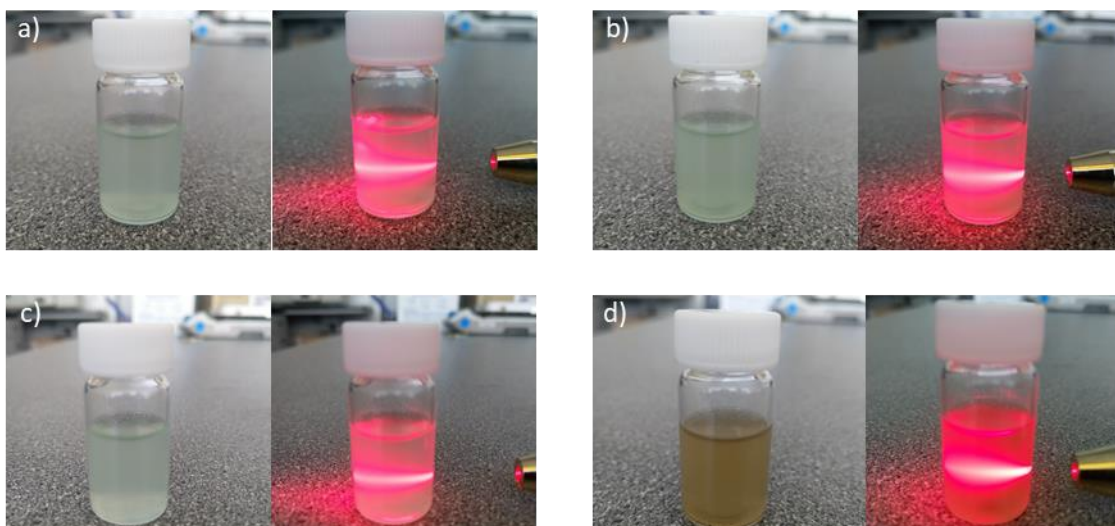
Figure S26. Images showing suspensions and associated Tyndall scattering of **a)** Cu(BDC-trz-CO$_2$H), **b)** Cu(BDC-trz-NMe$_2$), **c)** Cu(BDC-trz-OH), and **d)** Cu(BDC-trz-pyr) nanosheets.
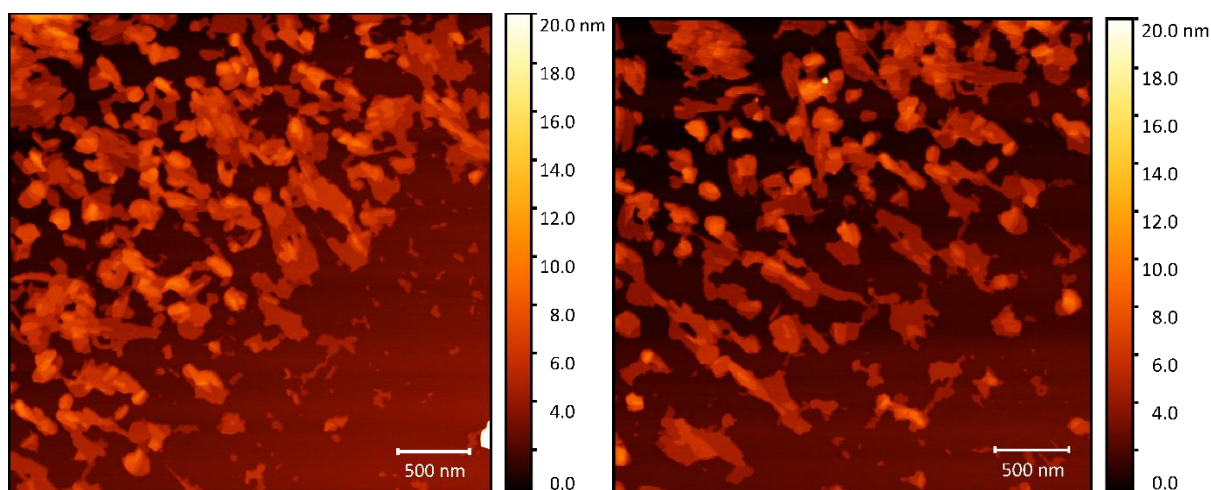
Figure S27. Additional AFM images of Cu(BDC-trz-CO$_2$H) nanosheets.
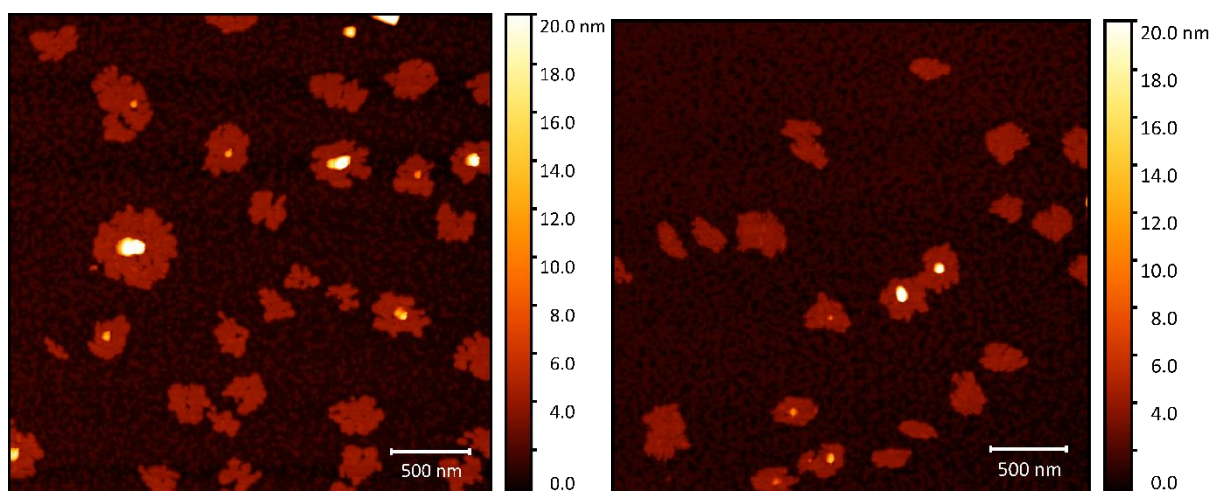
Figure S28. Additional AFM images of Cu(BDC-trz-NMe$_2$) nanosheets.
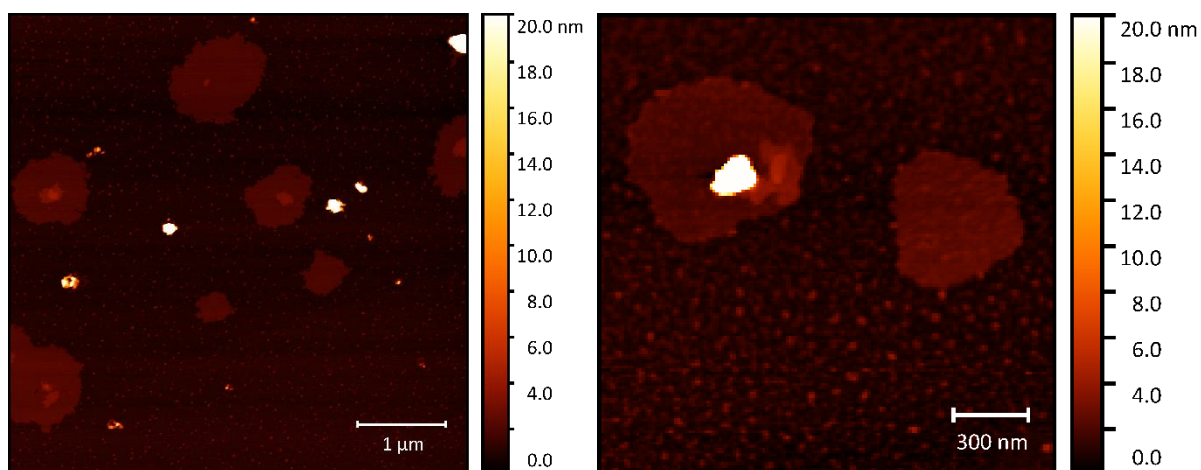
Figure S29. Additional AFM images of Cu(BDC-trz-OH) nanosheets.
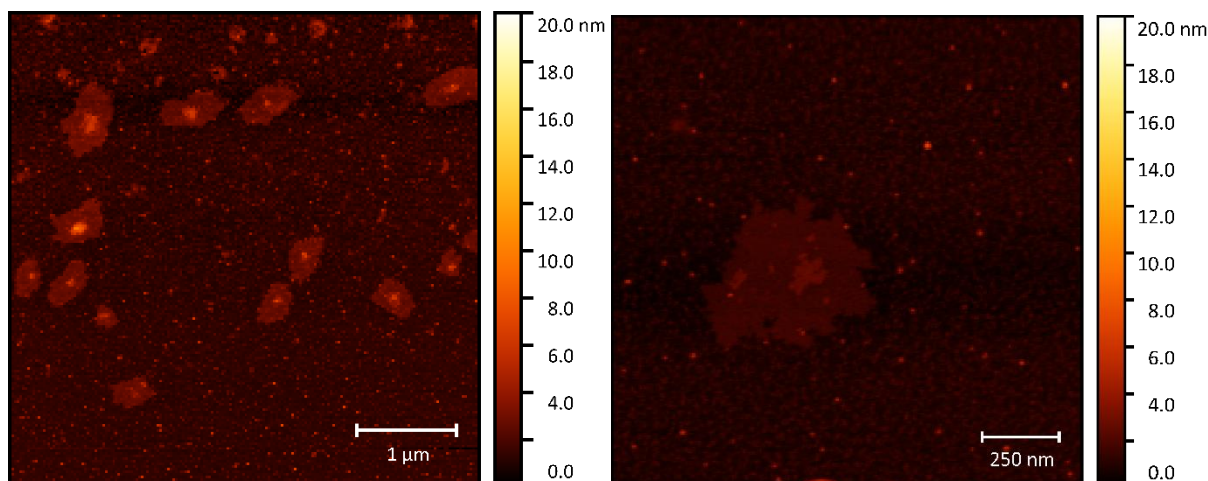
Figure S30. Additional AFM images of Cu(BDC-trz-pyr) nanosheets.
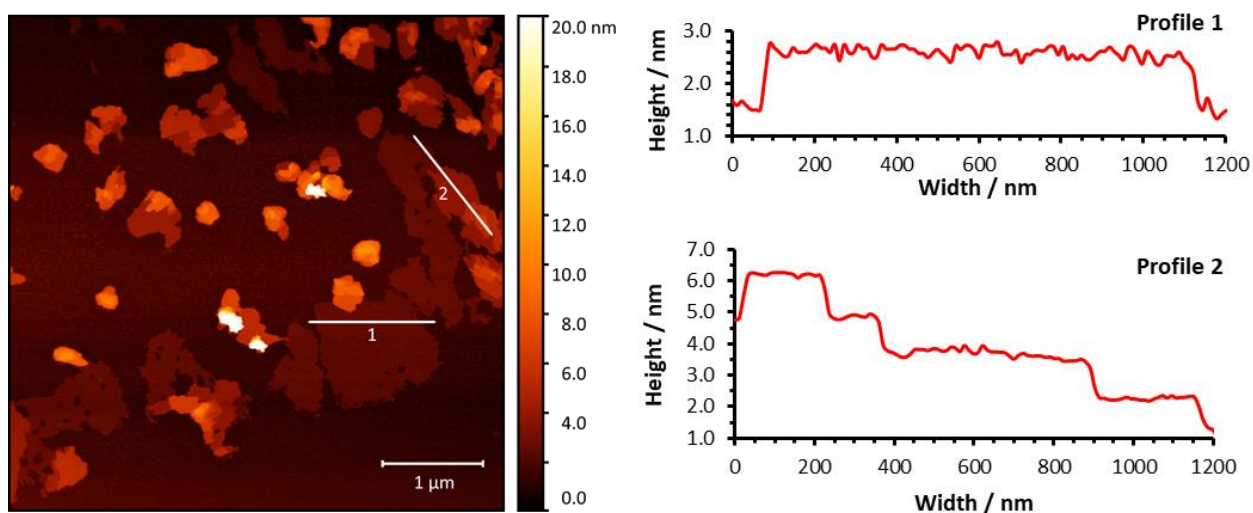
Figure S31. Height profiles for selected nanosheets shown in Figure 3a, for Cu(BDC-trz-CO$_2$H) nanosheets.
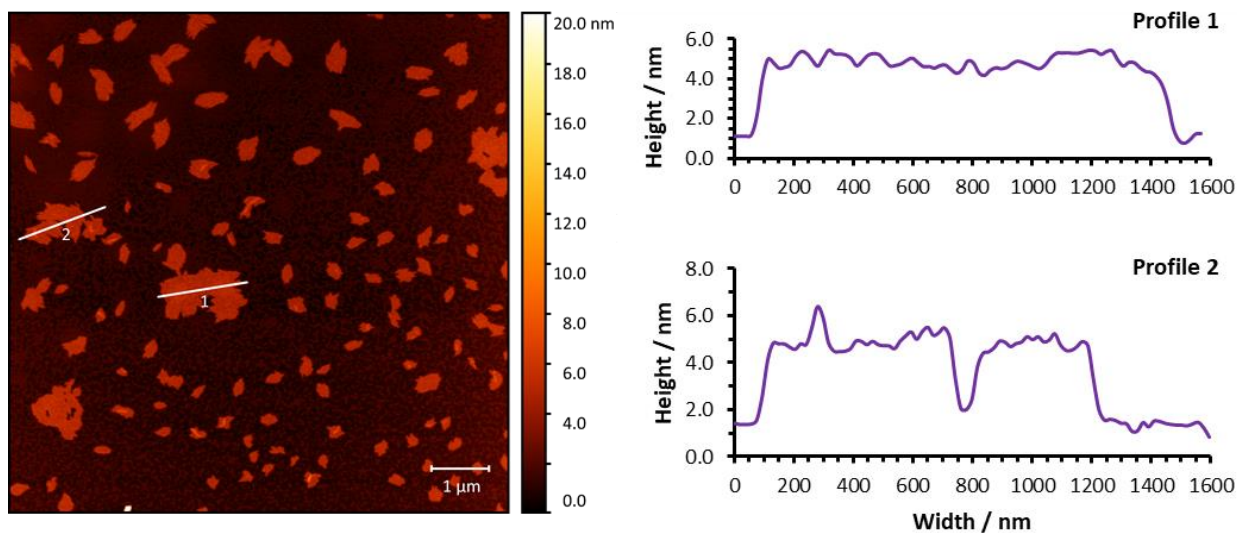
Figure S32. Height profiles for selected nanosheets shown in Figure 3b, for Cu(BDC-trz-NMe$_2$) nanosheets.
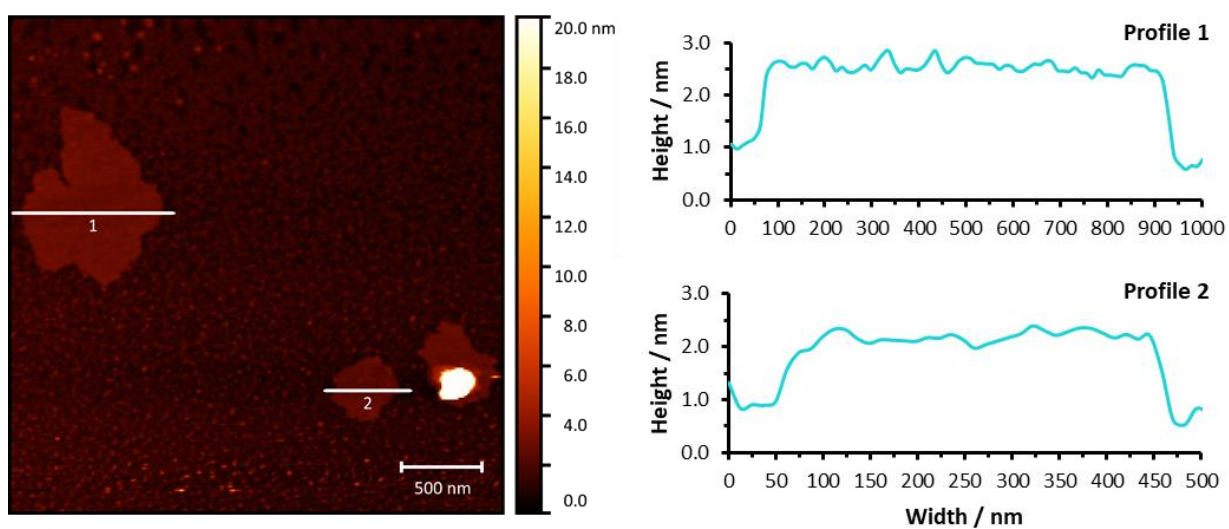
Figure S33. Height profiles for selected nanosheets shown in Figure 3c, for Cu(BDC-trz-OH) nanosheets.
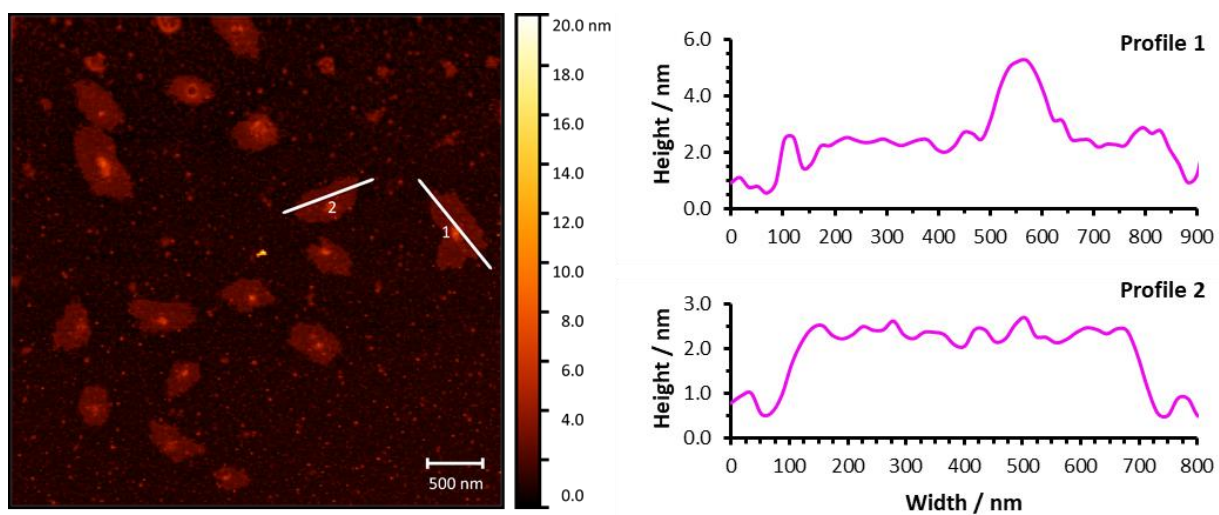
Figure S34. Height profiles for selected nanosheets shown in Figure 3d, for Cu(BDC-trz-pyr) nanosheets.

S5. Sensing
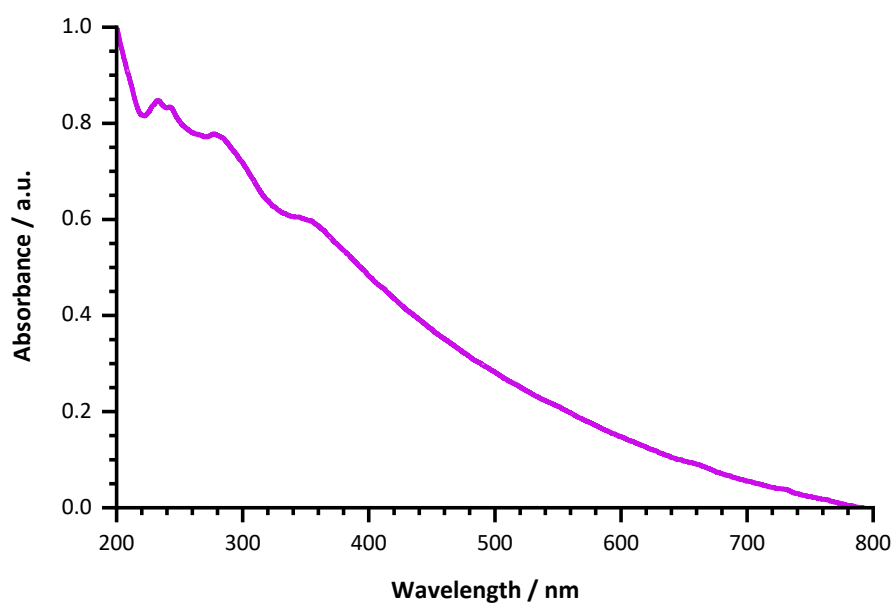
Figure S35. Absorption spectrum for the as prepared Cu(BDC-trz-pyr) nanosheets in acetonitrile (0.1 mg mL^{-1}).
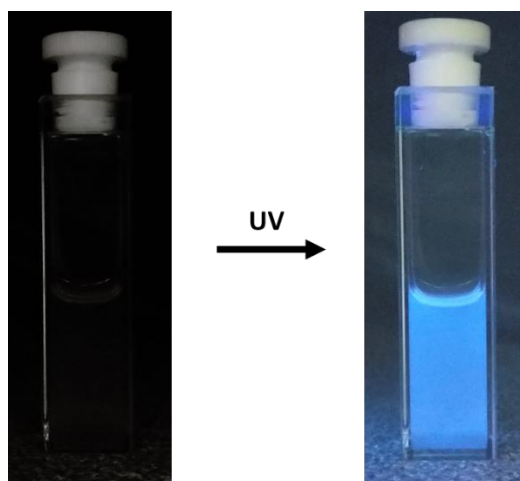
Figure S36. Images of the as prepared Cu(BDC-trz-pyr) nanosheets before and after applications of a UV lamp.

S6. References

1   J. Nicks, J. Zhang and J. A. Foster, Tandem catalysis by ultrathin metal–organic nanosheets formed through post-synthetic functionalisation of a layered framework, *Chem. Commun.*, 2019, **55**, 8788–8791.

2   M. E. Braun, C. D. Steffek, J. Kim, P. G. Rasmussen and O. M. Yaghi, 1,4-Benzenedicarboxylate derivatives as links in the design of paddle-wheel units and metal – organic frameworks, *Chem. Commun.*, 2001, **2**, 2532–2533.

Chapter 5

Liquid exfoliation of a series of expanded layered metal-organic frameworks to form nanosheets

Ligand expansion increases nanosheet aspect ratio
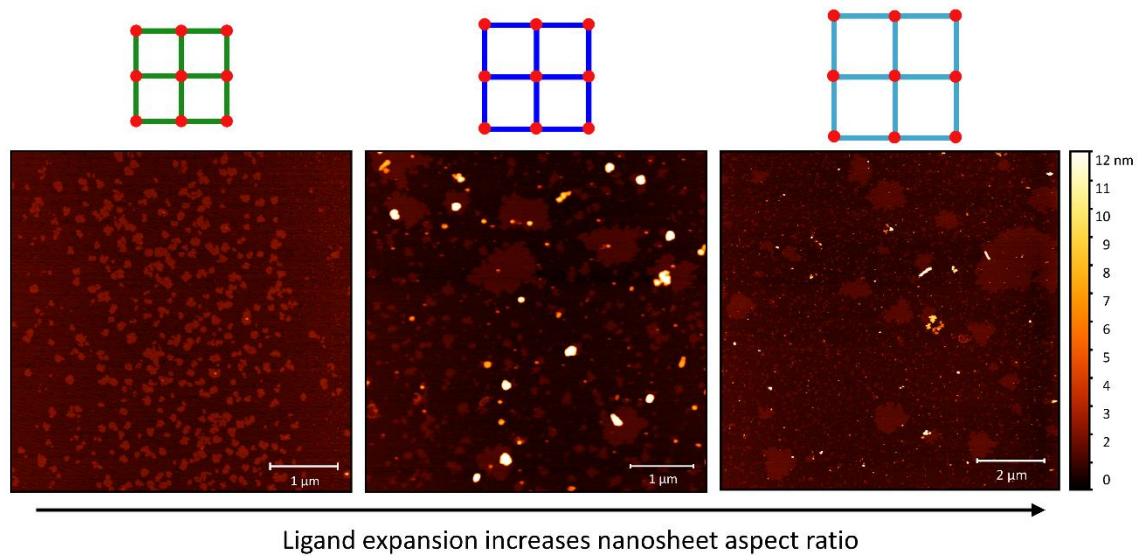
Chapter 5

Liquid exfoliation of a series of expanded layered metal-organic frameworks to form nanosheets

Unpublished paper (full article)

Joshua Nicks, Michael Harris, David J. Ashworth, George Danczuk and Jonathan A. Foster

Author Contributions

Joshua Nicks	Supervised GD. Worked with DJA on synthesis and characterisation of layered MOFs. Prepared and characterised all MON systems. Drafted manuscript and SI and created all figures. Assisted in editing of manuscript.
Michael Harris	Performed all SEM imaging.
David J. Ashworth	Worked with JN in synthesis and characterisation of layered MOFs.
George Danczuk	Performed initial syntheses and characterisation of layered MOFs and MONs from acetate series.
Jonathan A. Foster	Supervised all co-authors, assisted in editing of manuscript.

ARTICLE

Liquid exfoliation of a series of expanded layered metal-organic frameworks to form nanosheets

Joshua Nicks, Michael Harris, David J. Ashworth, George Danczuk and Jonathan A. Foster*

Metal–organic framework nanosheets (MONs) are attracting increasing attention as a diverse class of two-dimensional materials derived from metal–organic frameworks (MOFs). Although layered MOFs can be readily delaminated into nanosheets by liquid exfoliation, the effect of structural modifications and the MOFs starting morphology on the resulting nanosheets is poorly understood. In this work, we prepare an isoreticular series of layered MOFs based on linear benzenedicarboxylate derivatives with different lengths and using different copper salt sources. Liquid exfoliation of the large MOF crystals formed by the nitrate salt resulted in consistently monolayer nanosheets, but with low concentrations of material in suspension. In contrast, smaller MOF crystals formed using the acetate salt produced much thicker multi-layer nanosheets, but at high concentrations. The lateral dimensions of the monolayer nanosheets produced by the nitrate series were also significantly larger for the longer linker than the shorter linker. These insights help build our understanding of the principles behind the design of MONs and other two-dimensional materials.

Introduction

Metal-organic framework nanosheets (MONs) combine the highly tunable structures and properties of other metal-organic materials with the considerable surface areas and molecular thickness associated with two-dimensional (2D) materials.[1–4] As such, MONs have emerged as uniquely programmable 2D materials with applications in a variety of fields in which they are able to outperform their bulk counterparts, MOFs.[5] The vast number of known MOFs, specifically those with layered structures, have served as effective starting points for the formation of MONs through delamination.[6,7]

Liquid exfoliation has been widely applied to a range of different 2D materials, due to its ease of setup and wide applicability.[8,9] Recent work in this field has highlighted methods and mechanisms for the production of ultrathin nanosheets from these layered materials using liquid phase ultrasonication in particular.[10–13] In the case of MONs, their modular structure provides a unique opportunity to investigate the effect of systematic changes in the structure of layered materials on the size and properties of the nanosheets produced.[3,14] Identifying how the properties of these layered MOFs effect the process of their exfoliation into nanosheets is vital for understanding how to optimise the design of such materials. Despite this, few studies have examined what factors influence the exfoliation of MOFs and the thicknesses, lateral sizes, and concentrations of the nanosheets obtained.

The majority of work in this area has examined how the use of different solvent systems affect the exfoliation of layered MOFs into MONs. Moorthy et al. have probed the degree of exfoliation by correlating relative fluorescence intensity with nanosheet concentration in suspension, taking a screening approach to investigate the suitability of different solvents as exfoliation media, based on their hydrogen-bonding capabilties.[15,16] Yang et al. used a mixed methanol/n-propanol solvent system to obtain high quality $Zn_2(bim)_4$ nanosheets, attributing the enhanced exfoliation to smaller methanol molecules penetrating between the MOF layers, whilst larger n-propanol molecules adsorbed onto and stabilised the nanosheet surfaces.[17] Reports by Wang et al. and Ni et al. noted improved exfoliation, both in terms of concentration and aspect ratio, when using ionic liquids as exfoliation media, which stabilise nanosheets as they form by acting as surfactants.[18,19] Finally, a recent report by Fu and co-workers demonstrated that the introduction of monotopic modulators which reduce epitaxial crystal growth can facilitate enhanced dispersion of nanosheets.[20]

In our previous work, we have made use of isoreticular substitution to systematically tune the structure of layered MOFs and understand the effect on their exfoliation to form MONs. We demonstrated that incorporation of benzenedicarboxylate derivatives with hydrophilic or hydrophobic chains into paddlewheel-based layered MOFs highlighted significant differences in both the dispersion properties and the nanoscopic structures of these materials upon exfoliation in solvents of differing polarities.[21] Furthermore, blending of these ligands enhanced exfoliation into both polar and apolar solvents compared to either single-ligand system.[22] Though broad particle size distributions made drawing clear trends challenging, results in another study

showed that in MONs functionalised with different length alkyl chains, shorter chains gave the highest concentrations, but longer chains lead to thinner nanosheets with higher surface areas.[23] Blending of these ligands demonstrated that alkyl substituents with more disparate chain lengths produced thicker nanosheets than those close in chain length.[22] Finally, we have shown how post-synthetic introduction of a charged sulfonate group to a layered framework enhances exfoliation intro ultrathin nanosheets through an electrostatic repulsion effect.[24]

In this work, we look to investigate two different parameters and their effect on exfoliation of layered MOFs into nanosheets: (1) isoreticular linker expansion, and (2) choice of metal salt. The ligands chosen, shown in Figure 1a, were 1,4-naphthalenedicarboxylic acid (H_2(1,4-NDC)), 2,6-naphthalenedicarboxylic acid (H_2(2,6-NDC)), and biphenyl-4,4'-dicarboxylic acid (H_2(BPDC)). All three linkers contain two phenyl rings but the different connectivities mean they provide different linker lengths. Here we reacted them with copper salts to produce an expanded isoreticular series of layered MOFs based on the Cu_2 paddlewheel (PW) secondary building unit. This series therefore provides an ideal opportunity to test the effect of linker length/node spacing on the properties of the nanosheets.

This series of MOFs was prepared using copper nitrate trihydrate and copper acetate monohydrate. The nitrate salt has greater solubility which typically leads to slower crystallisation and large crystallites compared to the acetate salt which pre-arranges in the PW formation and facilitates faster deprotonation of the organic linker resulting in more rapid nucleation and smaller crystallites. This provides an opportunity to investigate the effect of the starting crystal size on the resulting nanosheets.

Results and discussion

Synthesis of the Isoreticular Layered MOF Series.

All MOFs were prepared according to the same procedure, in which separate DMF solutions of the chosen copper salt and the protonated linker were combined in glass reaction vials with Teflon-lined caps and heated to 110 °C for 18 hours. After formation, the MOFs were washed three times with DMF and diethyl ether to remove unreacted starting material and excess solvent. Full details of the synthetic procedure can be found in the experimental section and all data not included in the manuscript can be found in SI section S2. As we have previously observed desolvation of Cu_2-PW structures during exfoliation in acetonitrile, we sought to characterise these desolvated phases for the isoreticular series prepared in this report. Fully desolvated MOFs were obtained by washing of the solvated systems with acetonitrile five times before drying, ^{1}H NMR spectroscopy of the digested samples was used to confirm full desolvation for all samples (Section S3).
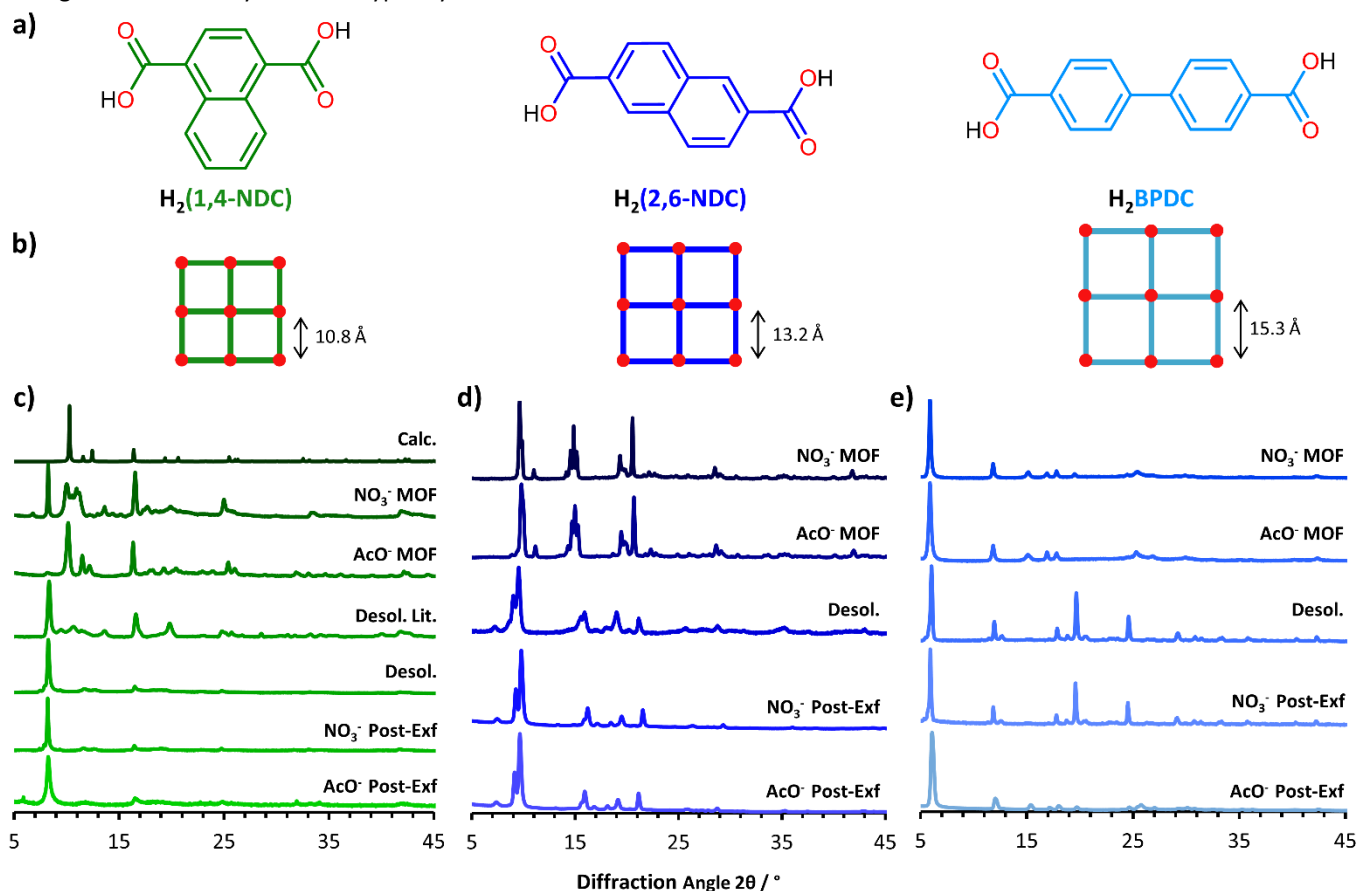
Figure 1. Structures of **a)** the three ligands used in this study: 1,4-napthalenedicarboxylic acid, 2,6-napthalenedicarboxylic acid, and biphenyl-4,4'-dicarboxylic acid, **b)** representations of the isoreticular square grids of each system. Stacked PXRD patterns of the as-synthesised, desolvated, and post-exfoliation powders for the **c)** Cu(1,4-NDC), **d)** Cu(2,6-NDC), and **e)** Cu(BPDC) systems.

ARTICLE

Figures 1b-d show the as-synthesised and desolvated powder X-ray diffraction (PXRD) patterns for each MOF in the series. Cu(1,4-NDC)(DMF) forms as a green powder from both salts. Elemental microanalysis and ^{1}H NMR spectroscopy of the digested samples indicated that the MOF prepared from the nitrate source is only 84% solvated. The acetate synthesised MOF has an excess of DMF present at 126% solvation, likely due to solvent molecules present in the pores. These degrees of solvation are reflected in the PXRD patterns of the MOFs. The nitrate pattern shows the presence of both the solvated and desolvated phase, whereas the acetate shows the solvated phase only. The fully desolvated phase has been previously documented by Maji and co-workers.[25]

Cu(2,6-NDC)(DMF) forms as a blue powder from both salts. In this instance, both the MOFs formed from the acetate and nitrate salts were found to be ~90% solvated by both microanalysis and ^{1}H NMR studies. A crystal structure for this compound has not been reported so these results cannot be compared to any calculated pattern. However, these patterns are consistent with those observed by Gascon *et al.*[26] As predicted, there is a phase change observed upon desolvation in acetonitrile, which matches closely with the structure calculated by Liu and Ma *et al.*[27]

Cu(BPDC) forms as a light blue powder from both salts in a fully desolvated form. Though neither a free-standing layered MOF nor nanosheets of this system have been reported, a SURMOF system demonstrated by Wöll and co-workers supports the structures obtained in this study, which indicate highly symmetrical P4-type stacking, in which each Cu$_2$-PW stacks directly above and below those in adjacent layers.[28] Microanalysis , ^{1}H NMR, and Fourier transform infrared (FT-IR) spectra indicate the presence of no DMF and one molecule of water per Cu(BPDC) unit, which likely occupy the pores of the framework to give four molecules of water per pore. Upon

treatment with acetonitrile, some changes in peak intensity are observed but peak positions remain unchanged.

A substantial difference in the rate of reaction between the layered MOFs formed from the two different salts was clearly observed. The acetate salts precipitated microcrystalline powders almost immediately at room temperature prior to heating, whereas no precipitate is observed for the nitrate systems until after they were heated (Figure S1). As shown in Figure 2, scanning electron microscopy (SEM) images of all MOFs synthesised from the nitrate salt showed material approximately 1-15 µm in size with clearly layered morphologies. This layering is also observed in SEM images of the desolvated forms of these systems (S13), which also show similar particle size ranges. In contrast, images of the systems formed from the acetate source showed only aggregates <1 µm in size, and no clear layering could be observed in these samples.

We attribute this difference in particle size and morphology to three different factors: (1) prearrangement of the Cu^{2+} ions in the paddlewheel structure with the acetate anion leads to an accelerated rate of reaction and thus faster crystallisation into smaller particles,[29] (2) the acetate ions facilitate faster deprotonation of the dissolved linkers also leading to faster crystallisation, and (3) the acetate acts as a monotopic crystal size modulator, restricting growth in the lateral dimensions.[30–33] This is further evidenced by ^{1}H NMR spectroscopy of the digested MOFs, (S2-S7) which shows 3-5% incorporation of acetate into each of the MOF structures.

Liquid Exfoliation to form MONs.

The clear difference in particle size between both series of layered MOFs serves as an ideal starting point to investigate the
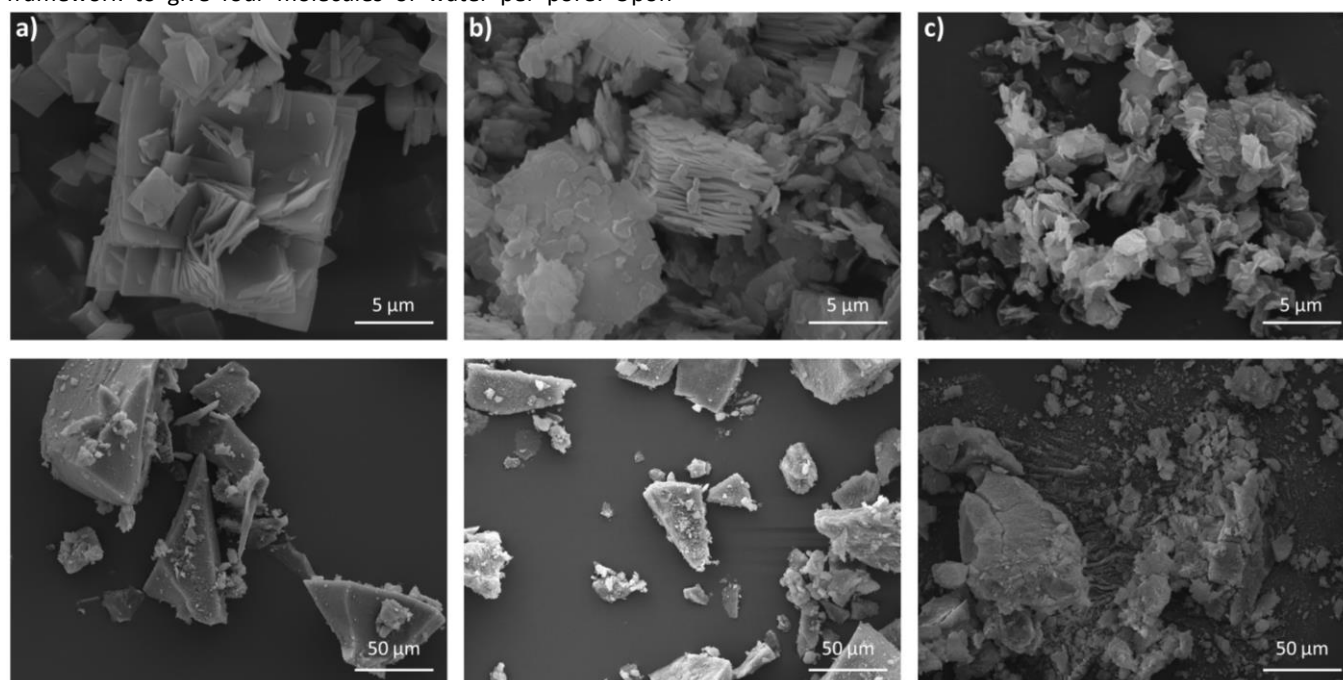
Figure 2. SEM images of the layered MOFs **a)** Cu(1,4-NDC)(DMF), **b)** Cu(2,6-NDC)(DMF) and **c)** Cu(BPDC), formed from nitrate (top) and acetate salts (bottom) respectively. Supplementary SEM images are provided in Figures S10-12.
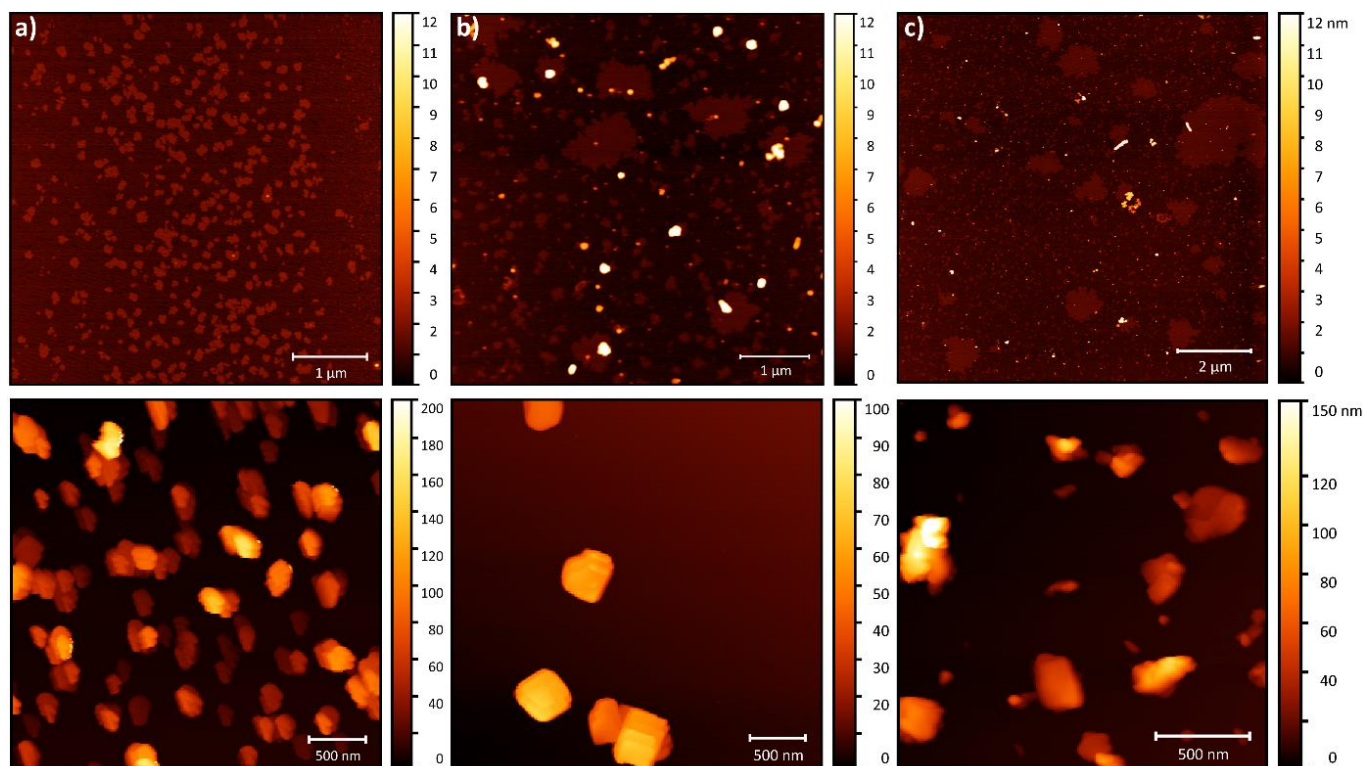
Figure 3. AFM topographical images of **a)** Cu(1,4-NDC), **b)** Cu(2,6-NDC) and **c)** Cu(BPDC) MONs obtained from liquid exfoliation of layered MOFs prepared from the nitrate (top) and the acetate (bottom) salts. Additional images are provided in Figures S25-27.

Table 1. Summary of statistical size distribution data of MONs obtained from exfoliation of the MOF isoreticular series. Additional AFM images used for size distribution analyses can be seen in Figures S25-27.

	Cu(1,4-NDC)		Cu(2,6-NDC)		Cu(BPDC)	
	NO_3^-	AcO^-	NO_3^-	AcO^-	NO_3^-	AcO^-
$\bar{x}$ T ± SD / nm	0.80 ±0.04	77 ±54	0.80 ±0.05	101 ±70	0.80 ±0.03	71 ±62
$\bar{x}$ LD ± SD / nm	220 ±172	374 ±152	400 ±335	414 ±128	821 ±441	183 ±97
$\bar{x}$ AR ± SD / nm	270 ±210	7.1 ±4.4	502 ±437	5.4 ±3.1	1020 ±550	3.6 ±1.9

LD = largest lateral dimension, T = thickness, AR = aspect ratio, and SD = standard deviation. Mean aspect ratios were determined for individual particles.

effect of the precursor systems size on its liquid exfoliation into MONs. In order to investigate these effects, all layered MOFs were subject to the same exfoliation procedure that we have previously reported, in which soft high frequency ultrasound is used to reduce fragmentation, whilst samples are stirred to minimize hot-spots and aid reproducibility. Acetonitrile was chosen as the exfoliation solvent, as our previous work has shown it to be an effective candidate for related copper benzenedicarboxylate-based systems.[21,34,35] MOF samples (5 mg) were suspended in acetonitrile (6 mL) in a sealed vial and subject to ultrasound at 80 kHz for 12 hours at <18 °C temperatures. Each sample was then centrifuged at 362 xG (1500 rpm) for 1 hour to remove bulk unexfoliated material, leaving nanosheets in suspension.

Suspension concentrations of both series were demonstrably different even from naked eye observations. MON suspensions obtained from exfoliation of the acetate series were significantly more intense in colour, as shown in Figure S15. This is reflected in Tyndall scattering observations, in which scattering is much stronger for the acetate series, suggesting a higher concentration of colloidal material in suspension. UV-visible spectroscopy was used to determine the obtained concentrations, which corroborated this qualitative evidence. As detailed in Table S2, concentrations of the nitrate series, 0.05-0.1 mg mL^{-1} are significantly reduced compared to those of the acetate series, which give high yields of 0.6-0.7 mg mL^{-1}. All MON samples are colloidally stable for at least 3 days. However, after this time MON suspensions obtained from the nitrate series began to crash out, whereas those from the acetate series remained stable for at least a month.

PXRD patterns of each system post-exfoliation indicate a phase change to the desolvated forms in all systems. We have observed this phenomenon in multiple previous reports in which we have performed liquid exfoliation of DMF solvated Cu$_2$-PW MOFs in acetonitrile.[22,23,36] This arises due to the ability of excess acetonitrile to displace DMF from the PW axial sites, but its inability to remain coordinated once dried. This is further evidenced by ^{1}H NMR spectra of the bulk material obtained after exfoliation, which indicates full desolvation in each system (Figures S22-24).

Atomic force microscopy (AFM) topographical imaging of all samples shows distinct trends in morphology for both series, with size distribution data for all samples detailed in Table 1. As shown in Figure 3, MONs obtained from the nitrate series are

consistently ultrathin, down to monolayer thicknesses of ~0.8 nm. In contrast, these images indicate that all MONs in the acetate series were clearly multilayer with average thicknesses between 71-101 nm. Though there is no clear trend in lateral size distribution between the two series, the aspect ratios of the nanosheets obtained from the nitrate salt are orders of magnitude larger, owing to their ultrathin thicknesses.

The key variable between the two series is the initial particle sizes of the layered MOFs exfoliated to obtain these nanosheets. As such, we attribute this difference in nanosheet thicknesses to the difference in the particle sizes of the precursor MOFs. SEM imaging of the bulk material removed by centrifugation post-exfoliation of the nitrate series continues to show particles of micrometres in size with defined layers, despite ultrasonication for extensive periods of time (Figures S29-31). This may suggest that the larger particles of the nitrate series preferentially delaminate into ultrathin nanosheets, fragmenting largely only once dispersed. In contrast, the smaller particles of the acetate series disperse much more easily, meaning ultrasound forces induce delamination and fragmentation simultaneously. This difference in precursor MOF particle size could also explain the difference in concentrations obtained from each series, with the smaller acetate systems dispersing more easily, leading to higher yields of exfoliation.

Within the consistently monolayer nanosheets produced by the nitrate series the lateral sizes and aspect ratios appear to increase with expansion of the ligand. Exfoliation of Cu(1,4-NDC) clearly gives smaller nanosheets 220 ±172 nm wide, whereas Cu(BPDC) yields much larger nanosheets with average lateral dimensions of 821 ±441 nm. Cu(2,6-NDC) appears to give a mixture of both small and large nanosheets, with intermediate widths of 400 ±335 nm. This is tentatively attributed to the higher density of metal nodes associated with shorter linkers, which are the most likely fragmentation sites. Interestingly, these nanosheets have highly irregular shapes, a phenomenon we have previously observed in similarly ultrathin supramolecular systems.[24,37] No clear trend in lateral size distributions was observed within the acetate series. However, in contrast to the nitrate series, nanosheet aspect ratios decrease with expansion of the linker.

Due to the low concentrations of the MON suspensions obtained from the nitrate series, dynamic light scattering (DLS) data could not be obtained for these systems. However, DLS measurements of the MON suspensions obtained from the acetate series corroborate the trend in the lateral size distributions obtained from AFM of each system, with number average diameters of 121 (Cu(1,4-NDC), 234 (Cu(2,6-NDC)), and 56 nm (Cu(BPDC)) (Figure S28). As noted in previous reports, DLS measurements underestimate the lateral dimensions of nanosheets with respect to AFM, due to the assumption of spherical particles made in the use of the Stokes–Einstein equation.

Conclusions

We have developed an isoreticular series of layered Cu_2-PW MOFs incorporating three different length ligands from two different copper salts, copper nitrate and acetate. The use of different copper salts with different reactivities resulted in layered MOF particles with different sizes. We investigated the effects of both ligand expansion and initial particle size, on the exfoliation of these layered systems into MONs. PXRD measurements indicated formation of all three MOFs from both salts with differing degrees of solvation at the PW axial sites, as determined by ^{1}H NMR spectroscopy and elemental microanalysis. SEM imaging of these layered MOFs illustrated substantial differences between the two series, with the nitrate series forming particles approximately 1-15 μm in size with clearly layered morphologies, whereas the acetate series present as aggregates of significantly smaller, <1 μm sized particles. This was attributed to the different rates of MOF crystallisation associated with the different salt sources. The nitrate salt has increased solubility, leads to slower crystallisation and larger crystallites, whereas the acetate salt pre-arranges the PW SBU and facilitates faster deprotonation of the organic linker, resulting in the faster crystal growth observed.

Ultrasound-assisted liquid exfoliation of these layered systems in acetonitrile produced suspensions of MONs with differing concentrations and morphologies between the two series. MONs formed from the acetate series were found to have significantly higher concentrations and multi-layer thicknesses, whereas those of the nitrate series were found to be significantly lower in concentration but with monolayer ~0.8 nm thicknesses. The difference in exfoliation behaviour of the two series was attributed to difference in particle size of the precursor layered MOFs. Expansion of the ligand resulted in increased aspect ratios within the consistently monolayer nitrate series, attributed to the higher density of metal nodes at which fragmentation can occur. In contrast, the multilayer nanosheets obtained from the acetate series decrease in aspect ratio with ligand expansion, with no clear trend in lateral size distributions.

Understanding how to control the dimensions of nanosheets obtained through liquid exfoliation is a key challenge to realising their use across diverse applications. This work identifies the importance of the starting size of the MOF particles in determining the dimensions and concentrations of MONs obtained through liquid exfoliation. It also demonstrates that ligand expansion within an isoreticular series of MOFs can also impact the dimensions of the nanosheets obtained. We hope that this systematic study of six MOFs will provide a useful starting point for developing generalizable rules to guide the design of MONs and other two-dimensional materials.

Experimental

Further details on materials, reagents, equipment and characterisation methods are available in the supporting information provided.

Layered MOF Syntheses.

To prepare each layered MOF, the copper salt of choice (0.125 mmol) and dicarboxylic acid ligand (0.131 mmol) were each dissolved in DMF (5 mL) then combined in reaction vials with Teflon-lined caps. The reaction mixtures were then placed in a reaction oven and heated to 110 °C at a rate of 1 °C min^{-1}, then maintained at this temperature for 18 hours, after which they were cooled to room temperature at a rate of 0.1 °C min^{-1}. Samples were then transferred to polypropylene centrifuge tubes, centrifuged at 3258 xG (4500 rpm, 5 mins), and the supernatant was removed. Samples were then washed with DMF (3 x 30 mL, 4500 rpm, 30 mins) and diethyl ether (2 x 25 mL. 4500 rpm, 2 mins), before being left to dry in air and then a vacuum oven (60 °C, 4 hours), affording each MOF as a microcrystalline powder.

Layered MOF Desolvation.

The layered MOFs (30 mg) were desolvated by suspension in acetonitrile (10 mL) followed by stirring for 3 hours. Sample were centrifuged at at 3258 xG (4500 rpm, 5 mins), then the solvent was cycled. This process was repeated 5 times, followed by removal of excess solvent by washing with diethyl ether (2 x 5 mL) and drying *in vacuo*.

Liquid Exfoliation.

Samples of layered MOF (5 mg) were suspended in acetonitrile (6 mL) in reaction vials with Teflon-lined caps. Samples were then sonicated at 80 kHz for 12 hours at 100% power, at a temperature <19 °C and with stirring of the vials to prevent hot spots. Sonication was followed by centrifugation for 1 hour at 362 xG (1500 rpm) to remove unexfoliated material, followed by separation of the supernatant to yield suspensions of MONs.

Author Contributions

J.N., D.J.A., and G.D. synthesised and characterised the layered MOFs. M.H. performed all SEM imaging. J.N. and G.D. prepared and characterised all MONs. J.N. drafted manuscript, SI, and created all figures. J.A.F. conceived project and edited manuscript. All authors have given approval to the final version of the manuscript.

Conflicts of interest

There are no conflicts to declare.

Acknowledgements

References

1   M. J. Allen, V. C. Tung and R. B. Kaner, *Chem. Rev.*, 2010, **110**, 132–145.

2   M. Zhao, Y. Huang, Y. Peng, Z. Huang and Q. Ma, *Chem. Soc. Rev.*, 2018, **47**, 6267–6295.

3   D. J. Ashworth and J. A. Foster, *J. Mater. Chem. A*, 2018, **6**, 16292–16307.

4   G. R. Bhimanapati, Z. Lin, V. Meunier, Y. Jung, J. Cha, S. Das, D. Xiao, Y. Son, M. S. Strano, V. R. Cooper, L. Liang, S. G. Louie, E. Ringe, W. Zhou, S. S. Kim, R. R. Naik, B. G. Sumpter, H. Terrones, F. Xia, Y. Wang, J. Zhu, D. Akinwande, N. Alem, J. A. Schuller, R. E. Schaak, M. Terrones and J. A. Robinson, *ACS Nano*, 2015, **9**, 11509–11539.

5   J. Nicks, K. Sasitharan, R. R. R. Prasad, D. J. Ashworth and J. A. Foster, *Adv. Funct. Mater. Mater.*, **31**, 2103723.

6   P. Z. Moghadam, A. Li, X.-W. Liu, R. Bueno-Perez, S.-D. Wang, S. B. Wiggin, P. A. Wood and D. Fairen-jimenez, *Chem. Sci.*, 2020, **11**, 8373–8387.

7   G. Chakraborty, I.-H. Park, R. Medishetty and J. J. Vittal, *Chem. Rev.*, **121**, 7, 3751-3891.

8   J. N. Coleman, M. Lotya, A. O. Neill, S. D. Bergin, P. J. King, U. Khan, K. Young, A. Gaucher, S. De, R. J. Smith, I. V Shvets, S. K. Arora, G. Stanton, H. Kim, K. Lee, G. T. Kim, G. S. Duesberg, T. Hallam, J. J. Boland, J. J. Wang, J. F. Donegan, J. C. Grunlan, G. Moriarty, A. Shmeliov, R. J. Nicholls, J. M. Perkins, E. M. Grieveson, K. Theuwissen, D. W. Mccomb, P. D. Nellist and V. Nicolosi, *Science*, 2011, **331**, 568–572.

9   H. Tao, Y. Zhang, Y. Gao, Z. Sun, C. Yan and J. Texter, *Phys. Chem. Chem. Phys.*, 2017, **19**, 921–960.

10   Z. Li, R. J. Young, C. Backes, W. Zhao, X. Zhang, A. A. Zhukov, E. Tillotson, A. P. Conlan, F. Ding, S. J. Haigh, K. S. Novoselov and J. N. Coleman, *ACS Nano*, 2020, **14**, 10976–10985.

11   A. Ciesielski and P. Samorì, *Chem. Soc. Rev.*, 2014, **43**, 381–398.

12   J. Shen, Y. He, J. Wu, C. Gao, K. Keyshar, X. Zhang, Y. Yang, M. Ye, R. Vajtai, J. Lou and P. M. Ajayan, *Nano Lett.*, 2015, **15**, 5449–5454.

13   C. Backes, T. M. Higgins, A. Kelly, C. Boland, A. Harvey, D. Hanlon and J. N. Coleman, *Chem. Mater.*, 2017, **29**, 243–255.

14   M. Zhao, Y. Huang, Y. Peng, Z. Huang, Q. Ma and H. Zhang, *Chem. Soc. Rev.*, 2018, **47**, 6267–6295.

15   S. Jindal, V. K. Maka, G. Anjum and J. N. Moorthy, *ACS Appl. Nano Mater.*, 2021, **4**, 1, 449-458.

16   P. Chandrasekhar, A. Mukhopadhyay, G. Savitha and J. N. Moorthy, *J. Mater. Chem. A*, 2017, **5**, 5402–5412.

17   Y. Peng, Y. Li, B. Yujie, H. Jin, W. Jiao, X. Liu and W. Yang, *Science*, **346**, 1356-1359.

18   D. Liu, B. Liu, C. Wang, W. Jin, Q. Zha, G. Shi, D. Wang and X. Sang, *ACS Sustain. Chem. Eng.*, 2020, **8**, 2167–2175.

19   X. Sang, D. Liu, J. Song, C. Wang, X. Nie, G. Shi, X. Xia, C. Ni and D. Wang, *Ultrason. Sonochem.*, 2021, **72**, 105461.

20   H. Zhou, L. Zhang, G. Wang, Y. Zhang, X. Wang, M. Li, F. Fan, Y. Li, T. Wang, X. Zhang and Y. Fu, *ACS Appl. Mater. Interfaces*, 2021, **13**, 33, 39755-3762.

21   D. J. Ashworth, A. Cooper, M. Trueman, R. W. M. Al-Saedi, L. D. Smith, A. J. H. M. Meijer and J. A. Foster, *Chem. - A*

Eur. J., 2018, **24**, 17986–17996.

22   D. J. Ashworth and J. A. Foster, *Nanoscale*, 2020, **12**, 7986–7994.

23   D. J. Ashworth, T. M. Roseveare, A. Schneemann, M. Flint, I. D. Bernáldes, P. Vervoorts, R. A. Fischer, L. Brammer and J. A. Foster, *Inorg. Chem.*, 2019, **58**, 10837–10845.

24   J. Nicks, J. Zhang and J. A. Foster, *Chem. Commun.*, 2019, **55**, 8788–8791.

25   P. Kanoo, K. L. Gurunatha and T. K. Maji, *J. Mater. Chem.*, 2010, **20**, 1322.

26   T. Rodenas, I. Luz, G. Prieto, B. Seoane, H. Miro, A. Corma, F. Kapteijn, F. X. Llabrés i Xamena and J. Gascon, *Nat. Mater.*, 2014, **14**, 48–55.

27   L. Liu, Y. Zhang, Y. Qiao, S. Tan, S. Feng, J. Ma, Y. Liu and J. Luo, *Nano Today*, 2021, **40**, 101262.

28   J. Liu, B. Lukose, O. Shekhah, H. K. Arslan, P. Weidler, H. Gliemann, S. Bräse, S. Grosjean, A. Godt, X. Feng, K. Müllen, I. B. Magdau, T. Heine and C. Wöll, *Sci. Rep.*, 2012, **2**, 1–5.

29   R. Ameloot, F. Vermoortele, W. Vanhove, M. B. J. Roeffaers, B. F. Sels and D. E. De Vos, *Nat. Chem.*, 2011, **3**, 382–387.

30   R. S. Forgan, *Chem. Sci.*, 2020, **11**, 4546–4562.

31   M. Pham, G. Vuong, F. ric-G. Fontaine and T. Do, *Cryst. Growth Des.*, 2012, **12**, 3091–3095.

32   K. A. S. Usman, J. W. Maina, S. Seyedin, M. T. Conato, L. M. Payawan, L. F. Dumée and J. M. Razal, *NPG Asia Mater.*, 2020, **12**, 1-18.

33   C. R. Marshall, S. A. Staudhammer and C. K. Brozek, *Chem. Sci.*, 2019, **10**, 9396–9408.

34   J. A. Foster, S. Henke, A. Schneemann, R. A. Fischer and A. K. Cheetham, *Chem. Commun.*, 2016, **52**, 10474–10477.

35   J. Nicks, J. Zhang and J. A. Foster, *Chem. Commun.*, 2019, **55**, 8788–8791.

36   D. J. Ashworth, A. Cooper, M. Trueman, R. W. M. Al-Saedi, S. D. Liam, A. J. Meijer and J. A. Foster, *Chem. - A Eur. J.*, 2018, **24**, 17986–17996.

37   J. Nicks, S. A. Boer, J. A. Foster and N. G. White, *Chem. Sci.*, 2021, **12**, 3322-3327.

Supporting Information

Liquid exfoliation of a series of expanded layered metal-organic frameworks to form nanosheets

Joshua Nicks, Michael Harris, David J. Ashworth, George Danczuk and Jonathan A. Foster*

a. Department of Chemistry, University of Sheffield, Sheffield, S3 7HF, UK

Contents.

S1. General remarks

S1.1. Materials

Commercial solvents, reagents and spectroscopic grade deuterated solvents were used as purchased without further purification, as listed: copper acetate monohydrate (98+%, Alfa Aesar), copper nitrate trihydrate (98%, SLS), 1,4-benzenedicarboxylic acid (99+%, Acros Organics), 1,4-napthalenedicarboxylic acid (98+%, Alfa Aesar), 2,6-naphthalenedicarboxylic acid (99%, Fluorochem), 4,4'-biphenyldicarboxylic acid (98%, Acros Organics), dimethylformamide (≥99%, Fischer), diethyl ether (≥99.8%, Sigma-Aldrich), acetonitrile (≥99%, Fisher), dimethyl sulfoxide-d_6 (99.5 atom % D, Sigma-Aldrich), deuterium chloride solution (35 wt. % in D2O, ≥99 atom % D, Sigma-Aldrich).

Solvothermal syntheses were carried out using borosilicate vials with Teflon-lined caps in a Carbolite Gero PF 60 Oven. Exfoliations were performed in a Fisher brand Elmasonic P30H ultrasonic bath (2.75 L, 380/350 W, UNSPSC 42281712) filled with water.

S1.2. Analytical Procedures

Powder X-ray diffraction data were collected using a Bruker-AXS D8 diffractometer using CuK$_\alpha$ (λ=1.5418 Å) radiation and a LynxEye position sensitive detector in Bragg Brentano parafocussing geometry using a packed glass capillary (MOFs) or a flat silicon plate (MONs).

Elemental microanalyses were performed by the microanalytical service at the Department of Chemistry, University of Sheffield using a Vario MICRO Cube in an atmosphere of pure O_2. Elemental contents are determined to a tolerance of ± 0.5 %.

^{1}H NMR spectra were recorded at 300 K using a Bruker Avance III HD 400 spectrometer equipped with a standard geometry 5mm BBFO probe with a single z-gradient at 400 MHz (1H). MOFs were digested prior to submission, using DCl (5 μL) and d_6-DMSO (1 mL).

Thermogravimetric analyses were performed using a Perkin-Elmer Pyris 1 instrument. Approximately 4 mg of sample was weighed into a ceramic pan, held under nitrogen flow of 20 cm^3 min^{-1} at 25 °C for 10 minutes to purge the sample and allow for equilibration, then ramped to end temperatures at 1 °C min^{-1}. Samples were then held at the final temperature for 10 minutes to allow sample burn off.

FT-IR spectra were recorded using a Perkin Elmer Spectrum 100 FT-IR spectrophotometer, equipped with a SenseIR diamond ATR module. Samples were analysed without further preparation, and spectra were obtained in reflectance mode, using 12 scans with a spectral resolution of 1 cm^{-1}.

SEM samples were loaded onto carbon sticky tab on aluminium sample stubs, coated with approximately 20 nm gold using an Edwards S150B sputter coater and loaded into a TESCAN VEGA3 LMU SEM, operated at 15 keV with images collected at 10,000x magnification using the secondary electron detector.

UV-vis absorption spectra were obtained on a Varian Cary 50 Bio spectrophotometer using standard 1 cm width quartz cells and Perkin Elmer Spectrum One software. Spectral data was formatted using Excel.

Atomic force microscopy images were recorded using a Bruker Multimode 5 Atomic Force Microscope, operating in soft-tapping mode in air under standard ambient temperature and pressure, fitted with Bruker OTESPA-R3 silicon cantilevers operated with a drive amplitude of ~18.70 mV and resonance frequency of ~236 kHz. Samples were prepared by drop-casting 10 μL drops of suspension onto the centre of freshly cleaved mica sheets heated to 100 °C on a hot plate. These sheets were stuck to stainless steel, magnetic Agar scanning probe microscopy specimen discs. Image data were processed using Gwyddion software. For size distribution analysis, particles with lateral dimensions <30 nm were not recorded to neglect defects and small fragments on the sample surface.

Dynamic light scattering measurements collected using a Malvern Zetasizer Nano Series particle size analyser, and a He-Ne laser at 633 nm, operating in backscatter mode (173 °). Samples were equilibrated at 298 K for 30 s prior to analysis.

S2. Supplementary data for the layered MOF series
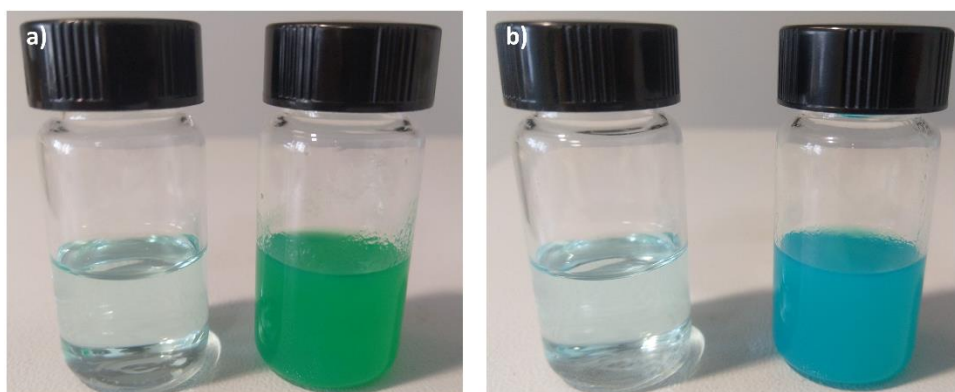
Figure S1. Images showing reaction solutions for the synthesis of **a)** Cu(1,4-NDC)(DMF) and **b)** Cu(2,6-NDC)(DMF) from nitrate (left) and acetate (right) salts approximately 20 seconds after mixing.
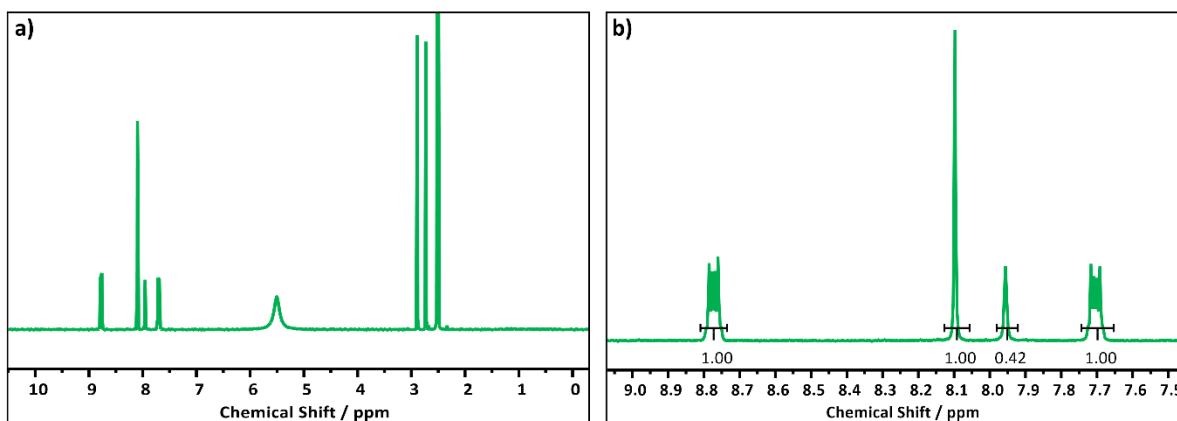
Figures S2. ^{1}H NMR spectra of the synthesised Cu(1,4-NDC)(DMF) MOF from the nitrate salt, digested in DCl and d_6-DMSO, showing **a)** the full spectrum and **b)** a focus on the linker region.
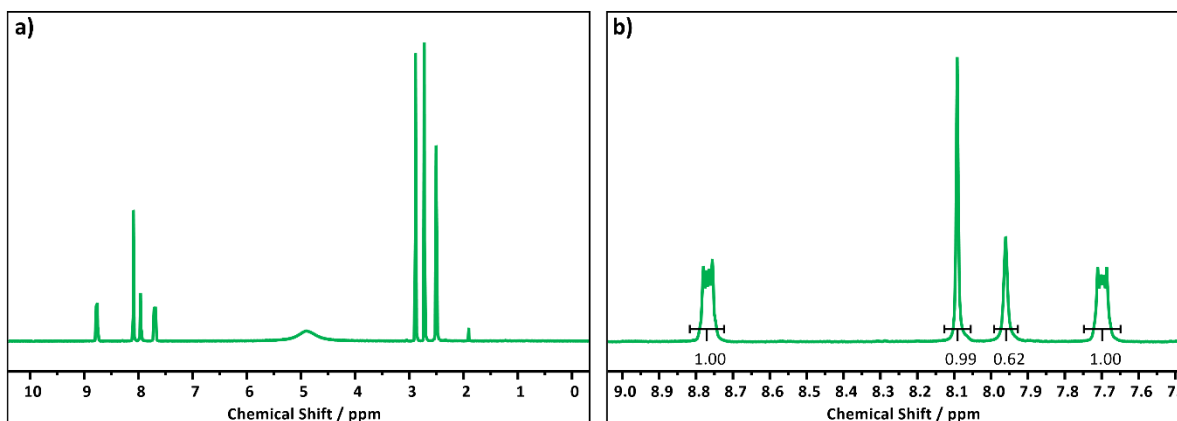
Figures S3. ^{1}H NMR spectra of the synthesised Cu(1,4-NDC)(DMF) MOF from the acetate salt, digested in DCl and d_6-DMSO, showing **a)** the full spectrum and **b)** a focus on the linker region.
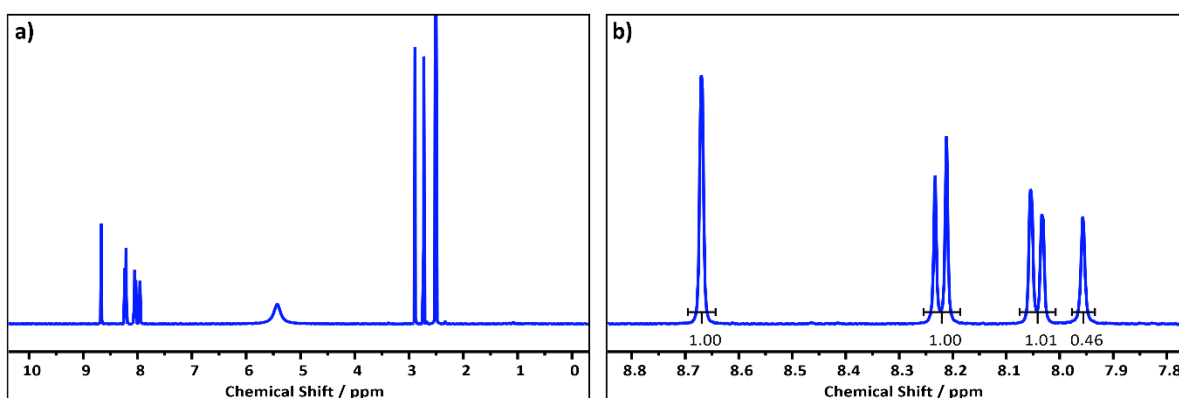
Figures S4. ^{1}H NMR spectra of the synthesised Cu(2,6-NDC)(DMF) MOF from the nitrate salt, digested in DCl and d_6-DMSO, showing **a)** the full spectrum and **b)** a focus on the linker region.
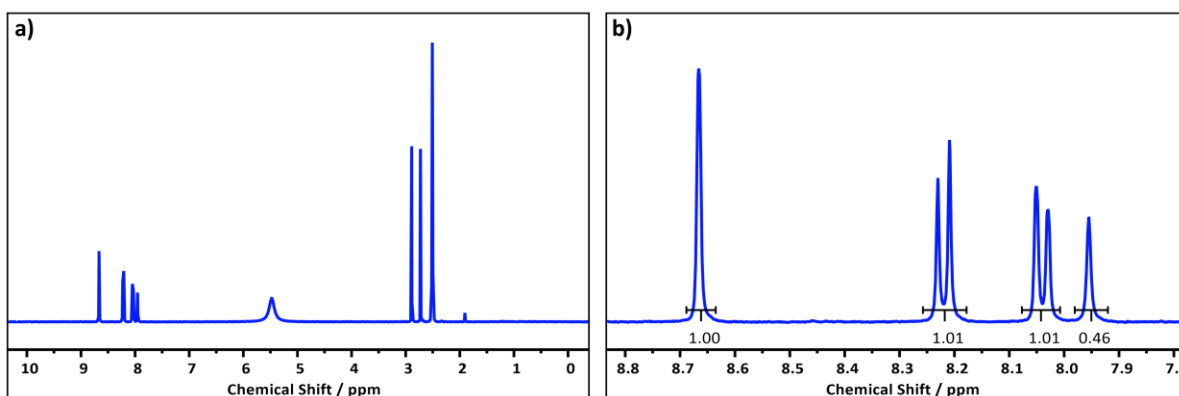
Figures S5. ^{1}H NMR spectra of the synthesised Cu(2,6-NDC)(DMF) MOF from the acetate salt, digested in DCl and d_6-DMSO, showing **a)** the full spectrum and **b)** a focus on the linker region.
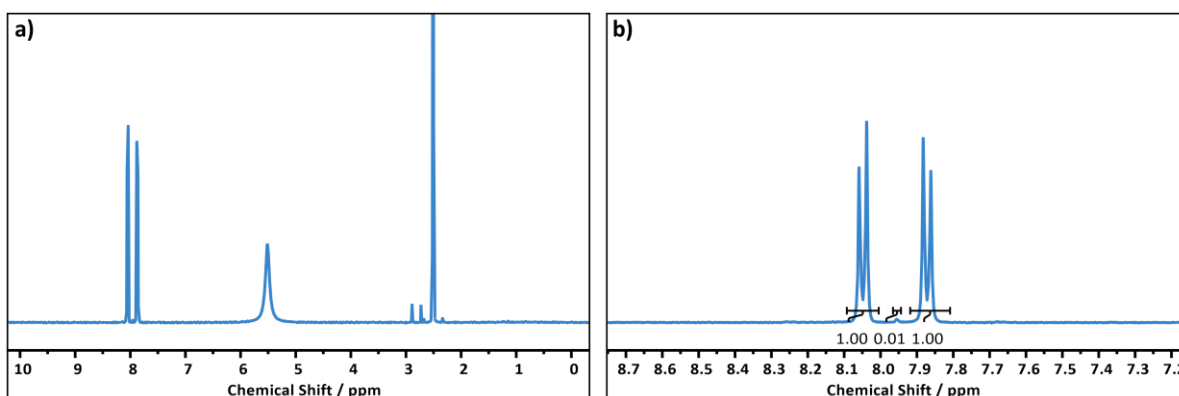
Figures S6. ^{1}H NMR spectra of the synthesised Cu(BPDC) MOF from the nitrate salt, digested in DCl and d_6-DMSO, showing **a)** the full spectrum and **b)** a focus on the linker region.
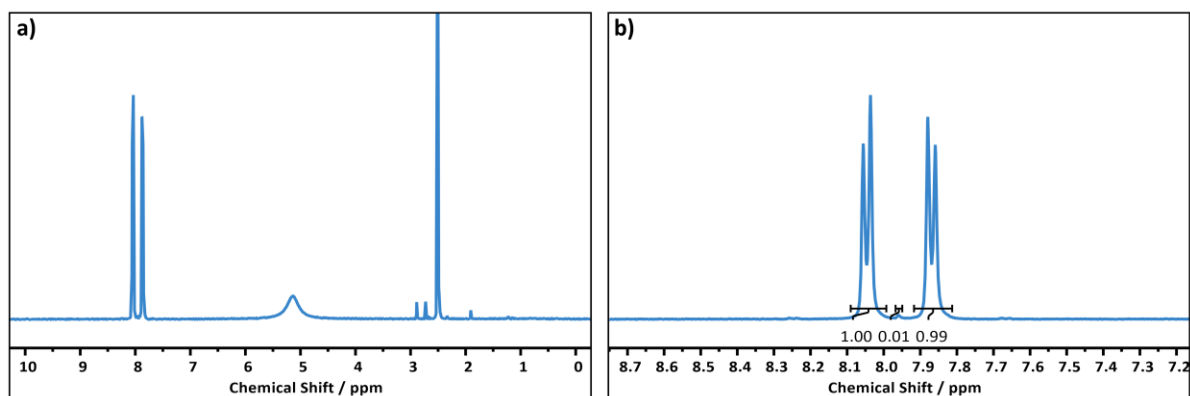
Figures S7. ^{1}H NMR spectra of the synthesised Cu(BPDC) MOF from the acetate salt, digested in DCl and d$_6$-DMSO, showing **a)** the full spectrum and **b)** a focus on the linker region.

Table S1. Elemental microanalysis data for all layered MOFs prepared in this study. Measurements are determined to a tolerance of ± 0.5%.

	Cu(1,4-NDC)(DMF) (NO$_3^-$)			
	Observed	**Calc. CuC$_{15}$H$_{13}$NO$_5$**	**Calc. CuC$_{14.52}$H$_{11.88}$N$_{0.84}$O$_{4.84}$***	**Δ**
C	49.91	51.35	51.43	-1.52
H	3.94	3.73	3.51	+0.43
N	3.35	3.99	3.47	-0.12

* Accounting for 84% solvation

	Cu(1,4-NDC)(DMF) (OAc$^-$)			
	Observed	**Calc. CuC$_{15}$H$_{13}$NO$_5$**	**Calc. CuC$_{15.78}$H$_{14.82}$N$_{1.26}$O$_{5.26}$***	**Δ**
C	49.97	51.35	51.25	-1.28
H	4.25	3.73	4.01	+0.24
N	4.52	3.99	4.77	-0.25

* Accounting for 126% solvation and 5% acetate inclusion

	Cu(2,6-NDC)(DMF) (NO$_3^-$)			
	Observed	**Calc. CuC$_{15}$H$_{13}$NO$_5$**	**Calc. CuC$_{14.76}$H$_{12.44}$N$_{0.92}$O$_{4.92}$***	**Δ**
C	51.37	51.35	51.39	-0.02
H	3.86	3.73	3.61	+0.25
N	3.83	3.99	3.74	-0.09

* Accounting for 92% solvation

	Cu(2,6-NDC)(DMF) (OAc$^-$)			
	Observed	**Calc. CuC$_{15}$H$_{13}$NO$_5$**	**Calc. CuC$_{15.78}$H$_{14.82}$O$_{5.26}$N$_{1.26}$***	**Δ**
C	51.10	51.35	51.32	-0.22
H	3.98	3.73	3.62	+0.36
N	3.93	3.99	3.71	+0.22

* Accounting for 92% solvation and 4% acetate inclusion

	Cu(BPDC) (NO$_3^-$)			
	Observed	**Calc. CuC$_{14}$H$_8$O$_4$**	**Calc. CuC$_{14}$H$_{10}$O$_5$***	**Δ**
C	51.70	55.37	52.26	-0.56
H	3.52	2.65	3.13	+0.39
N	0.00	0.00	0.00	0.00

* Accounting for 1 equivalent water

| Cu(BPDC) (OAc$^-$)				
	Observed	Calc. CuC$_{14}$H$_8$O$_4$	Calc. CuC$_{14.06}$H$_{10.09}$NO$_{5.06}$*	Δ
C	51.84	55.37	52.19	-0.35
H	3.44	2.65	3.12	+0.32
N	0.00	0.00	0.00	0.00

* Accounting for 1 equivalent water and 3% acetate inclusion
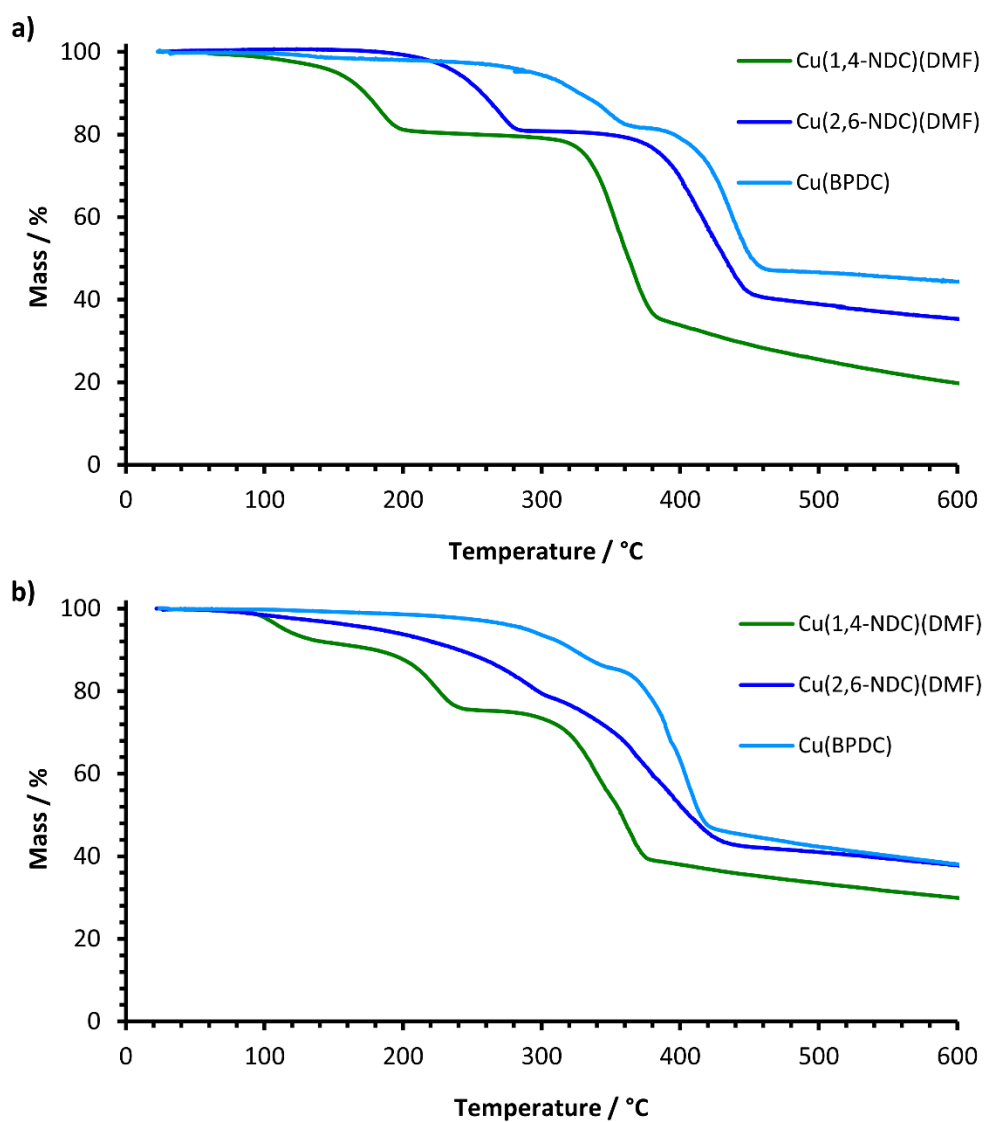
**Figure S8.** TGA profiles for the layered MOFs synthesised from **a)** the nitrate salt and **b)** the acetate salt.
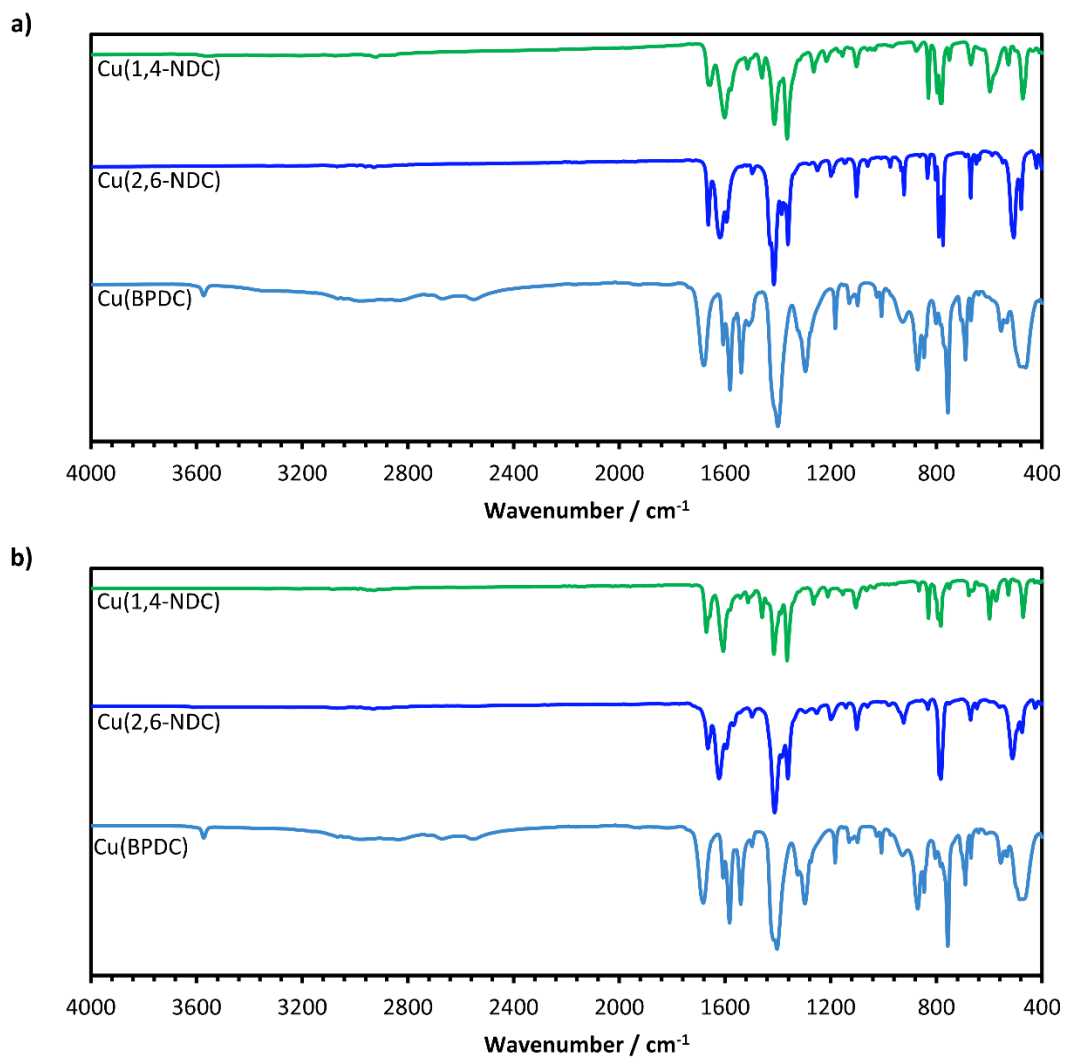
Figure S9. FT-IR spectra for the layered MOFs synthesised from **a)** the nitrate salt and **b)** the acetate salt.
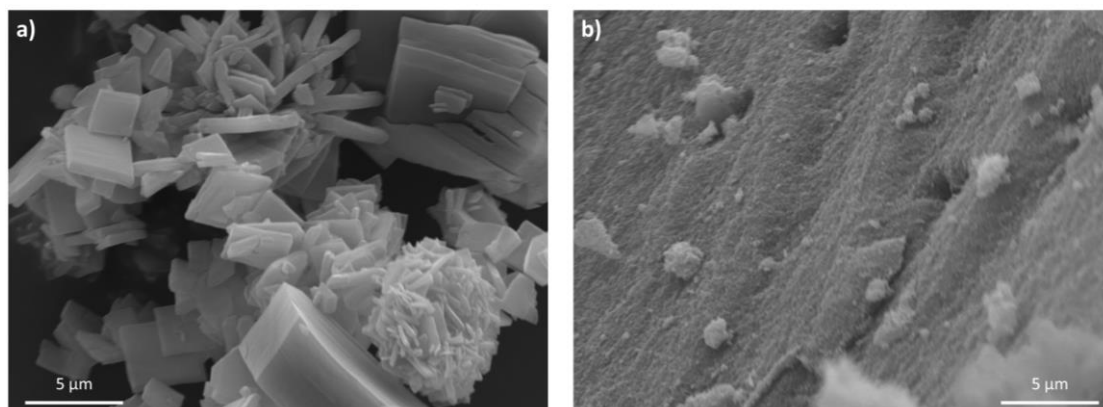
Figure S10. Supplementary SEM images of Cu(1,4-NDC)(DMF) formed from **a)** the nitrate and **b)** the acetate salt.
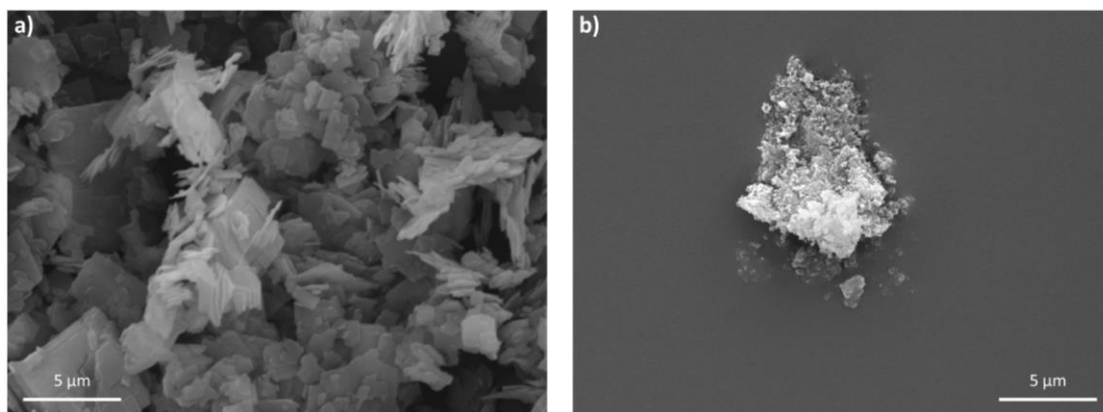
Figure S11. Supplementary SEM images of Cu(2,6-NDC)(DMF) formed from **a)** the nitrate and **b)** the acetate salt.
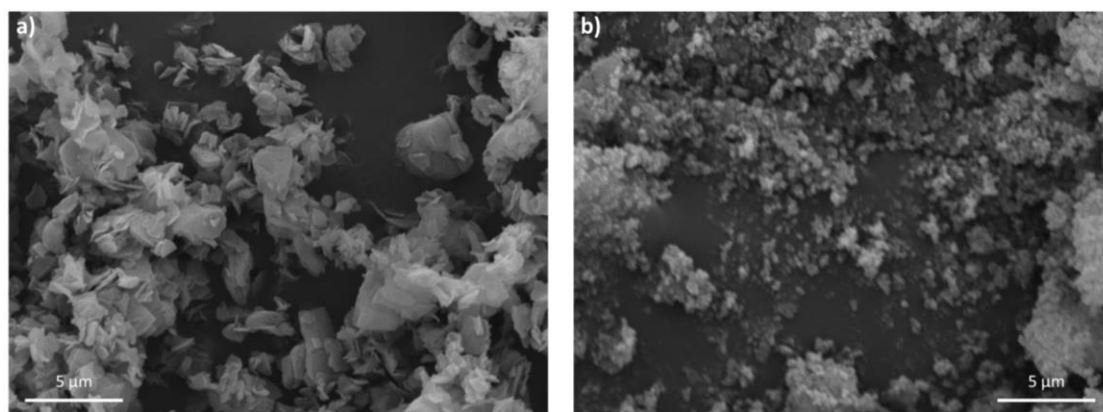
Figure S12. Supplementary SEM images of Cu(BPDC) formed from **a)** the nitrate and **b)** the acetate salt.

S3. Supplementary data for the desolvated layered MOF series
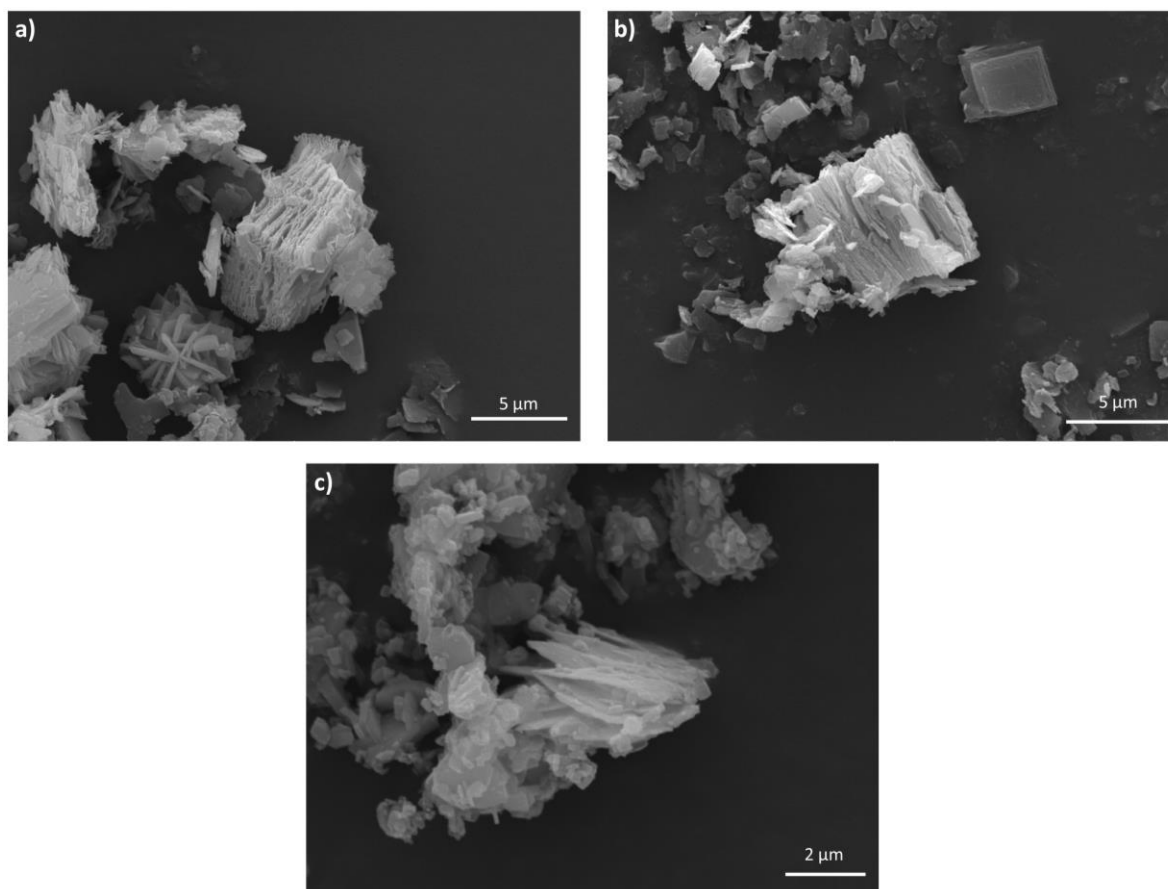
Figure S13. SEM images of the layered MOFs desolvated in acetonitrile: **a)** Cu(1,4-NDC), **b)** Cu(2,6-NDC) and **c)** Cu(BPDC). Note that while the axial sites of the Cu(BPDC) paddlewheel are already desolvated after synthesis, the MOF was subject to the same procedure to examine any effects on structure or morphology.
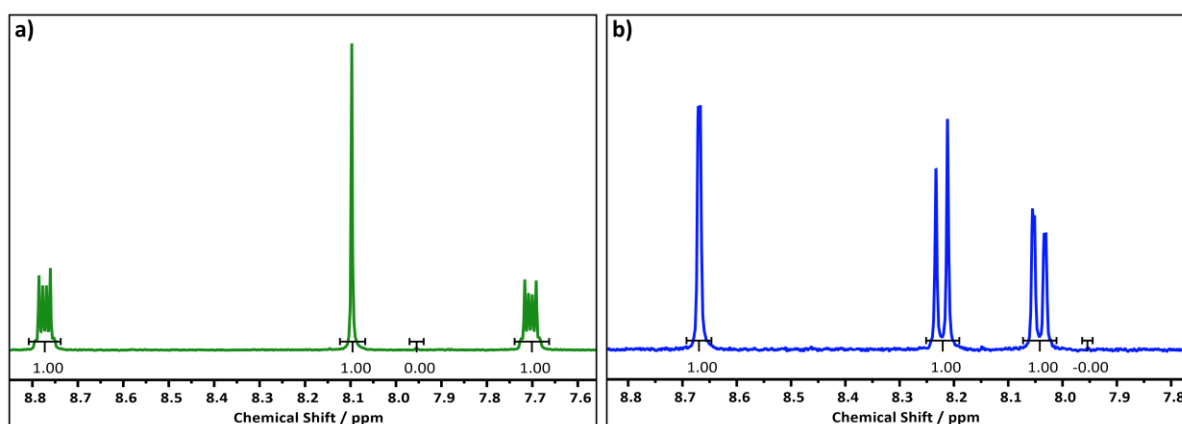
Figures S14. ^{1}H NMR spectra of desolvated **a)** Cu(1,4-NDC) and **b)** Cu(2,6-NDC) digested in DCl and d_6-DMSO. Integration of the 7.95 ppm region indicates full desolvation.

S4. Supplementary data for the exfoliated MON series
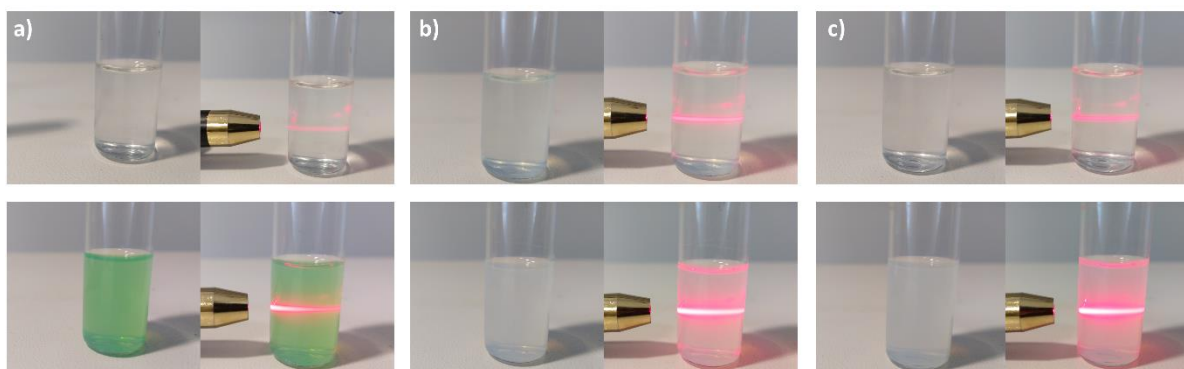
Figure S15. Images of suspensions and Tyndall scattering of MONs obtained from the nitrate salt (top) and the acetate salt (bottom) for **a)** Cu(1,4-NDC), **b)** Cu(2,6-NDC) and **c)** Cu(BPDC).
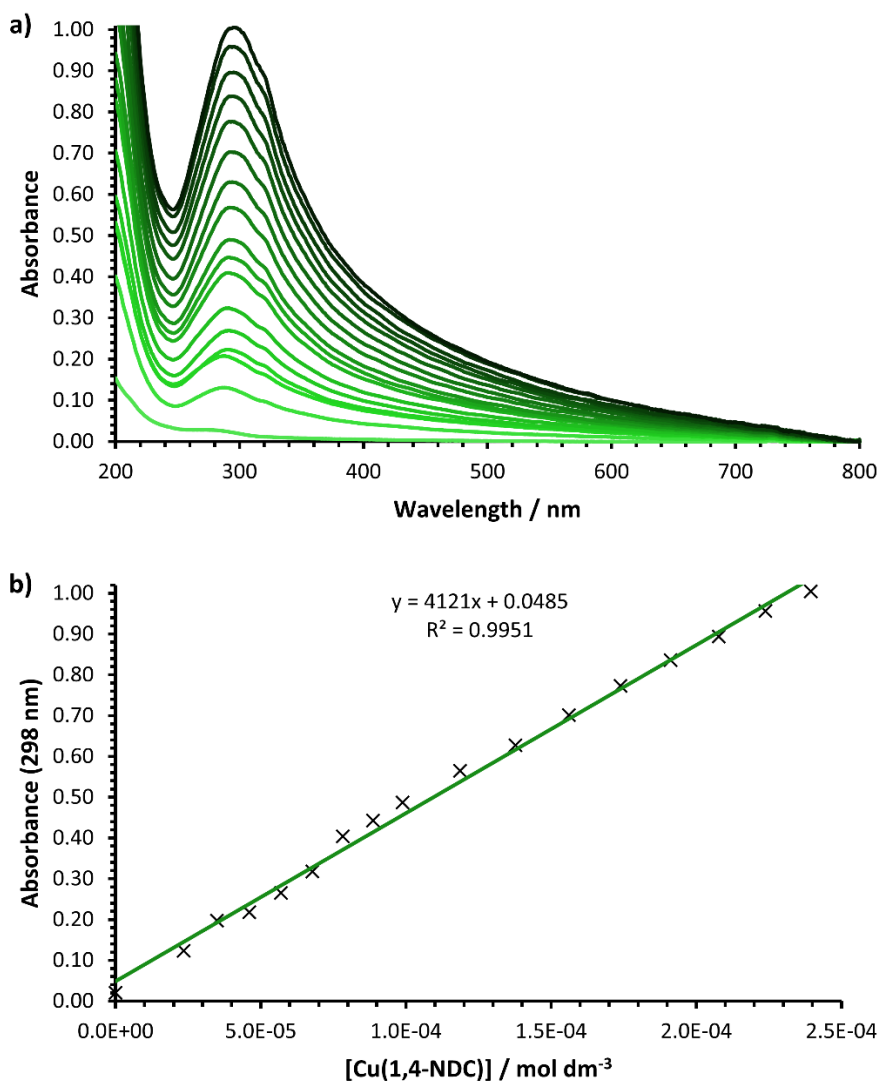
Figure S16. a) UV-visible spectra and **b)** line plots used to determination the extinction coefficient of Cu(1,4-NDC) at λ_{max} = 298 nm.
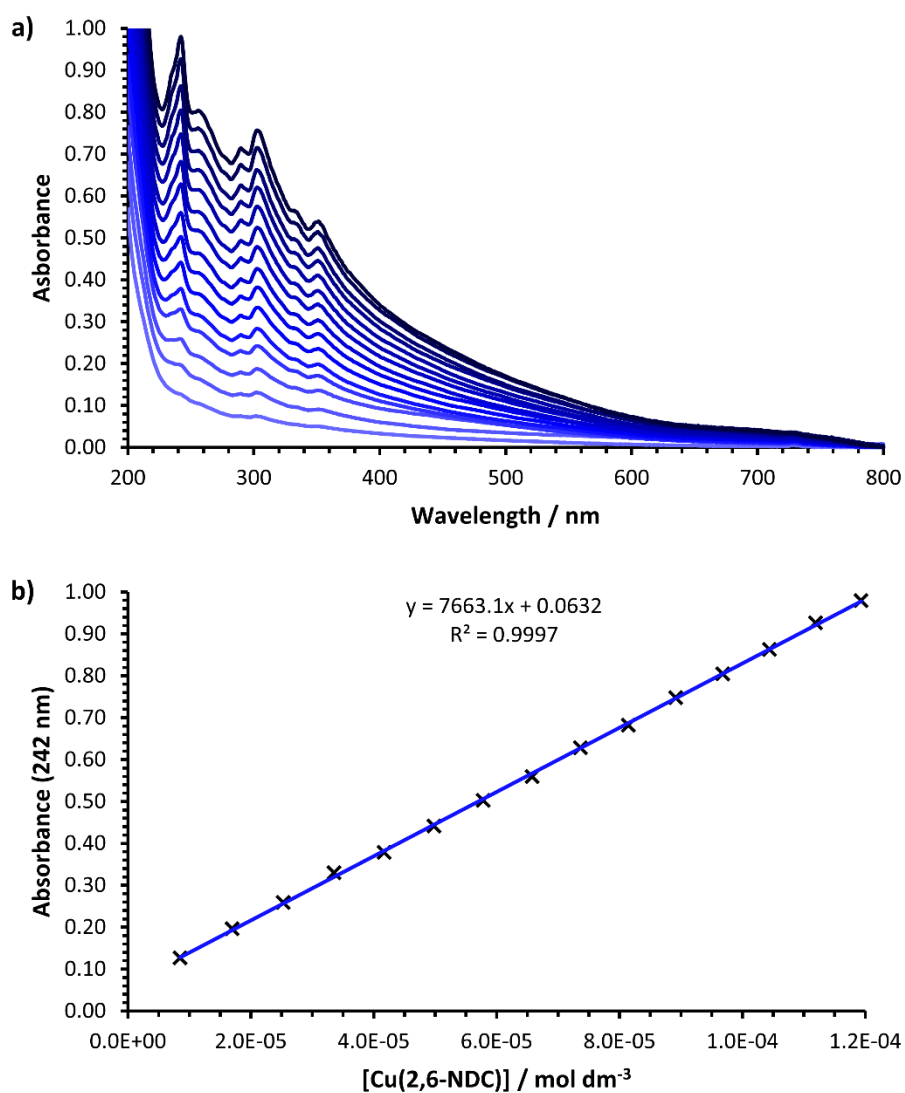
Figure S17. a) UV-visible spectra and **b)** line plots used to determination the extinction coefficient of Cu(2,6-NDC) at λ_{max} = 242 nm.
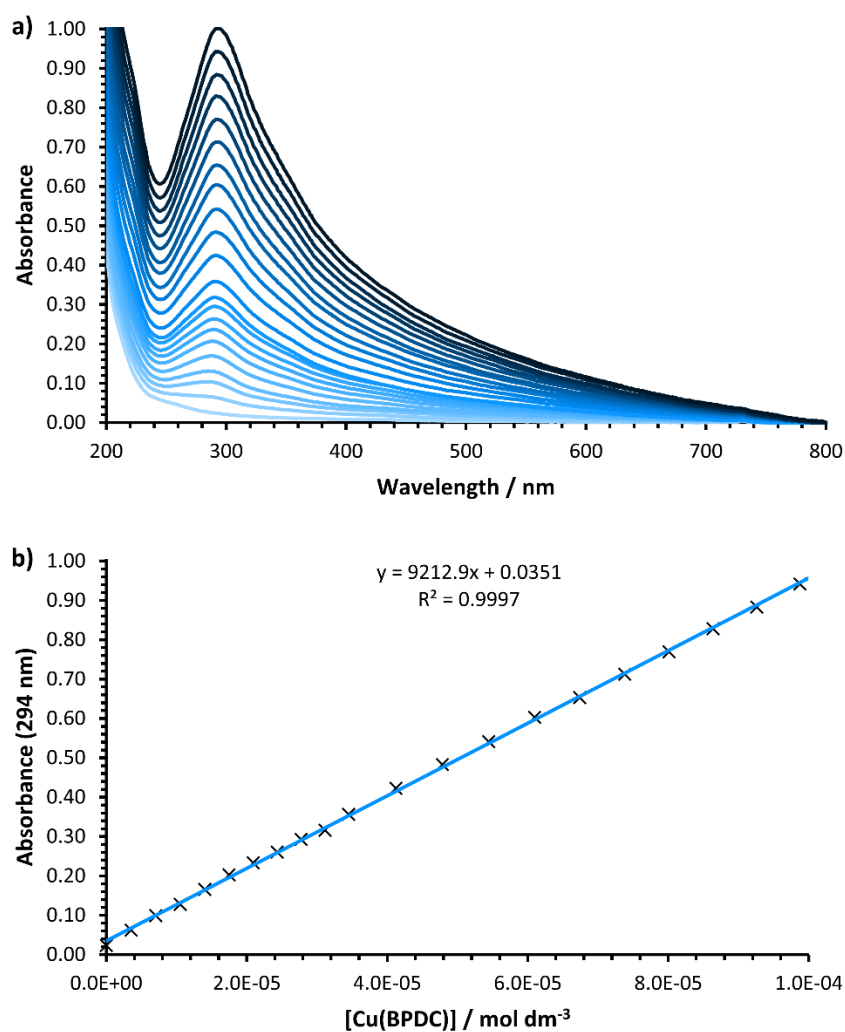
Figure S18. a) UV-visible spectra and **b)** line plots used to determination the extinction coefficient of Cu(BPDC) at λ_{max} = 294 nm.
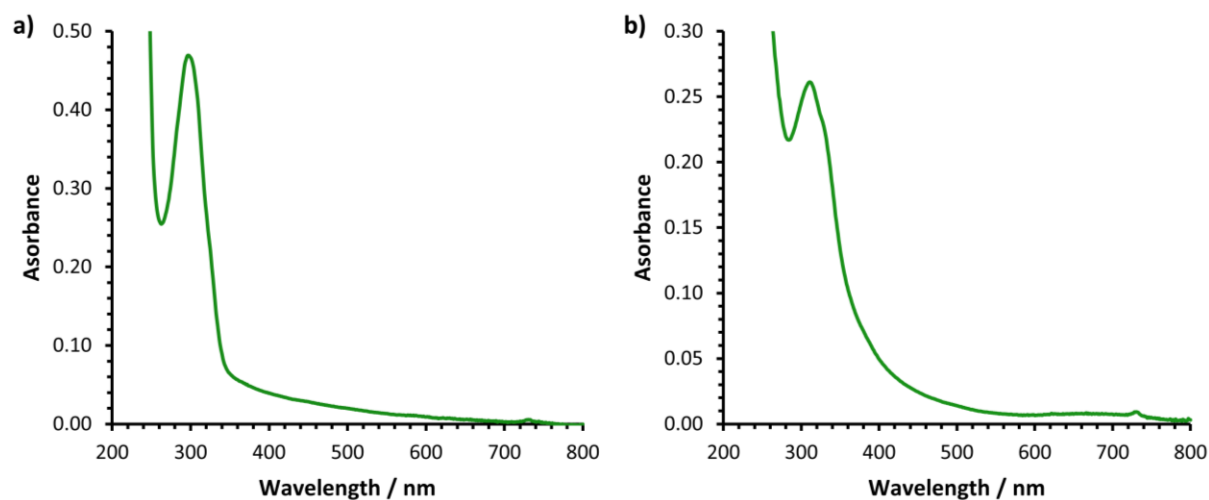

Figure S19. UV-visible absorption spectra used to determine concentrations of Cu(1,4-NDC) MON suspensions obtained from the **a)** nitrate and **b)** acetate salt.
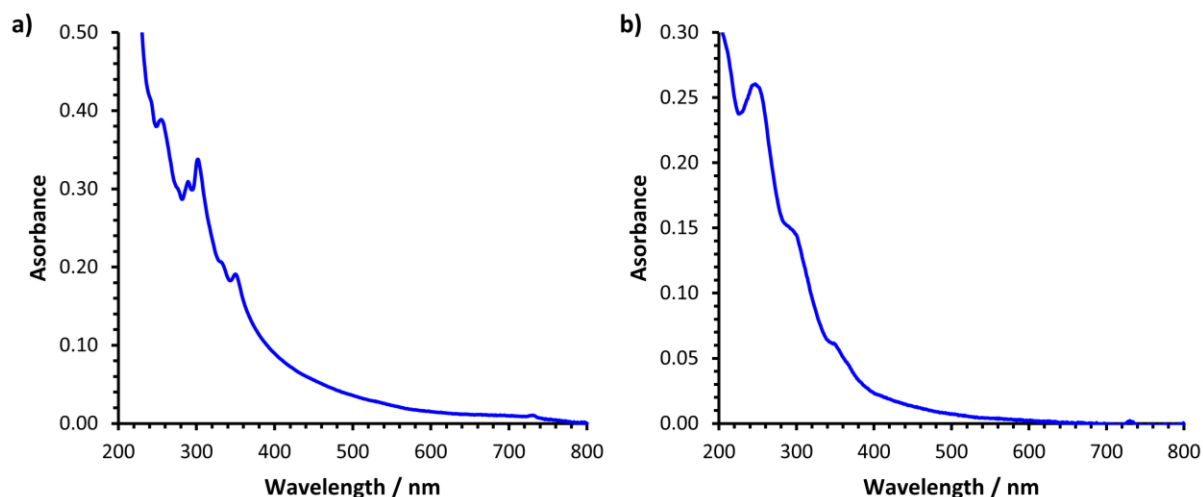
Figure S20. UV-visible absorption spectra used to determine concentrations of Cu(2,6-NDC) MON suspensions obtained from the **a)** nitrate and **b)** acetate salt.
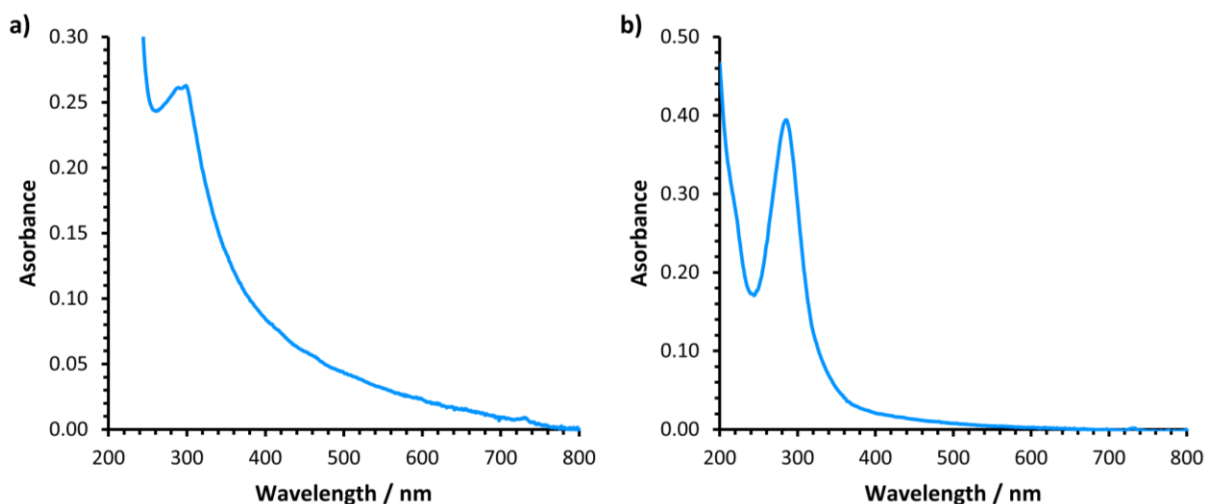
Figure S21. UV-visible absorption spectra used to determine concentrations of Cu(BPDC) MON suspensions obtained from the **a)** nitrate and **b)** acetate salt.

**Table S2.** Concentrations of MON suspensions as determined from the UV-Vis spectra in Figures S19-21.

| Conc. / mg mL^{-1}	Cu(1,4-NDC)		Cu(2,6-NDC)		Cu(BPDC)	
	Nitrate	Acetate	Nitrate	Acetate	Nitrate	Acetate
	0.1	0.7	0.1	0.6	0.05	0.7
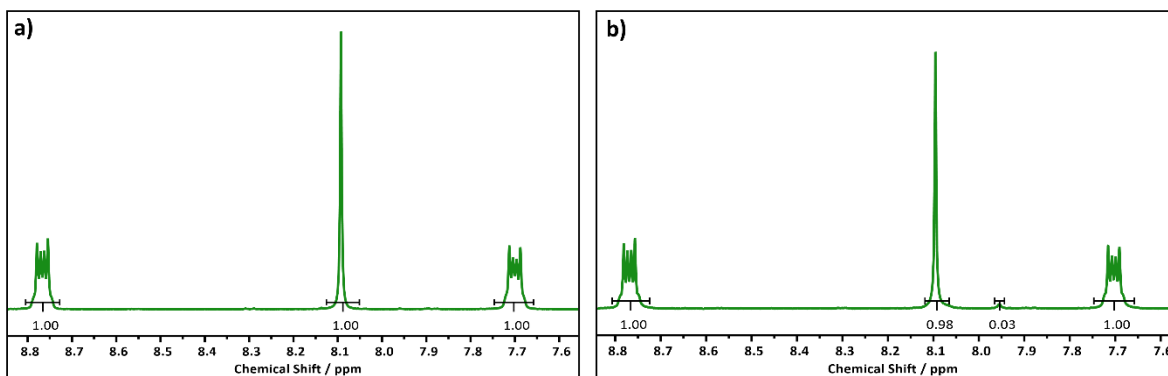
Figures S22. ^{1}H NMR spectra of the material obtained from centrifugation after exfoliation of Cu(1,4-NDC)(DMF) for the **a)** nitrate and **b)** acetate salts.
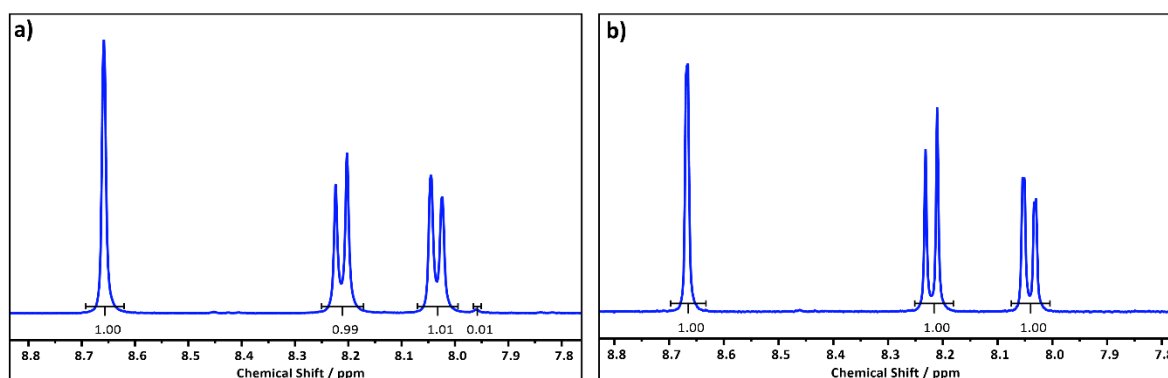

**Figures S23.** ^{1}H NMR spectra of the material obtained from centrifugation after exfoliation of Cu(2,6-NDC)(DMF) for the **a)** nitrate and **b)** acetate salts.
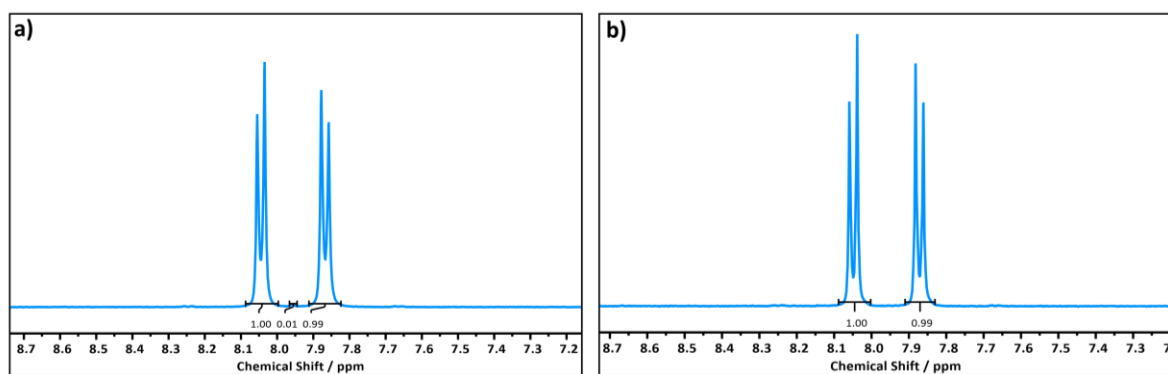
Figures S24. ^{1}H NMR spectra of the material obtained from centrifugation after exfoliation of Cu(BPDC) for the **a)** nitrate and **b)** acetate salts.
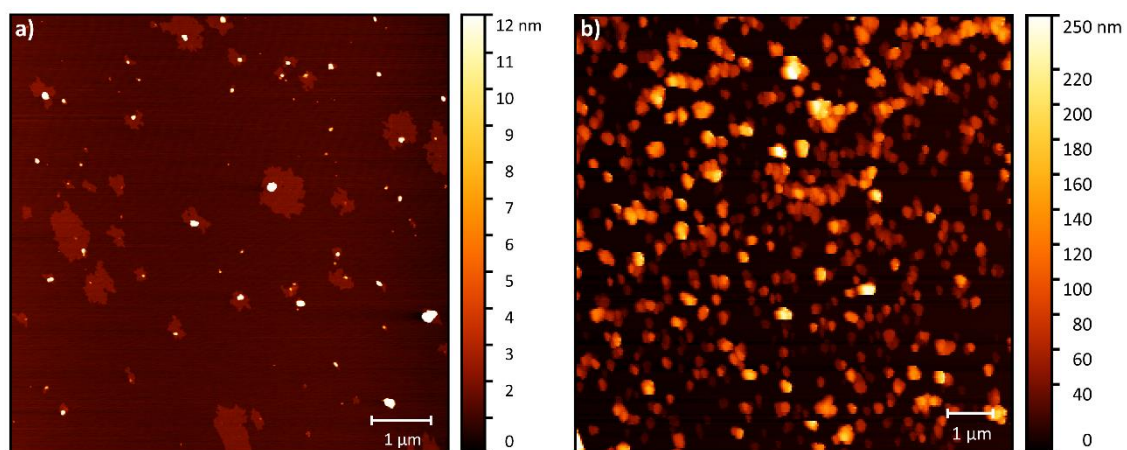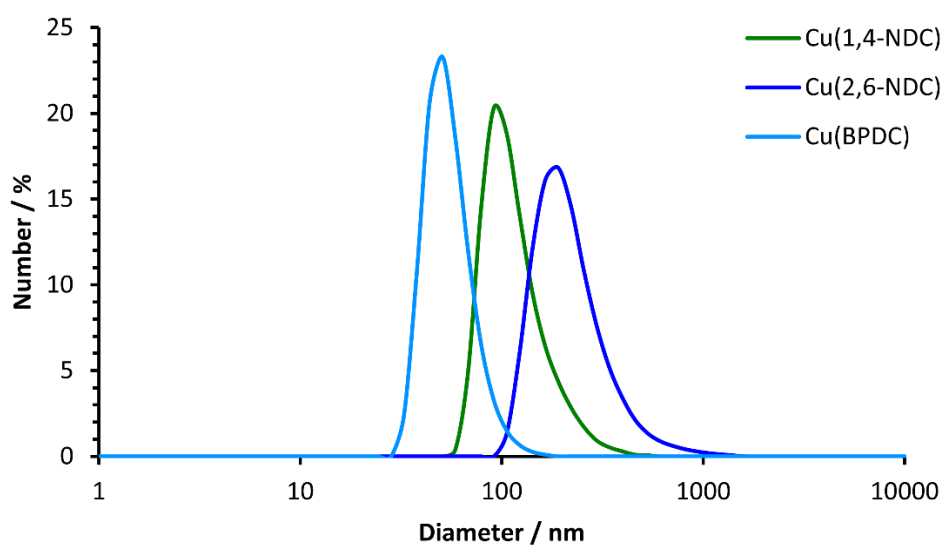
Figure S25. Supplementary AFM images of Cu(1,4-NDC) MONs from the **a)** nitrate and **b)** acetate salt.
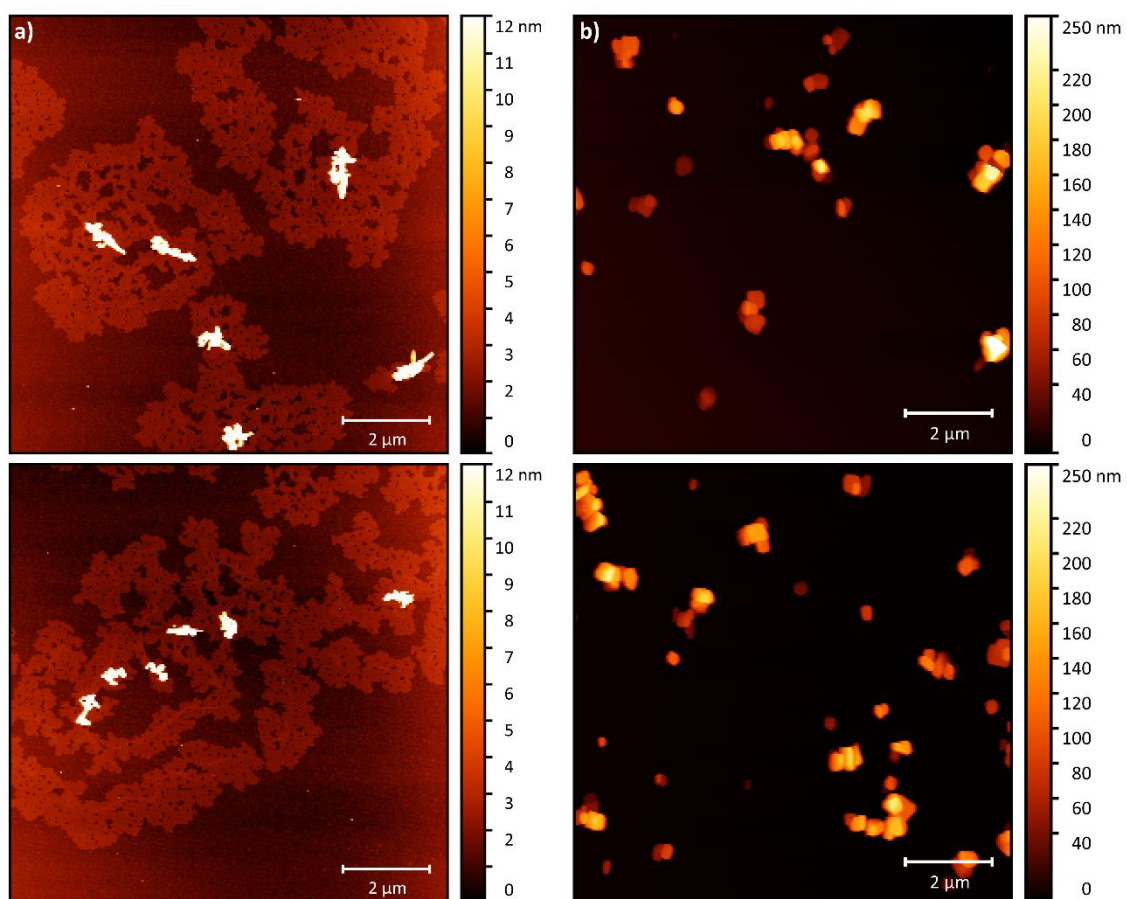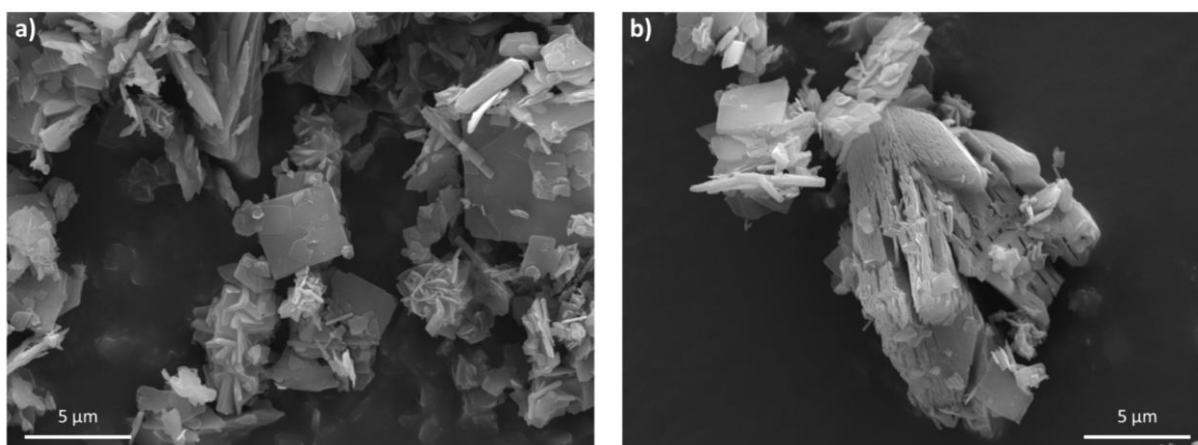

Figure S26. Supplementary AFM images of Cu(2,6-NDC) MONs from the **a)** nitrate and **b)** acetate salt.
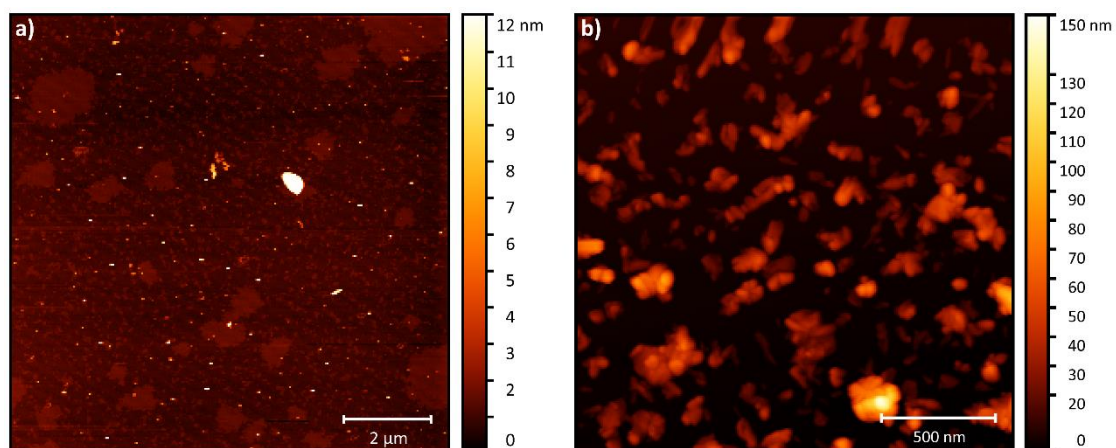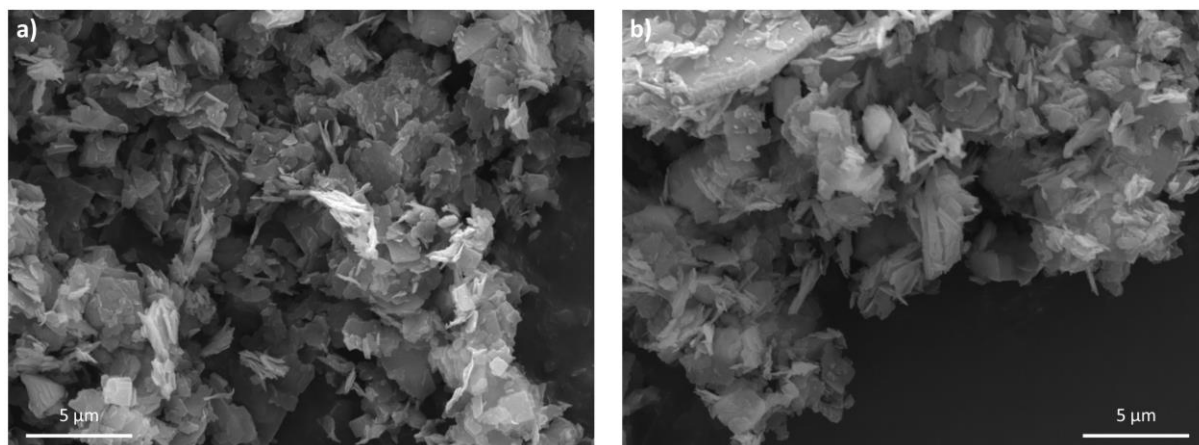
**Figure S27.** Supplementary AFM images of Cu(BPDC) MONs from the **a)** nitrate and **b)** acetate salt.

Figure S28. DLS number plot for MON suspensions of Cu(1,4-NDC), Cu(2,6-NDC) and Cu(BPDC). Suspensions were each diluted by a factor of 10 before analysis.

Figure S29. SEM images of Cu(1,4-NDC) bulk material post-exfoliation obtained from the nitrate salt.

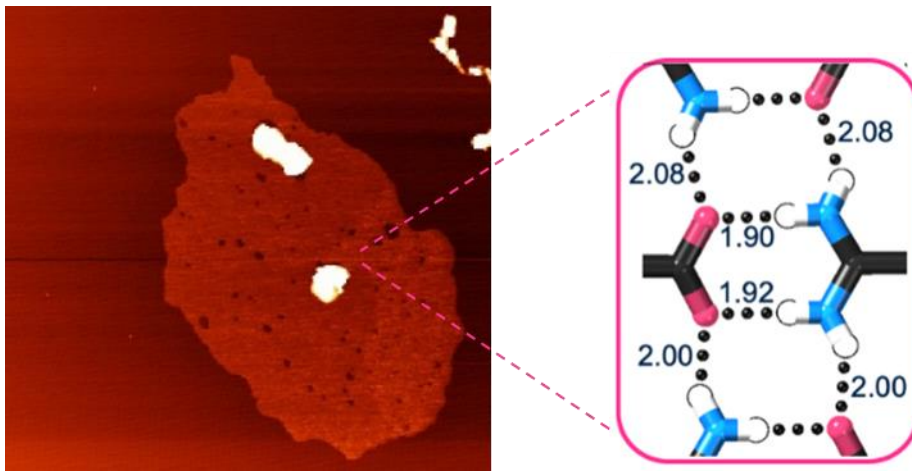

a)   b)

5 μm   5 μm

Figure S30. SEM images of Cu(2,6-NDC) bulk material post-exfoliation obtained from the nitrate salt.

a)   b)

5 μm   5 μm
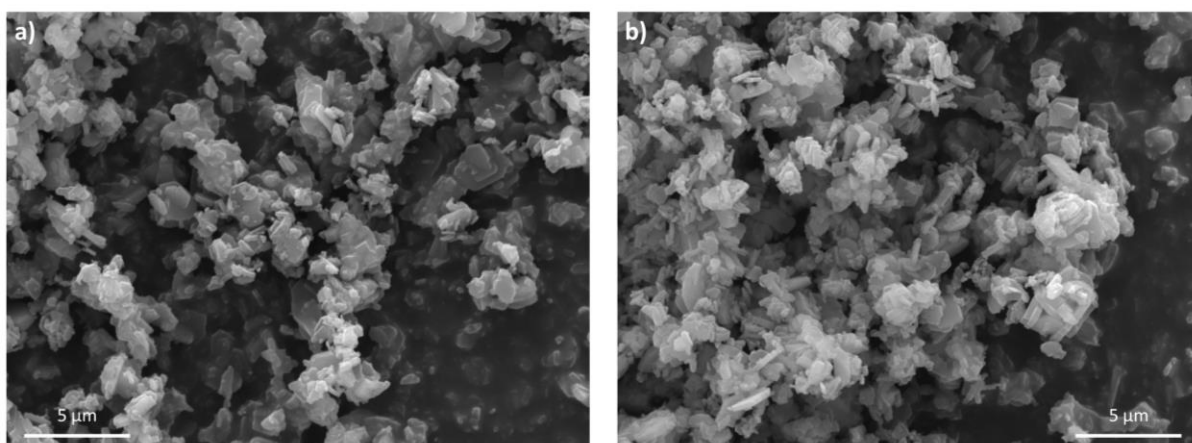
Figure S31. SEM images of Cu(BPDC) bulk material post-exfoliation obtained from the nitrate salt.

Chapter 6

Monolayer Nanosheets Formed by Liquid Exfoliation of Charge-Assisted Hydrogen-Bonded Frameworks

Chapter 6

Monolayer Nanosheets Formed by Liquid Exfoliation of Charge-Assisted Hydrogen-Bonded Frameworks

Chem. Sci., 2021, **12**, 3322-3327 (edge article)

Joshua Nicks, Stephanie A. Boer, Nicholas. G. White, and Jonathan A. Foster

Author Contributions

Joshua Nicks	Performed exfoliation studies, nanosheet characterisation, water stability tests, and quenching experiments. Drafted manuscript and SI and created all figures. Assisted in editing of manuscript.
Stephanie A. Boer	PhD student supervised by NGW, synthesised and characterised **1**.
Nicholas G. White	Synthesised and characterised **2·TP**, conceived project with JAF, and assisted in editing of manuscript.
Jonathan A. Foster	Supervised JN, conceived project with JAF, and assisted in editing of manuscript.

Check for updates

Monolayer nanosheets formed by liquid exfoliation of charge-assisted hydrogen-bonded frameworks†

Joshua Nicks,[a] Stephanie A. Boer, [ID][b] Nicholas G. White [ID] *[b] and Jonathan A. Foster [ID] *[a]

Hydrogen-bonded organic frameworks (HOFs) are a diverse and tunable class of materials, but their potential as free-standing two-dimensional nanomaterials has yet to be explored. Here we report the self-assembly of two layered hydrogen-bonded frameworks based on strong, charge-assisted hydrogen-bonding between carboxylate and amidinium groups. Ultrasound-assisted liquid exfoliation of both materials readily produces monolayer hydrogen-bonded organic nanosheets (HONs) with micron-sized lateral dimensions. The HONs show remarkable stability and maintain their extended crystallinity and monolayer structures even after being suspended in water at 80 °C for three days. These systems also exhibit efficient fluorescence quenching of an organic dye in organic solvents, superior to the quenching ability of the bulk frameworks. We anticipate that this approach will provide a route towards a diverse new family of molecular two-dimensional materials.

Introduction

Liquid exfoliation has been used to convert a diverse range of layered materials into two-dimensional nanosheets. This simple and scalable approach requires materials with strong in-layer interactions but weak inter-layer interactions to create free-standing single and few-layer nanosheets with high aspect ratios. Early studies focussed on two-dimensional materials formed using either covalent bonds, such as in graphene and boron nitride,[1,2] or ionic bonding such as in molybdenum disulphide and layered double hydroxides.[3,4] However, more recent examples have shown this approach can be adapted to exfoliate supramolecular structures formed using dynamic covalent bonds, to form covalent organic framework nanosheets (CONs),[5,6] or coordination compounds, to form metal–organic framework nanosheets (MONs).[7,8] The dynamic chemistry of these materials allows them to be produced under milder conditions than inorganic two-dimensional materials and their molecular nature allows their structure and properties to be more easily modified. The high surface area, aspect ratios, and nanoscopic dimensions of these nanosheets combined with their diverse and tunable chemistry make them ideal for a wide range of sensing,[9,10] catalysis,[11–13] electronics,[14,15] and separation applications.[16–18] However, despite intensive research into all these materials, the formation of monolayer nanosheets with high aspect ratios in good yields remains a challenge.

Hydrogen-bonds can play a varied range of roles within two-dimensional materials. Most commonly, they are located between layers providing relatively weak interactions that interact strongly with polar solvents aiding their exfoliation and dispersion. For example, interlayer hydrogen-bonding has been used to improve the properties of 2D COFs.[19–21] More relevantly, a variety of nanosheets containing hydrogen-bonds within the layers have also been reported. For example, liquid–air interfaces have been used to direct the self-assembly of a number of carboxylic acid and amide functionalised molecules to create ultrathin nanosheets with high aspect ratios.[22–24] Other reports have shown that naphthalene-diimide derivatives can self-assemble in solution to form nanosheets through face to face stacking of the monomeric units.[25,26] A range of urea-based gelators have also been shown to self-assemble into 2D nano-sheets rather than 1D tapes.[27,28] Cucurbituril-based nanosheets down to monolayer thickness have been reported which are held together through a combination of π–π stacking, CH/π interactions and CH/C=O hydrogen-bonding.[29] A bis-acylurea based organogelator was found to stack through hydrogen-bonds in two-dimensions to form nanosheets, rather than the usual 1-dimensional structure. A range of self-assembled peptides, and block-co-polymer-based nanosheets have also been reported.[30–33] All of these nanosheets are based on relatively weak hydrogen-bonding interactions in combination with hydrophobic aromatic or aliphatic groups which in most cases drive nanosheet formation through the hydrophobic effect.[34,35] These nanosheets have also all been formed "bottom-up"

[a]Department of Chemistry, University of Sheffield, Sheffield, UK. E-mail: jona.foster@sheffield.ac.uk

[b]Research School of Chemistry, The Australian National University, Canberra, ACT 2600, Australia. E-mail: nicholas.white@anu.edu.au

† Electronic supplementary information (ESI) available. CCDC 2047425–2047427. For crystallographic data in CIF or other electronic format see DOI: 10.1039/d0sc06906j

through dynamic self-assembly processes in solution. An array of 2D hydrogen-bonded materials on surfaces have also been demonstrated using a variety of building motifs, though these are not free-standing.[36,37] We are only aware of a few examples of "top-down" formation of nanosheets containing hydrogen-bonds within the layers, but in these examples hydrogen-bonds are only formed in one dimension and co-ordination bonds,[38] covalent bonds,[39] or pi-stacking,[40] hold the nanosheets together in the other. To our knowledge there are no examples of nanosheets connected in two-dimensions exclusively through strong hydrogen-bonding interactions.

Hydrogen-bonded organic frameworks (HOFs) are a class of porous supramolecular materials assembled through intermolecular hydrogen-bonding interactions.[41,42] Like MOFs and COFs, in order to create porous structures these materials typically rely on rigid aromatic linkers and strong directional hydrogen-bonding groups. HOFs possess a distinct set of properties in comparison to most other framework materials, including ease of synthesis, solution processability, and self-healing.[43] While many HOFs are constructed through hydrogen-bonding between neutral self-complementary groups,[41,42] some systems use charge-assisted hydrogen-bonds,[44–47] which may lead to more robust materials. In particular, amidinium cations and carboxylate anions are known to form strong charge-assisted hydrogen-bond donor–acceptor pairs, and we have shown that 3D frameworks prepared from this pair show high stability, including to prolonged boiling in water, and heating in polar solvents such as DMSO.[48,49]

Although a wide variety of layered HOFs have previously been reported,[50–52] to our knowledge there are currently no studies investigating their exfoliation to form free-standing hydrogen-bonded framework nanosheets (HONs). This is perhaps because it is not necessarily obvious that materials formed using relatively weak intra-layer hydrogen-bonding interactions would survive the high shear forces associated with liquid exfoliation. In other examples of nanosheets that include hydrogen-bonds within the layers, the hydrogen-bonds are typically shielded from polar solvent by hydrophobic groups. However, the rigid structures of HONs mean that exfoliation to form monolayer nanosheets would directly expose the hydrogen-bonds, making them accessible to solvent molecules and potentially leading to dissolution. HONs therefore currently represent a new and unexplored class of two-dimensional materials.

In this work, we report the formation of two layered hydrogen-bonded frameworks connected in two-dimensions through strong charge-assisted hydrogen-bonds between amidinium and carboxylate groups. We hypothesized that the strong in-layer interactions within these frameworks would enable them to undergo ultrasonic exfoliation to produce nanosheets. Remarkably, both materials were found to readily exfoliate to form micron-sized single-layer HONs in good yields. Furthermore, the nanosheets showed impressive stability in water and the ability to quench fluorescence of organic dyes emphasising the potential of HONs as a distinct new class of 2D materials.

Results and discussion

Synthesis of layered hydrogen-bonded frameworks

Two hydrogen-bonded systems incorporating amidinium and carboxylate synthons either within a single mixed linker (**1**) or as a co-crystal (**2·TP**) were prepared using simple high yielding syntheses, shown in Fig. 1. Commercially available 4-cyanobenzoic acid was converted to the amidinium compound $\mathbf{1^H \cdot Cl}$ using excess lithium bis(trimethylsilyl)amide (LiHMDS) followed by acidic work-up. Crystals of the zwitterionic form of 4-amidiniumbenzoate (**1**) were obtained by heating in DMF/H$_2$O at 120 °C for two days. Co-crystals of **2·TP** were obtained on a 300 mg scale by carefully layering an aqueous solution of bis(amidinium) **2·Cl$_2$** with an aqueous solution of sodium terephthalate (Na$_2$·**TP**).[53]

Single crystal X-ray diffraction studies show that the crystal structures of both **1** and **2·TP** are layered structures with strong in-layer hydrogen-bonding and weak inter-layer interactions. As shown in Fig. 2, both HONs consist of 1D hydrogen bonded chains, which propagate through short N–H···O hydrogen-bonds along the axis of the 1,4-disubstituted phenyl groups [H···O = 1.93, 1.94 Å in **1** and 1.88, 1.89 Å in **2·TP**]. The 1D chains are linked together through additional N–H···O hydrogen bonds perpendicular to this, which are slightly longer [H···O = 2.03, 2.06 Å in **1**, and 2.01, 2.07 Å in **2·TP**]. Overall, this assembles both structures into 2D hydrogen-bonded sheets.

The sheets stack with an interlayer distance of 3.77 and 3.72 Å respectively and there are no contacts between sheets that are shorter than the sum of the van der Waals radii (Fig. 2). The shortest centroid···centroid contacts between aromatic rings are >4.9 Å in both **1** and **2·TP**. Furthermore, the donor–acceptor pairs of the amidinium and carboxylate groups stack above/below the phenyl rings of the adjacent layers, indicating an absence of substantial interlayer electrostatic interactions between the charged groups. This lack of any significant interlayer hydrogen-bonding or electrostatic interactions combined with the non-interdigitated stacking mode of these hydrogen-bonded frameworks makes them ideal candidates for
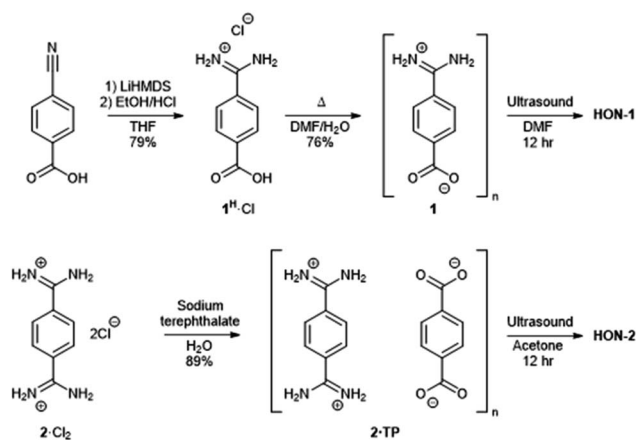

Fig. 1 Scheme showing the synthesis of hydrogen-bonded frameworks **1** and **2·TP** and their exfoliation to form **HON-1** and **HON-2**.
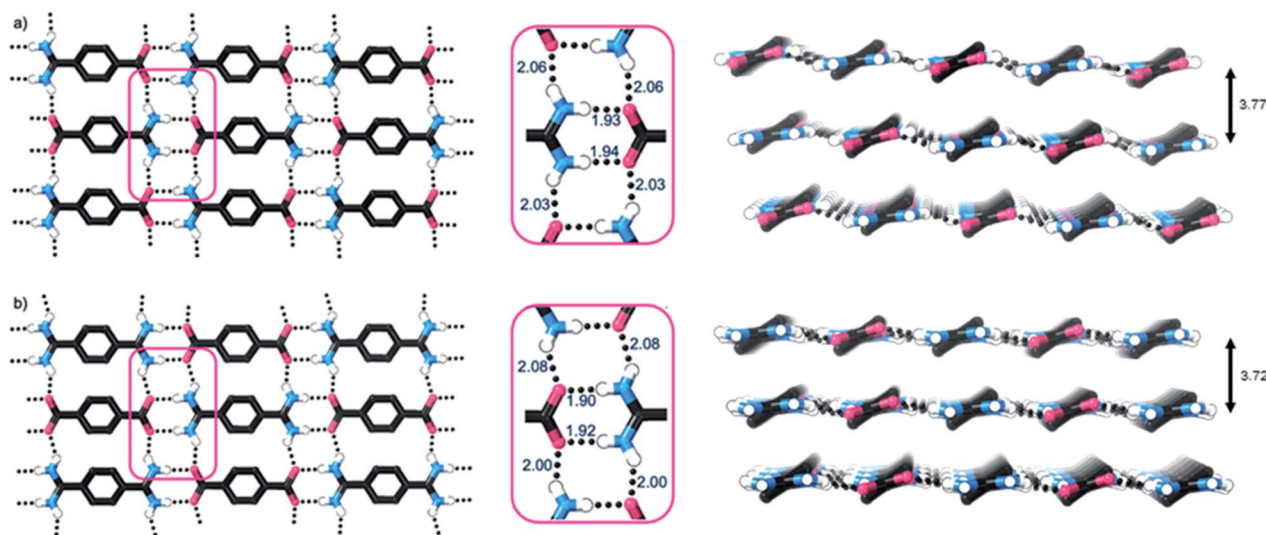
Fig. 2 (a) and (b) Views of the X-ray crystal structures of **1** and **2·TP** respectively, showing the 2D hydrogen bonded sheets (C−H hydrogen atoms omitted for clarity). Portions of the structures are expanded in pink boxes, which highlight the H-bonding distances (in Å). Views of the stacking of the 2D hydrogen bonded layers in each structure, with interlayer distances, are shown adjacent (C−H hydrogen atoms omitted for clarity).

ultrasound-assisted liquid exfoliation. SEM imaging of the crystalline powders (Fig. 3a, b, S11 and S12†) indicates the formation of rectangular prisms approximately 3–20 μm wide, with evidence of layers stacking along the long direction of the crystallites.
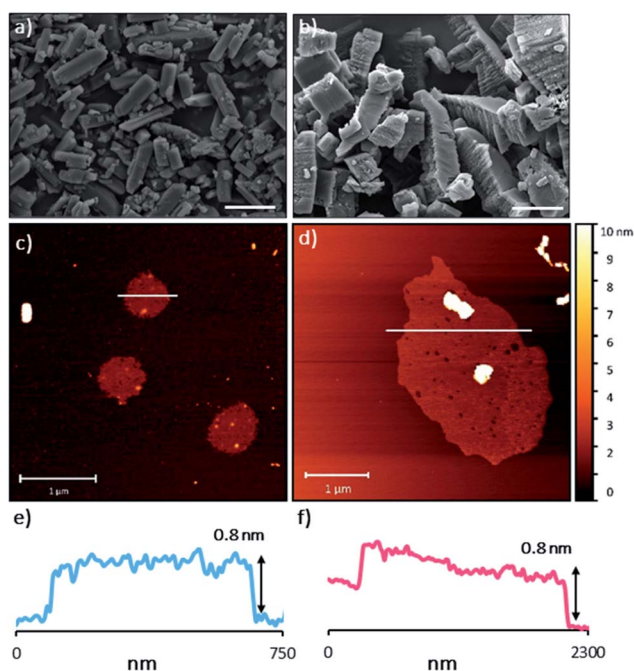

Fig. 3 (a) and (b) SEM images of bulk **1** and **2·TP** respectively. Scale bars represent 10 μm. (c) and (d) selected AFM topographical images of the nanosheets formed from exfoliation of **1** and **2·TP** respectively. (e) and (f) height profiles of the nanosheets shown in (c) and (d) (represented by white bars).

Preparation of HONs by liquid exfoliation

Exfoliation experiments were performed using a previously reported bath sonicator setup which we have used to exfoliate layered MOFs to form MONs.[54,55] Here, "softer" high frequency (80 kHz) ultrasound is used to minimise fragmentation and samples are stirred in a temperature-controlled bath to minimise hot-spots and ensure reproducibility.[54] During ultra-sonication, shear forces and cavitation exert force on the bulk material and induce exfoliation, after which the solvent–nanosheet interaction must overcome inter-sheet attraction to prevent reaggregation. As such, a range of polar solvents (acetone, acetonitrile, DMF, DMSO, and water) were initially investigated for the exfoliation of both **1** and **2·TP**, as it was hypothesized that these would best penetrate between the layers of each system, leading to enhanced exfoliation and colloidal stabilization.

Samples (5 mg) of **1** and **2·TP** were each suspended in 6 mL of solvent in a sealed vial, and subject to ultrasonication at 80 kHz for 12 hours at temperatures below 18 °C. The samples were then centrifuged at 1500 rpm for 1 hour to remove unexfoliated material and isolate nanosheets in suspension (illustrated in Fig. S13†). Tyndall scattering observations provided qualitative evidence indicating that DMF and acetone were optimal solvents for the exfoliation of **1** and **2·TP** into **HON-1** and **HON-2** respectively, with each exhibiting strong scattering effects (Fig. S14†). The other solvents showed weaker Tyndall scattering, indicating nanoparticle formation but with significantly reduced yields and thus were not further investigated.

Sample suspensions were drop-cast onto hot mica plates for topographical AFM imaging (Fig. 3c and d, S15 and S16†). Size distribution analysis of the recorded images indicated consistently ultrathin thicknesses of approximately 0.8 nm for both systems. The expected thickness of a monolayer is calculated as approximately 0.35 nm from the single crystal data. Graphene

has a nominal thickness of 0.34 nm but AFM imaging typically shows thickness of 0.4–1.7 nm which is typically attributed to tip surface interactions, image feedback settings and surface chemistry.[56] Whilst it is possible that bi- or tri-layer nanosheets (2–3 layers) have been consistently formed, the uniform thickness and lack of step edges is better explained by monolayer formation.

Analysis of the lateral dimensions of the imaged nanosheets indicated lengths between 0.3–1.5 μm for **HON-1**, and 0.9–3.4 μm for **HON-2**. As such, the as prepared HONs possess remarkably large aspect ratios and exposed surface areas as a result. The nanosheets have a consistently flat morphology, with no wrinkling or rolling observed *via* AFM. The smaller HONs are observed to be rounded in shape, whereas the larger >800 nm wide sheets have more irregular shapes. Dynamic light scattering measurements of the nanosheets in colloidal suspension corroborate these size distribution observations (Fig. S17†).

The as-prepared HON suspensions were colloidally stable for approximately two days before precipitation was observed. The nanosheets were removed from suspension by centrifugation at 10 000 rpm for 1 hour. Yields of 10 and 12% were obtained for **HON-1** and **HON-2** respectively. Ultrasonic liquid exfoliation of other supramolecular nanosheets such as MONs and CONs typically produce nanosheets with a range of thicknesses and sub-micron lateral dimensions. Only a few reports of monolayer nanosheets with micron-sized lateral dimensions have been reported,[57,58] and these are typically formed in much lower overall yields. The improved yields and aspect ratios of HONs relative to other MON and CON systems emphasizes the novelty of these new materials and may be related to the more reversible bonds that assemble them.

Powder X-ray diffractometry of the bulk crystalline powder, unexfoliated material, and isolated nanosheets indicates that the extended supramolecular structure is maintained post-exfoliation (Fig. 4a). In particular, for the **HON-2** system there is a noticeable reduction in the intensity of peaks corresponding to through-layer planes for the as synthesised HOF (28°, [1,

2, 2]), compared to the in-layer planes (24°, [1, −1, −1]). Line broadening of this type is caused by the finite number of unit cells as crystal dimensions become severely reduced, as described by the Scherrer equation. AFM shows that both systems form monolayer nanosheets so we would expect not to see the out of plane reflections at all. However, as seen with related MON systems,[11,59] some degree of restacking occurs when samples are dried for analysis. The differences in line broadening therefore most likely reflect different degrees of restacking during sample preparation. It is interesting to note that despite the strong hydrogen-bond donor capabilities of both acetone and DMF, the extended crystallinity is still maintained throughout treatment.

Water stability and fluorescence quenching activity

Encouraged by the formation of HONs in highly competitive solvents such as DMF, we decided to test the stability of HONs in water. Samples of each HON were heated for 3 days at 80 °C then re-investigated. Powder X-ray diffractometry of both hydrogen-bonded nanosheet systems indicates that the HONs maintain their extended crystallinity (Fig. 4a). This is further supported by the presence of Tyndall scattering in the aqueous suspensions post-treatment (Fig. S18†). AFM imaging of the aqueous suspensions drop-cast onto hot mica shows that the nanosheets maintain their monolayer nature (Fig. S19 and 20†). It is remarkable that atomically thin nanosheets with a supramolecular structure connected only through hydrogen-bonds and without any shielding hydrophobic groups should prove so stable under these conditions. This is particularly notable given that all starting materials dissolve readily in water. This highlights the potential of these materials and of HOFs more generally as stable materials with potential for real-world applications.

To demonstrate the potential for HONs in sensing applications, we investigated the quenching of a fluorescent dye in suspension and compared it to that of the bulk layered framework. Addition of **HON-1** or **HON-2** to a dilute solution of Rhodamine B in acetone resulted in 93 and 95% quenching of
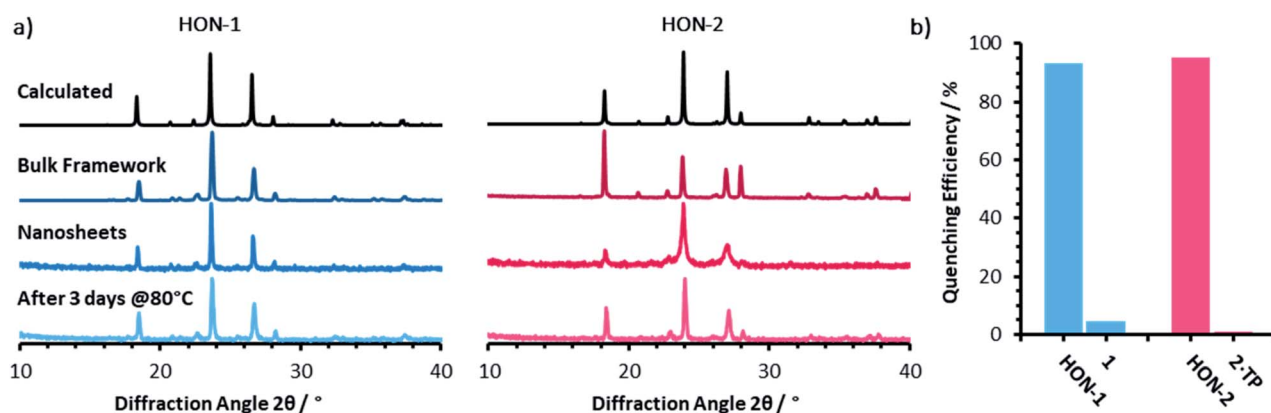

Fig. 4 (a) Powder X-ray diffractometry patterns for both the one (blue) and two (pink) component systems, of: the calculated and as synthesised frameworks, nanosheets, and water treated nanosheets. (b) The quenching efficiencies of hydrogen-bonded framework nanosheets and bulk frameworks towards Rhodamine B fluorescence (λ_{ex} = 556, λ_{em} = 577 nm). Emission titration spectra can be seen in Fig. S21–S24.†

the emission respectively (Fig. 4b, S21–S24†). Furthermore, addition of the same mass of respective bulk materials resulted in significantly less effective quenching of the emission, which is attributed to the much higher accessible surface area of the HONs. The nanosheets exhibit no absorption in the UV-visible region beyond 330 nm (acetone's cut-off). This indicates that quenching by the HONs, rather than competitive absorbance of the light, is responsible for the reduction in intensity. This quenching mechanism is widely employed by other nanosheet systems in a variety of biological and environmental sensing applications, particularly by quenching of dye-labelled single-stranded DNA for biomolecular detection.[60–63]

Conclusions

We have demonstrated a simple process for the top-down exfoliation of layered hydrogen-bonded frameworks into ultra-thin, high aspect ratio nanosheets with remarkable stability in water and sensing capabilities. Two frameworks incorporating amidinium and carboxylate synthons, either within a single mixed linker or as a co-crystal, were prepared using simple high-yielding syntheses. Single-crystal analysis show both systems formed layered materials held together in two-dimensions by strong, charge assisted hydrogen-bonding interactions, with only weak van der-Waal interlayer interactions. The systems underwent a "soft" liquid-phase ultrasonic exfoliation procedure to produce HONs with a thickness of 0.8 nm and micron sized lateral dimensions. The HONs exhibit remarkable stability in a range of highly competitive solvents, including maintaining structures after suspension in water at 80 °C for three days. This stability is particularly remarkable given that both components are highly water soluble and the nanosheets are only held together by strong hydrogen-bonds. The HONs also demonstrate the potential for use in sensing applications showing strong quenching of fluorescent dyes.

HOFs are a diverse class of materials with a variety of useful properties and promising applications. Exfoliation dramatically increases a materials surface area, exposes active sites, and aids incorporation within membranes and thin films unlocking distinct new opportunities for HONs. A wide range of extended and functionalised derivatives of **HON-1** and **HON-2** can readily be envisaged which could enable their use in a wide range of sensing, catalysis, separation, and electronics applications. We anticipate that this simple and scalable approach will be broadly applicable to a wide range of other layered HOFs, particularly those based on other strong hydrogen-bond donor–acceptor pairs.[45,64] The remarkable stability of these hydrogen-bond based materials also has broad implications for the design of a wide range of other supramolecular materials.

Author contributions

S. A. B. synthesized and characterized **1**. N. G. W. synthesized and characterized **2·TP**. J. N. performed exfoliation studies, nanosheet characterization, water stability tests, and quenching experiments. The project was conceived by N. G. W. and J. A. F. The manuscript was written by J. N. with editing by N. G. W. and J. A. F. All authors have given approval to the final version of the manuscript.

Conflicts of interest

There are no conflicts to declare.

Acknowledgements

References

1 M. J. Allen, V. C. Tung and R. B. Kaner, *Chem. Rev.*, 2010, **110**, 132–145.

2 L. H. Li and Y. Chen, *Adv. Funct. Mater.*, 2016, **26**, 2594–2608.

3 X. Huang, Z. Zeng and H. Zhang, *Chem. Soc. Rev.*, 2013, **42**, 1934–1946.

4 Q. Wang and D. O'Hare, *Chem. Rev.*, 2012, **112**, 4124–4155.

5 D. Rodríguez-San-Miguel, C. Montoro and F. Zamora, *Chem. Soc. Rev.*, 2020, **49**, 2291–2302.

6 W. Wang, W. Zhao, H. Xu, S. Liu, W. Huang and Q. Zhao, *Coord. Chem. Rev.*, 2020, 213616.

7 D. J. Ashworth and J. A. Foster, *J. Mater. Chem. A*, 2018, **6**, 16292–16307.

8 M. Zhao, Y. Huang, Y. Peng, Z. Huang and Q. Ma, *Chem. Soc. Rev.*, 2018, **47**, 6267–6295.

9 Y. Peng, Y. Huang, Y. Zhu, B. Chen, L. Wang, Z. Lai, Z. Zhang, M. Zhao, C. Tan, N. Yang, F. Shao, Y. Han and H. Zhang, *J. Am. Chem. Soc.*, 2017, **139**, 8698–8704.

10 G. Lan, K. Ni, E. You, M. Wang, A. Culbert, X. Jiang and W. Lin, *J. Am. Chem. Soc.*, 2019, **141**, 18964–18969.

11 J. Nicks, J. Zhang and J. A. Foster, *Chem. Commun.*, 2019, **55**, 8788–8791.

12 C. Tan, K. Yang, J. Dong, Y. Liu, Y. Liu, J. Jiang and Y. Cui, *J. Am. Chem. Soc.*, 2019, **141**, 17685–17695.

13 H. J. Zhu, M. Lu, Y. R. Wang, S. J. Yao, M. Zhang, Y. H. Kan, J. Liu, Y. Chen, S. L. Li and Y. Q. Lan, *Nat. Commun.*, 2020, **11**, 1–10.

14 K. Sasitharan, D. G. Bossanyi, N. Vaenas, A. J. Parnell, J. Clark, A. Iraqi, D. G. Lidzey and J. A. Foster, *J. Mater. Chem. A*, 2020, **8**, 6067–6075.

15 H. Chen, H. Tu, C. Hu, Y. Liu, D. Dong, Y. Sun, Y. Dai, S. Wang, H. Qian, Z. Lin and L. Chen, *J. Am. Chem. Soc.*, 2018, **140**, 896–899.

16 T. Rodenas, I. Luz, G. Prieto, B. Seoane, H. Miro, A. Corma, F. Kapteijn, F. X. Llabrés i Xamena and J. Gascon, *Nat. Mater.*, 2014, **14**, 48–55.

17 Y. Ying, M. Tong, S. Ning, S. K. Ravi, S. B. Peh, S. C. Tan, S. J. Pennycook and D. Zhao, *J. Am. Chem. Soc.*, 2020, **142**, 4472–4480.

18 H. Yang, L. Yang, H. Wang, Z. Xu, Y. Zhao, Y. Luo, N. Nasir, Y. Song, H. Wu, F. Pan and Z. Jiang, *Nat. Commun.*, 2019, **10**, 1–10.

19 S. B. Alahakoon, S. D. Diwakara, C. M. Thompson and R. A. Smaldone, *Chem. Soc. Rev.*, 2020, **49**, 1344–1356.

20 S. B. Alahakoon, K. Tan, H. Pandey, S. D. Diwakara, G. T. McCandless, D. I. Grinffiel, A. Durand-Silva, T. Thonhauser and R. A. Smaldone, *J. Am. Chem. Soc.*, 2020, **142**, 12987–12994.

21 A. Halder, S. Karak, M. Addicoat, S. Bera, A. Chakraborty, S. H. Kunjattu, P. Pachfule, T. Heine and R. Banerjee, *Angew. Chem., Int. Ed.*, 2018, **57**, 5797–5802.

22 X. Hou, M. Schober and Q. Chu, *Cryst. Growth Des.*, 2012, **12**, 5159–5163.

23 R. Makiura, K. Tsuchiyama, E. Pohl, K. Prassides, O. Sakata, H. Tajiri and O. Konovalov, *ACS Nano*, 2017, **11**, 10875–10882.

24 M. Vybornyi, Y. B. Hechevarria, M. Glauser, A. V Rudnev and R. Ha, *Chem. Commun.*, 2015, **51**, 16191–16193.

25 D. S. Pal and S. Ghosh, *Chem.–Eur. J.*, 2018, **24**, 8519–8523.

26 Y. Sun, C. He, K. Sun, Y. Li, H. Dong, Z. Wang and Z. Li, *Langmuir*, 2011, **27**, 11364–11371.

27 W. Bai, Z. Jiang, A. E. Ribbe and S. Thayumanavan, *Angew. Chem., Int. Ed.*, 2016, **55**, 10707–10711.

28 R. Davis, R. Berger and R. Zentel, *Adv. Mater.*, 2007, **19**, 3878–3881.

29 Q. An, Q. Chen, W. Zhu, Y. Li, C. A. Tao, H. Yang, Z. Li, L. Wan, H. Tian and G. Li, *Chem. Commun.*, 2010, **46**, 725–727.

30 I. W. Hamley, A. Dehsorkhi and V. Castelletto, *Chem. Commun.*, 2013, **49**, 1850–1852.

31 J. P. Joseph, A. Singh, D. Gupta, C. Miglani and A. Pal, *ACS Appl. Mater. Interfaces*, 2019, **11**, 28213–28220.

32 M. Tsuksamoto, K. Ebata, H. Sakiyama, S. Yamamoto, M. Mitsuishi, T. Miyashita and J. Matsui, *Langmuir*, 2019, **35**, 3302–3307.

33 T. Sato, M. Tsukamoto, S. Yamamoto, M. Mitsuishi, T. Miyashita, S. Nagano and J. Matsui, *Langmuir*, 2017, **33**, 12897–12902.

34 T. Govindaraju and M. B. Avinash, *Nanoscale*, 2012, **4**, 6102–6117.

35 L. Z. Jin, S. S. Wang, L. H. Xie and W. Huang, *Chin. J. Chem.*, 2019, **37**, 405–416.

36 A. G. Slater, L. M. A. Perdigão, P. H. Beton and N. R. Champness, *Acc. Chem. Res.*, 2014, **47**, 3417–3427.

37 D. P. Goronzy, M. Ebrahimi, F. Rosei, Arramel, Y. Fang, S. De Feyter, S. L. Tait, C. Wang, P. H. Beton, A. T. S. Wee, P. S. Weiss and D. F. Perepichka, *ACS Nano*, 2018, **12**, 7445–7481.

38 F. Moghzi and J. Soleimannejad, *Nanotechnology*, 2020, **31**, 245706.

39 M. Li, M. Song, G. Wu, Z. Tang, Y. Sun, Y. He, J. Li, L. Li, H. Gu, X. Liu, C. Ma, Z. Peng, Z. Ai and D. J. Lewis, *Small*, 2017, **13**, 1–7.

40 L. Xu, Y. Huang, J. Li, D. Wang, M. Chen, J. Tao, K. Cui, G. Pan, N. Huang and L. Li, *Langmuir*, 2013, **29**, 3813–3820.

41 R. B. Lin, Y. He, P. Li, H. Wang, W. Zhou and B. Chen, *Chem. Soc. Rev.*, 2019, **48**, 1362–1389.

42 J. Yang, J. Wang, B. Hou, X. Huang, T. Wang and Y. Bao, *Chem. Eng. J.*, 2020, **399**, 125873.

43 J. Luo, J. Wang, J. Zhang, S. Lai and D. Zhong, *CrystEngComm*, 2018, **20**, 5884–5898.

44 V. A. Russell, C. C. Evans, W. Li and M. D. Ward, *Science*, 1997, **276**, 575–579.

45 T. Adachi and M. D. Ward, *Acc. Chem. Res.*, 2016, **49**, 2669–2679.

46 G. Xing, T. Yan, S. Das, T. Ben and S. Qiu, *Angew. Chem., Int. Ed.*, 2018, **57**, 5345–5349.

47 G. Xing, I. Bassanetti, S. Bracco, M. Negroni, C. Bezuidenhout, T. Ben, P. Sozzani and A. Comotti, *Chem. Sci.*, 2019, **10**, 730–736.

48 S. A. Boer, M. Morshedi, A. Tarzia, C. J. Doonan and N. G. White, *Chem.–Eur. J.*, 2019, **25**, 10006–10012.

49 W. Liang, F. Carraro, M. B. Solomon, S. G. Bell, H. Amenitsch, C. J. Sumby, N. G. White, P. Falcaro and C. J. Doonan, *J. Am. Chem. Soc.*, 2019, **141**, 14298–14305.

50 Q. Huang, W. Li, Z. Mao, L. Qu, Y. Li, H. Zhang, T. Yu, Z. Yang, J. Zhao, Y. Zhang, M. P. Aldred and Z. Chi, *Nat. Commun.*, 2019, **10**, 1–8.

51 I. Hisaki, Y. Suzuki, E. Gomez, Q. Ji, N. Tohnai, T. Nakamura and A. Douhal, *J. Am. Chem. Soc.*, 2019, **141**, 2111–2121.

52 K. Ma, P. Li, H. John, R. R. Maldonado, R. Q. Snurr, O. K. Farha, K. Ma, P. Li, J. H. Xin, Y. Chen, Z. Chen and S. Goswami, *Cell Reports Phys. Sci.*, 2020, **1**, 100024.

53 M. Thomas, T. Anglim Lagones, M. Judd, M. Morshedi, M. L. O'Mara and N. G. White, *Chem.–Asian J.*, 2017, **12**, 1587–1597.

54 D. J. Ashworth, A. Cooper, M. Trueman, R. W. M. Al-Saedi, S. D. Liam, A. J. Meijer and J. A. Foster, *Chem.–Eur. J.*, 2018, **24**, 17986–17996.

55 J. A. Foster, S. Henke, A. Schneemann, R. A. Fischer and A. K. Cheetham, *Chem. Commun.*, 2016, **52**, 10474–10477.

56 C. J. Shearer, A. D. Slattery, A. J. Stapleton, J. G. Shapter and C. T. Gibson, *Nanotechnology*, 2016, **27**, 125705.

57 Y. Peng, Y. Li, Y. Ban, H. Jin, W. Jiao, X. Liu and W. Yang, *Science*, 2014, **346**, 1356–1359.

58 Y. Zhao, J. Wang and R. Pei, *J. Am. Chem. Soc.*, 2020, **142**, 10331–10336.

59 Z.-R. Tao, J.-X. Wu, Y.-J. Zhao, M. Xu, W.-Q. Tang, Q.-H. Zhang, L. Gu, D.-H. Liu and Z.-Y. Gu, *Nat. Commun.*, 2019, **10**, 2911.

60 B. J. Córdova Wong, D. M. Xu, S. S. Bao, L. M. Zheng and J. Lei, *ACS Appl. Mater. Interfaces*, 2019, **11**, 12986–12992.

61 M. Zhao, Y. Wang, Q. Ma, Y. Huang, X. Zhang, J. Ping, Z. Zhang, Q. Lu, Y. Yu, H. Xu, Y. Zhao and H. Zhang, *Adv. Mater.*, 2015, **27**, 7372–7378.

62 H. Q. Zhao, G. H. Qiu, Z. Liang, M. M. Li, B. Sun, L. Qin, S. P. Yang, W. H. Chen and J. X. Chen, *Anal. Chim. Acta*, 2016, **922**, 55–63.

63 Q. Wang, W. Wang, J. Lei, N. Xu, F. Gao and H. Ju, *Anal. Chem.*, 2013, **85**, 12182–12188.

64 V. A. Russell, M. C. Etter and M. D. Ward, *J. Am. Chem. Soc.*, 1994, **116**, 1941–1952.

65 N. P. Cowieson, D. Aragao, M. Clift, D. J. Ericsson, C. Gee, S. J. Harrop, N. Mudie, S. Panjikar, J. R. Price, A. Riboldi-tunnicliffe, R. Williamson and T. Caradoc-davies, *J. Synchrotron Radiat.*, 2015, 187–190.

Supporting Information

Monolayer nanosheets formed by liquid exfoliation of charge-assisted hydrogen bonded frameworks

Joshua Nicks,[a] Stephanie A. Boer,[b] Nicholas G. White*[b] and Jonathan A. Foster*[a]

a. Department of Chemistry, University of Sheffield, Sheffield, S3 7HF, UK

b. Research School of Chemistry, The Australian National University, Canberra, ACT 2600, Australia

Contents.

S1. Synthesis and Characterisation of 1 and 2·TP

General remarks

Na$_2$·**TP** [S1] was prepared from benzene-1,4-dicarboxylic acid, and **2**·Cl$_2$ [S2] was prepared from 1,4-dicyanobenzene as previously described, dry THF was distilled from sodium. All other compounds were bought from commercial suppliers and used as received.

NMR spectra were collected on a Bruker Avance spectrometer and are referenced to the residual solvent signal.[S3] Infrared spectra were recorded on a Perkin-Elmer Spectrum Two FTIR spectrometer. Electrospray ionization (ESI) mass spectrometry data were acquired on a Micromass Waters ZMD spectrometer. Elemental analyses were recorded at London Metropolitan University. Thermogravimetric analyses were recorded on a TA Instruments Q500 analyzer. PXRD data for bulk material were recorded at room temperature using a PANalytical Empyrean diffractometer using Cu Kα radiation and a PIXcel detector.
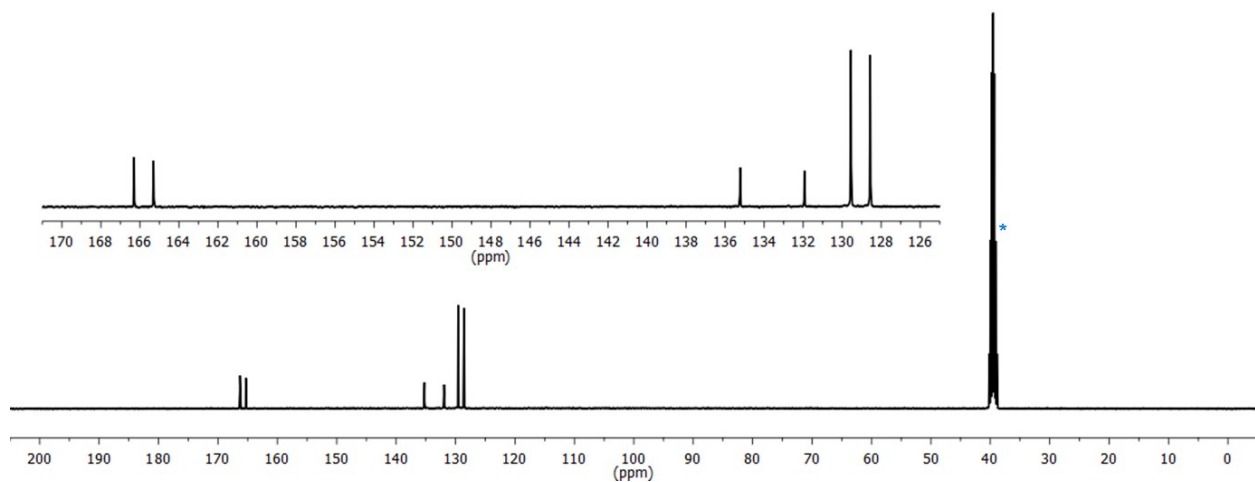
1^H·Cl

A solution of 4-cyanobenzoic acid (0.735 g, 5.00 mmol) in dry THF (25 mL) was cooled in a dry ice/acetone bath under a nitrogen atmosphere. A solution of LiHMDS in THF (1.0 M, 15 mL, 15 mmol) was added dropwise, resulting in the immediate formation of a precipitate. The mixture was allowed to warm to room temperature and stirred overnight. The reaction was then cooled in an ice-bath and ethanolic HCl (prepared by cautiously adding 2 mL acetyl chloride to 10 mL ethanol in an ice-bath) was added dropwise, resulting in the formation of a pale precipitate. All volatiles were removed under reduced pressure and the crude product was suspended in water (20 mL), sonicated for 20 minutes and then the mixture filtered. The precipitate was again suspended in water (10 mL), sonicated for 10 minutes), filtered and then thoroughly dried to give **1^H·Cl** as a pale brown powder. Yield: 0.789 g (3.93 mmol, 79%).

^{1}H NMR (d$_6$-DMSO): 13.50 (br. s, 1H), 9.52 (s, 2H), 9.28 (s, 2H), 8.12 (d, J = 8.5 Hz, 2H), 7.92 (d, J = 8.5 Hz, 2H) ppm. ^{13}C NMR (d$_6$-DMSO): 166.3, 165.3, 135.2, 131.9, 129.5, 128.5 ppm. HRESI-MS (pos.): 165.0654, calc. for [C$_8$H$_9$N$_2$O$_2$]$^+$ (*i.e.* loss of Cl$^-$): 165.0659 Da. ATR-IR (*inter alia*): 1705, 1665 cm^{-1} (C=O, C=N stretches).

*The ^{1}H and ^{13}C NMR spectra of **1^H·Cl** are provided in Figures S1 and S2.*
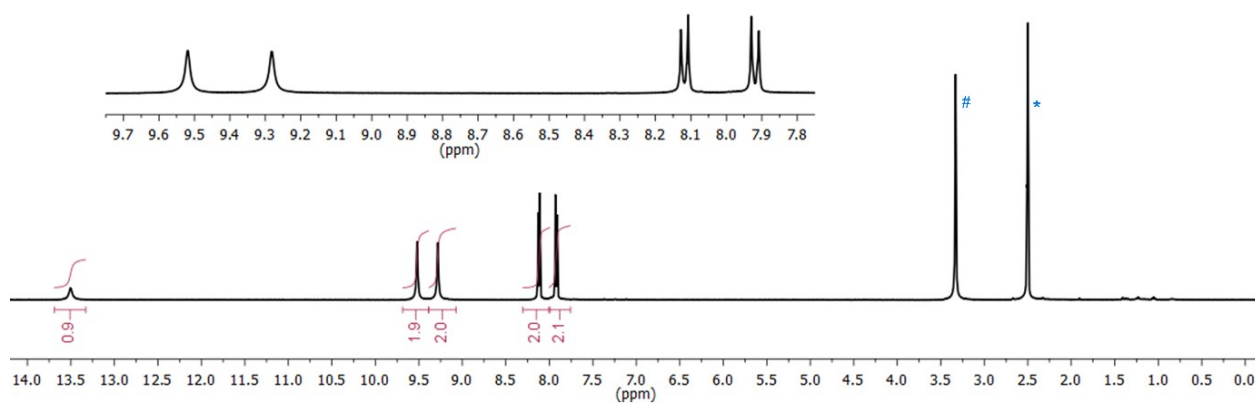
Figure S1. ¹H NMR spectrum of **1ᴴ·Cl**, residual solvent peak is marked * and water peak is marked # (d₆-DMSO, 298 K, 400 MHz).

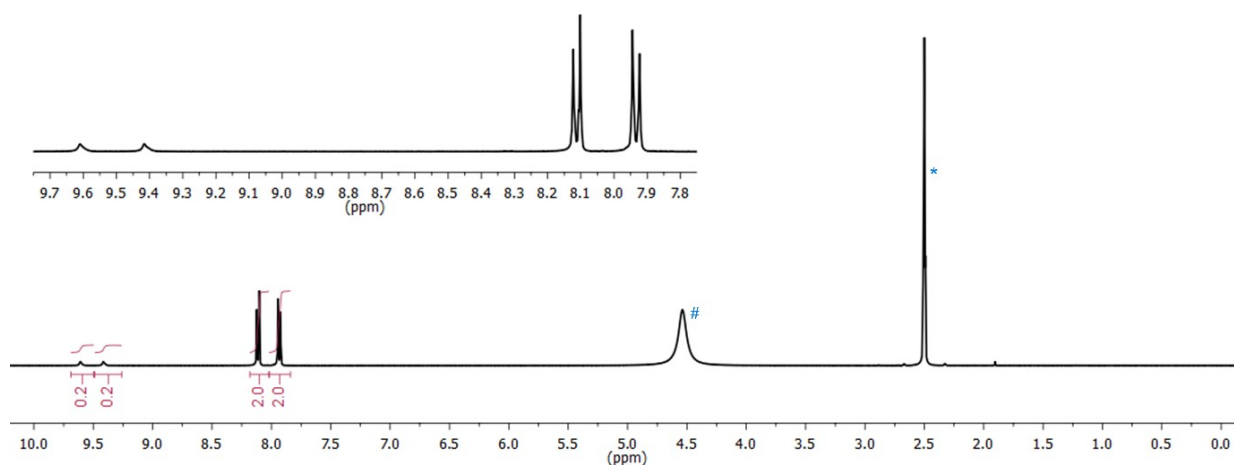**Figure S2.** ¹³C NMR spectrum of **1ᴴ·Cl**, residual solvent peak is marked * (d₆-DMSO, 298 K, 101 MHz).

1

The carboxylic acid-containing molecule **1**[H]·Cl (0.250 g, 1.25 mmol) was dissolved in a DMF/water (1:1 v:v, 130 mL) and heated to 120 °C for 2 days, during which time colourless crystals formed. These were isolated by filtration, washed with water (5 × 10 mL) and dried *in vacuo* to give **1**. Yield: 0.155 g (0.944 mmol, 76%).

^{1}H NMR (d$_6$-DMSO containing 1 drop of 20% DCl in D$_2$O): 9.62* (s, 2H), 9.43* (s, 2H), 8.10 (d, *J* = 8.4 Hz, 2H), 7.94 (d, *J* = 8.1 Hz, 2H). ATR-IR (*inter alia*): 1703, 1583 cm^{-1} (C=O, C=N stretches). EA: C 58.4, H 4.8, N. 17.0%, calc. for [C$_8$H$_8$N$_2$O$_2$]: C 58.5, H 4.9, N 17.1%.

*These peaks integrate to a value lower than expected due to H/D exchange.

*The ^{1}H NMR spectrum of acid-digested **1** is provided in Figure S3.*

Figure S3. ^{1}H NMR spectrum of acid-digested **1**, residual solvent peak is marked * and water peak is marked # (d$_6$-DMSO containing 20% DCl in D$_2$O, 298 K, 400 MHz). Note that the amidinium N–H resonances integrate to a much lower value than expected (2H each) due to H/D exchange.

The PXRD trace of bulk **1** is shown in Figure S4. Good agreement is observed between the measured data and that calculated from the room temperature SCXRD structure.
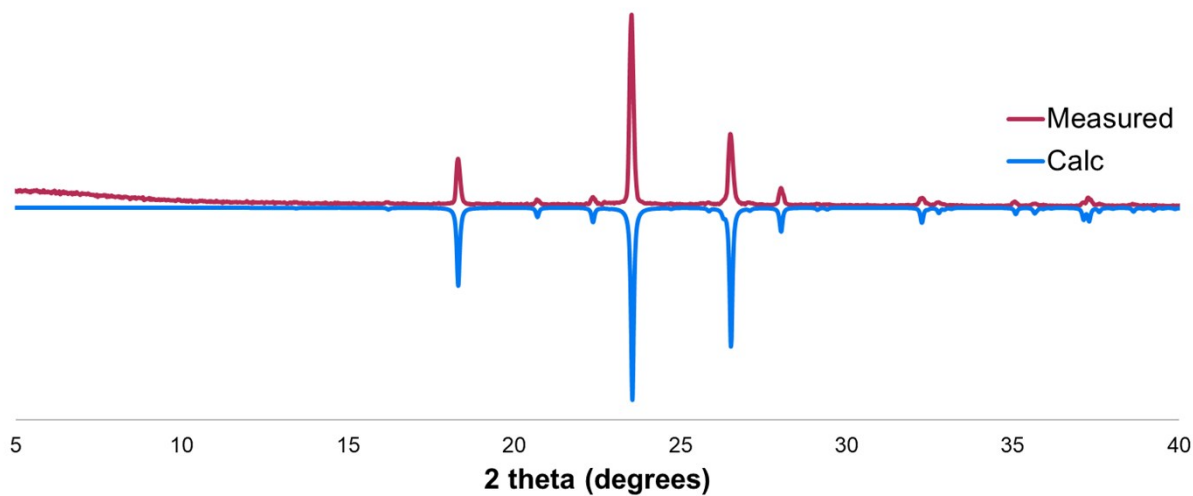
Figure S4. Measured PXRD trace of **1** (up, maroon) and comparison with that calculated from SCXRD data (down, blue).

The TGA trace of bulk **1** is shown in Figure S5. No mass loss is seen until > 300 °C, at which point thermal decomposition is observed.
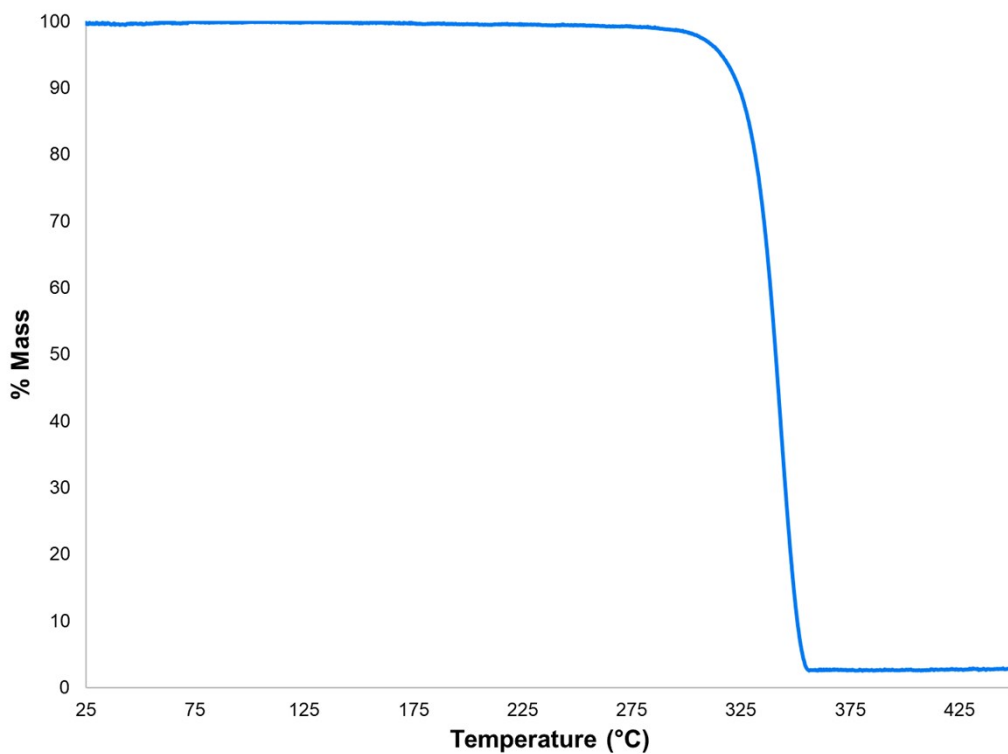
**Figure S5.** TGA trace of **1** (recorded under N_2 at a ramp rate of 5 °C/minute).

2·TP

We have previously reported the synthesis of this framework on a small (20 mg scale) from 2·Cl₂ and tetrabutylammonium terephthalate.[S4] The procedure was optimized to allow preparation of a larger sample of material. In this procedure, we have used sodium terephthalate as it is cheaper and easier to prepare than tetrabutylammonium terephthalate.

A solution of bis(amidinium) **2·Cl₂** (0.235 g, 1.00 mmol) in water (50 mL) was placed in a measuring cylinder. It was carefully layered with water (50 mL), and then sodium terephthalate (0.210 g, 1.00 mmol) in water (50 mL). After several days, the resulting white microcrystalline solid was isolated by filtration, washed with water (4 × 10 mL) and methanol (4 × 10 mL), and dried thoroughly to give **2·TP**. Yield: 0.293 g (0.892 mmol, 89%).

¹H NMR (Figure S6) and PXRD data (Figure S7) were consistent with those previously reported.[S4] Good agreement is observed between the measured PXRD data and that calculated from the room temperature SCXRD structure.
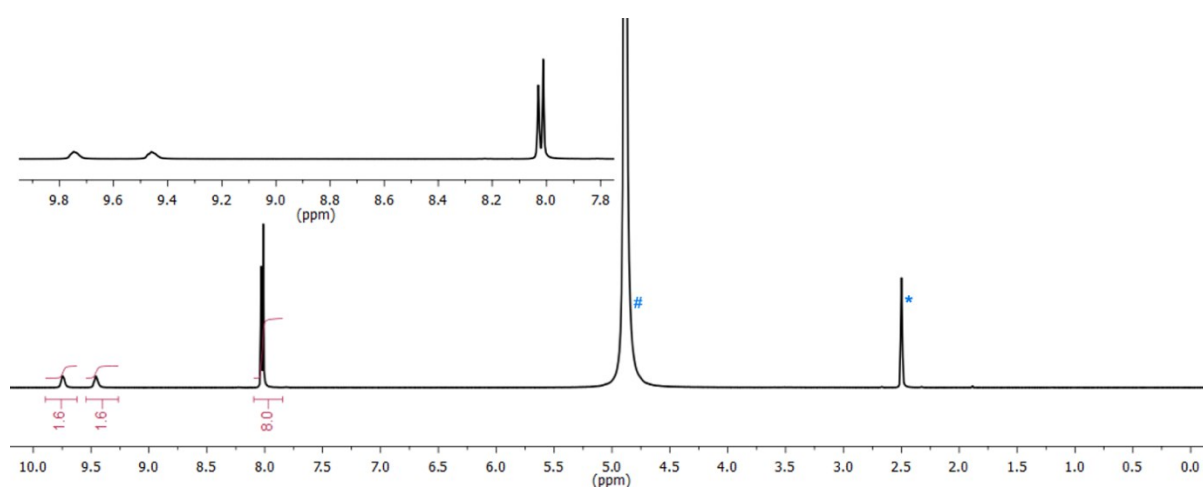
Figure S6. ¹H NMR spectrum of acid-digested **2·TP**, residual solvent peak is marked * and water peak is marked # (d₆-DMSO containing 20% DCl in D₂O, 298 K, 400 MHz). Note that the amidinium N–H resonances integrate to a much lower value than expected (2H each) due to H/D exchange.
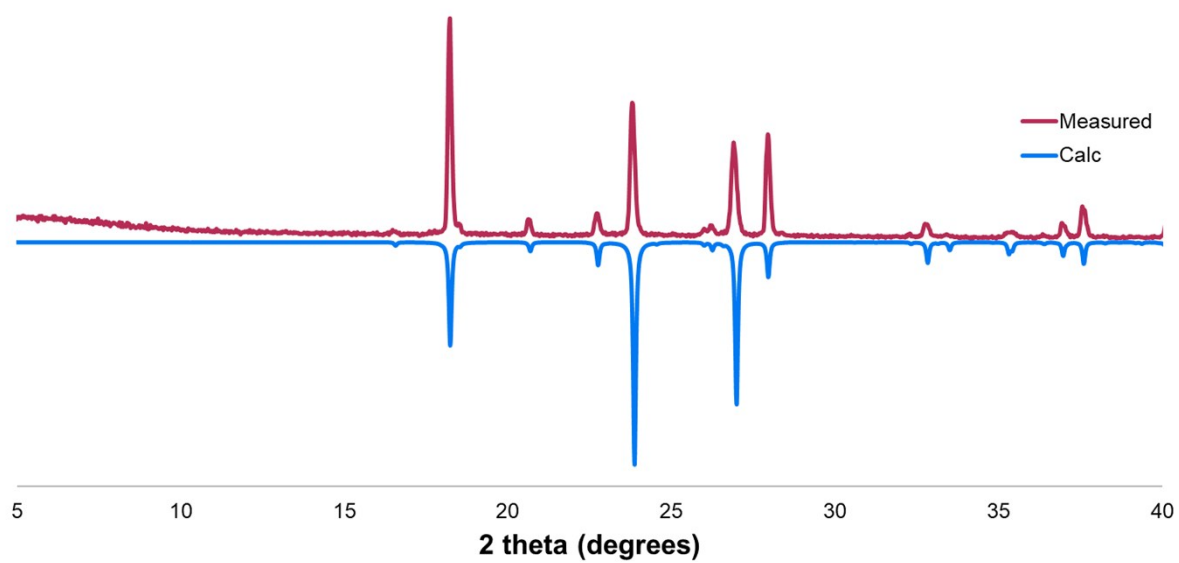
Figure S7. Measured PXRD trace of **2·TP** (up, maroon) and comparison with that calculated from SCXRD data (down, blue).

SCXRD studies

## Details of data collection and refinement

We have obtained two single crystal structures of **1**. The first was collected at the Australian Synchrotron at 100 K, and due to the weakly-diffracting crystal and limitations of the beamline has poor data completeness. We subsequently re-collected this structure on a home-source diffractometer at room temperature, using a better quality crystal. The data for the structure collected at room temperature are superior to those collected at 100 K. All figures, details of bond lengths and comparisons with PXRD data use the 293 K collection, however we have included both structures for completeness. We have also collected a structure of **2·TP** at 293 K, having previously reported a low temperature (150 K) structure of this compound.[S4]

Data were either collected using mirror-monochromated Cu Kα radiation on an Agilent SuperNova diffractometer at 293 K or using beamline MX1[S5] of the Australian Synchrotron at 100 K. Raw frame data for the structures collected at 293 K (including data reduction, interframe scaling, unit cell refinement and absorption corrections) were processed using CrysAlis Pro,[S6] while data for the structure collected at 100 K were processed using XDS.[S7]

All structures were solved using Superflip,[S8] and refined using full-matrix least-squares on F^2 within the Crystals suite.[S9] All non-hydrogen atoms were refined with anisotropic displacement parameters. All hydrogen atoms were clearly visible in the Fourier difference map: C–H hydrogen atoms were initially refined with restraints on bond lengths and angles, after which the positions were used as the basis for a riding model.[S10] The positions of N–H hydrogen atoms were refined with restraints on N–H and C–N–H angles.

Apart from restraints on the hydrogen atom positions, it was not necessary to use any crystallographic restraints in any of the refinements.

Crystallographic data for the structures reported in this paper (**1** at 100 K and 293 K, **2·TP** at 293 K) have been deposited with the Cambridge Crystallographic Data Centre (CCDC Numbers: 2047425–2047427). Thermal ellipsoid plots are shown in Figures S8–S10, and selected data are summarized in Table S1. Data for the previously-published[S4] low temperature structure of **2·TP** are also available from the CCDC (CSD reference code: ZEFSOV, CSD deposition number: 1537445).
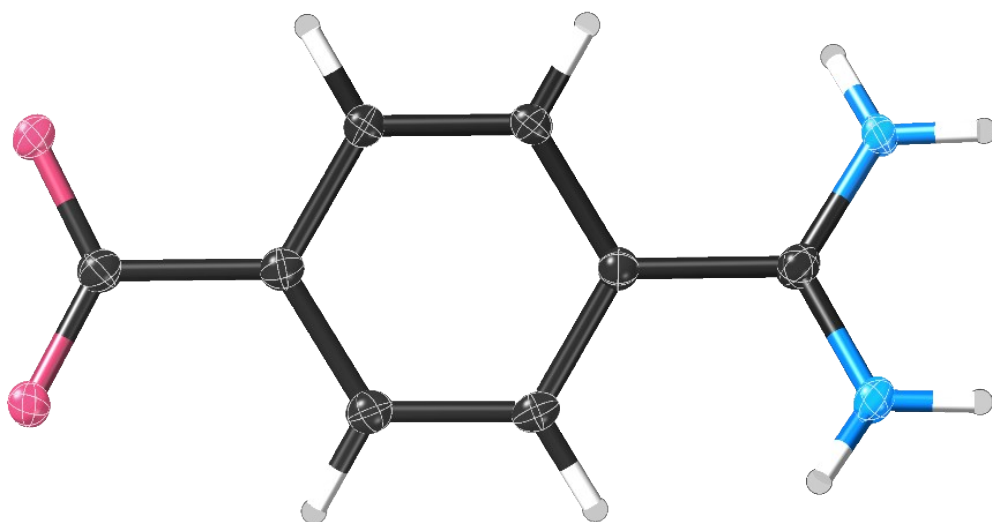
Figure S8. Thermal ellipsoid plot of the asymmetric unit of **1** at 100 K, ellipsoids shown at 50% probability level.
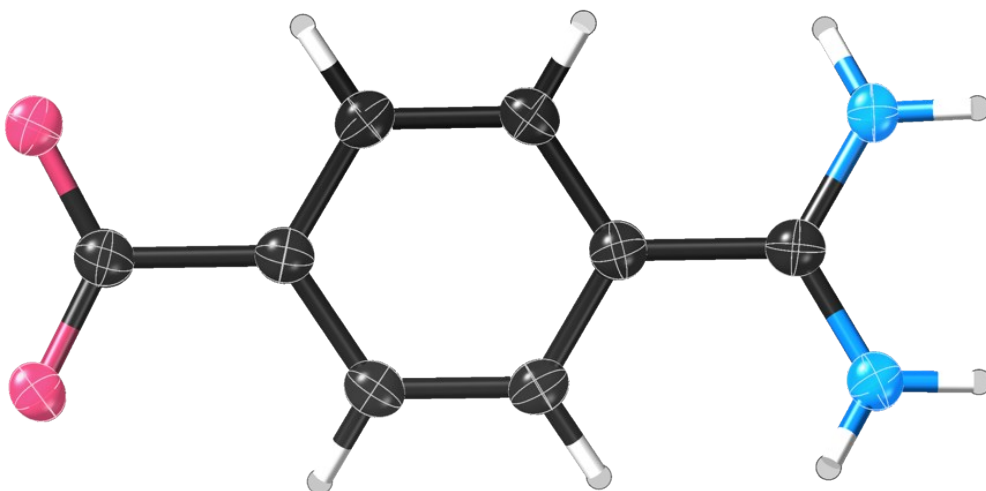
Figure S9. Thermal ellipsoid plot of the asymmetric unit of **1** at 293 K, ellipsoids shown at 50% probability level.
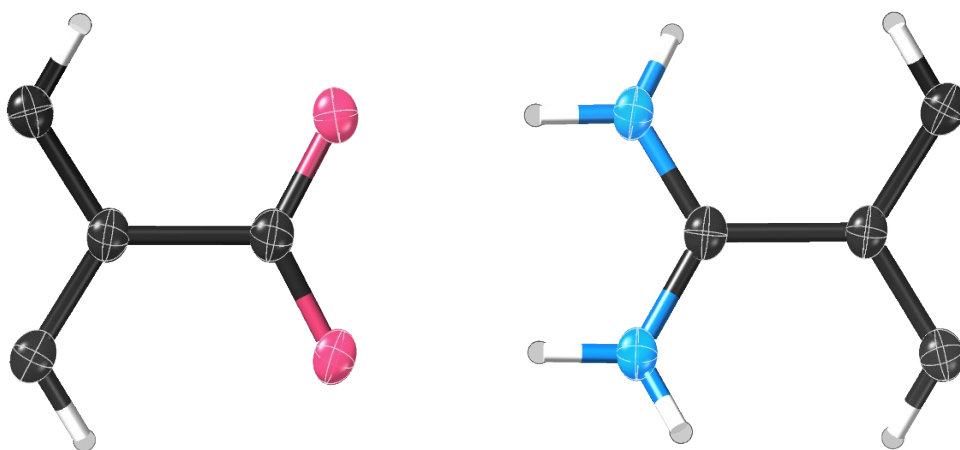
Figure S10. Thermal ellipsoid plot of the asymmetric unit of **2·TP** at 293 K, ellipsoids shown at 50% probability level.

Table S1. Selected crystallographic data.

	1 (100 K)	1 (293 K)	2_TP (293 K)
Radiation type	Synchrotron (λ = 0.7108 Å)	Cu Kα (λ = 1.54184 Å)	Cu Kα (λ = 1.54184 Å)
Temperature (K)	100	293	293
Formula	$C_8H_8N_2O_2$	$C_8H_8N_2O_2$	$(C_8H_{12}N_4)_{0.5} \cdot (C_8H_4O_4)_{0.5}$
Formula weight	164.16	164.16	164.16
a (Å)	6.9310(14)	7.03480(2)	5.5557(5)
b (Å)	7.5900(15)	7.85120(2)	7.8957(7)
c (Å)	7.7350(15)	7.88270(2)	9.0549(8)
α (°)	60.94(3)	61.268(5)	71.386(8)
β (°)	82.44(3)	74.309(4)	83.555(7)
γ (°)	75.12(3)	82.320(5)	74.217(7)
Unit cell volume (Å^3)	343.73(16)	367.540(19)	362.09(6)
Crystal system	triclinic	triclinic	triclinic
Space group	P–1	P–1	P–1
Z	2	2	2
Reflections (all)	3285	6926	5714
Reflections (unique)	1666	1434	1452
Min/max difference density (e A^{-3})	–0.79/0.68	–0.37/0.36	–0.20/0.25
R_{int}	0.037	0.029	0.024
R_1 [$I > 2\sigma(I)$]	0.093	0.072	0.046
$wR_2(F^2)$ (all data)	0.331	0.252	0.138
CCDC number	2047425	2047426	2047427

Effect of temperatures on structures

Increasing the temperature (from 100 K to 293 K for **1**, and from 150 K to 293 K for **2·TP**) causes small increases in the unit cell axes (0.2–3.4%) as well as small changes in the unit cell angles (up to ±1.1%). This results in an increase in unit cell volume of 6.9% for **1** and 1.7% for **2·TP**. Given the relatively low resolution of hydrogen atom positions in X-ray crystal structures, we have not speculated on the effect of temperature on hydrogen bonding parameters.

SEM Imaging of 1 and 2·TP

SEM images of **1** and **2·TP** are shown in Figures S12 and S13 at multiple magnifications.
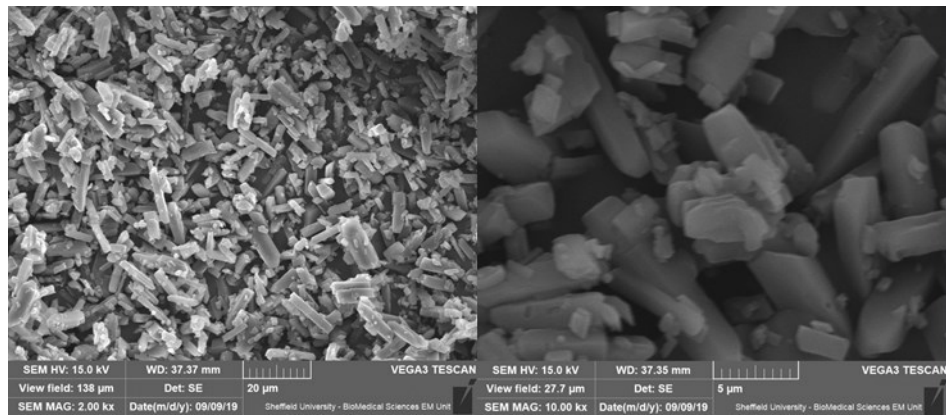
Figure S11. SEM images at 20 μm and 5 μm scales, indicating the layered morphology of **1**.
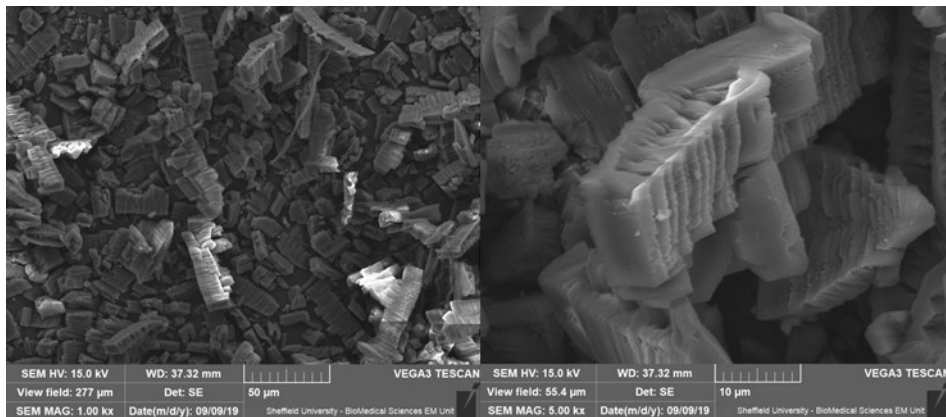
Figure S12. SEM images at 50 μm and 10 μm scales, indicating the layered morphology of **2·TP**.

S2. Preparation of HON1 and HON2

General Remarks

Atomic force microscopy images were recorded using a Bruker Multimode 5 atomic force microscope, operating in soft-tapping mode in air under standard ambient temperature and pressure, fitted with Bruker OTESPA-R3 silicon cantilevers operated with a drive amplitude of ~18.70 mV and resonance frequency of ~236 kHz. Samples were prepared by drop-casting 10 μL drops of suspension onto the centre of freshly cleaved mica sheets heated to 100 °C on a hot plate. These sheets were stuck to stainless steel, magnetic Agar scanning probe microscopy specimen discs. Images were processed using Gwyddion software.

DLS data were collected using a Malvern Zetasizer Nano Series particle size analyser, using a He-Ne laser at 633 nm, operating in backscatter mode (173 °). Samples were placed in quartz cuvettes and equilibrated at 298 K for 60 s prior to analysis.

Powder X-ray diffraction patterns were collected using a Bruker-AXS D8 diffractometer, using Cu K_α (λ=1.5418 Å) radiation, operating at 40 V and 40 mA, and fitted with an energy-dispersive LynxEye position sensitive detector in Bragg Brentano parafocussing geometry using a flat silicon plate.

Ultrasonic Exfoliation

Samples of **1** or **2·TP** were suspended in DMF or acetone respectively (5 mL) and vortexed for 20 s, followed by sonication for 12 hr using a Fisher brand Elmasonic P 30H ultrasonic bath operating at 80 kHz and 100% power (320 W). Samples were rotated using an overhead stirrer to ensure even exposure and prevent the occurrence of "hot spots", and the bath was fitted with a water coil to maintain temperature at approximately 18–21 °C. After sonication, samples were transferred into polypropylene centrifuge tubes and centrifuged for 1 hr at 1500 rpm, in order to sediment unexfoliated material and leave **HON-1** and **HON-2** in suspension.[S11]
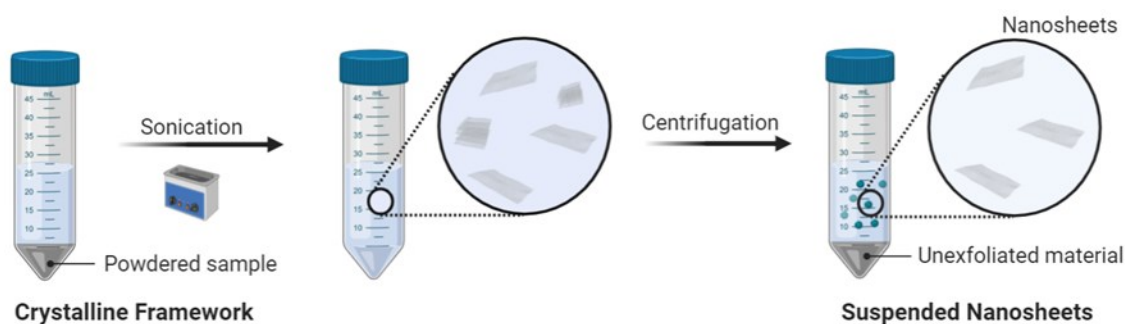
Figure S13. Illustration of the exfoliation of layered hydrogen bonded frameworks into nanosheets usind liquid-assisted sonication.

Nanosheet Characterisation
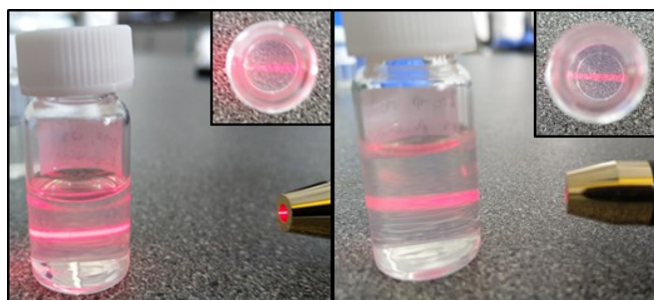
Figure S14. Tyndall scattering effects exhibited by as prepared suspensions HON1 in DMF (left) and HON2 in acetone (right).
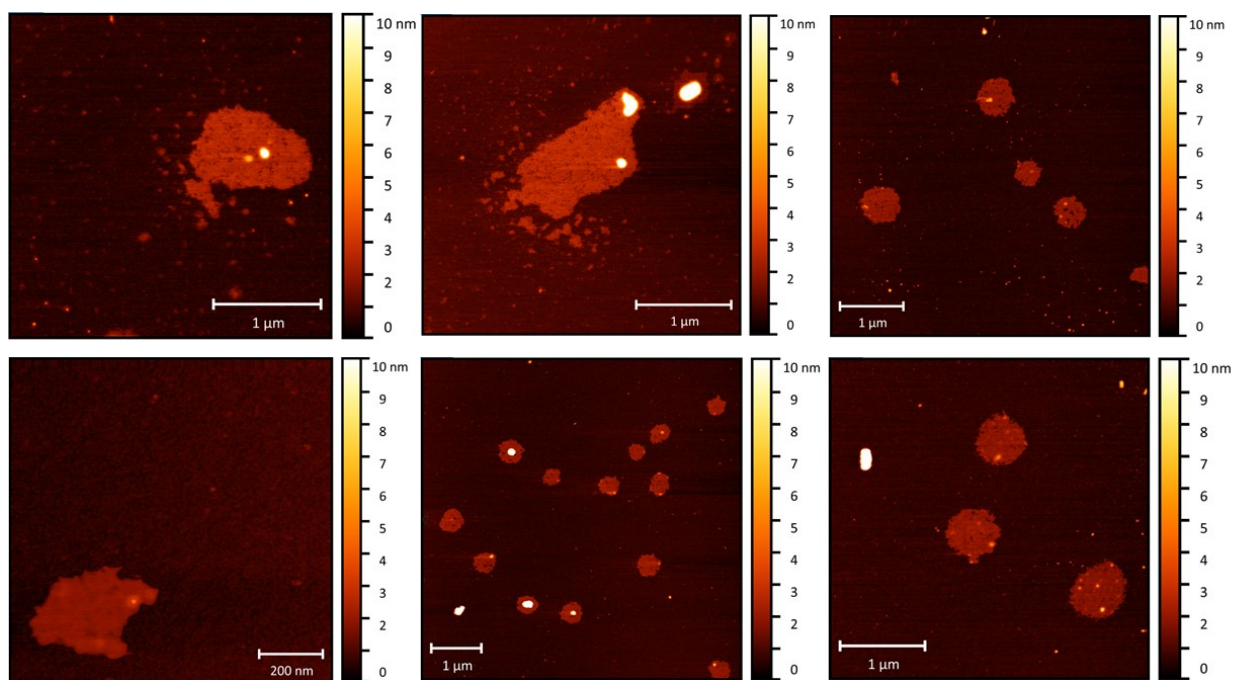
Figure S15. AFM topographical images of **HON1** nanosheets.

Figure S16. AFM topographical images of **HON2** nanosheets.
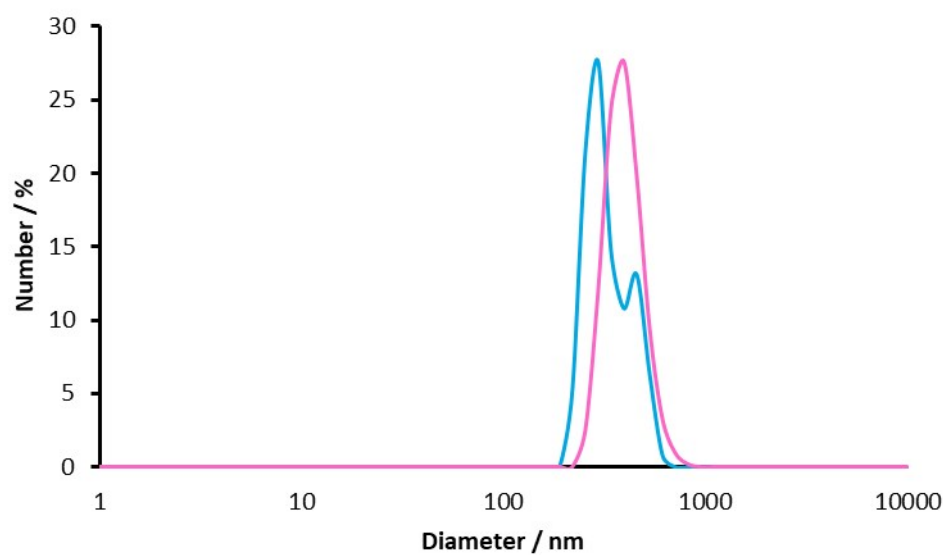
Figure S17. DLS number plots for suspensions of **HON-1** (blue) and **HON-2** (pink).

S3. Water Stability Experiments

Samples of both HON-1 and HON-2 were treated with distilled water (10 mL) and heated for 3 days at 80 °C in sealed reaction vials. HONs were then reisola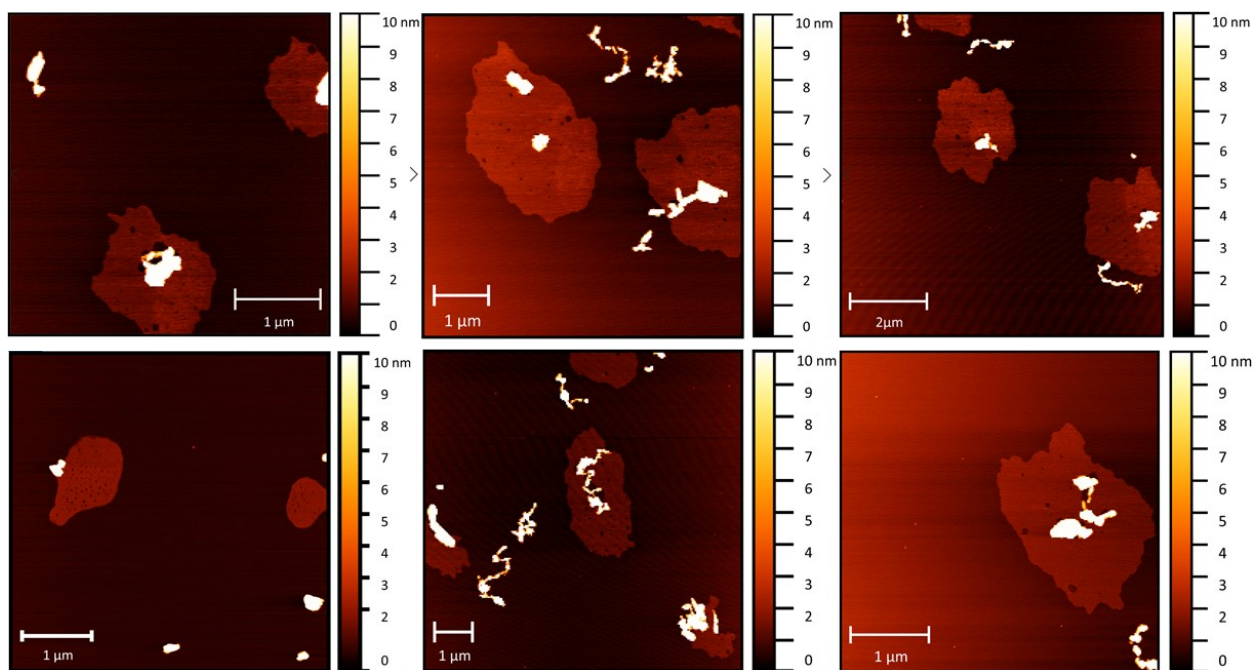ted by centrifugation at 10000 rpm for 1 hour, washed with acetone to remove residual water, then subject to XRD and AFM analysis.
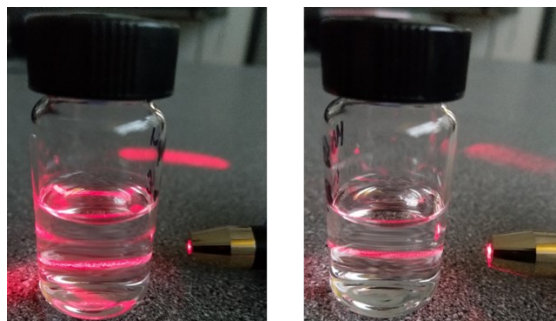
Figure S18. Tyndall scattering effects exhibited by suspensions of **HON-1** (left) and **HON-2** (right) after treatment in water.
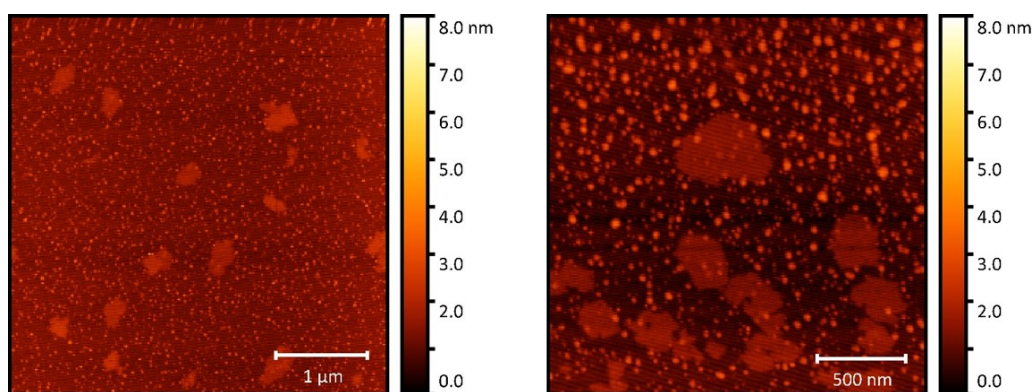
Figure S19. AFM topographical images of **HON-1** nanosheets after water treatment.
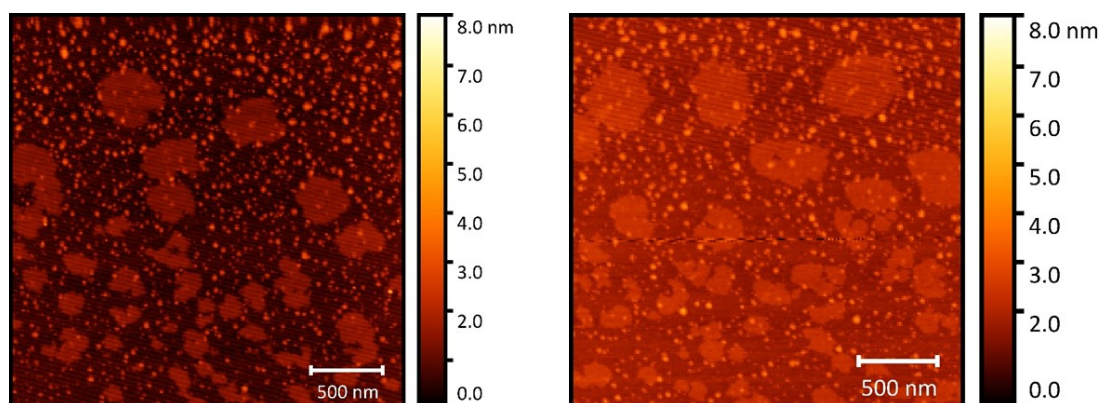
Figure S20. AFM topographical images of **HON-2** nanosheets after water treatment.

S4. Quenching Studies
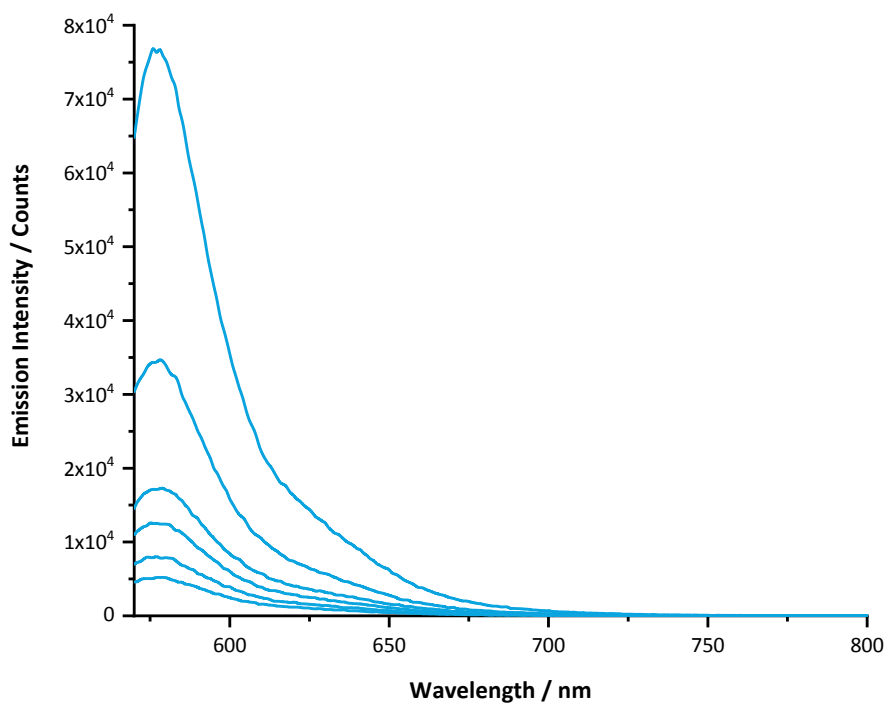
Figure S21. Emission spectra of Rhodamine B (top) in acetone with increasing quantities of HON-1 nanosheets (0.01 mg each).
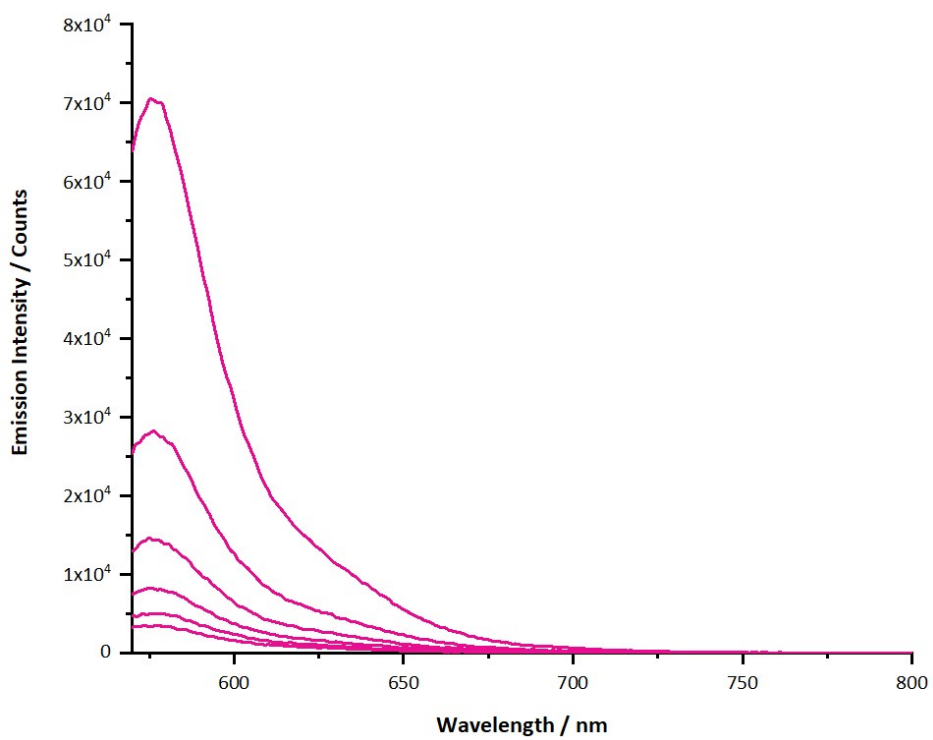
Figure S22. Emission spectra of Rhodamine B (top) in acetone with increasing quantities of HON-2 nanosheets (0.01 mg each).
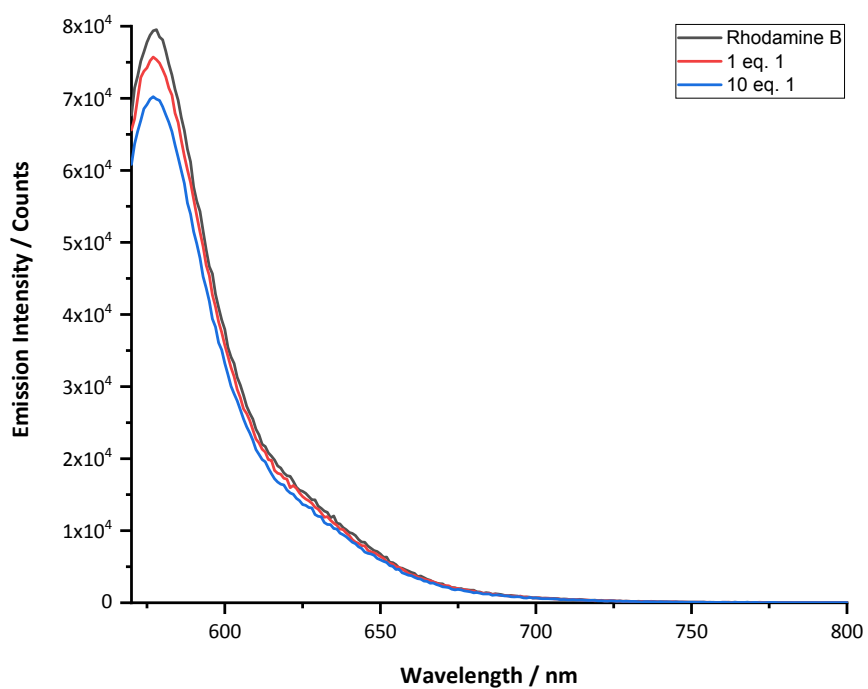
Figure S23. Emission spectra of Rhodamine B in acetone with increasing quantities of bulk framework **1**.
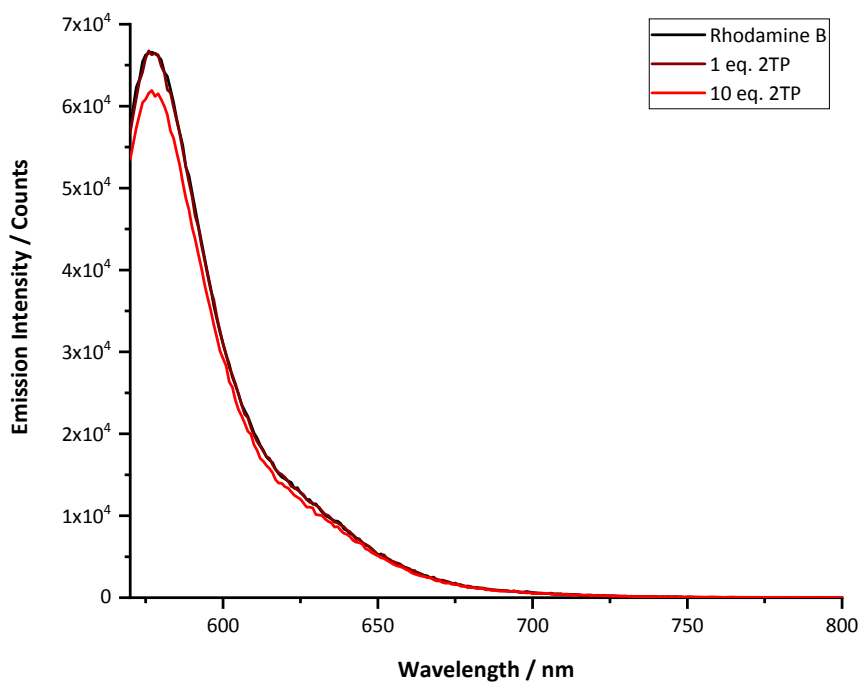
Figure S24. Emission spectra of Rhodamine B in acetone with increasing quantities of bulk framework **2TP**.

S5. References

[S1] M-F. Zaltariov, A. Vlad, M. Cazacu, S. Shova, M. Balan, C. Racles, A novel siloxane-containing dicarboxylic acid, 1,3-bis(*p*-carboxyphenylene-ester-methylene)tetramethyldisiloxane, and its derivatives: ester macrocycle and supramolecular structure with a copper complex, *Tetrahedron*, **2014**, *70*, 2661–2668.

[S2] K. Wang, L-M. Yang, X. Wang, L. Guo, G. Cheng, C. Zhang, S. Jin, B. Tan, A. Cooper, Covalent triazine frameworks via a low-temperature polycondensation approach, *Angew. Chem. Int. Ed.* **2017**, *56*, 14149–14513.

[S3] H. E. Gottlieb, V. Kotlyar, A. Nudelman, NMR chemical shifts of common laboratory solvents as trace impurities, *J. Org. Chem.* **1997**, *62*, 7512–7515.

[S4] M. Thomas, T. Anglim Lagones, M. Judd, M. Morshedi, M. L. O'Mara, N. G. White, Hydrogen bond-driven self–assembly between amidiniums and carboxylates: a combined MD, NMR and SCXRD study, *Chem. Asian J.* **2017**, *12*, 1587–1597.

[S5] N. P. Cowieson, D. Aragao, M. Clift, D. J. Ericsson, C. Gee, S. J. Harrop, N. Mudie, S. Panjikar, J. R. Price, A. Riboldi-Tunnicliffe, R. Williamson, T. Caradoc-Davies, MX1: a bending-magnet crystallography beamline serving both chemical and macromolecular crystallography communities at the Australian Synchrotron, *J. Synchrotron Radiat.* **2015**, *1*, 187–190.

[S6] Agilent Technologies, *CrysAlisPro*, **2011**.

[S7] W. Kabsch, Automatic processing of rotation diffraction data from crystals of initially unknown symmetry and cell constants, *J. Appl. Cryst.* **1993**, *26*, 795–800.

[S8] L. Palatinus, G. Chapuis, *SUPERFLIP* – a computer program for the solution of crystal structures by charge flipping in arbitrary dimensions, *J. Appl. Cryst.* **2007**, *40*, 786–790.

[S9] P. W. Betteridge, J. R. Carruthers, R. I. Cooper, K. Prout, D. J. Watkin, *CRYSTALS* version 12: software for guided crystal structure analysis, *J. Appl. Cryst.* **2003**, *36*, 1487.

[S10] R. I. Cooper, A. L. Thompson, D. J. Watkin, *CRYSTALS* enhancements: dealing with hydrogen atoms in refinement, *J. Appl. Cryst.* **2010**, *43*, 1100–1107.

[S11] D. J. Ashworth, A. Cooper, M. Trueman, R. W. M. Al-Saedi, S. D. Liam, A. J. Meijer and J. A. Foster, Chem. - A Eur. J., **2018**, *24*, 17986-17996.

Chapter 7

Reactive Inkjet Printing of Metal-Organic Frameworks

HKUST-1
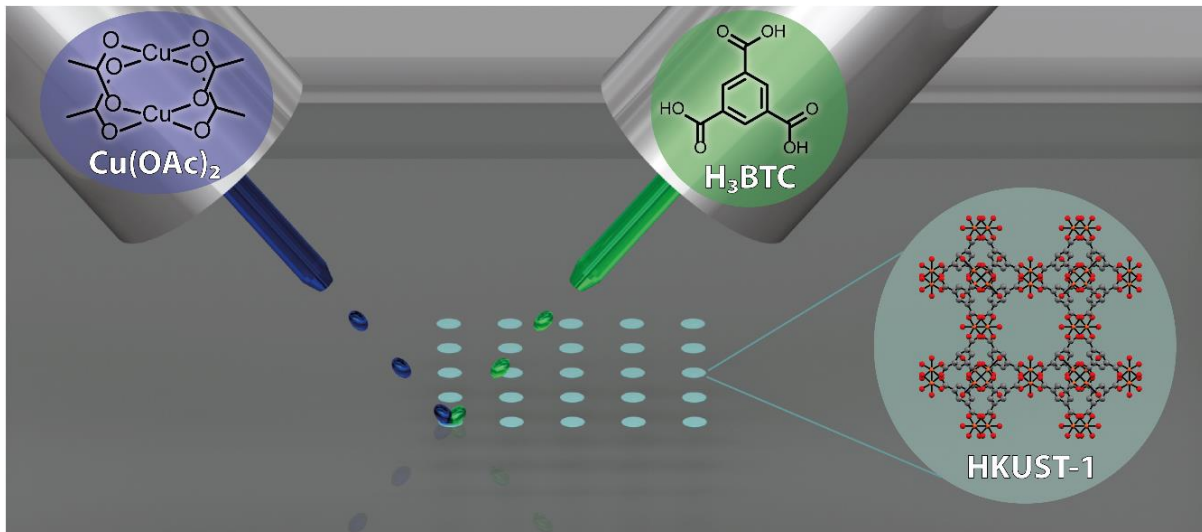
Chapter 7

Reactive Inkjet Printing of Metal-Organic Frameworks

Unpublished paper (full article)

David. A. Gregory, **Joshua Nicks**, Joaquin Artigas-Arnaudas, Jonathan A. Foster, and Patrick J. Smith

Author Contributions

David A. Gregory	Performed all printing experiments and Raman characterisation. Aided in drafting and editing of manuscript and SI.
Joshua Nicks	Supervised JJA**,** synthesised all bulk MOFs, performed initial small scale room temperature experiments and collected all XRD data. Aided in drafting and editing of manuscript.
Joaquin Artigas-Arnaudas	MEng student supervised by JN and JAF, performed initial investigations into printing of HKUST-1.
Jonathan A. Foster	Supervised JN and JJA, coordinated body of work with PJS and drafted manuscript.
Patrick J. Smith	Supervised DAG and JJA, coordinated body of work with JAF, aided in editing of manuscript.

Reactive Inkjet Printing of Metal-Organic Frameworks

David A. Gregory,[a] Joshua Nicks,[b] Joaquin Artigas-Arnaudas,[c] Jonathan A. Foster,*[b] and Patrick J. Smith*[c]

Reactive inkjet printing (RIJ) is demonstrated as a new approach to the patterning of surfaces with metal-organic frameworks (MOFs). An inkjet printer fitted with an angled jetting device was used to print picolitre quantities of separate solutions of metal ions and ligands onto a surface which then reacted at room temperature to form the MOFs. The MOFs were printed into a variety of different shapes and the structure of the material was confirmed by XRPD, Raman spectroscopy and SEM studies. Different combinations of ligand and metal ion solutions were used to print five different MOFs: Cu(BTC), Cu(BDC), Cu(ABDC), Zn(BIM)$_2$ and Co(BIM)$_2$. Furthermore, gradients where the structure printed gradually changed from one MOF to another could be printed by gradually changing the ratio of ligand or metal ions printed. The porosity of the printed MOF -1 was utilised through size-selective absorption of a fluorescent dye. We anticipate RIJ will be broadly applicable to a wide range of MOFs enabling their use in a broad range of separation, sensing, storage, release, and catalysis applications.

Introduction

Metal-organic frameworks (MOFs) are a diverse class of materials formed by reacting organic ligands with metal-ions to form crystalline co-ordination compounds consisting of porous networks. The high internal surface areas and readily tuneable chemistry of MOFs mean they have found use in a wide variety of applications,[1] including gas-storage and separation,[2] catalysis,[3] sensing,[4] water-purification,[5] drug release,[6] and electronics applications.[7] However, the insolubility of MOFs makes it challenging to process them into the often complex shapes and patterns required for real world applications and use in sophisticated devices.[8] As such, a diverse range of approaches have been explored for growing, depositing and patterning MOFs onto surfaces (SURMOFs)[9] including: spray coating,[10] spin coating,[11] dip-coating,[11,12] soft lithography,[13] microfluidic[14] and 3D printing,[15,16] electrospinning,[17] and gel monolith approaches.[16,18,19]

Inkjet printing is a widely used approach to depositing complex patterns onto surfaces and offers a variety of advantages including minimal wastage, large-area depositions and integration with computer-aided design (CAD) information.[20] Inkjet printing has been applied to a wide variety of organic and inorganic functional materials for use in applications as diverse as flexible displays,[21,22] solar cells,[23] catalysts,[24] explosive sensors,[25] transistors,[26,27] data and energy storage devices,[28,29] as well as biological materials,[30,31] and medical devices.[32] As porous materials, printed MOFs have the potential to create selective channels allowing for the transport, separation and sequestration, sensing and catalysis of analytes within lab-on-a-chip type devices. However, to our knowledge only three studies exist in which inkjet printing of MOFs are reported. These demonstrate the printing of several different MOFs for use in sensing,[33] anti-counterfeiting,[34] and electrocatalysis applications.[35]

The first report of inkjet printed MOFs was in 2013 by Zhuang et al.,[36] who used a commercial inkjet printer to deposit a single MOF precursor solution containing both ligands and metal-ions onto a variety of plastic, paper and textile substrates. Stable inks were achieved through formulation of the subcomponents in DMSO, ethanol and ethylene glycol but samples required drying in an oven and washing with methanol to remove the ethylene glycol from the MOF (HKUST-1). A similar approach was used by Luz et al.,[34] who printed aqueous inks consisting of a suspension of pre-formed nanoparticles of three different lanthanide MOFs along with ethanol as an anti-solvent to accelerate precipitation. With this approach it is important to use fresh precursor solution because crystal nucleation obstructs the cartridge. A more recent report by Su et al.,[35] described the inkjet printing of porphyrinic metal–organic framework thin films using well-dispersed suspensions of MOF crystals. The authors discuss the challenges associated with this approach in creating stable suspensions which can otherwise clog print-heads and avoided this by making nanosized MOFs. Given the widespread use of inkjet printing, and the extensive literature on MOFs, we suggest the lack of examples highlights the challenges in printing MOFs using these approaches.

Reactive inkjet printing (RIJ) is an additive manufacturing technique which aspires to overcome the challenges associated with creating stable suspensions/inks and so broaden the pallet of materials which can be printed.[20,30,31] In RIJ, stable solutions

[a.] a. Department of Materials Science and Engineering, University of Sheffield, Sheffield S1 3JD, UK
[b.] b. Department of Chemistry, University of Sheffield, Brook Hill, Sheffield, S3 7HF, UK
[c.] c. Department of Mechanical Engineering, University of Sheffield, Garden Street, Sheffield, UK, S1 4BA
[d.] Electronic Supplementary Information (ESI) available: additional characterisation details, Raman spectra and XRPD patterns.

of two or more reactants are printed in the same location and react on a surface to produce the desired material *in situ*. RIJ enables precise control of picolitre size droplets which improves mixing and heat transfer making the reaction more efficient and the overall process consume less material. This can also improve safety by reducing the quantity of hazardous components used, as in the work of Lennon *et al.*,[37] who created patterned layers of SiO_2 and SiN_x by direct etching with HF via RIJ. Additionally, the use of an inkjet printer allows for the reactant stoichiometry, synthesis conditions and composition to be readily varied during printing.[20]

Here we demonstrate the use of RIJ as a new approach to the synthesis and patterning of MOFs onto substrates. Separate inks consisting of ligand or metal-ions dissolved in DMF are deposited simultaneously onto a substrate, where they mix and react resulting in MOF formation. The picolitre droplet size results in efficient mixing and rapid evaporation of the solvent allowing for well-defined patterns. In this work we demonstrate the synthesis of a range of MOF architectures which have found applications in numerous fields. Furthermore, by not using pre-formed MOF crystallites the RIJ techniques allows for the patterning of surfaces with gradients of MOFs with different ratios of building blocks. As a step towards these types of lab-on-a-chip applications, we demonstrate that printed MOFs retain their well-defined pores and can therefore be used to selectively encapsulate specific dyes whilst rejecting others.

Results and discussion

Inks were formed by separately dissolving the respective metal acetate salt and ligand in DMF as 0.25 M solutions of each. Acetate salts, rather than the more commonly used nitrate salts, were chosen as it is known to accelerate the synthesis of paddlewheel-based MOFs by pre-forming the desired secondary building unit. DMF was selected as its high boiling point and the ability to dissolve both the organic ligands and metal salts in the same solvent made it attractive for this first study. The rheological properties of the solutions were characterised to investigate the jet-ability of different inks (Table S1). Notably, although the Z number for the inks lie outside the typical range for a printable ink of between 1-10,[38,39] both inks jetted well (Figure 1).
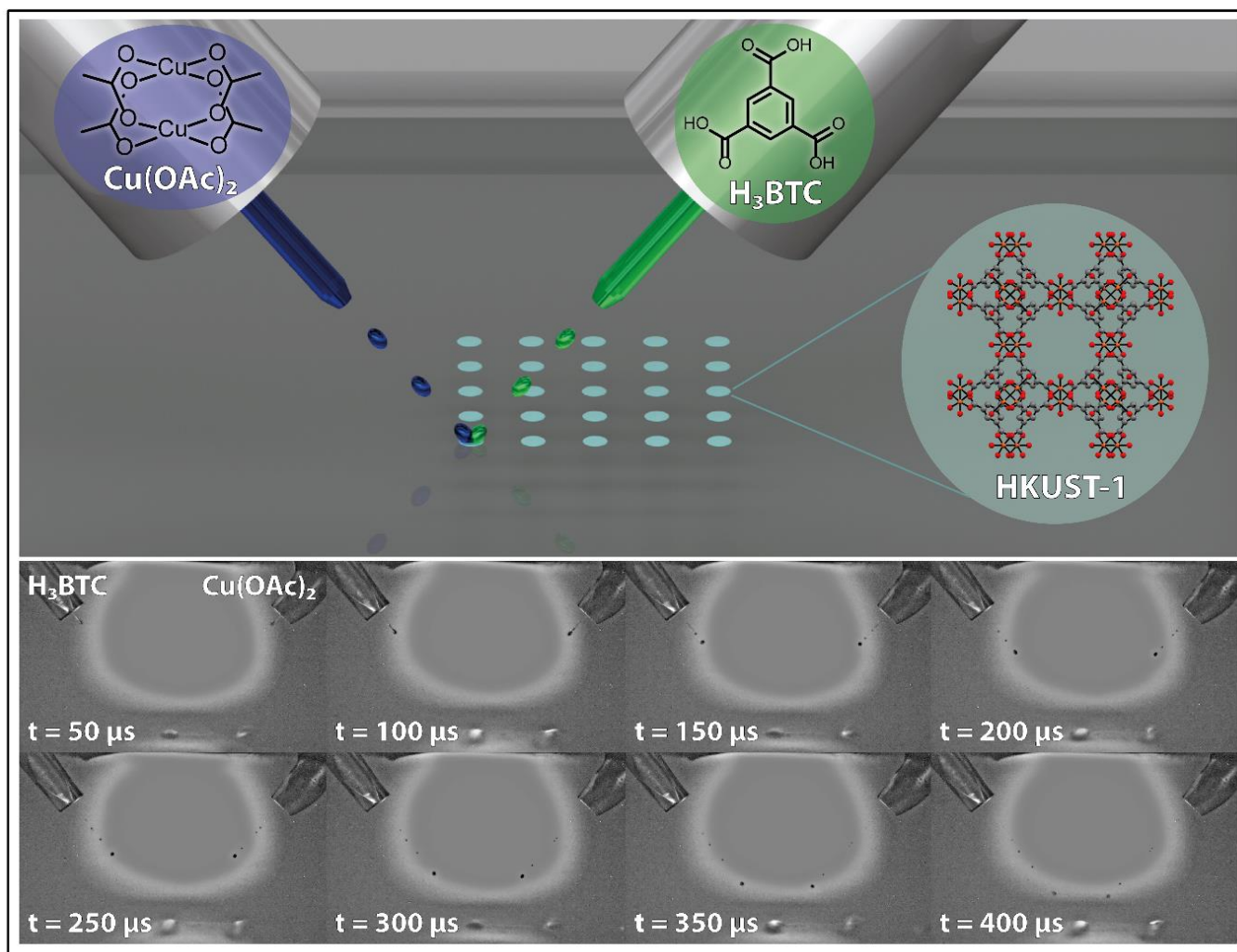
Figure 1. (Top) Schematic representation of the printing process of a 5 x 5 dot array: Green droplets and jetting nozzle (60 μm nozzle diameter) represent the ligand ink (H_3BTC 0.25 M in DMF), blue droplets and jetting nozzle (60 μm nozzle diameter) depict the metal ink ($Cu(OAc)_2$ 0.25 M in DMF), with the light blue dot array representing synthesised HKUST-1 MOF. **(Bottom)** Strobe time lapse images of droplet formation of the ligand ink (left) and metal ink (right) from microFab jetting devices during printing of MOF lines with a custom-built printer platform.
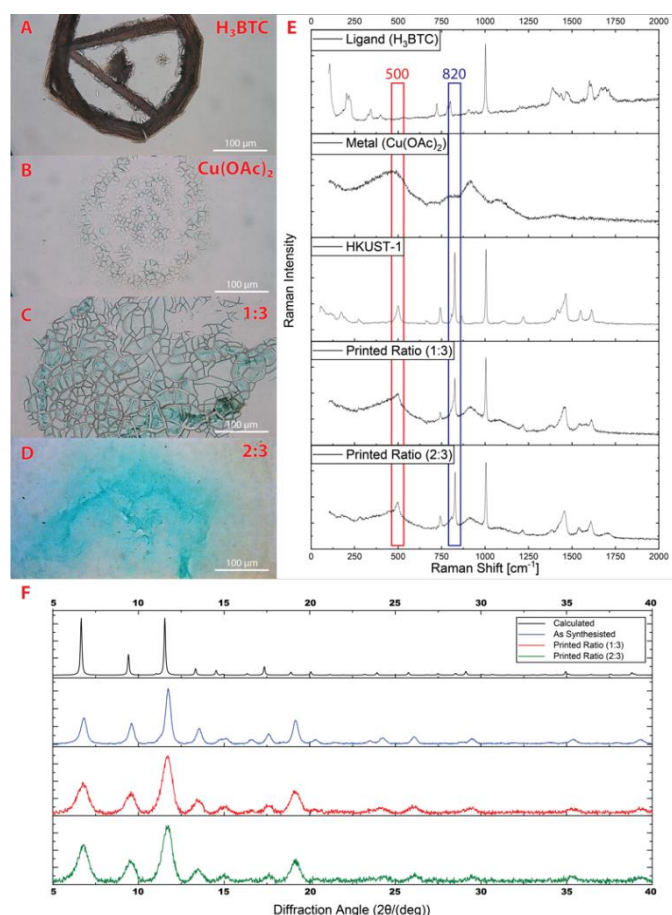
Figure 2. Representative optical microscopy images of the ligand (H₃BTC 0.25 M in DMF) and copper acetate (Cu(OAc)₂ 0.25 M in DMF) printed on coverglass substrates: **(A)** Ligand, **(B)** Cu(OAc)₂ and different ratios of RIJ printed ligand and Cu(OAc)₂: **(C)** 1:3, **(D)** 2:3. **(E)** Raman spectrographs of the ligand, Cu(OAc)₂, bulk synthesised HKUST-1 and printed MOPF corresponding to the microscopy images. **(F)** Comparison of XRPD patterns for HKUST-1 calculated (black)[36], bulk synthesised HKUST-1 (red) and HKUST-1 as-printed (blue), demonstrating the phase pure nature of the printed MOF.

RIJ of the MOFs was achieved using a custom-built inkjet printer fitted with an angled jetting device assembly as depicted in Figure 1. The setup was designed to allow the simultaneous printing of two inks onto the same location on the substrate. The sample stage was adjusted to ensure that the droplets touched the surface at exactly the intercept point leading to the formation of clearly defined droplets. Using HKUST-1 as an example, Figure 1 (bottom) shows strobe time lapse images of the ligand (H₃BTC) and metal salt inks being deposited on glass substrates during the printing of lines from the glass jetting nozzles. The copper acetate ink was observed to result in slightly smaller droplets than the H₃BTC ink. The small ink volume (2–10 pL) allows for fast drying of the ink solvent and samples appeared fully dry after about 10-30 s dependant on the deposited droplet amount.

Reactive inkjet printing of the two components (H₃BTC and Cu(OAc)₂) at different ratios (1:1, 1:2, 1:3, 2:3, 3:2, 3:1, 2:1) was undertaken. Successive droplets were jetted at a frequency of 25 Hz. As an example, a dot array with a ratio of 1:3 was achieved by simultaneously jetting one drop of H₃BTC and one drop of Cu(OAc)₂ followed by two additional drops of Cu(OAc)₂ at 25 Hz. In order to improve signal to noise ratios for

the various analysis techniques required to confirm structure and purity, this process was repeated five times at each location (more deposited material) before moving to the next.

Optical micrographs (Figure 2A and Figure S1) show that printing of H₃BTC only onto a glass substrate produced needle-like crystals whilst printing only Cu(OAc)₂ produced pale turquoise, cracked microcrystalline powders. Based on the stoichiometry of HKUST-1, Cu₃(BTC)₂(DMF)₃, a 2:3 ratio of ligand:metal solutions are expected to be optimal. Reactive ink-jet printing of samples with the expected stoichiometry produced a blue microcrystalline powder, the colour of which matched that of bulk HKUST-1. Samples with an excess of metal ions present (1:2, 1:3) produced similar blue powders although with a greater degree of cracking observed during the drying process. Scanning electron microscopy (SEM) micrographs (Figure S3) further illustrate the cracks in the printed MOF. For ratios where an excess of ligand was present (1:1, 2:1, 3:1, 3:2), large needle like crystals were observed to varying degrees. This was attributed to the relatively low solubility of H₃BTC in DMF compared to Cu(OAc)₂ resulting in nucleation of crystals of H₃BTC before crystallisation to form HKUST-1 could occur.

Raman spectroscopy was used to screen the droplets for HKUST-1 formation. Key new peaks were observed at 500 and 820 cm⁻¹ which were present in bulk MOF produced through conventional synthesis but not present in reference samples of either the ligand or metal ions (Figure 2E and Figure S2).[40] The presence of these new peaks were observed most strongly in the 2:3, 1:3 and 1:2 ratio samples but were also observed to a lesser extent in the 3:2 and 3:1 ratio samples where an excess of ligand is present. Broad peaks were observed at 500 and 900 cm⁻¹ for the 3:2 and 3:1 ratio prints which are also observed in the Cu(OAc)₂ reference sample consistent with the presence of excess metal ions. The formation of HKUST-1 was confirmed by printing dot arrays onto zero background silicon wafers (Si100) in 1:3 and 2:3 ratios and analysing them using X-ray powder diffraction (XRPD) (Figure 2F). The patterns for the printed materials match closely with those of the calculated patterns for HKUST-1 and that of bulk material synthesised by repeating a previously reported hydrothermal synthesis.[40]

In addition to dots and line prints (Figures S1 and S6) we demonstrated the printability of the RIJ-MOF inks by printing the University of Sheffield Crest (Figures 3A and S6). Printing was done using 60 micron nozzle diameters, on glass substrates. These could be considered non-optimal conditions for printing of high-definition structures, and may be remedied by decreasing the nozzle diameters, modifying ink properties for more even coverage, or the use of different substrates. This RIJ approach, unlike the use of MOF particles in ink suspension which may block nozzles, allows for decreased nozzle diameters to the smallest dimensions desired.

Printing of MOF gradients.

A key advantage of MOFs is that they have a modular structure, which allows for mixing and matching of different combinations of ligands and metal ions without changing the underlying structure of the MOFs. This concept of isoreticular

substitution has been used to create diverse libraries of different frameworks with different functionalities.[41] It has also enabled the creation of "multivariate" frameworks which blend two or more different ligands or metal ions within a single framework with the same structure.[42,43] Applying these principles to RIJ printing opens up the possibility of using the same inks to print different MOFs and using spatial control to enable the printing of gradients transitioning from one structure to another *via* a multivariate phase. To our knowledge no previous examples of such MOF gradients have been printed, likely owing to the pre-formed MOF particle approach that is common in the literature.

Six inks were prepared as DMF solutions of acetate salts of Cu, Zn and Co as well as ligands H$_2$BDC (1,4-benzenedicarboxylic acid), H$_2$ABDC (2-amino-1,4-benzenedicarboxylic acid) and HBIm (benzimidazole). The relevant inks were then combined through RIJ printing at ratios of 1:1, with ink concentrations of 0.25 M for all inks except BIm which was 0.5 M to preserve the correct stoichiometry. These were used to produce four well-studied previously reported MOFs: Cu(BDC),[44] Cu(ABDC),[45] Zn(BIm)$_2$ and Co(BIm)$_2$.[46] The structure of each printed MOF was then analysed by XRPD and Raman spectroscopy and compared to bulk synthesised frameworks, which confirmed the expected structures (Figures S7 and S8).

Gradient printing was achieved by printing a variety of ink mixtures to mimic the altering of droplet amount due to equipment limitations. In an upgraded RIJ system with three nozzles this could be achieved simply by altering the droplet amounts similar to the previously shown ratio changes in the above example with HKUST-1. As shown in Figure 4, by keeping the amount of Cu ink constant but varying the ratio of H$_2$BDC to H$_2$ABDC, a MOF gradient from Cu(BDC) to Cu(ABDC) could be achieved. Raman microscopy was used to record spectra along
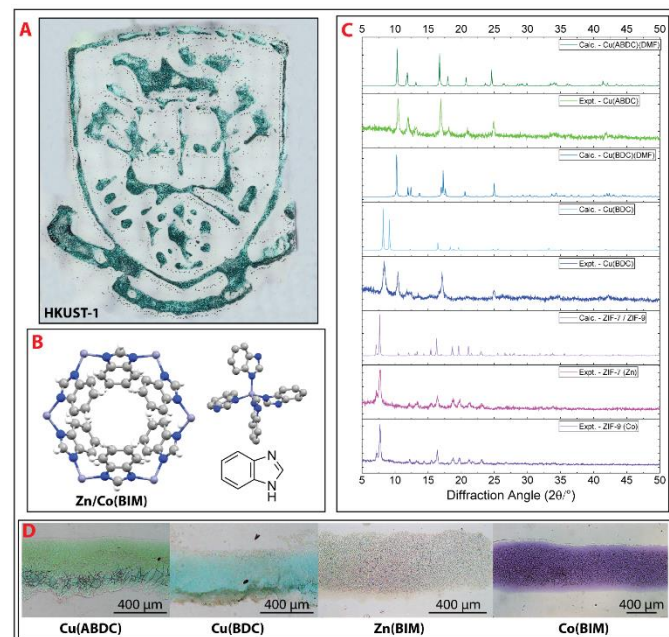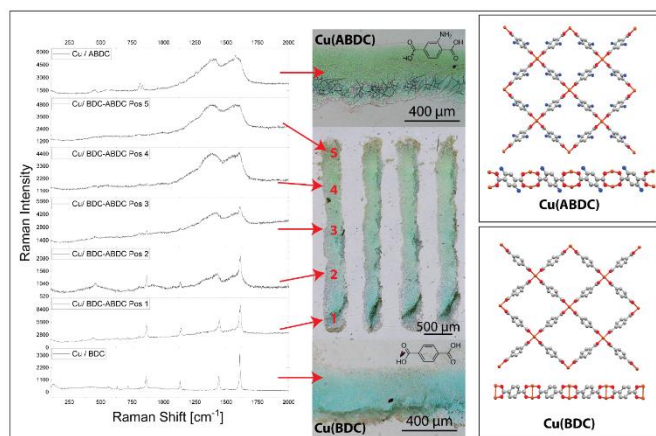
Figure 4. Raman spectra and optical micrographs showing gradient printing of multivariate Cu(ABDC):Cu(BDC) MOFs and their crystal structures.

the printed line which showed the gradual loss of bands associated with Cu(BDC) and growth of broader bands characteristic of the Cu(ABDC) MOF. The broad size of the Cu(ABDC) bands was attributed to the smaller size of the crystallites obtained by the more basic H$_2$ABDC linker. As shown by the powder patterns in Figure 3C and crystal structures in Figure 4, Cu(BDC) and Cu(ABDC) have isoreticular structures when DMF is co-ordinated, but loss of DMF results in a reversible phase change, which involves slippage of the layers in such a way that the paddlewheel SBU's of each layer stack on top of each other.[44]

A gradient of metal ions was produced in a similar way by varying the ratio of Zn and Co inks combined with the BIm linker ink, as shown in Figure S6. Raman analysis shows no significant changes along the printed gradient line, consistent with Raman inactive metal ions forming a constant structure (Figures S9 and S10). However, a clear change in colour from the purple Co(BIm)$_2$ to the white Zn(BIm)$_2$ was observed. Some breaking of the printed lines was observed as this method was less well optimised to the different growth kinetics of these systems, as was clear when printing the more complex University of Sheffield crests (Figure S6).

Selective adsorption of dyes.

As a step towards lab-on-a-chip type applications, we investigated whether printed MOFs could be used to selectively encapsulate dyes. Two dyes, methylene blue (λ_{ex} 662-666 nm, λ_{em} 686 nm) and rhodamine B (λ_{ex} 542-554 nm, λ_{em} 567 nm) were investigated as these have sizes greater, and less than, the aperture sizes of HKUST-1 (10 Å and 14 Å). We hypothesised that methylene blue would be encapsulated inside the MOF whilst rhodamine B would not. This size selectivity has been previously demonstrated for HKUST-1 grown in nano-confined fluidic channels.[47]

Lines of HKUST-1 (10 mm long) were printed onto glass substrates at 1:3 and 2:3 ratios (Figures 3A and S4). These lines were then immersed for 24 hours in solutions of ethanol saturated with either dye. The samples were removed from the dye solution and carefully rinsed with fresh ethanol. Some small fragments of MOF were lost during washing indicating relatively weak adhesion between the MOF and substrate as can be seen

Figure 3. (A) Optical images showing printed University of Sheffield crest using HKUST-1 **(B)** Crystal structure of Zn/Co(BIm)$_2$ MOFs. **(C)** XRPD patterns confirming the phase of printed MOFs. **(D)** Optical microscopy images of printed lines of Cu(ABDC), Cu(BDC), Zn(BIm)$_2$ and Co(BIm)$_2$ MOFs.

in Figure S4. The lines of MOF immersed in methylene blue (Figure S4b) show a deep blue colour under bright-field illumination and blue fluorescence in the dark field images. In contrast, no distinctive red stains and no visible fluorescence was observed following immersion in the rhodamine B dye solution (Figure S4C). These observations indicate that as expected, the smaller methylene blue molecules are adsorbed within the pores of the framework whilst the larger rhodamine B molecules are simply washed away.

Interestingly, rhodamine B was observed to adsorb onto needle-like ligand crystals present in the 3:2 ratio samples as can be clearly seen in Figure S4C. We attribute this to electrostatic interactions between the positively charged rhodamine dyes and excess H_3BTC ligand crystals. The presence of ligand crystals appears most pronounced at the start of lines (Figure S4C), due to the jetting not yet being fully stabilised. As noted previously, the low solubility of the ligand and slightly smaller size of the droplets may account for the excess of ligand present in these samples and the system may take 1-3 drops to stabilise. It is also worth noting that the precursor solution used by Terfort and co-workers to print HKUST-1 report that they used an excess of metal-ions.[34] An advantage of reactive inkjet printing is the ease with which the stoichiometry can be changed simply by changing the number of drops of each solution printed and no needle like ligands were observed when printing at a 1:3 ratio.

Conclusions

Here we demonstrate RIJ as a new approach to the patterning of surfaces with MOFs and their use in the separation and sequestration of dyes. RIJ overcomes many of the challenges associated with the printing of materials from suspension and removes the need for additives and careful formulation to ensure the stability of preformed material in suspension. Simple inks of metal ion and ligand solutions were printed to a single point on a glass substrate using a custom-built inkjet printer system fitted with a custom-designed angled jetting device holder. Reactions proceeded at room temperature and no washing or curing steps were required. The formation of the archetypal MOF, HKUST-1, as well as MOF-46 (CuBDC/ABDC) and ZIF-7 $(Zn/Co(BIm)_2)$ analogues was confirmed by Raman spectroscopy and XRPD analysis. The RIJ approach allows the ratio of components to be readily varied, which we exploited for the printing of MOF gradients, one MOF structure transitions to another isostructural MOF *via* a multivariate phase. Soaking of the printed MOFs in dye solutions resulted in size selective encapsulation of the smaller methylene blue dye inside the MOF whilst the larger rhodamine B dye was excluded and washed away. We anticipate this approach will be applicable to the printing of a wide variety of other MOFs and related supramolecular and nanomaterials enabling their use as sensors and catalysts and in separation and controlled release within lab-on-a-chip type devices.

Experimental

Materials and reagents were obtained from multiple different commercial suppliers and used without further purification: copper acetate monohydrate (98+%, Fisher), zinc acetate dihydrate (98+% Fisher), cobalt acetate tetrahydrate (98+% Acros Organics), benzene-1,3,5-tricarboxylic acid (95% Sigma Aldrich), 1,4-benzenedicarboxylic acid (99+%, Acros Organics), 2-amino-1,4-benzenedicarboxylic acid (99%, Sigma Aldrich), rhodamine B (95%, Sigma Aldrich), methylene blue (high purity biological stain, Alfa Aesar), N,N'-dimethylformamide (99.8+% HPLC grade, Fisher), and ethanol (99.8+% HPLC grade, Fisher).

Ink solutions. All inks were prepared at room temperature with no heating to avoid decomposition of DMF. Mechanical stirring was applied until full dissolution was achieved. All inks were prepared at concentrations of 0.25 M except for the BIm ink which prepared at 0.5 M. For printing of MOF gradients, H_2BDC/H_2ABDC or Zn/Co inks were prepared at 100:0; 80:20, 60:40, 50:50, 40:60, 20:80, 0:100 ratios with 0.25 M concentrations maintained.

Reactive inkjet printing. A custom-built Inkjet printer with an angled jetting device assembly using MicroFab jetting devices (MJ-AT-01) with 60 μm nozzle diameters was used for all printing experiments. For standard MOF printing, inks were loaded into separate reservoirs and mounted into the printhead assembly of the printer. The two jetting devices were mounted onto a holder at an X° angle. Jetting parameters were adjusted to ensure good droplet formation and minimise the formation of satellite drops. As it was essential that both droplets arrive simultaneously onto the substrate at the same location, different jetting parameters (rise, fall and dwell times) were used in each case to adjust for the differences in viscosity and surface tension of the two inks (Table 1S). This was achieved by initially using the same parameters for both inks and then altering the fall time parameter and voltages until both drops were synchronised (Figure 1). Gradient printing was performed in the same way, but the varied ink was rapidly exchanged every 5 dots ensuring the ink had not fully dried, by briefly pausing the printing process.

Characterisation. Viscosity measurements were performed using a Vibro Viscometer SV-1 A. All measurements were performed on the same day at room temperature (~20 °C) to avoid errors relating from ambient condition fluctuations. Surface tension was measured with a K11 Krüss Tensiometer at 20 °C with a Wilhelmy Plate (w = 19.9 mm, h = 10 mm, d = 0.2 mm) and a density for DMF of 0.944 g cm^{-3}. X-ray powder diffractometry was performed using a Bruker-AXS D8 diffractometer using CuKα (λ=1.5418 Å) radiation and a LynxEye position sensitive detector in Bragg Brentano parafocussing geometry, with samples on a flat silicon plate. Samples were scanned from 5 to 50° over 8 hours to improve signal to noise ratios. Raman spectroscopy was performed using a Renishaw inVia Raman microscope, working with a green laser of 514 nm wavelength powered with 20 mW. The power used was the 10% of the laser to avoid destroying the samples. Samples were directly printed onto precleaned cover glass substrates. As printed samples were prepared for scanning electron microscopy analysis on a carbon sticky tab loaded on an

aluminium sample stub and coated with approximately 20 nm gold using an Edwards S150B sputter coater. SEM micrographs were collected using a TESCAN VEGA3 LMU SEM instrument operating in secondary electron mode.

Author Contributions

J.A.F and P.J.S. coordinated this body of work. J.A.A. performed initial investigations into printing of HKUST-1. D.A.G. performed all printing experiments and Raman characterisation. J.N. synthesised all bulk MOFs, performed preliminary small scale room temperature experiments and collected all XRPD data. J.A.F drafted manuscript with editing by D.A.G. and J.N.

Conflicts of interest

There are no conflicts to declare.

Acknowledgements

References

1   J. Nicks, K. Sasitharan, R. R. R. Prasad, D. J. Ashworth and J. A. Foster, *Adv. Funct. Mater. Mater.*, **31**, 2103723.

2   Q. Qian, P. A. Asinger, M. J. Lee, G. Han, K. M. Rodriguez, S. Lin, F. M. Benedetti, A. X. Wu, W. S. Chi and Z. P. Smith, *Chem. Rev.*, 2020, **120**, 8161–8266.

3   A. Bavykina, N. Kolobov, I. S. Khan, J. A. Bau, A. Ramirez and J. Gascon, *Chem. Rev.*, 2020, **120**, 8468–8535.

4   L. E. Kreno, K. Leong, O. K. Farha, M. Allendorf, R. P. Van Duyne and J. T. Hupp, *Chem. Rev.*, 2012, **112**, 1105–1125.

5   E. M. Dias and C. Petit, *J. Mater. Chem. A*, 2015, **3**, 22484–22506.

6   L. Wang, L. Wang and M. Zheng, *J. Mater. Chem. B*, 2018, **6**, 707–717.

7   V. Stavila, A. A. Talin and M. D. Allendorf, *Chem. Soc. Rev.*, 2014, **43**, 5994–6010.

8   P. Falcaro, D. Buso, A. J. Hill and C. M. Doherty, *Adv. Mater.*, 2012, **24**, 3153–3168.

9   O. Shekhah, J. Liu, R. A. Fischer and C. Wöll, *Chem. Soc. Rev.*, 2011, **40**, 1081-1106.

10   B. Hoppe, K. D. J. Hindricks, D. P. Warwas, H. A. Schulze, A. Mohmeyer, T. J. Pinkvos, S. Zailskas, M. R. Krey, C. Belke, S. König, M. Fröba, J. Haug and P. Behrens, *CrystEngComm*, 2018, **20**, 6458–6471.

11   Y. Huang, C. Tao, R. Chen, L. Sheng and J. Wang, *Nanomaterials*, 2018, **8**, 1–10.

12   L. Sarango, L. Paseta, M. Navarro, B. Zornoza and J. Coronas, *J. Ind. Eng. Chem.*, 2018, **59**, 8–16.

13   O. Dalstein, D. R. Ceratti, C. Boissière, D. Grosso, A. Cattoni and M. Faustini, *Adv. Funct. Mater.*, 2016, **26**, 81–90.

14   D. Witters, N. Vergauwe, R. Ameloot, S. Vermeir, D. De Vos, R. Puers, B. Sels and J. Lammertyn, *Adv. Mater.*, 2012, **24**, 1316–1320.

15   I. D. Williams, *Nat. Chem.*, 2014, **6**, 6–7.

16   G. J. H. Lim, Y. Wu, B. B. Shah, J. J. Koh, C. K. Liu, D. Zhao, A. K. Cheetham, J. Wang and J. Ding, *ACS Mater. Lett.*, 2019, **1**, 147–153.

17   R. Zhao, Y. Tian, S. Li, T. Ma, H. Lei and G. Zhu, *J. Mater. Chem. A*, 2019, **7**, 22559–22570.

18   J. Hou, A. F. Sapnik and T. D. Bennett, *Chem. Sci.*, 2020, **11**, 310–323.

19   I. Imaz, M. Cano-Sarabia, D. Maspoch and A. Carne, *Nat. Chem.*, 2013, **5**, 203–211.

20   P. J. Smith and A. Morrin, *J. Mater. Chem.*, 2012, **22**, 10965.

21   R. A. Street, W. S. Wong, S. E. Ready, M. L. Chabinyc, A. C. Arias, S. Limb, A. Salleo and R. Lujan, *Mater. Today*, 2006, **9**, 32–37.

22   C. Amruth, M. Z. Szymański, B. Łuszczyńska and J. Ulański, *Sci. Rep.*, 2019, **9**, 8493.

23   S. K. Karunakaran, G. M. Arumugam, W. Yang, S. Ge, S. N. Khan, X. Lin and G. Yang, *J. Mater. Chem. A*, 2019, **7**, 13873–13902.

24   H. Maleki and V. Bertola, *Catal. Sci. Technol.*, 2020, **10**, 3140–3159.

25   J. R. Verkouteren, J. Lawrence, T. M. Brewer and E. Sisco, *Anal. Methods*, 2017, **9**, 3441–3449.

26   P. M. Grubb, H. Subbaraman, S. Park, D. Akinwande and R. T. Chen, *Sci. Rep.*, 2017, **7**, 1–8.

27   S. Chung, K. Cho and T. Lee, *Adv. Sci.*, 2019, **6**, 1801445.

28   B. Huber, P. Popp, M. Kaiser, A. Ruediger and C. Schindler, *Appl. Phys. Lett.*, 2017, **110**, 143503.

29   T. Huang and W. Wu, *J. Mater. Chem. A*, 2019, **7**, 23280–23300.

30   D. A. Gregory, Y. Zhang, P. J. Smith, X. Zhao and S. J. Ebbens, *Small*, 2016, **12**, 4048–4055.

31   Y. Zhang, D. A. Gregory, Y. Zhang, P. J. Smith and S. J. Ebbens, *Small*, 2019, **15**, 1–9.

32   R. D. Boehm, P. R. Miller, J. Daniels, S. Stafslien and R. J. Narayan, *Biochem. Pharmacol.*, 2014, **17**, 247–252.

33   P. Goel, S. Singh, H. Kaur, S. Mishra and A. Deep, *Sensors Actuators B. Chem.*, 2021, **329**, 129157.

34   L. L. Luz, R. Milani, J. F. Felix and I. R. B. Ribeiro, *ACS Appl. Mater. Interfaces*, 2015, **7**, 27115–27123.

35   C. Su, C. Kung, T. Chang, H. Lu and K. Ho, *J. Mater. Chem. A*, 2016, **4**, 11094–11102.

36   J. Zhuang, D. Ar, X. Yu, J. Liu and A. Terfort, *Adv. Mater.*, 2013, **25**, 4631–4635.

37   A. J. Lennon, A. W. Y. Ho-baillie and S. R. Wenham, *Sol. Energy Mater. Sol. Cells*, 2009, **93**, 1865–1874.

38   J. E. Fromm, *IBM J. Res. Dev.*

39   B. Derby, *Annu. Rev. Mater. Res.*, 2010, **40**, 395–414.

40   S. S. Chui, S. M. Lo, J. P. H. Charmant, A. G. Orpen and I. D. Williams, *Science*, 1999, **283**, 1148–1150.

41   M. Eddaoudi, J. Kim, N. Rosi, D. Vodak, J. Wachter, M. O'Keeffe and O. M. Yaghi, *Science*, 2002, **295**, 469–472.

42   H. Deng, C. J. Doonan, H. Furukawa, R. B. Ferreira, J. Towne, C. B. Knobler, B. Wang and O. M. Yaghi, *Science*, 2010, **327**, 846–850.

43   D. J. Ashworth and J. A. Foster, *Nanoscale*, 2020, **12**, 7986–7994.

44   C. G. Carson, K. Hardcastle, J. Schwartz, X. Liu, C. Hoffmann, R. A. Gerhardt and R. Tannenbaum, *Eur. J. Inorg. Chem.*, 2009, 2338–2343.

45   J. Nicks, J. Zhang and J. A. Foster, *Chem. Commun.*, 2019, **55**, 8788–8791.

46   J. Y. Choi, R. Huang, F. J. Uribe-romo, H. K. Chae, K. S. Park, Z. Ni, A. P. Co, M. O. Keeffe and O. M. Yaghi, *Proc. Natl. Acad. Sci. USA*, 2006, **103**, 8–13.

47   S. Guthrie, L. Huelsenbeck, A. Salahi, W. Varhue, N. Smith, X. Yu, L. U. Yoon, J. J. Choi and N. Swami, *Nanoscale Adv.*, 2019, **1**, 2946–2952.

Supplementary Information

Reactive Inkjet Printing of Metal-Organic Framework

David Alexander Gregory,[1] Joshua Nicks,[2] Joaquin Artigas-Arnaudas,[3] Jonathan A. Foster,[2]* and Patrick J. Smith[3]*

1. Department of Materials Science and Engineering, University of Sheffield, Sheffield S1 3JD, UK

2. Department of Chemistry, University of Sheffield, Brook Hill, Sheffield, S3 7HF, UK

3. Department of Mechanical Engineering, University of Sheffield, Garden Street, Sheffield, UK, S1 4BA

Physical Property Measurements

Definition of the dimensionless Z number:

$$Z = \frac{Re}{\sqrt{We}} = \frac{\sqrt{\gamma \rho a}}{\eta}$$

Table S1. Comparison of the rheological properties of the printed inks.

Ink	Concentration	Viscosity (mPa/s)	Surface tension (mN/m)	Density (kg/m³)	Z number (for 60 μm printhead)
DMF		1.29 mPas (20.1°C)	37.19 ± 0.013	948.0	35.7
H_3BTC	0.25 M	1.71 mPas (18.9°C)	37.79 ± 0.047	996.3	27.7
$Cu(OAc)_2$	0.25 M	1.41 mPas (19.3°C)	37.29 ± 0.024	993.9	33.2
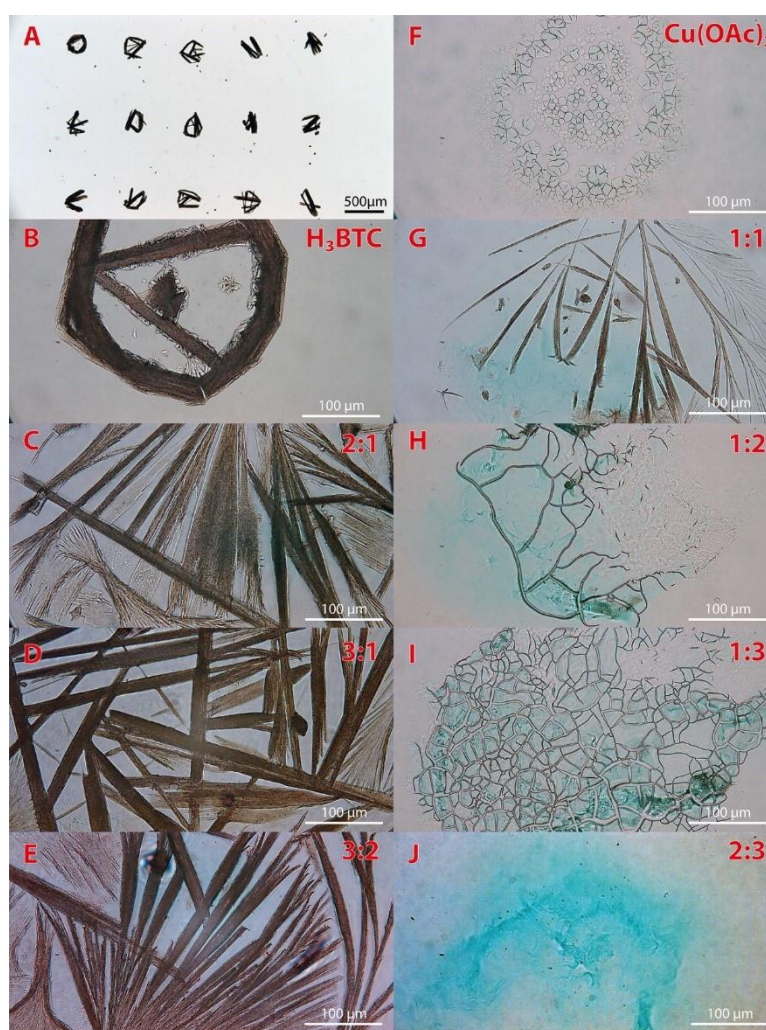
Figure S1. Representative optical microscopy images of: **A** and **B)** overview dot array images of ligand (H_3BTC 0.25 M in DMF)) printed on cover glass substrates. Copper(II) acetate 0.25 M in DMF (**F**), and different ratios of ligand and copper printed respectively, 2:1 **(C)**, 3:1 **(D)**, 3:2 **(E)**, 1:1 **(G)**, 1:2 **(H)**, 1:3 **(I)**, 2:3 **(J)**.
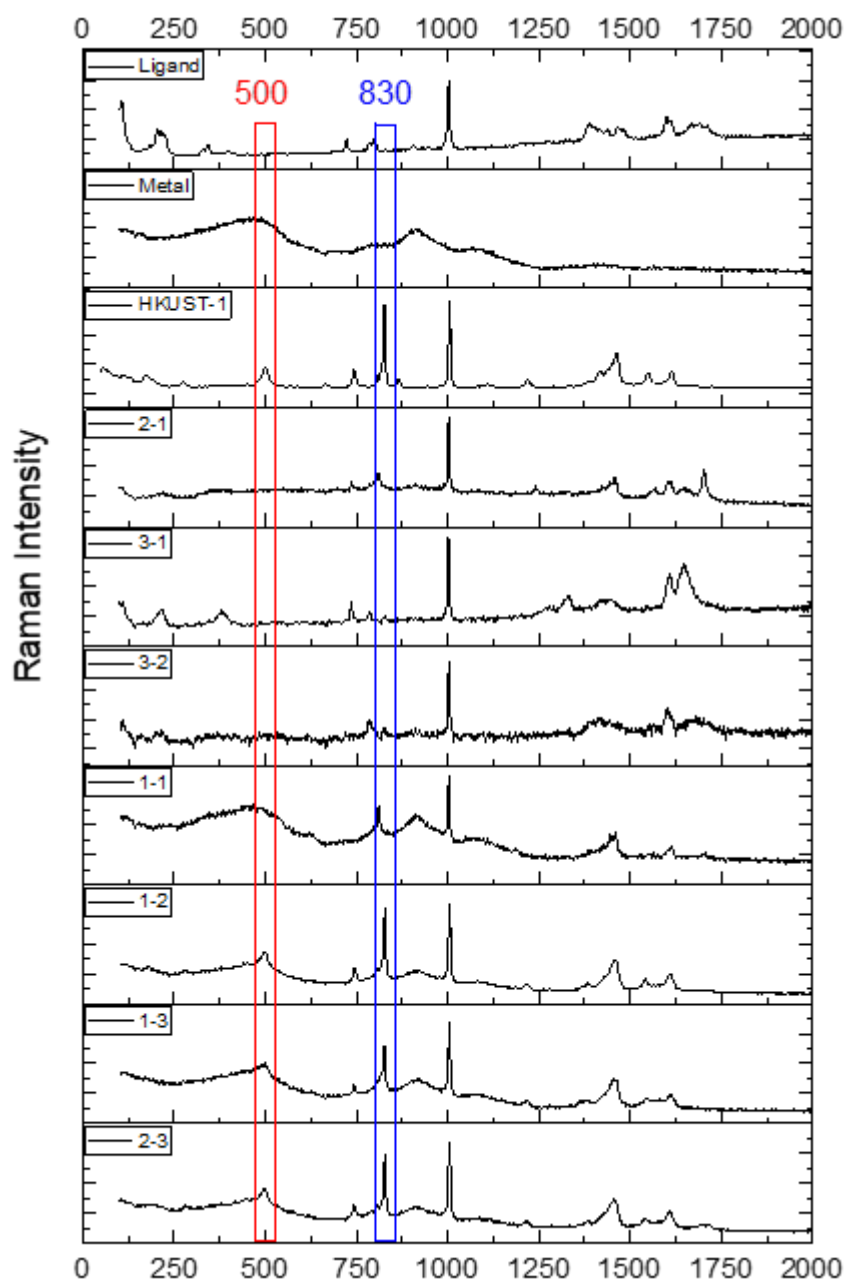
Figure S2. Raman spectroscopy results of Ligand (H₃BTC 0.25 M in DMF)) printed on cover glass substrates of the ligand, copper acetate 0.25 M in DMF, and different ratios of ligand and copper printed respectively, 2:1, 3:1, 3:2, 1:1, 1:2, 1:3, 2:3.
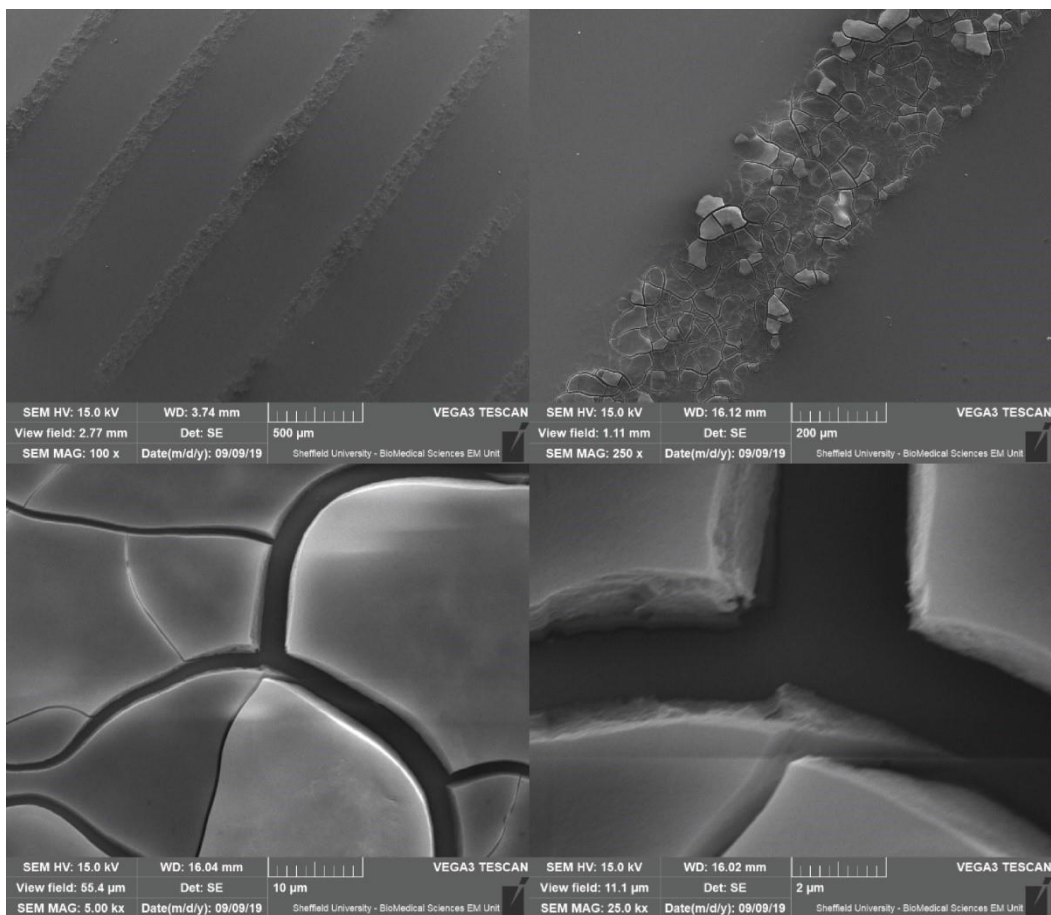
Figure S3. Representative SEM images of RIJ printed lines at ratio 1:3 ligand:metal.
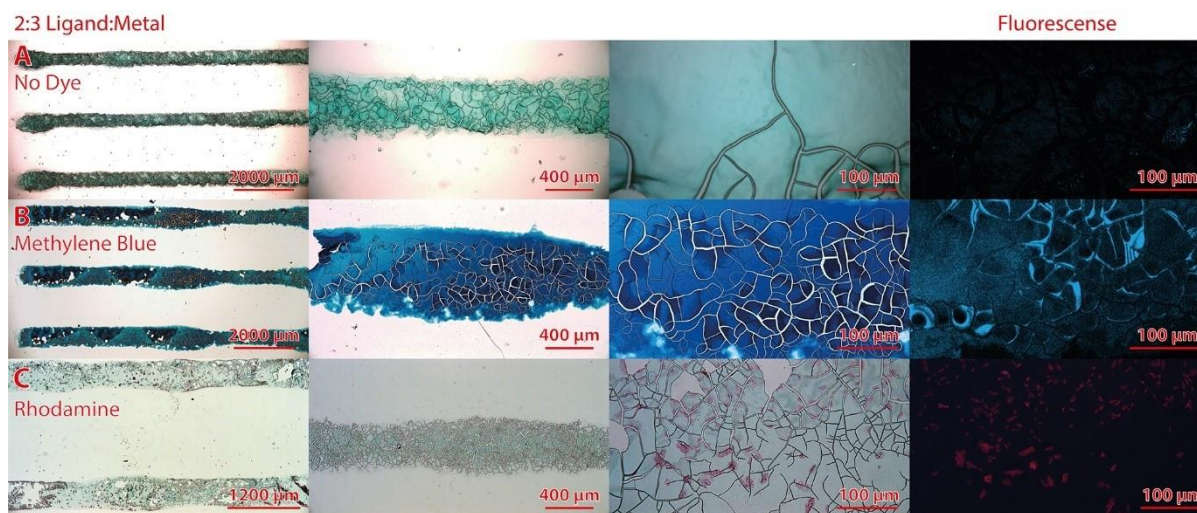
Figure S4. Optical microscope brightfield and fluorescence images of representative printed MOF lines on coverglass substrates with five times material printed at a ratio of 2:3 **(A-C)** (H$_3$BTC:Cu(OAc)$_2$ 0.25 M in DMF): Before **(A)** and after 24 h incubation in methylene blue **(B)** solution (in pure ethanol) and rhodamine B solution (in pure Ethanol) **(C)**.
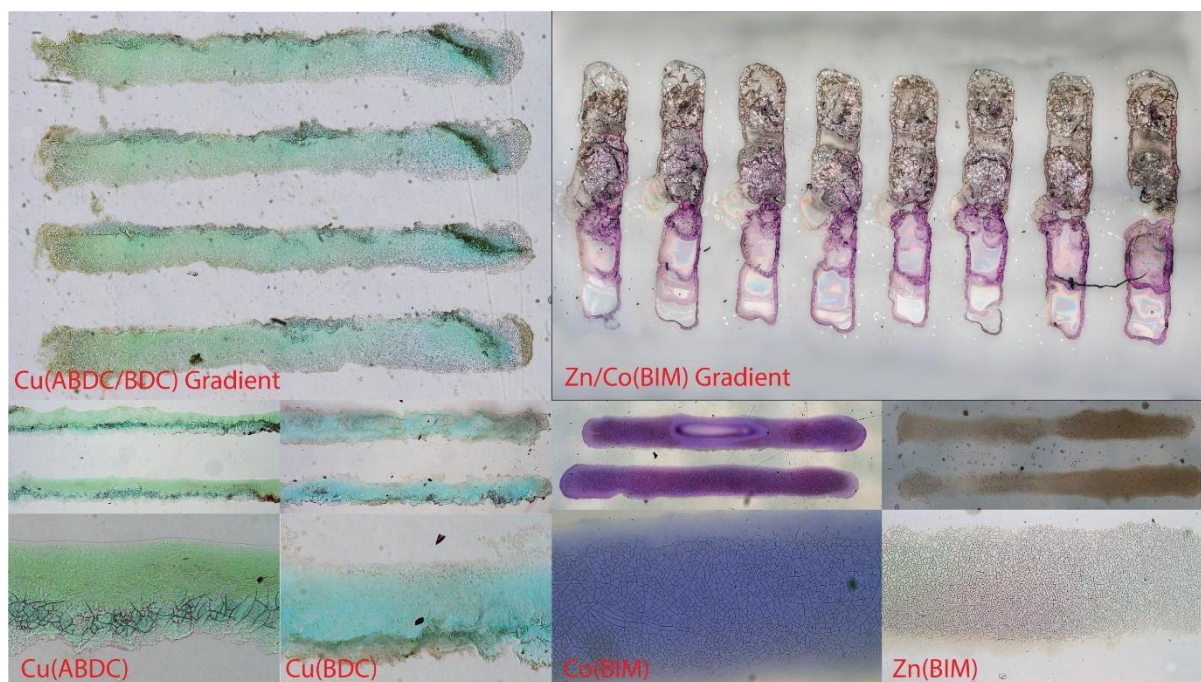
Figure S5. Optical microscopy images of MOF gradients and pure MOFs.
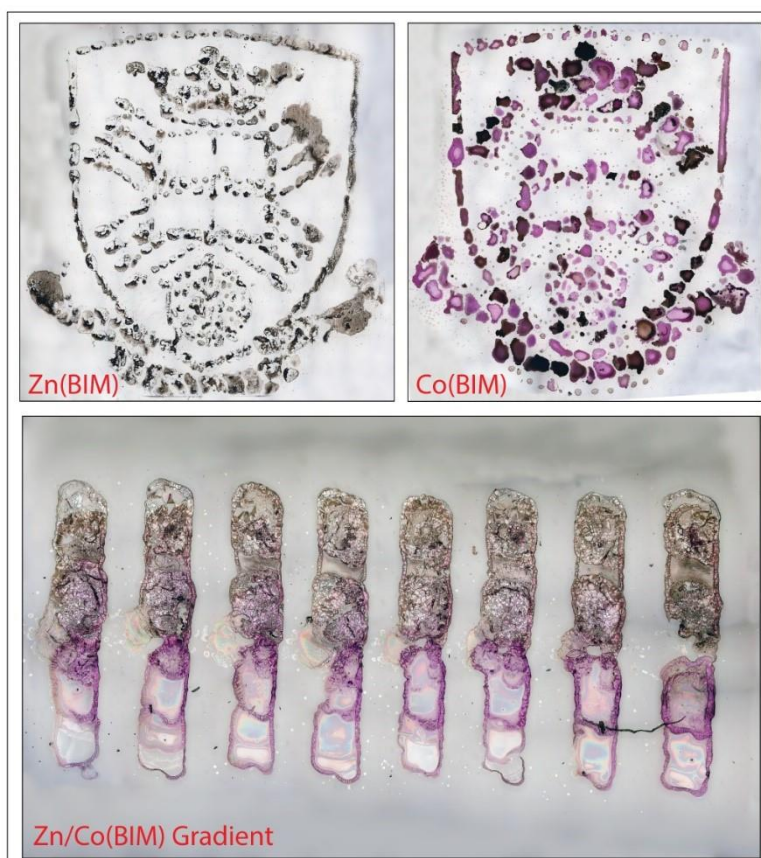
Figure S6. Optical microscopy images of Zn and Co(BIm)$_2$ University of Sheffield crests and gradients.
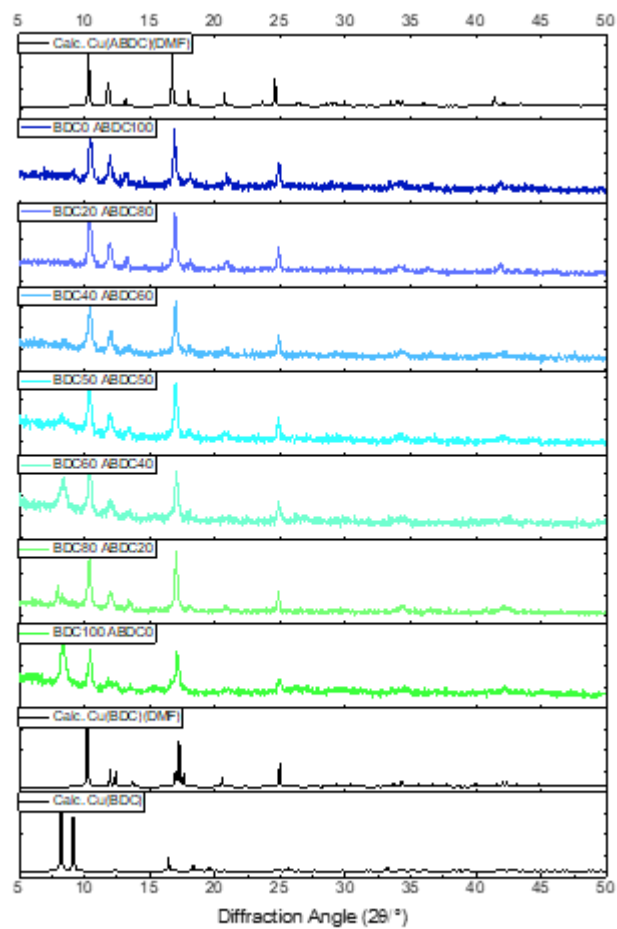
Figure S7. XRPD patterns for the Cu(BDC)/(ABDC) MOF gradient.
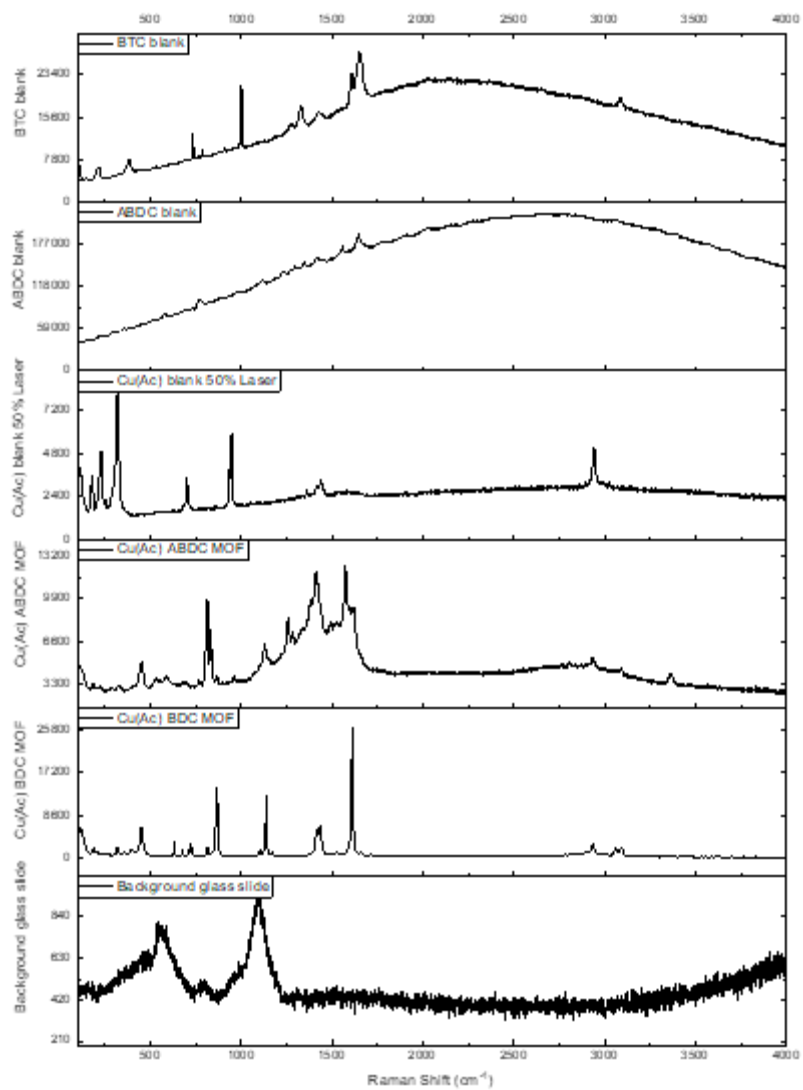
Figure S8. Raman spectroscopy of bulk synthesised MOFs and blank unreacted metals and linkers.
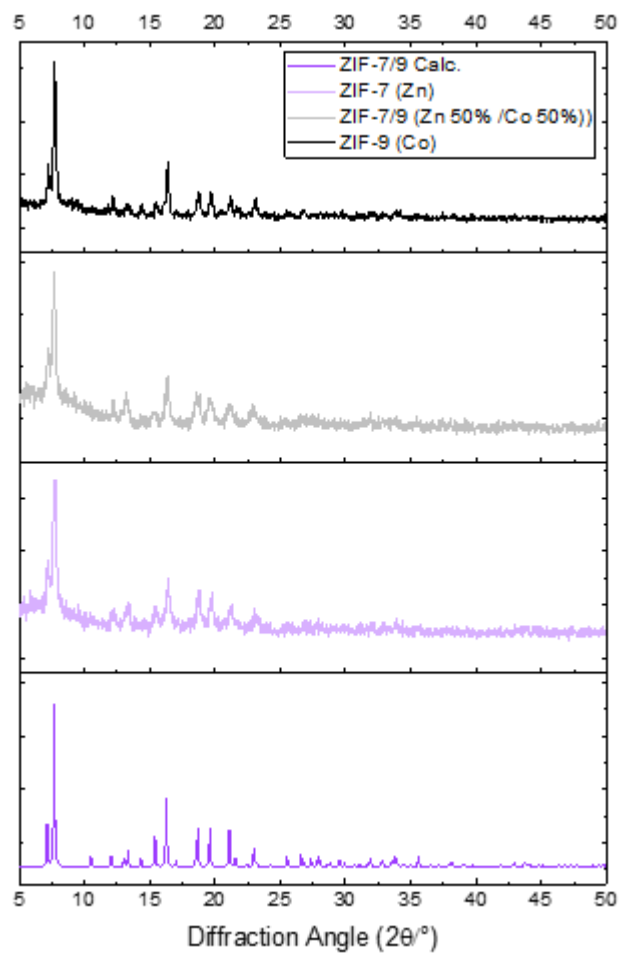
Figure S9. XRPD patterns for the printed Zn(BIm)$_2$ and Co(BIm)$_2$ MOFs and the centre of the gradient.
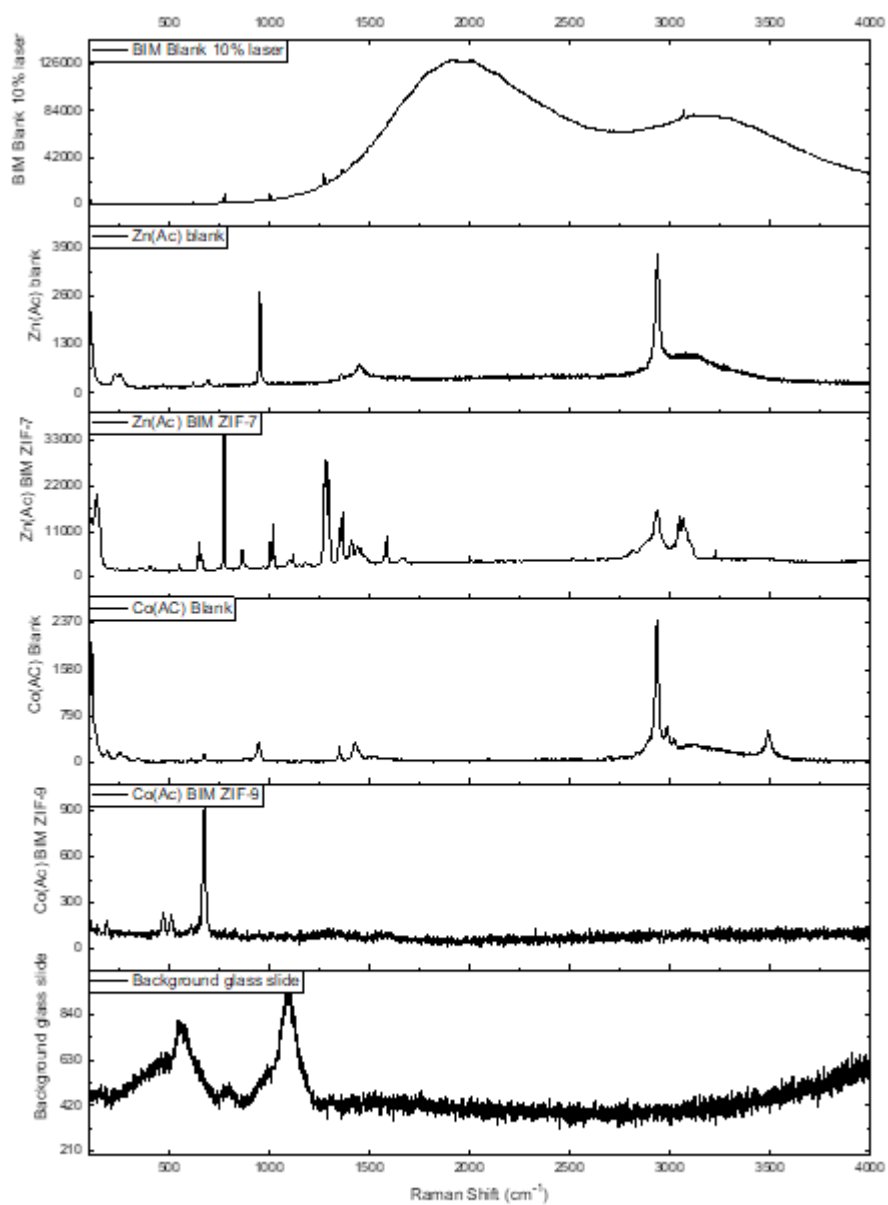
Figure S10. Raman spectra of bulk synthesized Zn and Co(BIm)$_2$ and blank unreacted metals and linkers.

Chapter 8

Conclusions and Outlook

The Great Glen Way, Scotland. Photo credit Jordan Davies, 2018.

Chapter 8

8.1. Summary of Aims

Coordination and supramolecular nanosheets have emerged as 2D materials with uniquely programmable structures and properties with applications in a range of fields. In this thesis, multiple modification techniques were used to explore the programmable nature of metal-organic framework nanosheets (MONs), in order to understand the effects this toolkit of chemistries have on both their dimensions and properties. Furthermore, this work aimed to expand this supramolecular approach to 2D materials to hydrogen-bonded structures and explore new ways to prepare these nanosheets. This chapter reflects on the progress made within this thesis towards these aims and explore the opportunities and barriers associated with the future of this work.

8.2. Programming MON Structures

In **Chapter 3,** we showed that partial functionalisation and subsequent exfoliation of a layered MOF results in the formation of bi-functional nanosheets capable of tandem catalysis. Specifically, reaction of an amino-functionalised Cu_2-PW framework with 1,3-propanesultone results in the formation of an acid-base functionalised structure capable of performing tandem deacetylation and Knoevenagel condensations. Performed as a proof-of-concept study, it is clear from the large body of literature on the post-synthetic modification of layered amino- MOFs that this technique could be widely applicable for the formation of multi-functional MON systems. However, it is noted in this work that functionalisation of this system is not facile, even after desolvation of the PW. Reaction times up to one week were required to obtain conversions that plateau at 25%, due to the occupation of the MOFs pores by the sulfonate chains. In this case, the lack of void space within these dense layered frameworks has a direct impact on the programmable nature of these materials.

Chapter 4 focussed on developing a post-exfoliation approach for the programming of MON structures through click chemistry. In this case, PSF of the same amino-MOF used in **Chapter 3** was used to obtain azide-functionalised systems with controllable degrees of conversion of 0-100%. Here the smaller size of the reagent allowed complete functionalisation. The fully functionalised MOF formed few-layer nanosheets when exfoliated, which were then further functionalised through post exfoliation functionalisation using Cu(I)-catalysed click chemistry and alkyne-tagged functional groups. These PEF reactions were high yielding and allowed for facile tuning of the MONs surface chemistry and functionality. Direct functionalisation of nanosheets in this way, rather than the bulk layered MOF, enabled significantly conversions and introduction of bulkier substituents by removal of the pore size limitation. In particular, the use of click chemistry as a PEF technique provides regioselectivity, versatility, and high yields under milder conditions than are typically reported for MOF modifications.[1] As such, the combination of liquid exfoliation and post-exfoliation click chemistry is a widely applicable approach with huge potential as a procedure for the programming of the structures of MONs. This strategy is already being applied to other systems within the Foster group, targeting the

functionalisation of more robust UiO, MIL, and ZIF-based MON architectures with a range of peptides, polymers, and catalysts for a variety of applications.

In **Chapter 5**, isoreticular expansion of a series of MONs was explored as an alternative, pre-synthetic approach to the preparation of programmable 2D materials. This pre-synthetic expansion proved to be straight forward for the linkers reported, but in preliminary work we found systems with linkers longer than 4,4'-bipyridine could not be prepared, due to the insoluble nature of these linkers under the conditions used. However, it is likely that with some modifications to the synthetic procedure, such as the inclusion of base or lower concentrations, that these MOFs could also obtained. An initial aim of this work had been to use this series of MONs with differing inter-PW distances for multidentate sensing of N-donor analytes, but issues with stability in suspension during sensing experiments could not be overcome. Nevertheless, the development of expanded MONs has great potential for use in a variety of size-selective separation and sensing applications. Other pre-synthetic modifications, such as mixed-component MONs, could not be explored due to time constraints. However, the use of these methods to design MONs with multiple reactive sites, such as an amine and an azide/alkyne, could allow for orthogonal functionalisation of these nanosheets, providing greater control over their surface functionalities through rational use of both pre- and post-synthetic techniques.

Pre- and post-synthetic modifications are likely to become much more widely explored as research into MONs develops and the field grows, and it is already highly prevalent for Zr/Hf-cluster type nanosheets. For 3D MOFs, they have become vital techniques for realising the potential of these materials and enhancing their functionality, stability and processability. This work has focused on the development of covalent modifications has been targeted, but this contributes to a broader toolkit of MONs as programmable 2D materials thanks to their diverse chemistry, modular structure and other methods for adding functional groups and properties to MONs such as coordinative PSF,[2,3] SALE,[4] and blending with polymers, enzymes, or nanoparticles into composite materials.[5,6] These techniques will almost certainly be exploited by those researching MONs, particularly as classically structured 2D materials fall short in this area.

8.3. New Supramolecular 2D Materials

Covalent and metal-organic nanosheets have become well-established materials in recent years, with their dynamic chemistry and molecular natures allowing their structures and properties to be more easily modified towards desired applications. In **Chapter 6**, hydrogen-bonded organic nanosheets (HONs) were demonstrated as a novel class of supramolecular 2D material through liquid exfoliation of two isoreticular layered HOFs. The two layered frameworks were based on amidinium-carboxylate synthons, incorporated either within a single linker or as a co-crystal. Both frameworks were held together in two-dimensions by strong, charge-assisted hydrogen-bonding interactions, with only weak van der-Waal interlayer interactions identified. The exfoliation protocol utilised in **Chapters 3-5** was applied to both systems, yielding HONs with 0.8 nm thick with micron-sized lateral dimensions that

exhibit remarkable stability despite their hydrogen-bonded structures, maintaining their crystallinity even after suspension in water at 80 °C for three days. These HONs also demonstrated similar properties to a number of previously reported MONs, with enhanced fluorescence quenching capabilities of organic dyes when compared to their layered analogues.

HOFs themselves are a well-established class of supramolecular materials with a number of promising applications.[12,13] The use of exfoliation significantly increases the surface area of layered materials whilst simultaneously exposing active sites. Thus, it is possible that this simple ultrasonic approach could be applied to a wide range of other layered HOFs, especially those based on strong hydrogen-bond donor–acceptor pairs. However, considering the large lateral dimensions obtained in this work, it may be possible that the use of weaker hydrogen-bonds could still yield nanosheets, potentially at the cost of these sizes. Regardless, a range of HONs with tailored pore sizes and functionalities can readily be predicted, which could enable their use in a wide range of catalysis, sensing, separation, and electronics applications.

Finally, the results in **Chapter 6** make one question the term "strong in-layer interactions" when referring to 2D materials and opens up the possibility of accessing nanosheets from layered materials based on other intermolecular interactions. To this end, we have already obtained promising results in the exfoliation of halogen-bonded frameworks, presenting the first example of halogen-bonded nanosheets (XONs). However, with the likelihood of these materials being significantly less stable as the average bond energy decreases, the uses for these new supramolecular materials could be limited. On the other hand, this weakness could be exploited for applications in which disassembly as a response to stimuli is appealing, such as drug delivery.

8.4. Liquid Exfoliation

Work within the Foster group prior to this thesis had developed an exfoliation protocol for the preparation of Cu_2-PW MONs.[7,8] In this work, we sought to further develop this method, whilst investigating the effects of modifying the structures of layered MOFs on their exfoliation.

In **Chapter 3,** it was demonstrated that partial post-synthetic functionalisation of a layered amino- MOF with a sulfonic acid chain results in synthesis of a zwitterionic structure which, when exfoliated, forms monolayer nanosheets, rather than the multi-layer nanosheets formed by the unfunctionalised framework. This substantial increase in the degree of exfoliation was attributed to the increased charge associated with functionalisation, with no change in interlayer distance observed on functionalisation. This method increases the surface charge of these layered systems and enhances electrostatic repulsion between the layers, but also simultaneously improves solvent-MON interactions, reducing the loss of larger nanosheets during centrifugation.

In **Chapter 5,** the effect of linker expansion within an isoreticular series of layered MOFs on their exfoliation into nanosheets was investigated, alongside the effect of initial MOF particle

size. The use of nitrate and acetate copper salts yielded layered MOFs with large, clearly layered particles and small aggregated particles respectively. Liquid exfoliation of the larger particles gave exclusively monolayer nanosheets, whereas the smaller particles gave multilayer systems. This was attributed to differing amounts of delamination and fragmentation based on the initial MOF morphology.

In **Chapters 3-6,** it has been shown that ultrasound-assisted liquid exfoliation can be used to obtain MONs with tailored structures and functionalities, with insights provided into how these thicknesses have been achieved. This suggests that is not only the method of MON preparation that is important in determining their resulting morphologies, but also the properties of the layered MOFs and MONs themselves that will dictate these results. Thus, it is vital to consider properties such as initial particle size, solvent interactions, and surface charge when studying liquid exfoliation of these materials.

From this work, it is clear that the initial particle size of the layered MOFs can have dramatic effects on the thickness, lateral dimensions, and concentrations of the obtained nanosheets, and as such it is crucial to characterise this before attempting any optimisation of exfoliation conditions. Similarly, different solvents have drastically different suitabilities for the exfoliation of these materials, and what governs this is not necessarily simple to determine before exfoliation. A method which has been useful in much of this work is the use of solvent screening by multiple small-scale exfoliations in a range of solvents, which can allow one to quickly determine what solvent properties, such as polarity or hydrogen bonding ability, may be best for exfoliation of a desired system.

Reactive Inkjet Printing

In **Chapter 7**, reactive inkjet printing (RIJ) was demonstrated as a novel approach to the direct patterning of surfaces with various MOF architectures. This method removes the requirement for additives and careful formulation of inks to ensure the stability of any preformed material in suspension, thus overcoming many of the problems associated with current printing methods. Inks, comprised of solutions of metal ions or ligands, were printed onto a glass substrate using a custom-built inkjet printer system. A significant advantage of the RIJ approach is the ability to alter the ratio of components easily, allowing for the printing of multi-component systems and real-time tuning of structures and properties.

This approach has the potential to be widely applicable to the printing of a wide range of other MOFs and related supramolecular and nanomaterials. However, it is likely that many systems will require modifications to the RIJ procedure in order for the synthesis to succeed. In this work, MOFs that form readily at room temperature were targeted, but many well-established MOF systems are formed under solvothermal conditions with few studies into greener methods of preparation. During this study, a variety of other metal and linker combinations were attempted that formed amorphous material or unknown crystalline phases. As such, it may be necessary to develop these milder preparation procedures, in order to expand the versatility of this approach, as heating the surface or inks prior to deposition is likely to result in faster evaporation of the solvent, impeding any reaction from taking place. A possible solution to this issue that is utilised in multiple "green" MOF syntheses is the use

of linker salts, rather than protonated linkers, in cases where protic linkers are used.[9,10] This would require a small amount of additional setup, but would facilitate significantly faster rate of crystallisation, potentially removing the need for solvothermal conditions. In the wider context of this thesis, this printing method has significant potential as a method for the direct, bottom-up formation of MONs and MON films, due to the picolitre amounts of ink used for each printing step and the nanoscale size of the particles produced in this setup. This could be widely applicable, as many of the most prevalent architectures used in the MON literature are capable of forming at room temperature, including the metal paddlewheel motif, 2D ZIFs, and square planar metal SBUs.

In this work, printed HKUST-1 was used for the size selective encapsulation of dyes, specifically the smaller methylene blue, whilst the larger rhodamine B was excluded and removed upon washing. Though this was intended as a simple proof-of-concept application, the versatility and ability of this printing method to incorporate multiple functionalities may facilitate its use in the preparation of lab-on-a-chip type devices for more advanced applications,[11] due to the ease in which both MOFs and MON could be positioned on such surfaces. However, it is clear that studies into printing on different surface materials, understanding crystal orientation and size distribution, and methods for improving the stability (how much the material can resist being washed or removed) of the printed material, would be necessary.

8.5. Outlook

This work has explored supramolecular 2D materials, their preparation and aspects of their programmability. Both pre- and post-synthetic modifications have been used for the modification of the structures and properties of these supramolecular nanosheets, and all of these techniques have been shown to have significant effects on the resulting dimensions of the materials produced. Moreover, these techniques can be used to impart a range of functionalities, which have been exploited for both catalysis and sensing applications in these studies. Liquid exfoliation has been further established as a widely applicable means towards the preparation of both metal-organic and hydrogen-bonded organic nanosheets from their layered analogues, and is heavily impacted by structural modifications made both pre-and post-synthetically, which can be exploited to obtain ultrathin nanosheets with maximised surface areas and exposed active sites. Reactive inkjet printing has also been demonstrated as a novel route for the patterning of surfaces with a range of MOF architectures, with great potential to be used for the bottom-up fabrication of MONs. These supramolecular 2D materials and the programmability associated with their structures represent a unique opportunity in the field of materials science, and I look forward to seeing the further development of these materials and their applications.

8.6. References

1   J. E. Moses, A. D. Moorhouse, J. E. Moses and K. B. Sharpless, *Chem. Soc. Rev.*, 2007, **8**, 1249–

1262.

2   Z. Wang and S. M. Cohen, *Chem. Soc. Rev.*, 2009, **38**, 1315–1329.

3   R. S. Forgan, *Chem. Sci.*, 2020, **11**, 4546–4562.

4   S. Mandal, S. Natarajan, P. Mani and A. Pankajakshan, *Adv. Funct. Mater.*, 2021, **31**, 1–22.

5   T. Kitao, Y. Zhang, S. Kitagawa, B. Wang and T. Uemura, *Chem. Soc. Rev.*, 2017, **46**, 3108–3133.

6   S. Li and F. Huo, *Nanoscale*, 2015, **7**, 7482–7501.

7   D. J. Ashworth, A. Cooper, M. Trueman, R. W. M. Al-Saedi, L. D. Smith, A. J. H. M. Meijer and J. A. Foster, *Chem. Eur. J.*, 2018, **24**, 17986–17996.

8   D. J. Ashworth, T. M. Roseveare, A. Schneemann, M. Flint, I. D. Bernáldes, P. Vervoorts, R. A. Fischer, L. Brammer and J. A. Foster, *Inorg. Chem.*, 2019, **58**, 10837–10845.

9   S. Kumar, S. Jain, M. Nehra, N. Dilbaghi, G. Marrazza and K. Kim, *Coord. Chem. Rev.*, 2020, **420**, 213407.

10   P. A. Julien, T. Fri and P. Julien, *Green Chem.*, 2017, **19**, 2729–2747.

11   P. Falcaro, R. Ricco, C. M. Doherty, K. Liang, A. J. Hill and M. J. Styles, *Chem. Soc. Rev.*, 2014, **43**, 5513–5560.

12   J. Luo, J. Wang, J. Zhang, S. Lai and D. Zhong, *CrystEngComm*, 2018, **20**, 5884–5898.

13   J. Yang, J. Wang, B. Hou, X. Huang, T. Wang and Y. Bao, *Chem. Eng. J.*, 2020, **399**, 125873.